



This is to certify that the

dissertation entitled

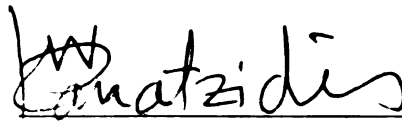
LOW-TEMPERATURE SYNTHESIS OF NEW TERNARY CHALCOGENIDE
COMPOUNDS OF Cu, Au, AND Hg USING ALKALI METAL
POLYCHALCOGENIDE FLUXES

presented by

Younbong Park

has been accepted towards fulfillment
of the requirements for

PhD degree in Chemistry



Major professor

Date 2/24/92

**LIBRARY
Michigan State
University**

**PLACE IN RETURN BOX to remove this checkout from your record.
TO AVOID FINES return on or before date due.**

DATE DUE	DATE DUE	DATE DUE
_____	_____	_____
_____	_____	_____
_____	_____	_____
_____	_____	_____
_____	_____	_____
_____	_____	_____
_____	_____	_____

MSU is An Affirmative Action/Equal Opportunity Institution

c:\cric\datedue.pm3-p.1

**LOW-TEMPERATURE SYNTHESIS OF NEW TERNARY
CHALCOGENIDE COMPOUNDS OF Cu, Au, AND Hg USING
ALKALI METAL POLYCHALCOGENIDE FLUXES**

**By
Younbong Park**

A DISSERTATION

**Submitted to
Michigan State University
in partial fulfillment of the requirements
for the degree of**

DOCTOR OF PHILOSOPHY

Department of Chemistry

1992

ABSTRACT

LOW-TEMPERATURE SYNTHESIS OF NEW TERNARY CHALCOGENIDE COMPOUNDS OF Cu, Au, AND Hg USING ALKALI METAL POLYCHALCOGENIDE FLUXES

By

Younbong Park

In last two decades great efforts have been exerted to find new materials with interesting optical, electrical, and catalytic properties. Metal chalcogenides have been studied extensively because of their interesting physical properties and rich structural chemistry, among the potential materials.

Prior to this work, most known metal chalcogenides had been synthesized at high temperature ($T > 500$ °C). Intermediate temperature synthesis in solid state chemistry was seldom pursued because of the extremely slow diffusion rates between reactants. This intermediate temperature regime could be a new synthesis condition if one looks for new materials with unusual structural features and properties. Metastable or kinetically stable compounds can be stabilized in this intermediate temperature regime, in contrast to the thermodynamically stable high temperature compounds. Molten salts, especially alkali metal polychalcogenide fluxes, can provide a route for

exploring new chalcogenide materials at intermediate temperatures. These fluxes are very reactive and melt as low as 145 °C (mp of K₂S₄).

Using these fluxes as reaction media, we have encountered many novel chalcogenide compounds with unusual structures and interesting electrical properties (semiconductors to metallic conductors). Low-dimensional polychalcogenide compounds of α -ACuQ₄ (A=K, Cs; Q=S, Se), β -KCuS₄, KAuQ₅ (Q=S, Se), K₃AuSe₁₃, Na₃AuSe₈, and CsAuSe₃ exhibit the beautiful structural diversity and bonding flexibility of the polychalcogenide ligands. In addition, many novel chalcogenide compounds of Cu, Hg, and Au with low-dimensional structures. The preparation of novel mixed-valence Cu compounds, K₂Cu₅Te₅, Cs₃Cu₈Te₁₀, Na₃Cu₄Se₄, K₃Cu₈S₄Te₂, and KCu₄S₂Te, which show interesting metallic properties, especially underscores the enormous potential of the molten salt method for the synthesis of new chalcogenide materials with interesting physical properties. The materials prepared in this study can be classified as a new class of chalcogenide compounds due to their unique structures. In this dissertation the synthesis, characterization with emphasis on structures, charge transport properties, and magnetic susceptibilities of the materials will be illustrated.

To my lovely wife, Jiyeon, and son, Sangjune

ACKNOWLEDGEMENTS

None of the work described in this dissertation would have been possible without the dedication, patient guidance and support of my research advisor, Professor Mercouri G. Kanatzidis. I would also thank the other members of my committee: Drs. Babcock, Jackson, and especially Eick for his helpful comments as a second reader.

I also thank Professor Kannewurf for charge transport property measurements, Professor Cowen for his helpful comments on magnetic susceptibility measurements, and Dr. Ward for helpful discussions on X-ray single crystal study.

I would like to extend my deepest gratitude and heart-felt thanks to all the Kanatzidis group members, who made graduate school an enjoyable learning experience.

Most importantly I am grateful to my wife, Jiyeon, and son, Sangjune for all the love and understanding they have given me over the years. Their patience and encouragements were essential to the completion of this dissertation.

I like to extend my love and thanks for being so supportive to my parents and parent-in-laws who have been behind me always.

Financial support given by BASF summer fellowship (1991), Center for Fundamental Material Research, the Department of Chemistry at Michigan State University, and National Science Foundation is greatly acknowledged and appreciated.

TABLE OF CONTENTS

	Page
List of Tables	xv
List of Figures	xxiii
I. Introduction	1
1. Discrete Molecular Metal Chalcogenide Chemistry.....	1
2. High Temperature Metal Chalcogenide Chemistry.....	6
3. Molten Salt Synthetic Methods.....	12
4. New Materials from Polychalcogenide Flux at Intermediate Temperatures.....	17
II. Synthesis and Characterization of Low-Dimensional (Poly)chalcogenide Compounds in the A/Cu/Q System (A=Na, K, Cs; Q=S, Se).....	19
1. Introduction.....	19
2. Experimental Section	20
2.1. Reagents.....	20
2.2. Physical Measurements.....	21
2.3. Synthesis.....	22
Potassium sulfide, K_2S	22
Cesium selenide, Cs_2Se	23
α -Potassium (1,2- μ_2 -tetrasulfido)cuprate(I), α - $KCuS_4$ (I).....	23

	Page
β -Potassium (1,4- μ_2 -tetrasulfido)cuprate(I), β -KCuS ₄ (II).....	24
α -Potassium (1,2- μ_2 -tetraselenido)cuprate(I), α -KCuSe ₄ (III).....	24
α -Cesium (1,2- μ_2 -tetraselenido)cuprate(I), α -CsCuSe ₄ (IV).....	24
Trisodium tetra(μ_3 -selenido)tetracuprate(I,II), Na ₃ Cu ₄ Se ₄ (V).....	25
Sodium bis(μ_4 -selenido)dicuprate(I)-copper oxide Na _{1.9} Cu ₂ Se ₂ Cu ₂ O (VI).....	25
2.4. X-ray Crystallographic Studies.....	26
3. Results and Discussion	40
3.1. Synthesis and Spectroscopy.....	40
3.2. Description of Structures.....	47
3.2.1. Structure of α -KCuS ₄ (I), α -KCuSe ₄ (III), and α -CsCuSe ₄ (IV).....	47
3.2.2. Structure of β -KCuS ₄ (II).....	54
3.2.3. Structure of Na ₃ Cu ₄ Se ₄ (V).....	58
3.2.4. Structure of Na _{1.9} Cu ₂ Se ₂ Cu ₂ O (VI).....	63
3.3. Close Structural Relationships between α - and β - [Cu(S ₄)] _n ⁿ⁻ Chains.....	68
3.4. Charge Transport Properties of α -KCuSe ₄ (III) and Na _{1.9} Cu ₂ Se ₂ Cu ₂ O (VI).....	71

	Page
III. Low-Dimensional Compounds Incorporating (Poly)chalcogenide Ligands in the A/Au/Q (A=Na, K, Cs; Q=S, Se) Systems.....	76
1. Introduction.....	76
2. Experimental Section.....	77
2.1. Reagents.....	77
2.2. Physical Measurements.....	77
2.3. Synthesis.....	78
Potassium (1,5- μ_2 -pentasulfido)aurate(I), K ₂ AuS ₅ (I).....	79
Potassium (1,5- μ_2 -pentaselenido)aurate(I), K ₂ AuSe ₅ (II).....	79
Cesium (1,3- μ_2 -triselenido)aurate(I), CsAuSe ₃ (III).....	79
Tripotassium bis(pentaseleido) (1,3- μ_2 -triselenido)aurite(III), K ₃ AuSe ₁₃ (IV).....	80
Potassium bis(μ_2 -selenido)aurite(III), KAuSe ₂ (V).....	80
Trisodium bis(triselenido)(μ_2 -diselenido) aurite(III), Na ₃ AuSe ₈ (VI).....	81
Potassium bis(μ_2 -selenido)aurite(III), NaAuSe ₂ (VII).....	81
2.4. X-ray Crystallographic Studies.....	82
3. Results and Discussion	101
3.1. Synthesis and Spectroscopy.....	101
3.2. Description of Structures.....	107
3.2.1. Structure of K ₂ AuS ₅ (I) and K ₂ AuSe ₅ (II).....	107
3.2.2. Structure of CsAuSe ₃ (III).....	112

	Page
3.2.3. Structure of K_3AuSe_{13} (IV).....	115
3.2.4. Structure of $KAuSe_2$ (V).....	120
3.2.5. Structure of Na_3AuSe_8 (VI).....	122
3.2.6. Structure of $NaAuSe_2$ (VII).....	126
3.3. Structures.....	130
IV. Molten Salt Synthesis of Low-Dimensional Ternary Chalcogenides. Novel Structure Types in the A/Hg/Q System (A=K, Cs; Q=S, Se).....	136
1. Introduction.....	136
2. Experimental Section	137
2.1. Reagents.....	137
2.2. Physical Measurements.....	137
2.3. Synthesis.....	138
Dipotassium tetra(μ_2 -sulfido)trimercurate(II), $K_2Hg_3S_4$ (I).....	138
Dipotassium tetra(μ_2 -selenido)trimercurate(II), $K_2Hg_3Se_4$ (II).....	139
Dicesium tetra(μ_2 -selenido)trimercurate(II), $Cs_2Hg_3Se_4$ (III).....	139
Dipotassium hepta(μ_2 -sulfido)hexamercurate(II), $K_2Hg_6S_7$ (IV).....	140
Dicesium hepta(μ_2 -selenido)hexamercurate(II), $Cs_2Hg_6Se_7$ (V).....	140
2.4. X-ray Crystallographic Studies.....	141
3. Results and Discussion.....	153
3.1. Synthesis.....	153

	Page
3.2. Description of Structures.....	155
3.2.1. Structure of $K_2Hg_3S_4(I)$, $K_2Hg_3Se_4(II)$, and $Cs_2Hg_3Se_4(III)$	155
3.2.2. Structures of $K_2Hg_6S_7(IV)$ and $Cs_2Hg_6Se_7(V)$	162
3.3. Structures.....	170
V. Synthesis and Characterization of Novel Layered Compounds of $K_2Cu_5Te_5$ and $NaCuTe$.....	172
1. Introduction.....	172
2. Experimental Section	173
2.1. Reagents.....	173
2.2. Physical Measurements.....	173
2.3. Synthesis.....	175
Dipotassium (μ_8 -ditelluro)tris(μ_4 -telluro) pentacuprate(I,II), $K_2Cu_5Te_5(I)$	175
Sodium (μ_4 -telluro)cuprate(I), $NaCuTe(II)$	175
2.4. X-ray Crystallographic Studies.....	176
3. Results and Discussion.....	182
3.1. Synthesis.....	182
3.2. Description of Structures.....	183
3.2.1. Structure of $K_2Cu_5Te_5(I)$	183
3.2.2. Structure of $NaCuTe(II)$	190
3.3. Structural Relationships of the $[Cu_5Te_5]_n^{2n-}$ Layers in (I) to Those of $[CuTe]_n^{n-}$ in (II) and $CuTe$	192
3.4. Charge Transport Properties of $K_2Cu_5Te_5(I)$	194
3.5. Magnetic Susceptibility of $K_2Cu_5Te_5(I)$	197

	Page
VI. Synthesis and Characterization of $K_4Cu_8Te_{11}$ and $Cs_3Cu_8Te_{10}$: Novel Solid State Chalcogenide Compounds with a Dodecahedral Cluster as a Building Block.....	200
1. Introduction.....	200
2. Experimental Section.....	201
2.1. Reagents.....	201
2.2. Physical Measurements.....	201
2.3. Synthesis.....	203
Tetrapotassium bis(μ_4 -ditelluro)tris(μ_8 -ditelluro) (μ_4 -telluro) octacuprate(I), $K_4Cu_8Te_{11}$ (I).....	203
Tricesium bis(μ_4 -ditelluro)bis(μ_8 -ditelluro) bis(μ_4 -telluro) octacuprate(I,II), $Cs_3Cu_8Te_{10}$ (II).....	203
2.4. X-ray Crystallographic Studies.....	204
3. Results and Discussion.....	212
3.1. Synthesis.....	212
3.2. Description of Structures.....	214
3.2.1. Structure of $K_4Cu_8Te_{11}$ (I).....	214
3.2.2. Structure of $Cs_3Cu_8Te_{10}$ (II).....	223
3.3. Comparison of $Cu_8(Te_2)_6$ Cluster Size in $K_4Cu_8Te_{11}$ (I) and $Cs_3Cu_8Te_{10}$ (II).....	228
3.4. Charge Transport Properties of $K_4Cu_8Te_{11}$ (I) and $Cs_3Cu_8Te_{10}$ (II).....	231
3.5. Magnetic Susceptibility of $Cs_3Cu_8Te_{10}$ (II).....	236

	Page
VII. Synthesis and Characterization of Mixed Chalcogenide	
Compounds of $\text{KCu}_4\text{S}_2\text{Te}$, $\text{K}_3\text{Cu}_8\text{S}_4\text{Te}_2$, and $\text{Cu}_{17.6}\text{Te}_8\text{S}_{26}$	238
1. Introduction.....	238
2. Experimental Section.....	239
2.1. Reagents.....	239
2.2. Physical Measurements.....	239
2.3. Synthesis.....	243
Potassium bis(μ_4 -sulfido)(μ_8 -telluro) tetracuprate(I,II), $\text{KCu}_4\text{S}_2\text{Te}$ (I).....	243
Tripotassium tetra(μ_4 -sulfido)bis(μ_6 -telluro) octacuprate(I,II) $\text{K}_3\text{Cu}_8\text{S}_4\text{Te}_2$ (II).....	243
Copper tellurium sulfide, $\text{Cu}_{17.6}\text{Te}_8\text{S}_{26}$ (III).....	244
2.4. X-ray Crystallographic Studies.....	244
3. Results and Discussion.....	253
3.1. Synthesis.....	253
3.2. Description of Structures.....	255
3.2.1. Structure of $\text{KCu}_4\text{S}_2\text{Te}$ (I).....	255
3.2.2. Structure of $\text{K}_3\text{Cu}_8\text{S}_4\text{Te}_2$ (II).....	261
3.2.3. Structure of $\text{Cu}_{17.6}\text{Te}_8\text{S}_{26}$ (III).....	268
3.3. Charge Transport Properties of $\text{KCu}_4\text{S}_2\text{Te}$ (I).....	273
3.4. Magnetic Susceptibility of $\text{KCu}_4\text{S}_2\text{Te}$ (I), $\text{K}_3\text{Cu}_8\text{S}_4\text{Te}_2$ (II), and $\text{Cu}_{17.6}\text{Te}_8\text{S}_{26}$ (III).....	276

	Page
VIII. AuCuSe₄, a Novel Mixed Metal Chalcogenide Compound	
Incorporating Se ₃ ²⁻ ligands.....	283
1. Introduction.....	283
2. Experimental Section	284
2.1. Reagents.....	284
2.2. Physical Measurements.....	284
2.3. Synthesis.....	285
Copper gold tetraselenide, AuCuSe ₄ (I).....	285
2.4. X-ray Crystallographic Studies.....	286
3. Results and Discussion.....	291
3.1. Synthesis and Spectroscopy.....	291
3.2. Description of Structure.....	294
IX. Conclusion.....	302
List of References.....	304

LIST OF TABLES

	Page
1. Types of Metal Polychalcogenide Complex Containing Q_2^{2-}	3
2. Types of Metal Polychalcogenide Complex Containing Q_x^{2-} ($X \geq 3$).....	5
3. Melting Points ($^{\circ}C$) of Some Known Alkali Metal Polychalcogenides.....	16
4. Calculated and Observed Powder Diffraction Pattern for α - $KCuS_4$	27
5. Calculated and Observed Powder Diffraction Pattern for β - $KCuS_4$	28
6. Calculated and Observed Powder Diffraction Pattern for α - $KCuSe_4$	29
7. Calculated and Observed Powder Diffraction Pattern for α - $CsCuSe_4$	30
8. Calculated and Observed Powder Diffraction Pattern for $Na_3Cu_4Se_4$	31
9. Calculated and Observed Powder Diffraction Pattern for $Na_{1.9}Cu_2Se_2 \cdot Cu_2O$	32
10. Summary of Crystallographic Data for α - $KCuS_4$, β - $KCuS_4$, α - $KCuSe_4$, α - $CsCuSe_4$, $Na_3Cu_4Se_4$, and $Na_{1.9}Cu_2Se_2 \cdot Cu_2O$	35
11. Fractional Atomic Coordinates and B_{eq} Values for α - $KCuS_4$ with Their Estimated Standard Deviations in Parentheses.....	37

	Page
12. Fractional Atomic Coordinates and B_{eq} Values for β -KCuS ₄ with Their Estimated Standard Deviations in Parentheses.....	37
13. Fractional Atomic Coordinates and B_{eq} Values for α -KCuSe ₄ with Their Estimated Standard Deviations in Parentheses.....	38
14. Fractional Atomic Coordinates and B_{eq} Values for α -CsCuSe ₄ with Their Estimated Standard Deviations in Parentheses.....	38
15. Fractional Atomic Coordinates and B_{eq} Values for Na ₃ Cu ₄ Se ₄ with Their Estimated Standard Deviations in Parentheses.....	39
16. Fractional Atomic Coordinates and B_{eq} Values for Na _{1.9} Cu ₂ Se ₂ ·Cu ₂ O with Their Estimated Standard Deviations in Parentheses.....	39
17. Frequencies (cm ⁻¹) of Spectral Absorption of (I), (II), (III), and (IV) Due to Q-Q and M-Q Stretching Vibrations.....	46
18. Selected Bond Distances (Å) and Angles (Deg) in α -KCuS ₄ with Standard Deviations in Parentheses.....	51
19. Selected Bond Distances (Å) and Angles (Deg) in α -KCuSe ₄ with Standard Deviations in Parentheses.....	52
20. Selected Bond Distances (Å) and Angles (Deg) in α -CsCuSe ₄ with Standard Deviations in Parentheses.....	53
21. Selected Bond Distances (Å) and Angles (Deg) in β -KCuS ₄ with Standard Deviations in Parentheses.....	57
22. Selected Bond Distances (Å) and Angles (Deg) in Na ₃ Cu ₄ Se ₄ with Standard Deviations in Parentheses.....	62
23. Selected Bond Distances (Å) and Angles (Deg) in Na _{1.9} Cu ₂ Se ₂ ·Cu ₂ O with Standard Deviations in Parentheses.....	66

	Page
24. Calculated and Observed Powder Diffraction Pattern for KAuS_5	83
25. Calculated and Observed Powder Diffraction Pattern for KAuSe_5	84
26. Calculated and Observed Powder Diffraction Pattern for CsAuSe_3	85
27. Calculated and Observed Powder Diffraction Pattern for $\text{K}_3\text{AuSe}_{13}$	86
28. Calculated and Observed Powder Diffraction Pattern for KAuSe_2	88
29. Calculated and Observed Powder Diffraction Pattern for Na_3AuSe_8	89
30. Calculated and Observed Powder Diffraction Pattern for NaAuSe_2	91
31. Summary of Crystallographic Data for KAuS_5 , KAuSe_5 , CsAuSe_3 , $\text{K}_3\text{AuSe}_{13}$, KAuSe_2 , Na_3AuSe_8 , and NaAuSe_2	93
32. Fractional Atomic Coordinates and B_{eq} Values for KAuS_5 with Their Estimated Standard Deviations in Parentheses.....	96
33. Fractional Atomic Coordinates and B_{eq} Values for KAuSe_5 with Their Estimated Standard Deviations in Parentheses.....	96
34. Fractional Atomic Coordinates and B_{eq} Values for CsAuSe_3 with Their Estimated Standard Deviations in Parentheses.....	97
35. Fractional Atomic Coordinates and B_{eq} Values for $\text{K}_3\text{AuSe}_{13}$ with Their Estimated Standard Deviations in Parentheses.....	98

	Page
36. Fractional Atomic Coordinates and B_{eq} Values for KAuSe_2 with Their Estimated Standard Deviations in Parentheses.....	99
37. Fractional Atomic Coordinates and B_{eq} Values for Na_3AuSe_8 with Their Estimated Standard Deviations in Parentheses	99
38. Fractional Atomic Coordinates and B_{eq} Values for NaAuSe_2 with Their Estimated Standard Deviations in Parentheses.....	100
39. Frequencies (cm^{-1}) of Spectral Absorption of (I), (II), (III), (IV), (V), (VI), and (VII) Due to Q-Q and M-Q Stretching Vibrations.....	103
40. Selected Bond Distances (\AA) and Angles (Deg) in KAuS_5 and KAuSe_5 with Standard Deviations in Parentheses.....	111
41. Selected Bond Distances (\AA) and Angles (Deg) in CsAuSe_3 with Standard Deviations in Parentheses.....	114
42. Selected Bond Distances (\AA) and Angles (Deg) in $\text{K}_3\text{AuSe}_{13}$ with Standard Deviations in Parentheses.....	119
43. Selected Bond Distances (\AA) and Angles (Deg) in KAuSe_2 with Standard Deviations in Parentheses.....	120
44. Selected Bond Distances (\AA) and Angles (Deg) in Na_3AuSe_8 with Standard Deviations in Parentheses.....	124
45. Selected Bond Distances (\AA) and Angles (Deg) in NaAuSe_2 with Standard Deviations in Parentheses.....	128
46. Calculated and Observed Powder Diffraction Pattern for $\text{K}_2\text{Hg}_3\text{S}_4$	142
47. Calculated and Observed Powder Diffraction Pattern for $\text{K}_2\text{Hg}_3\text{Se}_4$	143

	Page
48. Calculated and Observed Powder Diffraction Pattern for $\text{Cs}_2\text{Hg}_3\text{Se}_4$	144
49. Calculated and Observed Powder Diffraction Pattern for $\text{K}_2\text{Hg}_6\text{S}_7$	145
50. Calculated and Observed Powder Diffraction Pattern for $\text{Cs}_2\text{Hg}_6\text{Se}_7$	146
51. Summary of Crystallographic Data for $\text{K}_2\text{Hg}_3\text{S}_4$, $\text{K}_2\text{Hg}_3\text{Se}_4$, $\text{Cs}_2\text{Hg}_3\text{Se}_4$, $\text{K}_2\text{Hg}_6\text{S}_7$, and $\text{Cs}_2\text{Hg}_6\text{Se}_7$	148
52. Fractional Atomic Coordinates and B_{eq} Values for $\text{K}_2\text{Hg}_3\text{S}_4$ with Their Estimated Standard Deviations in Parentheses.....	150
53. Fractional Atomic Coordinates and B_{eq} Values for $\text{K}_2\text{Hg}_3\text{Se}_4$ with Their Estimated Standard Deviations in Parentheses.....	150
54. Fractional Atomic Coordinates and B_{eq} Values for $\text{Cs}_2\text{Hg}_3\text{Se}_4$ with Their Estimated Standard Deviations in Parentheses.....	151
55. Fractional Atomic Coordinates and B_{eq} Values for $\text{K}_2\text{Hg}_6\text{S}_7$ with Their Estimated Standard Deviations in Parentheses.....	151
56. Fractional Atomic Coordinates and B_{eq} Values for $\text{Cs}_2\text{Hg}_6\text{Se}_7$ with Their Estimated Standard Deviations in Parentheses.....	152
57. Selected Bond Distances (Å) and Angles (Deg) in $\text{K}_2\text{Hg}_3\text{S}_4$ with Standard Deviations in Parentheses.....	159
58. Selected Bond Distances (Å) and Angles (Deg) in $\text{K}_2\text{Hg}_3\text{Se}_4$ with Standard Deviations in Parentheses.....	160
59. Selected Bond Distances (Å) and Angles (Deg) in $\text{Cs}_2\text{Hg}_3\text{Se}_4$ with Standard Deviations in Parentheses.....	161

	Page
60. Selected Bond Distances (Å) and Angles (Deg) in $K_2Hg_6S_7$ with Standard Deviations in Parentheses.....	168
61. Selected Bond Distances (Å) and Angles (Deg) in $Cs_2Hg_6Se_7$ with Standard Deviations in Parentheses.....	169
62. Calculated and Observed Powder Diffraction Pattern for $K_2Cu_5Te_5$	177
63. Calculated and Observed Powder Diffraction Pattern for $NaCuTe$	178
64. Summary of Crystallographic Data for $K_2Cu_5Te_5$ and $NaCuTe$	180
65. Fractional Atomic Coordinates and B_{eq} Values for $K_2Cu_5Te_5$ with Their Estimated Standard Deviations in Parentheses.....	181
66. Fractional Atomic Coordinates and B_{eq} Values for $NaCuTe$ with Their Estimated Standard Deviations in Parentheses.....	181
67. Selected Bond Distances (Å) and Angles (Deg) in $K_2Cu_5Te_5$ with Standard Deviations in Parentheses.....	189
68. Selected Bond Distances (Å) and Angles (Deg) in $NaCuTe$ with Standard Deviations in Parentheses.....	190
69. Calculated and Observed Powder Diffraction Pattern for $K_4Cu_8Te_{11}$	205
70. Calculated and Observed Powder Diffraction Pattern for $Cs_3Cu_8Te_{10}$	207
71. Summary of Crystallographic Data for $K_4Cu_8Te_{11}$ and $Cs_3Cu_8Te_{10}$	209
72. Fractional Atomic Coordinates and B_{eq} Values for $K_4Cu_8Te_{11}$ with Their Estimated Standard Deviations in Parentheses.....	210

	Page
73. Fractional Atomic Coordinates and B_{eq} Values for $\text{Cs}_3\text{Cu}_8\text{Te}_{10}$ with Their Estimated Standard Deviations in Parentheses.....	211
74. Selected Bond Distances (\AA) and Angles (Deg) in $\text{K}_4\text{Cu}_8\text{Te}_{11}$ with Standard Deviations in Parentheses.....	220
75. Selected Bond Distances (\AA) and Angles (Deg) in $\text{Cs}_3\text{Cu}_8\text{Te}_{10}$ with Standard Deviations in Parentheses.....	227
76. Selected Metric Data for the $\text{KCu}_8(\text{Te}_2)_6$ Cluster (A) and the $\text{CsCu}_8(\text{Te}_2)_6$ Cluster (B).....	229
77. Calculated and Observed Powder Diffraction Pattern for $\text{KCu}_4\text{S}_2\text{Te}$	245
78. Calculated and Observed Powder Diffraction Pattern for $\text{K}_3\text{Cu}_8\text{S}_4\text{Te}_2$	246
79. Calculated and Observed Powder Diffraction Pattern for $\text{Cu}_{17.6}\text{Te}_8\text{S}_{26}$	247
80. Summary of Crystallographic Data for $\text{KCu}_4\text{S}_2\text{Te}$, $\text{K}_3\text{Cu}_8\text{S}_4\text{Te}_2$, and $\text{Cu}_{17.6}\text{Te}_8\text{S}_{26}$	250
81. Fractional Atomic Coordinates and B_{eq} Values for $\text{KCu}_4\text{S}_2\text{Te}$ with Their Estimated Standard Deviations in Parentheses.....	251
82. Fractional Atomic Coordinates and B_{eq} Values for $\text{K}_3\text{Cu}_8\text{S}_4\text{Te}_2$ with Their Estimated Standard Deviations in Parentheses.....	251
83. Fractional Atomic Coordinates and B_{eq} Values for $\text{Cu}_{17.6}\text{Te}_8\text{S}_{26}$ with Their Estimated Standard Deviations in Parentheses.....	252
84. Selected Bond Distances (\AA) and Angles (Deg) in $\text{KCu}_4\text{S}_2\text{Te}$ with Standard Deviations in Parentheses.....	260

	Page
85. Selected Bond Distances (Å) and Angles (Deg) in $K_3Cu_8S_4Te_2$ with Standard Deviations in Parentheses.....	266
86. Selected Bond Distances (Å) and Angles (Deg) in $Cu_{17.6}Te_8S_{26}$ with Standard Deviations in Parentheses.....	272
87. Calculated and Observed Powder Diffraction Pattern for $AuCuSe_4$	287
88. Summary of Crystallographic Data for $AuCuSe_4$	289
89. Fractional Atomic Coordinates and B_{eq} Values for $AuCuSe_4$ with Their Estimated Standard Deviations in Parentheses.....	290
90. Selected Bond Distances (Å) and Angles (Deg) in $AuCuSe_4$ with Standard Deviations in Parentheses.....	300

LIST OF FIGURES

	Page
1. ORTEP representation of the unit cell of (A) Zinc-blende (ZnS) and (B) Wurtzite (ZnS). Open circles are S atoms and octant-shaded ellipsoids are Zn atoms.	8
2. ORTEP representation of the unit cell of (A) TiS (NIAs-type) and (B) TiS ₂ (CdI ₂ -type). Open circles are S atoms and octant-shaded ellipsoids are Ti atoms.	9
3. ORTEP representation of the unit cell of (A) Pyrite (FeS ₂) and (B) Marcasite (FeS ₂). Open circles are S atoms and octant-shaded ellipsoids are Fe atoms.	11
4. Phase diagrams of (A) Na ₂ S/S ⁴⁷ and (B) K ₂ S/S ⁴⁸ systems.	14
5. Far-IR spectra of (A) α-KCuS ₄ , (B) β-KCuS ₄ , (C) α-KCuSe ₄ , and (IV) α-CsCuSe ₄	44
6. Stereoview of the unit cell of α-ACuQ ₄ (A=K, Cs; Q=S, Se). The alkali atoms have been omitted for clarity.	48
7. ORTEP representation of the one-dimensional infinite α-[CuQ ₄] _n ⁿ⁻ chain with labeling scheme.	49
8. Stereoview of the unit cell of β-KCuS ₄ . The alkali atoms have been omitted for clarity.	55
9. ORTEP representation of the one-dimensional infinite β-[CuS ₄] _n ⁿ⁻ chain with labeling scheme.	56
10. ORTEP representation of the unit cell of Na ₃ Cu ₄ Se ₄	59

	Page
11. Two views of the one-dimensional structure of $[\text{Cu}_4\text{Se}_4]_n^{3n-}$ with labeling scheme.	60
12. ORTEP representation of the unit cell of $\text{Na}_{1.9}\text{Cu}_2\text{Se}_2\text{Cu}_2\text{O}$ with labeling scheme.	64
13. ORTEP representation of (A) $[\text{CuSe}]_n^{n-}$ layer (B) Cu_2O layer viewed down [001] direction. Octant-shaded ellipsoids are Cu atoms and open circles are Se and O atoms.	65
14. Schematic representation of the structural transformation of (A) the $\alpha\text{-}[\text{CuS}_4]_n^{n-}$ chain to (D) the $\beta\text{-}[\text{CuS}_4]_n^{n-}$ chain via (B) the hypothetical $[\text{CuS}_4]_n^{n-}$ intermediate which is similar in structure to (C) the known $[\text{AgSe}_4]_n^{n-}$ chain.	69
15. Four probe electrical conductivity (Scm^{-1}) data as a function of temperature for a single crystal of $\alpha\text{-KCuSe}_4$	72
16. Four probe resistivity ($\mu\Omega\text{-cm}$) data as a function of temperature for a single crystal of $\text{Na}_{1.9}\text{Cu}_2\text{Se}_2\text{Cu}_2\text{O}$	73
17. Thermoelectric power ($\mu\text{V/K}$) data as a function of temperature for a single crystal of $\text{Na}_{1.9}\text{Cu}_2\text{Se}_2\text{Cu}_2\text{O}$	74
18. Far-IR spectra of (A) KAuS_5 , (B) CsAuSe_3 , and (C) KAuSe_5	104
19. Far-IR spectra of (A) $\text{K}_3\text{AuSe}_{13}$ and (B) Na_3AuSe_8	105
20. Far-IR spectra of (A) KAuSe_2 and (B) NaAuSe_2	106
21. ORTEP representation of the unit cell of KAuQ_5 (Q=S, Se).	108
22. One-dimensional structure of $[\text{AuQ}_5]_n^{n-}$ chains, showing the mode of dimerization.	110

	Page
23. ORTEP representation of two axial views of CsAuSe ₃ : (A) viewed down [100] direction, (B) viewed down [011] direction.	113
24. Stereoview of the unit cell of K ₃ AuSe ₁₃	116
25. ORTEP representation of two views of the one-dimensional [AuSe ₁₃] _n ³ⁿ⁻ chain.	117
26. Coordination environments of K atoms with labeling scheme.	118
27. ORTEP representation of the unit cell of KAuSe ₂	121
28. ORTEP representation of two views of the one-dimensional [AuSe ₈] _n ³ⁿ⁻ chain.	123
29. Coordination environments of Na atoms with labeling scheme.	125
30. ORTEP representation of the layered structure of [AuSe ₂] _n ⁿ⁻ , looking perpendicular to the layer.	127
31. ORTEP representation of the unit cell of NaAuSe ₂	129
32. Schematic representation of the counter cation size effect on structures of [AuSe ₂] _n ⁿ⁻ : (A) layer structure of [AuSe ₂] _n ⁿ⁻ in (VII) vs (B) chain structure of [AuSe ₂] _n ⁿ⁻ in (V).	134
33. Two axial views of the unit cell of A ₂ Hg ₃ Q ₄ (A=K, Cs; Q=S, Se): (A) <i>b</i> -axial view and (B) projection view along (001) plane.	156
34. Two views of the one-dimensional structure of [Hg ₃ Q ₄] _n ²ⁿ⁻ with labeling scheme.	157
35. Stereoview of the unit cell of K ₂ Hg ₆ S ₇	163
36. Stereoview of the unit cell of Cs ₂ Hg ₆ Se ₇	164

	Page
37. ORTEP representation of (A) the unit cell of $K_2Hg_6S_7$ and (B) the unit cell of $Cs_2Hg_6Se_7$. The origin of the unit cell of $Cs_2Hg_6Se_7$ has been moved to (1/2, 0, 0) for clear comparison.	165
38. ORTEP representation and labeling scheme of the unit cell of $K_2Cu_5Te_5$	184
39. Structural relationship of the $[Cu_5Te_5]_n^{2n-}$ layer to those of CuTe (above) and $[CuTe]_n^{n-}$ (below) as a function of oxidation state.	185
40. Two axial views of the layered structure of CuTe: (A) <i>a</i> -axial view and (B) <i>b</i> -axial view.	186
41. ORTEP representation of the layered structure of NaCuTe.	191
42. ORTEP representation of (A) the $[CuTe]_n^{n-}$ layer and (B) the unit cell of KCuTe.	193
43. Four probe resistivity ($\mu\Omega\cdot\text{cm}$) data as a function of temperature for a single crystal of $K_2Cu_5Te_5$	195
44. Variable-temperature thermoelectric power ($\mu\text{V/K}$) data for a single crystal of $K_2Cu_5Te_5$	196
45. Variable-temperature magnetic susceptibility (emu/mol) data for polycrystalline $K_2Cu_5Te_5$. Insert: χ_m^{-1} (mol/emu) vs T.	198
46. ORTEP representation of the unit cell of $K_4Cu_8Te_{11}$ viewed down [010] direction.	215

	Page
47. ORTEP representation and labeling scheme of (A) the $[\text{KCu}_8\text{Te}_{12}]$ dodecahedral cluster, (B) two edge-shared $[\text{KCu}_8\text{Te}_{12}]$ units with capping Te^{2-} ions, (C) a one-dimensional column of edge-shared double clusters, and (D) the empty Cu_8Te_8 cluster.	216
48. ORTEP representation of (A) sideview and (B) top view of one Cu/Te layer. The $\text{Cu}_8(\text{Te}_2)_6$ and Cu_8Te_8 clusters are shaded for emphasis.	219
49. ORTEP representation of the unit cell of $\text{Cs}_3\text{Cu}_8\text{Te}_{10}$	224
50. ORTEP representation of (A) sideview and (B) top view of one $[\text{Cu}_8\text{Te}_{10}]_n^{3n-}$ layer. The $\text{Cu}_8(\text{Te}_2)_6$ and Cu_8Te_8 clusters are shaded for emphasis.	225
51. Four probe electrical conductivity (Scm^{-1}) data as a function of temperature for a single crystal of $\text{K}_4\text{Cu}_8\text{Te}_{11}$	232
52. Four probe resistivity ($\mu\Omega\text{-cm}$) data as a function of temperature for a single crystal of $\text{Cs}_3\text{Cu}_8\text{Te}_{10}$	233
53. Variable-temperature thermoelectric power ($\mu\text{V/K}$) data for a single crystal of $\text{Cs}_3\text{Cu}_8\text{Te}_{10}$	235
54. Variable-temperature magnetic susceptibility (emu/mol) data for polycrystalline $\text{Cs}_3\text{Cu}_8\text{Te}_{10}$. Insert: χ_m^{-1} (mol/emu) vs T.	237
55. Magnetization (emu) data for polycrystalline $\text{Cu}_{17.6}\text{Te}_8\text{S}_{26}$ as a function of applied magnetic field (H).	241

	Page
56. ORTEP representation of (A) the unit cell and (B) the layered framework of $\text{KCu}_4\text{S}_2\text{Te}$. The origin of the unit cell has been moved to (0,0,1/2) in (A) for clear view of a building unit.	256
57. ORTEP representation of the $[\text{Cu}_4\text{S}_2\text{Te}]_n^{n-}$ layer. Black circles are Te, open circles are S, and crossed circles are Cu atoms.	257
58. ORTEP representation of the unit cell of $\text{K}_3\text{Cu}_8\text{S}_4\text{Te}_2$	262
59. ORTEP representation and labeling scheme of the $[\text{Cu}_6\text{S}_4\text{Te}_2]_n^{3n-}$ layer.	263
60. ORTEP representation and labeling scheme of the unit cell of $\text{Cu}_{17.6}\text{Te}_8\text{S}_{26}$	269
61. Coordination environments of (A) Cu(1) atom, (B) Cu(2) atom, (C) Te atom, (D) S(1) atom, and (E) S(2) atom in $\text{Cu}_{17.6}\text{Te}_8\text{S}_{26}$	271
62. Four probe resistivity ($\mu\Omega\cdot\text{cm}$) data as a function of temperature for a single crystal of $\text{KCu}_4\text{S}_2\text{Te}$	274
63. Variable-temperature thermoelectric power ($\mu\text{V}/\text{K}$) data for a single crystal of $\text{KCu}_4\text{S}_2\text{Te}$	275
64. Variable-temperature magnetic susceptibility (emu/mol) data for polycrystalline $\text{KCu}_4\text{S}_2\text{Te}$. Insert: χ_m^{-1} (mol/emu) vs T.	277
65. Variable-temperature magnetic susceptibility (emu/mol) data for polycrystalline $\text{K}_3\text{Cu}_8\text{S}_4\text{Te}_2$. Insert: χ_m^{-1} (mol/emu) vs T.	278
66. Variable-temperature magnetic susceptibility (emu/mol) data for polycrystalline $\text{Cu}_{17.6}\text{Te}_8\text{S}_{26}$	280
67. Temperature dependence of calculated magnetic moments (BM) of $\text{Cu}_{17.6}\text{Te}_8\text{S}_{26}$	281

	Page
68. Far-IR spectrum of AuCuSe ₄	293
69. ORTEP representation of the unit cell of AuCuSe ₄ . Crossed circles are Cu atoms, black circles are Au, and open circles are Se atoms.	295
70. Two views of the [Au(Se ₃)(Se)] _n ⁿ⁻ chains with labeling scheme.	296
71. ORTEP representation and labeling scheme of one layer fragment of AuCuSe ₄	297

CHAPTER 1

Introduction

For the last two decades the synthetic chemistry of new metal chalcogenide compounds has been developed considerably due to their interesting electrical, optical, and catalytic properties as well as unusual structural features. Most metal chalcogenide compounds known to date have been synthesized either at ambient temperature or at temperatures higher than 500 °C^{1,2}. However, there is increased interest in new and unusual synthetic conditions which may help to stabilize new chalcogenide materials with interesting physical properties and unusual structure that would not be possible by conventional techniques. One possible synthesis approach we have undertaken is the use of molten salts at intermediate temperature regime (150 °C < T < 500 °C).

1. Discrete Molecular Metal Chalcogenide Chemistry

Molecular metal chalcogenide chemistry, especially metal sulfide chemistry, has been developed extensively due to (a) potential application as hydrodesulfurization catalysts^{3,4}, (b) the importance of some M/S complexes in modeling bioinorganic systems⁵, and (c) the structural diversity associated with polysulfide (S_x²⁻) ligands. Recently there also have been increased interests in the heavier chalcogenide (Se, Te) compounds.^{6,7} This has been stimulated

mainly by their distinct structural chemistry and potential uses as low temperature precursor compounds to either new or old, but useful electronic solid state materials^{6,8}. Molecular metal chalcogenide compounds generally have been synthesized by reacting metal salts with alkali metal polychalcogenides (A_2Q_x) in polar non-aqueous solvents at ambient temperature as shown in eq 1.6, 7(a)



The anionic M/Q complexes are crystallized from solution with large organic cations such as R_4N^+ and R_4P^+ . Less common method such as the reaction of low valent metal carbonyls with a polychalcogenide source also has been used.^{7(b),9}

Molecular metal chalcogenide compounds exhibit structural diversity featuring various polychalcogenide species, from monochalcogenides (Q^{2-} ; in $[Na_2Fe_{18}S_{30}]^{8-}$,¹⁰) to nanochalcogenides (Q_9^{2-} ; in $[Au(S_9)]^{1-}$,¹¹). The usual binding modes of polychalcogenides are numerous and are given in Tables 1 and 2. They can assume bridging or chelating modes or bind to multiple metals simultaneously. The internal Q atoms of the Q_x^{2-} ligands are considered to have nearly zero formal charges and will be less likely to participate in bonding interactions with other metals than the negatively charged terminal Q atoms. However, it has been found that not only terminal atoms but also internal atoms are available for bonding to metal ions. The ability of chalcogens to bind to multiple metal centers and to catenate, gives rise to the enormous structural diversity and bonding characteristics of the polychalcogenide compounds.

Table 1. Types of Metal Polychalcogenide Complexes Containing Q_2^{2-}

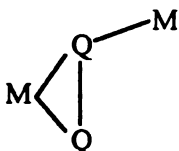
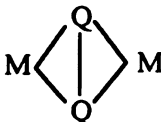
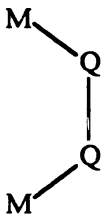
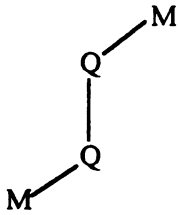
Type	Example	Reference
	$(Ph_4P)_2[W_2Se_4(Se_2)(Se_4)]$	12
	$(\eta^5-C_5H_5)Fe(CO)_2(Se_2)Cr(CO)_2(\eta^5-C_5H_5)$	13
	$(\eta^5-C_5H_5)_2Cr_2(CO)_4Se_2$	14
	$(\eta^5-C_5H_4Me)_2V_2Se(Se_2)_2$	15
	$[(\eta^5-C_5H_4Me)_2Ti]_2(Se_2)_2$	16

Table 1. (cont'd)

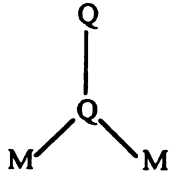
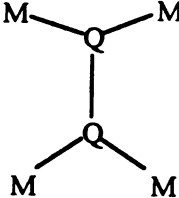
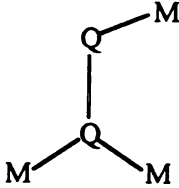
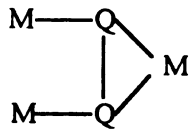
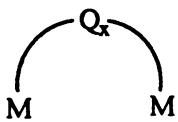
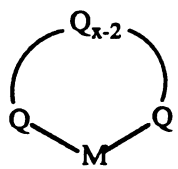
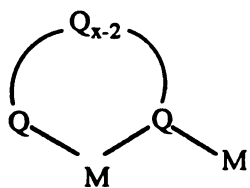
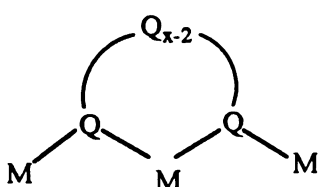
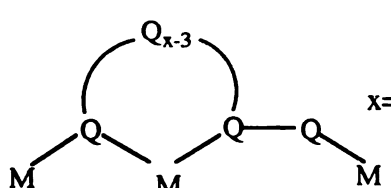
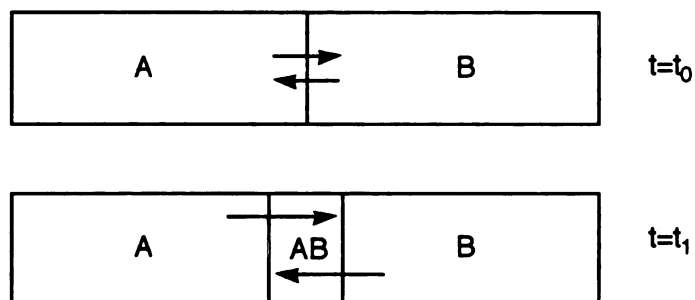
Type	Example	Reference
	[K-2,2,2-crypt] ₂ [Mo ₄ (Te ₂) ₅ (Te ₃) ₂ (en) ₄]	17
	[NBu ₄] ₄ [Hg ₄ Te ₁₂]	18
	[{(η ⁵ -C ₅ H ₅)(CO) ₂ Fe} ₃ (Se ₂)] [BF ₄]	19
	[(CO) ₅ W(μ-Te ₂)] [W(CO) ₅] ₂	20

Table 2. Types of Metal Polychalcogenide Complexes Containing Q_x^{2-} ($x \geq 3$)

Type	Q_x^{2-}	Example	Reference
	x=3	$(Ph_4P)_2[Au_2(Se_3)(Se_2)]$	21
	x=4	$(Ph_4P)_2[Au_2(Se_2)(Se_4)_2]$	21
	x=5	$(Ph_4P)_2[In_2(Se_4)_4(Se_5)]$	22
	x=3	$(Ph_4P)_2[W_2Se_4(Se_3)_2]$	12
	x=4	$[(Ph_3P)_2N]_2[Au_2Se_2(Se_4)_2]$	23
	x=5	$(Ph_4P)_2[Fe_2Se_2(Se_5)_2]$	24
	x=4	$(Ph_4P)_2[Hg_2(Se_4)_3]$	25
	x=4	$(Pr_4N)_2[Ag_4(Se_4)_3]$	26
	x=5	$(Me_4N)[Ag(Se_5)]$	26

2. High Temperature Metal Chalcogenide Chemistry

Metal chalcogenide compounds possess interesting physical properties which can be applied to many uses such as HDS catalysts²⁷, detectors for IR radiation and night vision²⁸, solar cells²⁹, energy storage systems³⁰, and non-linear optical materials³¹. The great majority of metal chalcogenide compounds known to date have been synthesized at temperatures higher than 500 °C. High temperature conditions are primarily used because the starting materials are often solids and a reasonable diffusion rate between solid reactants is necessary for reaction to take place. During the reaction period, for example, the reactant solids (A and B; the elements of simple binary chalcogenides) partially react to form a layer of product AB at the interface, as shown in the following scheme.



As the layer of product AB becomes thicker, further reaction slows down due to the greater pathlength that A and B must travel (through the AB layer) to react. Thus, in some cases, even though high reaction temperatures are involved, frequent regrindings followed by repeated heating are still necessary to obtain a homogeneous product. Even if a homogeneous product is obtained, growth of single crystals, a necessary prerequisite for proper characterization of new

materials, is not readily achieved. To facilitate crystal growth, other techniques such as chemical vapor transport (CVT)³² and molten salts (or flux growth)³³ are often employed. CVT works well with binary chalcogenides but often fails with ternary systems and when alkali metals are involved. On the other hand, flux growing is a promising technique and has proven to be successful in a number of binary and ternary chalcogenide systems³⁴. This molten salt technique will be discussed in more detail in the next section.

Metal chalcogenide compounds exhibit enormous structural diversity associated with the multi-bonding characteristics of the chalcogens. For simple binary systems, compounds with MQ stoichiometry often adopt either the zincblende (e.g. ZnS) or wurtzite-type structure (e.g. ZnS) as shown in Figure 1. In both of these structures the metal and chalcogen atoms are tetrahedrally coordinated. Another major structure type found amongst monochalcogenide compounds is the NiAs-type structure as shown in Figure 2 (A). Each Q atom is surrounded by a trigonal prism of 6 metal atoms while each metal atom has eight-fold coordination, being surrounded octahedrally by six chalcogen atoms and by two additional metal atoms which are coplanar with four of chalcogen atoms. Furthermore, there are many known defect structures of these major structure types. For example, the two dimensional TiS_2 or CdI_2 -type structure is a defect NiAs structure. Figure 2 shows the close structural relationships between TiS (NiAs-type) and TiS_2 (or CdI_2) by removing alternate M atom layers in the TiS structure, which leads to AB_2 stoichiometry. Another related layer structure is that of MoS_2 where the metal atom has trigonal prismatic geometry and the chalcogens have trigonal pyramidal geometry.

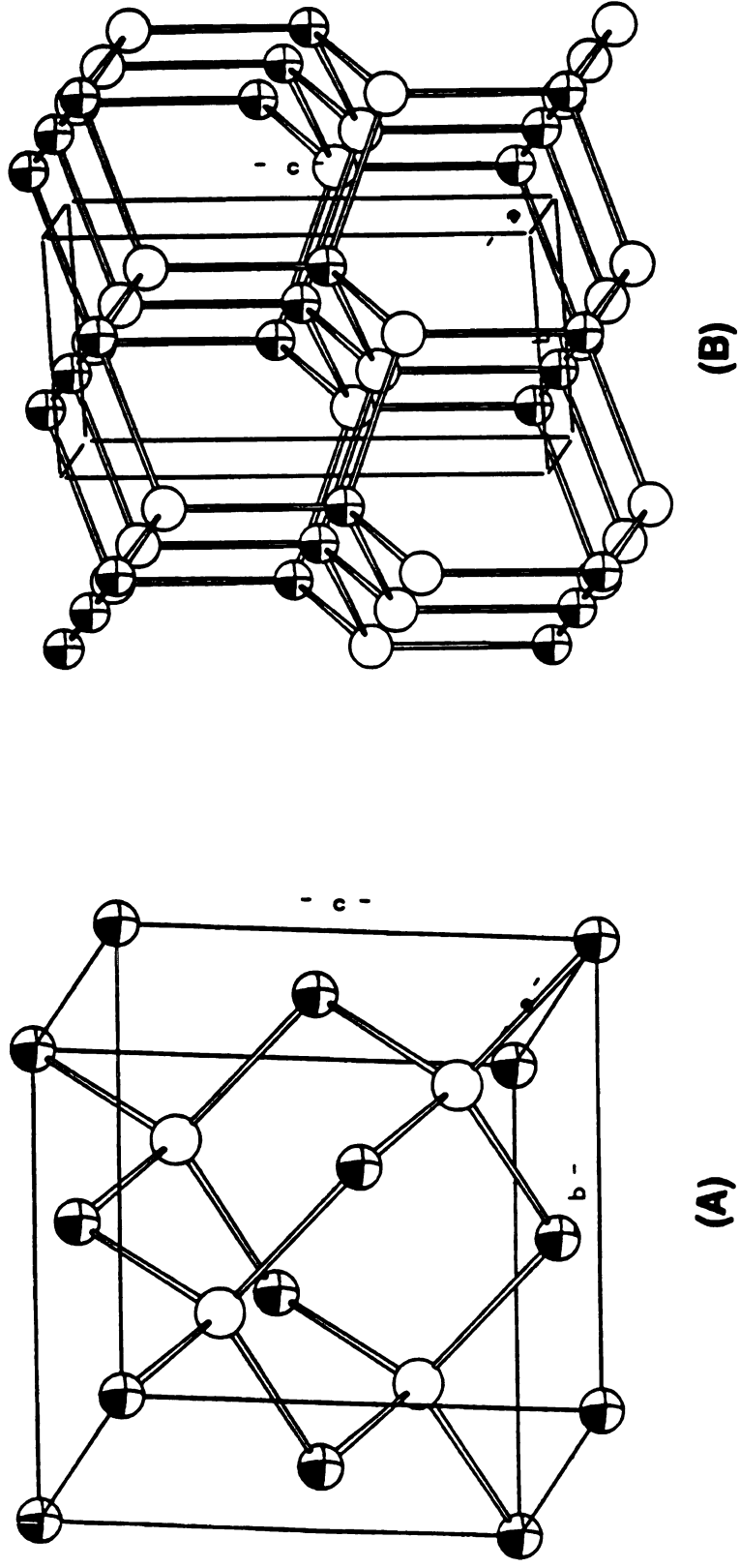


Figure 1. ORTEP representation of the unit cell of (A) Zinc-blende (ZnS) and (B) Wurtzite (ZnS). Open circles are S atoms and octant-shaded ellipsoids are Zn atoms.

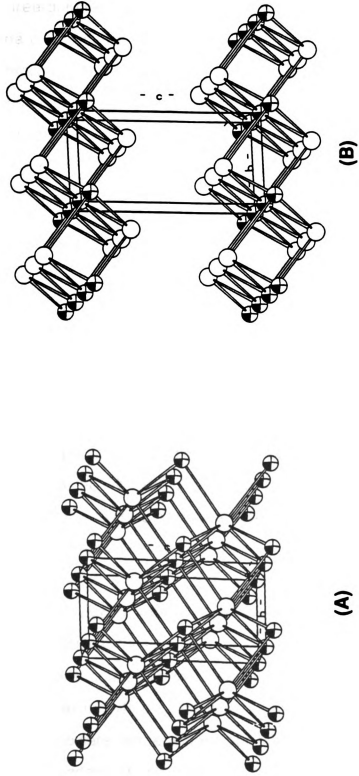


Figure 2. ORTEP representation of the unit cell of (A) TiS (NIA5-type) and (B) TiS₂ (CdI₂-type). Open circles are S atoms and octant-shaded ellipsoids are Ti atoms.

Many dichalcogenides have a quite different structural motif, being composed of infinite three-dimensional networks of M and discrete Q_2^{2-} units. The predominate structural types are pyrites (e.g. FeS_2) and marcasite (orthorhombic modifications of FeS_2) and are shown in Figure 3. Pyrite can be described as a distorted NaCl-type structure in which S_2 units are centered on the Cl positions.

Contrary to the well-developed monochalcogenide chemistry, the corresponding chemistry of Q_x^{2-} ($x > 2$) ligands in the solid state is rare and extends only to Q_2^{2-} compounds. Polychalcogenide compounds are thermally unstable at high temperature even in an excess of chalcogen. This instability increases with increasing chain length of polychalcogenide ligands, with the result of smaller chain fragments as shown in eq 2.



A classical example of such instability is the transformation of $TiS(S_2)$ to TiS_2 and S above 500 °C.³⁵ Polychalcogenide ligands are more likely to be incorporated into the solid state lattice at lower reaction temperatures. At room temperature few metal polychalcogenide polymers have been crystallized directly from the reaction mixture. These are one-dimensional $NH_4Cu(S_4)$ ³⁶, $(Ph_4P)_2Hg_2Te_5$ ³⁷, $(Me_4N)Ag(Q_5)$ ($Q=S$ ³⁸, Se ²⁶), $(Ph_4P)Ag(Se_4)$ ^{26(b),39}, and two-dimensional $(NH_4)_2Pd(S_5)(S_6)$ ⁴⁰. However, room temperature conditions are not particularly conducive to single-crystal growth of compounds with extended structures despite the exceptions mentioned above. It becomes clear that low to intermediate temperatures ($150\text{ °C} < T < 500\text{ °C}$) must be used for such systems. In addition to polychalcogenide incorporation into the solid state lattice, new phases stabilized at this intermediate temperature regime will likely

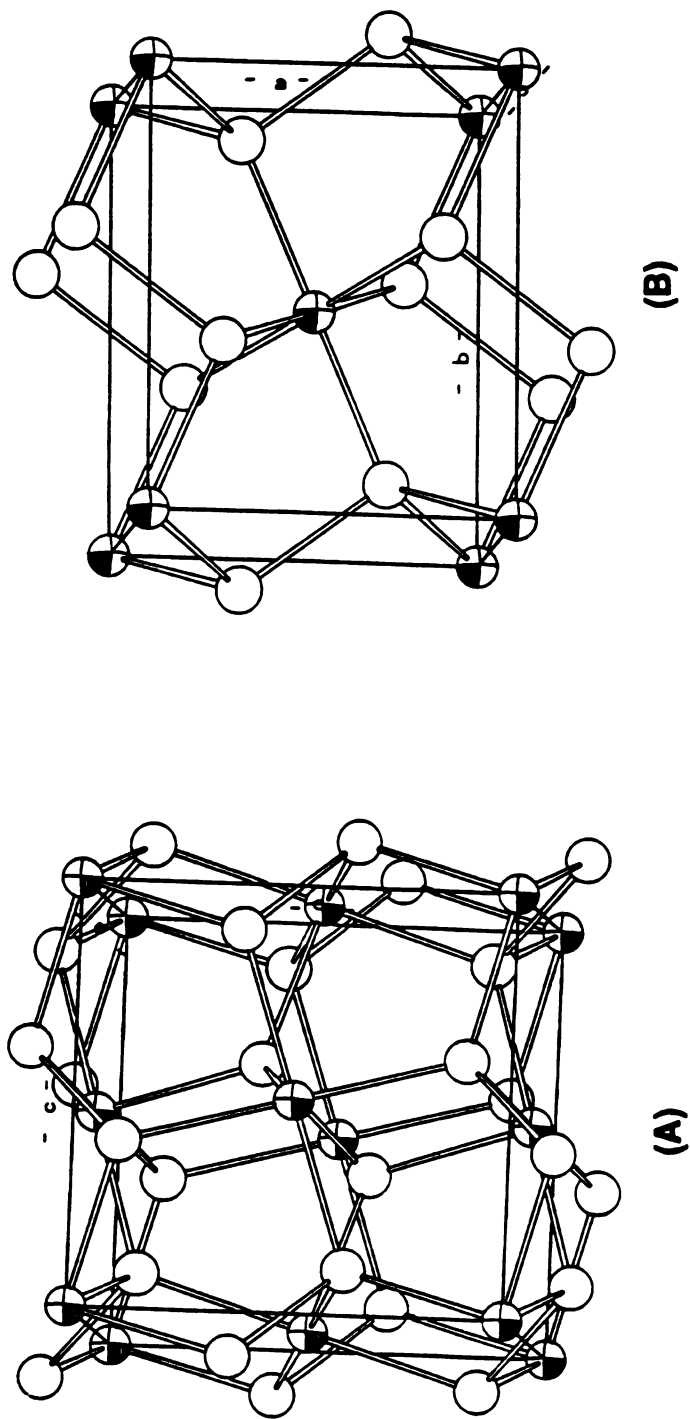


Figure 3. ORTEP representation of the unit cell of (A) Pyrite (FeS₂) and (B) Marcasite (FeS₂). Open circles are S atoms and octant-shaded ellipsoids are Fe atoms.

be metastable or kinetically stable with respect to thermodynamically more stable phases prepared at higher temperatures and thus may have unique properties. One structural consideration associated with incorporation of polychalcogenide ligands into solid state lattice is that low-dimensional and perhaps microporous structures may be possible. This is because of the decreased charge/length ratio of polychalcogenide ligands. Metal chalcogenide compounds containing Q_2^{2-} , except for the pyrite structure of MQ_2 , often have low-dimensional structures (e.g. $NbSe_3$ -type compounds). Prior to this work, the only case known to contain a Q_3^{2-} ligand was $P_2Nb_4S_{21}$ ⁴¹.

Surprisingly, the intermediate temperature regime ($150\text{ }^\circ\text{C} < T < 500\text{ }^\circ\text{C}$) has not been explored extensively for the synthesis of new chalcogenide compounds. This intermediate temperature range was probably considered too hot for the synthesis of molecular species due to the lack of suitable organic solvents and too cold for most solid state reactions because of the difficulty in achieving a reasonable diffusion rate between solid reactants. However, this intermediate temperature regime is accessible by use of the old molten salt technique. Generally speaking, molten salts are well studied, can be prepared to span a wide temperature range, and thus are attractive for use as solvents for the synthesis of new chalcogenide (or other) compounds⁴².

3. Molten Salt Synthetic Methods

Crystallization from flux is very similar to crystallization from solutions, the only difference usually being the temperature; Molten salts (or Flux) are high temperature liquids whereas common organic solvents are liquids at ambient temperatures. Molten salts have been used as solvents to grow large single

crystals of known binary and ternary compounds for more than a hundred years at high temperatures (>700 °C). However, they have not been used exclusively as reaction media for the synthesis of new materials. Three types of molten salts have been used for recrystallization of known chalcogenide materials. These are (a) metal halides, (b) metal chalcogenides, and (c) alkali metal polysulfides.^{33(a),43} Among them, alkali metal polysulfide fluxes, or more generally alkali metal polychalcogenide fluxes, are quite attractive for the synthesis of new ternary chalcogenide compounds because they can be used not only as solvents but also as sources of alkali metal and chalcogen.

The potential of the polychalcogenide fluxes as reaction media was noted by Scheel about 15 years ago. In his only published paper⁴⁴ he wrote "The polysulfides of the larger alkali ions are not investigated in detail; they are **also** potential solvents although the tendency of compound formation increases **with** ionic radius." However, these fluxes were used only as recrystallization **media** of known materials at high temperatures. Materials such as ZnS, CdS, **MnS**, PbS, NaCrS₂, KCrS₂, NaInS₂, KFeS₂, FeS₂, NiS₂, CoS₂, MoS₂, NbS₂, **LaS_{2-x}**, Cu₃VS₄, and HgS were grown successfully from sodium polysulfide **flux** at high temperatures (>700 °C) by Scheel⁴⁴ and others⁴⁵.

An alkali metal polychalcogenide flux can be prepared easily by fusing **an** alkali metal chalcogenide with stoichiometric amounts of chalcogens above **450** °C as shown in eq 3.



One of the most studied systems is the Na₂S/S flux due to its potential use in **sodium/β-alumina/sulfur** rechargeable batteries.⁴⁶ Typical phase diagrams of the polysulfide fluxes (e.g. Na₂S/S⁴⁷ and K₂S/S⁴⁸) are shown in Figure 4. The

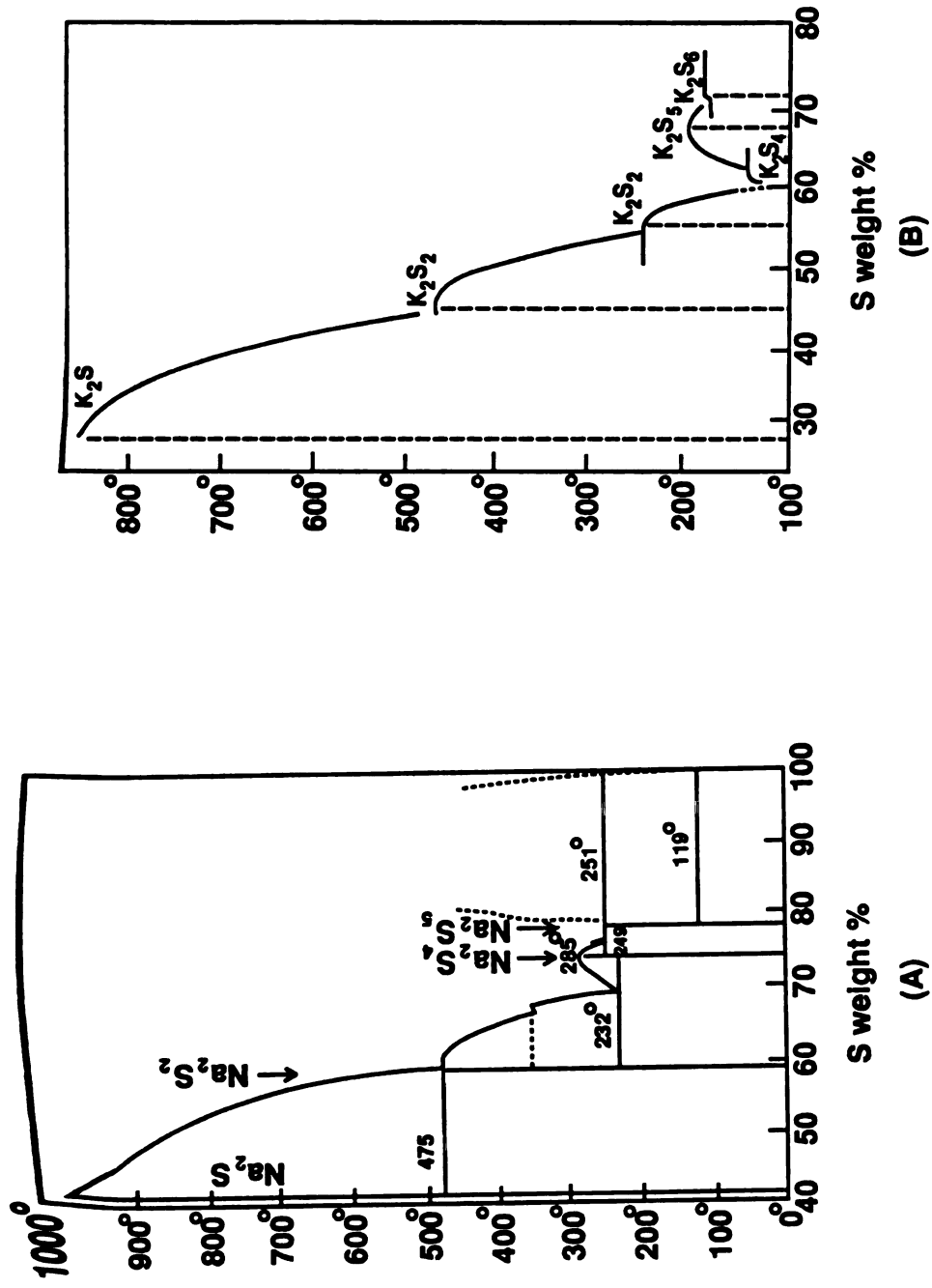


Figure 4. Phase diagrams of (A) Na₂S/S₄₇ and (B) K₂S/S₄₈ systems.

local minima in the melting point curves correspond to the eutectic compositions. It is clear that for stoichiometric compositions of Na_2S_x and K_2S_x ($x \geq 3$) the melting points are well below 400 °C and reach 145 °C for K_2S_4 . Thus, the lowest possible temperature for synthetic chemistry in these system is ca. 145 °C. This temperature lies at the upper limit at which most organic solvents boil off or decompose, yet is low enough to form kinetically stable or metastable products. Similar considerations apply for the other A_2Q_x systems.⁴⁹ A desirable feature of polychalcogenide fluxes is that upon cooling they solidify to a glassy solid. This glassy matrix can be removed by dissolution in water or nonaqueous solvent and does not interfere with the isolation of the crystalline products. Of course, the products must not dissolve in these solvents. In the corresponding alkali metal polyselenides, the minimum accessible temperature is somewhat higher at 250 °C. Since no other phase diagram information on the heavier chalcogenide (Se, Te) fluxes is available, the reaction temperatures for the $\text{A}_2\text{Q}/\text{Q}$ systems are found out in an empirical way. Table 3 contains melting point information on most known alkali metal polychalcogenides. One important property of these alkali metal polychalcogenide fluxes is the wide temperature range of their melting points (145~1000 °C). This allows great flexibility in the choice of reaction temperature. In addition, the polychalcogenide flux is a highly oxidizing (corrosive) medium as well as a basic (nucleophilic) one. The oxidizing ability allows one to use the elemental form of the metals in a redox reaction. The basicity of the medium, which can be controlled by varying the $\text{A}_2\text{Q}/\text{Q}$ ratio, governs the reactivity of the polychalcogenide flux and provides the appropriate ligand to the oxidized, positively charged metal.

Table 3. Melting Points ($^{\circ}\text{C}$) of Some Known Alkali Metal Polychalcogenides⁴⁶⁻⁴⁹

Li_2S 900-975	Li_2S_2 369.5				
Na_2S 1180	Na_2S_2 490	Na_2S_3 228.8	Na_2S_4 275	Na_2S_5 251.8	
Na_2Se >875	Na_2Se_2 495	Na_2Se_3 313	Na_2Se_4 290		Na_2Se_6 258
Na_2Te 953	Na_2Te_2 (Na_3Te_2) 348				Na_2Te_6 436
K_2S 840	K_2S_2 470	K_2S_3 252	K_2S_4 145	K_2S_5 206	K_2S_6 189
K_2Se	K_2Se_2 460	K_2Se_3 380	K_2Se_4 205	K_2Se_5 190	
K_2Te	K_2Te_2	K_2Te_3			
Rb_2S 530	Rb_2S_2 420	Rb_2S_3 213	Rb_2S_4 160	Rb_2S_5 225	Rb_2S_6 201
Rb_2Se					
Rb_2Te	Rb_2Te_2	Rb_2Te_3			
Cs_2S	Cs_2S_2 460	Cs_2S_3 217	Cs_2S_4 160	Cs_2S_5 210	Cs_2S_6 186
Cs_2Se					
Cs_2Te					

Recrystallization of a solid metal sulfide from such fluxes suggests that at some point partial or complete dissolution of the solid metal sulfide occurs through attack by the S_x^{2-} ion present in solution to form soluble species as shown in eq 4.50



As with hydrothermal synthesis, a dissolution-reprecipitation mechanism ("mineralizer effect") is very important and promotes crystal growth. Given the appropriate conditions of temperature and concentration, certain solids, known or new, could crystallize out of solution.

4. New Materials from Polychalcogenide Flux at Intermediate Temperatures

Since polychalcogenide fluxes allow easy access to the intermediate temperature region, there are a tremendous number of possibilities for the synthesis of new chalcogenide materials using them. As I already mentioned above, this intermediate temperature range can afford new chalcogenide compounds with the following characteristics: (i) the incorporation of polychalcogenide ligands into extended solid state lattices, (ii) metastable or kinetically stable compounds, (iii) low-dimensional structures, and (iv) unique properties related to novel structures. Furthermore, this new class of compounds can bridge the gap between two extremes of chemistry (i.e., solution and solid state).

In 1987 Ibers and co-workers published the first examples of the use of alkali metal polychalcogenides to synthesize new metal chalcogenide compounds. The compounds, $K_4Ti_3S_{14}$ ⁵¹ and $Na_2Ti_2Se_8$ ⁵², were obtained from K_2S_x and Na_2Se_x fluxes, respectively, at 375-470 °C. These new compounds contain infinite one-dimensional chains of $[Ti_3(S_2)_6(S)_2]_n^{4n-}$ and $[Ti_2(Se_2)_3(Se)_2]_n^{2n-}$, respectively, and are composed of Ti^{4+} centers bonded to Q_2^{2-} and Q^{2-} ligands. Even though they pointed out the potential of this molten salt method for the synthesis of new materials, they did not take advantage of the full potential of these polychalcogenide fluxes and confined their efforts to the relatively higher temperature region (>375 °C).

Our initial approach for the systematic investigation of new ternary chalcogenide compounds concentrated primarily on lower reaction temperatures ($T < 375$ °C except for Te_x^{2-}); we attempted to obtain materials containing even higher polychalcogenide ligands. Indeed, the lower reaction temperature region (215 °C $< T < 310$ °C) afforded new metal chalcogenide compounds containing Q_x^{2-} ($Q=S, Se$; $x=2, 3, 4,$ and 5) ligands (see Chapter II and III and VIII)^{50,53}. Furthermore, many new structural features with properties ranging from semiconducting to metallic are obtained (see Chapters IV-VIII).⁵⁴ In this dissertation, I will describe the synthesis, characterization, and structural chemistry of new metal chalcogenide compounds prepared by the use of alkali metal polychalcogenide fluxes at intermediate temperature.

CHAPTER 2

Synthesis and Characterization of Low-Dimensional (Poly)chalcogenide Compounds in the A/Cu/Q System

(A=Na, K, Cs; Q=S, Se)

1. Introduction

Thus far, the great majority of synthetic metal/chalcogenide chemistry has been carried out either in solution at (or near) room temperature or in the solid state at high temperatures ($T > 500$ °C). The compounds obtained at low temperatures are soluble, discrete molecular species containing a diverse repertoire of Q_x^{2-} (Q=S, Se, Te) ligands with x ranging from 1 (e.g., $[Na_2Fe_{18}S_{30}]^{8-}$)¹⁰ to 9 (e.g., $[AuS_9]^{1-}$)¹¹. By far, among the discrete polychalcogenides, the Q_4^{2-} ligands occur most frequently. The high temperature compounds tend to be extended, three dimensional, solid state structures containing either Q^{2-} or Q_2^{2-} ligands. This is because the polychalcogenides are thermally unstable at high temperatures and dissociate into lower polychalcogenides and chalcogen. In general, low-temperature compounds can be viewed as metastable and thus capable of transforming to their high temperature solid state counterparts via interesting and perhaps isolable low-dimensional intermediates in the intermediate temperature range (150-500 °C). Increasing interest in metastable low-dimensional polychalcogenides derives not only from the catalytic²⁷ and electronic⁵⁵

properties of these materials but also because they offer a bridge between molecular and solid state chemistry.

Most known binary and ternary Cu/S compounds exhibit interesting electronic properties and even mixed-valency associated with $\text{Cu}^{1+/2+}$ ions is often achieved. Thus, our initial investigation concentrated on the ternary A/Cu/Q systems. In this chapter, we shall illustrate that novel one-dimensional compounds of $\alpha\text{-ACuQ}_4$ and $\beta\text{-KCuS}_4$ ^{53(a)} containing tetrachalcogenide (Q_4^{2-}) ligands, one-dimensional mixed-valence compound of $\text{Na}_3\text{Cu}_4\text{Se}_4$, and mixed selenide and oxide phase of $\text{Na}_{1.9}\text{Cu}_2\text{Se}_2\cdot\text{Cu}_2\text{O}$ are readily formed in the polychalcogenide flux at intermediate temperatures.

2. Experimental Section

2.1 Reagents

Chemicals were used as obtained: copper powder, electrolytic dust, **purified**, Fisher Scientific Co., Fair Lawn, NJ; copper (II) oxide (Cu_2O), 97 % **purity**, Aldrich Chemical Co., Milwaukee, WI; selenium powder, 100 mesh, **99.95%** purity, Aldrich Chemical Co., Milwaukee, WI; sulfur powder, sublimed, **J. T. Baker Chemical Co.**, Phillipsburg, NJ; potassium and sodium metal, **analytical reagent**, Mallinckrodt Inc., Paris, KY; cesium metal, 99.98% purity, **AESAR**, Johnson Matthey, Seabrook, NH.

2.2. Physical Measurements

The FT-IR spectra of the compounds were measured as pellets in a CsI matrix. Each sample was ground with dry CsI into a fine powder and a pressure of about 6 tons was applied to the mixture to make a translucent pellet. The spectrum was recorded in the far IR region (600 to 100 cm^{-1}) with the use of a Nicolet 740 FT-IR spectrometer.

Variable temperature four-probe dc resistivity and thermoelectric power data for $\text{Na}_{1.9}\text{Cu}_2\text{Se}_2\cdot\text{Cu}_2\text{O}$ (5~300 K) and four-probe dc conductivity data for $\alpha\text{-KCuSe}_4$ (80~300 K) were provided by Prof. Carl R. Kannewurf (Northwestern University). A computer automated measurement system was employed to obtain thermopower and/or resistivity data with both thermal gradient and/or the current applied along the needle axis of $\alpha\text{-KCuSe}_4$ and the (001) plane of $\text{Na}_{1.9}\text{Cu}_2\text{Se}_2\cdot\text{Cu}_2\text{O}$. For all measurements electrode connections to the small single crystals were made with the use of 25 and 60 μm gold wires and gold bonding paste.

Quantitative microprobe analysis of the compounds was performed on a Jeol 35CF scanning electron microscope (SEM) equipped with Tracor Northern TN 5500 X-ray microanalysis attachment. Single crystals of each sample were carefully picked and mounted on an aluminum stub using conducting silver paint to help dissipate charges that developed on the sample surface during measurements. Energy Dispersive Spectra (EDS) were obtained using the following experimental set-up:

X-ray detector position : 55mm

Working distance : 39mm

Accelerating voltage : 20 KV

Take-off angle : 27 deg

Beam current : 200 picoamps

Accumulation time : 100 seconds

Window : Be

A standardless quantitative (SQ) analysis program was used to analyze the X-ray spectra obtained. Since the selenium ratio is always underestimated due to an artifact of the program, a correction factor (x1.86), which was determined with the known K/Cu/Se ternary compounds, was used to evaluate the selenium ratio. The analyses reported here are the average of four to six individual measurements on different crystals of each compound.

2.3. Synthesis

Chemicals were measured and loaded in Pyrex tubes under a dry nitrogen atmosphere in a Vacuum Atmospheres Dri-Lab glovebox.

Potassium sulfide, K_2S 3.2 g (0.1 mol) of sulfur powder was combined with 7.8 g (0.2 mol) of sliced potassium metal in a round-bottom flask equipped with a Teflon valve and a stirbar. A 100-mL volume of liquid ammonia was condensed into a flask at $-78\text{ }^\circ\text{C}$ (dry ice/acetone bath) and the mixture stirred for a couple of hours or until the potassium metal had dissolved completely. When a dark blue solution formed, the NH_3 was removed by evaporation at room temperature (by allowing the cold bath to warm slowly) under a flow of nitrogen. The resulting light yellow solid was dried in vacuo, flame-dried, and ground to a fine powder in the glovebox. It was used without any further characterization.

Preparation of Na_2Se and K_2Se was accomplished by following the procedure used for the K_2S preparation with sodium or potassium metal and elemental selenium in a 2:1 ratio.

Cesium selenide, Cs_2Se 13.3 g (0.10 mol) of melted cesium metal was put in a round-bottom flask fitted with a Teflon valve by using a pipet. A 100-mL volume of liquid ammonia was condensed into the flask at $-78\text{ }^\circ\text{C}$ (dry ice/acetone bath), and then 3.9 g (0.05 mol) of elemental selenium and a stirbar were added to the solution. The mixture was stirred for a couple of hours or until the cesium metal had dissolved completely. When a dark brown solution formed, the NH_3 was removed by evaporation at room temperature (by allowing the cold bath to warm slowly) under a flow of nitrogen. The resulting orange red solid was dried in vacuo, flame-dried, and ground to a fine powder in the glovebox. It was used without any further characterization.

Caution: Direct addition of elemental selenium to cesium metal in a round-bottom flask is dangerous, particularly, if the cesium is not solidified completely. To avoid a spontaneous and violent reaction between the two reactants, we decided to dissolve cesium metal in liquid ammonia first and then to add elemental selenium.

α -Potassium (1,2- μ_2 -tetrasulfido)cuprate(I), $\alpha\text{-KCuS}_4$ (I)
0.221 g (2.0 mmol) of K_2S , 0.064 g (1.0 mmol) of Cu powder, and 0.256 g (8.0 mmol) of S powder were mixed together and loaded in a Pyrex tube which was flame-sealed under vacuum ($\sim 10^{-3}$ torr). The tube was placed in a computer-controlled furnace and heated at $215\text{ }^\circ\text{C}$ for 72 hrs and cooled slowly to $50\text{ }^\circ\text{C}$ at a rate of $2\text{ }^\circ\text{C/hr}$. Orange red needle-like crystals were obtained by removing excess molten potassium polysulfides with water under an N_2 atmosphere (yield; 72 % based on the Cu used). A quantitative microprobe analysis performed on a number of crystals with the EDS/SEM system gave an average composition of $\text{K}_{1.0}\text{Cu}_{1.0}\text{S}_{4.1}$.

β -Potassium (1,4- μ_2 -tetrasulfido)cuprate(I), β -KCuS₄ (II)

0.221 g (2.0 mmol) of K₂S, 0.064 g (1.0 mmol) of Cu powder, and 0.256 g (8.0 mmol) of S powder were mixed together and loaded in a Pyrex tube which was flame-sealed under vacuum ($\sim 10^{-3}$ torr). The tube was placed in a computer-controlled furnace and heated at 250 °C for 72 hrs and cooled slowly to 50 °C at a rate of 2 °C/hr. Orange red needle-like crystals were obtained by removing excess potassium polysulfides with water under an N₂ atmosphere (yield; 53 % based on the Cu used). A quantitative microprobe analysis performed on a number of crystals with the EDS/SEM system gave an average composition of K_{1.0}Cu_{1.0}S_{4.1}.

 α -Potassium (1,2- μ_2 -tetraselenido)cuprate(I), α -KCuSe₄ (III)

0.157 g (1.0 mmol) of K₂Se, 0.032 g (0.5 mmol) of Cu powder, and 0.316 g (4.0 mmol) of Se powder were mixed together and loaded in a Pyrex tube which was flame-sealed under vacuum ($\sim 10^{-3}$ torr). The tube was placed in a computer-controlled furnace and heated 250 °C for 96 hrs and cooled slowly to 50 °C at a rate of 2 °C/hr. Dark red needle-shaped crystals were obtained by removing excess potassium polyselenides with water under an N₂ atmosphere (63 % based on the Cu used). A quantitative microprobe analysis performed on a number of crystals with the EDS/SEM system gave an average composition of K_{1.0}Cu_{1.0}Se_{4.2}.

 α -Cesium (1,2- μ_2 -tetraselenido)cuprate(I), α -CsCuSe₄ (IV)

0.345 g (1.0 mmol) of Cs₂Se, 0.032 g (0.5 mmol) of Cu powder, and 0.316 g (4.0 mmol) of Se powder were mixed together and loaded in a Pyrex tube which was flame sealed under vacuum ($\sim 10^{-3}$ torr). The tube was placed in a computer-controlled furnace and heated at 250 °C for 72 hrs and cooled slowly to 50 °C at a rate of 2 °C/hr. Black needle-like crystals were obtained in

quantitative yield by removing excess molten cesium polyselenides with water under N₂ atmosphere (57% based on the Cu used). A quantitative microprobe analysis performed on a number of crystals with the EDS/SEM system gave an average composition of Cs_{1.0}Cu_{1.0}Se_{4.2}.

Trisodium tetra(μ_3 -selenido)tetracuprate(I,II), Na₃Cu₄Se₄ (V)
 0.250 g (2.0 mmol) of Na₂Se, 0.048 g (0.75 mmol) of Cu powder, and 0.316 g (4.0 mmol) of Se powder were mixed together and loaded in a Pyrex tube which was flame-sealed under vacuum ($\sim 10^{-3}$ torr). The tube was placed in a computer-controlled furnace and heated at 350 °C for 96 hrs and cooled slowly to 50 °C at a rate of 2 °C/hr. Black needle-shaped crystals were obtained by removing excess sodium polyselenides with dimethylformamide (DMF) under an N₂ atmosphere (yield; 58 % based on the Cu used). However, repeated reactions did not always yield a homogeneous product. The product was often contaminated with a competing phase, Na_{1.9}Cu₂Se₂·Cu₂O (see below). A quantitative microprobe analysis performed on a number of crystals with the EDS/SEM system gave an average composition of Na_{3.0}Cu_{3.9}Se_{3.9}.

Sodium bis(μ_4 -selenido)docuprate(I)-copper oxide, Na_{1.9}Cu₂Se₂·Cu₂O (VI)
 0.187 g (1.5 mmol) of Na₂Se, 0.034 g (0.50 mmol) of Cu powder, and 0.316 g (4.0 mmol) of Se powder were mixed together and loaded in a Pyrex tube which was flame-sealed under vacuum ($\sim 10^{-3}$ torr). The tube was placed in a computer-controlled furnace and heated at 340 °C for 96 hrs and slowly cooled to 50 °C at a rate of 2 °C/hr. The black, thin plate crystals were obtained by removing excess sodium polyselenides with DMF under an N₂ atmosphere (yield; 76 % based on the Cu used). The product was often contaminated with a competing phase, Na₃Cu₄Se₄ (see above).

Since the product contains oxygen, we have used Cu_2O instead of Cu metal. 0.187 g (1.5 mmol) of Na_2Se , 0.143 g (1.0 mmol) of Cu powder, and 0.316 g (4.0 mmol) of Se powder were mixed together and loaded in a Pyrex tube which was flame-sealed under vacuum ($\sim 10^{-3}$ torr). The tube was placed in a computer-controlled furnace and heated at 330 °C for 7 days and cooled slowly to 50 °C at a rate of 2 °C/hr. Black, thin plate crystals were obtained by removing excess sodium polyselenides with DMF under an N_2 atmosphere (yield; 84 % based on the Cu used). The product was also contaminated with $\text{Na}_3\text{Cu}_4\text{Se}_4$.

2.4. X-ray Crystallographic Studies

All compounds were examined by X-ray powder diffraction for the purpose of phase characterization and identification. The d-spacings for each compound were obtained from the powder patterns recorded on a Phillips XRG-3000 computer-controlled powder diffractometer, operating at 40KV, 35 mA. $\text{Cu-K}\alpha$ radiation was obtained by use of a graphite monochromator. To verify product homogeneity, d-spacings observed for the bulk materials were compared, and found to be in accord, with the d-spacings calculated from the single crystal X-ray structure analysis data. The d-spacings observed for (V) and (VI) showed extra reflections due to coexisting phase, (VI) and (V), respectively. Calculation of d-spacings was performed using the POWD10 program⁵⁶. The results are summarized in Tables 4-9.

Table 4. Calculated and Observed X-ray Powder Diffraction Pattern of α -KCuS₄

H K L	d_{calc} (Å)	d_{obs} (Å)	I/I _{max} (obs.)
0 1 1	6.94	7.05	100
0 0 2	6.26	6.35	23.9
0 1 2	5.01	5.06	68.1
1 1 0	4.43	4.48	7.0
0 2 1	3.95	3.98	31.9
1 2 0	3.26	3.29	33.9
0 0 4	3.13	3.15	87.0
1 1 3	3.04	3.06	20.1
0 1 4	2.93	2.94	41.1
1 2 2	2.89	2.91	48.9
0 3 1	2.71	2.72	46.4
1 0 4	2.69	2.70	19.3
1 2 3 (1 1 4)	2.57	2.58	52.7
0 3 2	2.540	2.55	41.7
2 1 1	2.453	2.466	35.6
1 3 1	2.410	2.420	42.2
2 1 2	2.323	2.323	28.0
2 1 3	2.146	2.155	14.5
0 4 0	2.084	2.093	57.4
1 3 4	1.9332	1.9402	28.5
1 1 6 (2 3 1)	1.8908	1.8975	9.3
0 3 5	1.8619	1.8694	16.5
1 2 6	1.7599	1.7623	42.8
2 3 3	1.7352	1.7412	15.5
0 5 1 (3 1 2)	1.6530	1.6551	42.8
3 2 0 (0 5 2)	1.6123	1.6158	17.1
(2 1 6)			
2 4 2	1.5792	1.5823	21.3

Table 5. Calculated and Observed X-ray Powder Diffraction Pattern of β -KCuS₄

H K L	d _{calc} (Å)	d _{obs} (Å)	I/I _{max} (obs.)
0 2 0	8.38	8.52	100
0 1 1	5.94	6.02	67.3
-1 1 2	3.26	3.28	11.9
1 2 1	3.04	3.06	13.4
0 5 1	2.96	2.98	78.4
0 6 1	2.55	2.56	19.9
-2 3 1	2.379	2.369	11.9
-2 3 3	1.9220	1.9174	9.6
-2 8 2	1.5922	1.5918	10.5

Table 6. Calculated and Observed X-ray Powder Diffraction Pattern of α -
 KCuSe₄

H K L	d_{calc} (Å)	d_{obs} (Å)	I/I _{max} (obs.)
0 1 1	7.17	7.25	22.8
0 0 2	6.41	6.49	23.1
0 1 2	5.15	5.20	100
0 1 3	3.83	3.87	5.7
1 1 2	3.76	3.79	8.2
1 2 0	3.40	3.42	12.5
1 2 1	3.29	3.31	30.6
0 0 4	3.20	3.23	72.1
1 1 3	3.14	3.17	12.1
0 2 3	3.04	3.06	48.4
0 1 4 (1 2 2)	3.00	3.02	61.7
0 3 1	2.81	2.83	19.9
1 0 4	2.77	2.79	19.4
1 2 3	2.66	2.68	42.5
1 1 4 (0 3 2)	2.63	2.65	22.6
2 1 1	2.57	2.58	37.7
1 3 1	2.50	2.52	13.1
2 1 2	2.429	2.444	12.9
2 2 1	2.286	2.299	4.0
2 1 3	2.237	2.221	18.9
0 4 0	2.165	2.174	17.4
2 1 4	2.031	2.043	9.4
1 3 4	1.999	2.011	17.9
2 3 1	1.969	1.979	9.9
0 3 5	1.9175	1.931	10.5
2 2 4	1.8818	1.892	3.5
1 3 5	1.8109	1.822	26.9
3 1 2	1.7299	1.738	17.6
2 3 4	1.6926	1.699	30.1
0 5 2	1.6721	1.680	15.1
2 1 6	1.6576	1.667	13.1
2 4 2	1.6452	1.651	12.7
2 4 3	1.5814	1.589	5.3

Table 7. Calculated and Observed X-ray Powder Diffraction Pattern of α -
CsCuSe₄

H K L	d_{calc} (Å)	d_{obs} (Å)	I/Imax (obs.)
0 1 1	7.56	7.67	12.6
0 0 2	6.96	7.04	13.7
0 1 2	5.51	5.56	19.2
1 1 0	4.73	4.77	18.2
1 1 1	4.48	4.54	14.5
0 2 1	4.28	4.32	17.6
1 1 2	3.91	3.94	22.7
0 2 2	3.78	3.80	4.8
0 0 4	3.48	3.50	75.7
1 2 1	3.39	3.41	50.9
1 1 3	3.31	3.33	31.0
0 1 4	3.24	3.26	100
1 2 2	3.13	3.14	49.3
1 0 4	2.95	2.96	67.3
1 2 3	2.79	2.81	66.7
0 3 2	2.75	2.77	19.6
2 1 1	2.61	2.62	63.0
0 3 3	2.52	2.53	9.1
2 1 2	2.486	2.493	14.8
1 1 5	2.401	2.409	8.2
0 2 5	2.369	2.376	24.6
2 1 3	2.309	2.315	19.6
0 4 0	2.253	2.262	16.4
1 2 5	2.180	2.185	7.9
1 3 4	2.106	2.115	25.8
1 1 6	2.085	2.091	11.0
2 3 2	1.960	1.964	8.1
1 4 3	1.9051	1.9082	7.6
2 3 3	1.8698	1.8753	10.0
0 2 7	1.8205	1.8241	22.7
2 2 5	1.8050	1.8082	14.5
0 5 1	1.7878	1.7915	13.1
3 1 2	1.7598	1.7648	26.1
2 4 1	1.7382	1.7447	29.8
2 4 2	1.6990	1.7039	35.0
1 0 8	1.6620	1.6639	16.7
2 1 7	1.5938	1.5919	8.2

Table 8. Calculated and Observed X-ray Powder Diffraction Pattern of $\text{Na}_3\text{Cu}_4\text{Se}_4$

H K L	d_{calc} (Å)	d_{obs} (Å)	I/I _{max} (obs.)
0 2 0	7.60	7.57	60.3
1 1 0	6.65	6.63	100
1 2 0	5.30	5.28	12.9
0 4 0	3.80	3.80	62.2
2 0 0	3.69	3.69	29.7
1 4 0	3.38	3.38	41.0
1 2 1	3.15	3.15	18.1
1 5 0	2.81	2.81	26.6
2 4 0 (2 1 1)	2.65	2.65	31.1
0 6 0	2.53	2.53	35.4
3 1 0	2.433	2.432	9.6
2 3 1	2.377	2.373	11.2
0 6 1	2.129	2.125	15.4
3 2 1	2.013	2.013	29.3
0 0 2	1.962	1.958	14.8
1 1 2	1.8820	1.8737	5.9
2 6 1	1.8451	1.8397	36.4

Ta

Na

Table 9. Calculated and Observed X-ray Powder Diffraction Pattern of $\text{Na}_{1.9}\text{Cu}_2\text{Se}_2\cdot\text{Cu}_2\text{O}$

H K L	d_{calc} (Å)	d_{obs} (Å)	I/I _{max} (obs.)
0 0 2	10.81	10.79	12.2
0 0 4	5.40	5.41	100
0 0 6	3.60	3.61	32.0
1 0 3	3.43	3.44	2.7
1 0 5	2.90	2.91	5.9
0 0 8	2.70	2.71	24.7
1 1 4	2.463	2.463	7.0
1 0 9	2.048	2.047	2.6
1 1 8	1.9340	1.9330	5.1
2 0 2	1.9250		
0 0 12	1.8032	1.8041	32.5
1 0 11	1.7575	1.7573	3.8

The X-ray single crystal data of α -KCuS₄, β -KCuS₄, α -KCuSe₄, and α -CsCuSe₄ were collected on a Nicolet P3 four circle diffractometer with graphite monochromated Mo-K α radiation using the θ -2 θ scan mode. The data for Na₃Cu₄Se₄ and Na_{1.9}Cu₂Se₂·Cu₂O were collected on a Rigaku AFC6S diffractometer with graphite monochromated Mo-K α radiation using the ω -2 θ scan mode. Accurate unit cell parameters for all compounds were obtained by the least-squares refinement of the 2θ , ω , χ , and ϕ values of 20-25 machine-centered reflections. The stability of the experimental setup and crystal integrity were monitored by measuring three standard reflections periodically (every 100~150 reflections) during the data collection period. The intensities did not show any appreciable decay. Two absorption corrections were applied to the data of all compounds: an empirical absorption correction based on ψ scans for 3 reflections followed by a DIFABS⁵⁷ correction. The structures of α -KCuS₄, β -KCuS₄, α -KCuSe₄, α -CsCuSe₄ were solved with direct methods using SHELXS-86⁵⁸ and were refined with the SDP⁵⁹ package of crystallographic programs performed on a VAXstation 2000 computer. Since (I), (III) and (IV) have a non-centrosymmetric space group (P2₁2₁2₁), their enantiomorphs were checked at the final least square cycle. Among them, only α -KCuSe₄ gave significant change in the R/R_w value from 4.1/5.4 to 3.5/5.0. Based on this, its absolute configuration was determined. The structures of Na₃Cu₄Se₄ and Na₂Cu₂Se₂·Cu₂O were solved with direct methods using the SHELXS-86 program and were refined with the TEXSAN⁶⁰ package of crystallographic programs on a VAXstation 3100 computer. The systematic extinction conditions of Na₂Cu₂Se₂·Cu₂O ($h+k+l=2n$, $hk0$, $0kl$, hhl) correspond to 8 possible space groups (I4, I-4, I4/m, I422, I4mm, I-42m, I-4m2, and I4/mmm). Among them, the structure was successfully refined in space groups I4/m, I4mm, I-42m, I-42m, and I4/mmm. All refined atomic positions are related to those in space group

I4/mmm and the relatively lower R/Rw value of 5.3/7.7 was obtained in space group of I4/mmm. Therefore, the space group of I4/mmm was chosen. The temperature factors of Cu(2) atoms situated on the (0, 1/2, 0) position were large in all refined space groups, implying partial site occupancy of Cu(2) atom. We tried to refine its site occupancy. However, creation of a vacancy on this site caused relatively higher R/Rw value and the automatic refinements gave more than 100 % occupancy (104 %) and even larger temperature factors (7.8 Å²). Since 104 % occupancy is physically unrealistic, this site occupancy was fixed at 100 %. Instead, the refinements of Na site occupancy yielded slightly the lower R/Rw value of 5.3/7.7 versus 5.7/7.9 at the final least square cycle. Based on this refinement, the nonstoichiometric formula of Na_{1.9}Cu₂Se₂·Cu₂O was established. All atoms were refined anisotropically. The complete data collection parameters and details of the structure solution and refinement for every compound are given in Table 10. The final coordinates, temperature factors and their estimated standard deviations of all atoms are shown in Tables 11-16.

Table 10. Summary of Crystallographic Data for α -KCuS₄, β -KCuS₄, α -KCuSe₄, α -CsCuSe₄, Na₃Cu₄Se₄, and Na_{1.9}Cu₂Se₂·Cu₂O

	compound		
	I	II	III
Formula	α -KCuS ₄	β -KCuS ₄	α -KCuSe ₄
Formula weight	230.54	230.54	418.48
space group	P2 ₁ 2 ₁ 2 ₁	P2 ₁ /C	P2 ₁ 2 ₁ 2 ₁
<i>a</i> (Å)	5.245(1)	5.260(2)	5.509(2)
<i>b</i> (Å)	8.338(3)	16.771(6)	8.660(3)
<i>c</i> (Å)	12.539(3)	6.928(5)	12.826(4)
α (deg)	90.0	90.0	90.0
β (deg)	90.0	113.52(1)	90.0
γ (deg)	90.0	90.0	90.0
Vol (Å ³), Z	548.4(4), 4	560(1), 4	612.0(3), 4
Temperature (°C)	23	23	-98
Crystal size (mm)	0.4x0.08x0.05	0.4x0.06x0.06	0.4X0.05X0.04
Radiation	Mo-K α	Mo-K α	Mo-K α
μ (Mo-K α , cm ⁻¹)	60.6	59.3	276.8
<i>D</i> _{calc} (g/cm ³)	2.80	2.74	4.54
2 θ _{max} (deg)	49	46	50
Scan method	$\theta/2\theta$	$\theta/2\theta$	$\theta/2\theta$
No. of data collected	1158	917	1322
No. of unique data	921	823	1064
No. of data used ($F_o^2 > 3\sigma(F_o^2)$)	877	711	994
No. of atoms	6	6	6
No. of variables	55	55	56
Phasing technique	Direct methods	Direct methods	Direct methods
Final R/Rw	4.9/5.5	3.4/4.2	3.5/5.0
Max. shift/esd (final cycle)	0.0	0.0	0.0
Extinction coefficient	N/A	N/A	2.96x10 ⁻⁷

Table 10. (cont'd)

	compound		
	IV	V	VI
Formula	α -CsCuSe ₄	Na ₃ Cu ₄ Se ₄	Na _{1.9} Cu ₂ Se ₂ ·Cu ₂ O
Formula weight	512.29	638.99	474.08
space group	P2 ₁ 2 ₁ 2 ₁	Pbam	I4/mmm
a (Å)	5.571(2)	7.396(4)	3.914(2)
b (Å)	9.014(4)	15.207(5)	3.914(2)
c (Å)	13.931(6)	3.924(4)	21.623(4)
α (deg)	90.0	90.0	90.0
β (deg)	90.0	90.0	90.0
γ (deg)	90.0	90.0	90.0
Vol (Å ³), Z	699.6(5), 4	441.4(5), 2	331.3(4), 2
Temperature (°C)	23	23	23
Crystal size (mm)	0.38X0.05X0.03	0.39x0.03x0.03	0.03x0.16x0.18
Radiation	Mo-Kα	Mo-Kα	Mo-Kα
μ (Mo-Kα, cm ⁻¹)	287.1	259.4	236.2
D _{calc} (g/cm ³)	4.86	4.81	4.75
2θ _{max} (deg)	48	60	55
Scan method	θ/2θ	ω/2θ	ω/2θ
No. of data collected	1380	700	254
No. of unique data	1105	700	151
No. of data used (Fo ² >3σ(Fo ²))	965	438	107
No. of atoms	6	6	5
No. of variables	56	35	13
Phasing technique	Direct methods	Direct methods	Direct methods
Final R/Rw	2.7/3.0	3.0/3.6	5.3/7.7
Max. shift/esd (final cycle)	0.0	0.0	0.0
Extinction coefficient	4.60x10 ⁻⁷	N/A	N/A

Table 11. Fractional Atomic Coordinates and B_{eq} Values for α -KCuS₄ with Their Estimated Standard Deviations in Parentheses

Atom	x	y	z	$B_{\text{eq}}^a, \text{\AA}^2$
Cu	0.0214(3)	0.3558(2)	0.5680(1)	1.97(2)
K	0.3279(6)	0.5696(3)	0.3455(2)	2.64(5)
S(1)	-0.1317(5)	0.3042(3)	0.3978(2)	1.58(5)
S(2)	0.1243(5)	0.1389(4)	0.3326(2)	1.64(4)
S(3)	0.0478(5)	-0.0745(3)	0.4149(2)	1.77(5)
S(4)	-0.3361(6)	-0.1092(3)	0.3887(2)	1.90(5)

^a B values for anisotropically refined atoms are given in the form of the isotropic equivalent displacement parameter defined as $B_{\text{eq}} = (4/3)[a^2B_{11} + b^2B_{22} + c^2B_{33} + ab(\cos \gamma)B_{12} + ac(\cos \beta)B_{13} + bc(\cos \alpha)B_{23}]$.

Table 12. Fractional Atomic Coordinates and B_{eq} Values for β -KCuS₄ with Their Estimated Standard Deviations in Parentheses

Atom	x	y	z	$B_{\text{eq}}^a, \text{\AA}^2$
Cu	0.2456(2)	0.49577(6)	0.4965(2)	2.22(2)
K	0.2754(4)	0.6199(1)	0.0476(3)	2.67(4)
S(1)	0.0695(4)	0.3985(1)	0.6585(3)	1.95(4)
S(2)	-0.0991(4)	0.1883(1)	-0.0715(3)	2.15(4)
S(3)	0.5195(4)	0.6803(1)	0.6497(4)	2.72(5)
S(4)	0.3777(4)	0.4359(1)	0.2423(3)	1.91(4)

^a B values for anisotropically refined atoms are given in the form of the isotropic equivalent displacement parameter defined as $B_{\text{eq}} = (4/3)[a^2B_{11} + b^2B_{22} + c^2B_{33} + ab(\cos \gamma)B_{12} + ac(\cos \beta)B_{13} + bc(\cos \alpha)B_{23}]$.

Table 13. Fractional Atomic Coordinates and B_{eq} Values for α -KCuSe₄ with Their Estimated Standard Deviations in Parentheses

Atom	x	y	z	B_{eq}^{a} , Å ²
Se(1)	1.1417(3)	0.6855(2)	0.6029(1)	0.42(2)
Se(2)	0.8567(3)	0.8596(2)	0.6782(1)	0.41(2)
Se(3)	0.9272(3)	1.0848(2)	0.5762(1)	0.40(3)
Se(4)	1.3440(3)	1.1198(2)	0.6076(1)	0.50(3)
Cu	0.9733(4)	0.6422(2)	0.4301(2)	0.59(3)
K	0.6816(8)	0.4418(4)	0.6579(3)	1.19(7)

^a B values for anisotropically refined atoms are given in the form of the isotropic equivalent displacement parameter defined as $B_{\text{eq}} = (4/3)[a^2B_{11} + b^2B_{22} + c^2B_{33} + ab(\cos \gamma)B_{12} + ac(\cos \beta)B_{13} + bc(\cos \alpha)B_{23}]$.

Table 14. Fractional Atomic Coordinates and B_{eq} Values for α -CsCuSe₄ with Their Estimated Standard Deviations in Parentheses

Atom	x	y	z	B_{eq}^{a} , Å ²
Cs	0.3330(2)	0.56051(9)	0.33090(6)	2.36(2)
Se(1)	-0.1351(2)	0.3034(1)	0.40335(9)	1.71(2)
Se(2)	0.1543(2)	0.1385(1)	0.33804(9)	1.78(2)
Se(3)	0.0861(2)	-0.0798(2)	0.43006(9)	1.99(2)
Se(4)	-0.3281(2)	-0.1150(1)	0.40809(9)	1.91(2)
Cu	0.0414(3)	0.3634(2)	0.5587(1)	2.14(3)

^a B values for anisotropically refined atoms are given in the form of the isotropic equivalent displacement parameter defined as $B_{\text{eq}} = (4/3)[a^2B_{11} + b^2B_{22} + c^2B_{33} + ab(\cos \gamma)B_{12} + ac(\cos \beta)B_{13} + bc(\cos \alpha)B_{23}]$.

Table 15. Fractional Atomic Coordinates and B_{eq} Values for $\text{Na}_3\text{Cu}_4\text{Se}_4$ with Their Estimated Standard Deviations in Parentheses

Atom	x	y	z	B_{eq}^{a} , Å ²
Se(1)	0.2720(1)	0.15334(7)	0	1.26(4)
Se(2)	0.7472(1)	0.08944(7)	1/2	1.26(4)
Cu(1)	0.5694(2)	0.0899(1)	0	1.73(6)
Cu(2)	0.3461(2)	0.0647(1)	1/2	1.93(6)
Na(1)	0	0	1.0000	1.8(3)
Na(2)	0.5103(6)	0.2629(3)	1/2	2.0(2)

^a B values for anisotropically refined atoms are given in the form of the isotropic equivalent displacement parameter defined as $B_{\text{eq}} = (4/3)[a^2B_{11} + b^2B_{22} + c^2B_{33} + ab(\cos \gamma)B_{12} + ac(\cos \beta)B_{13} + bc(\cos \alpha)B_{23}]$.

Table 16. Fractional Atomic Coordinates and B_{eq} Values for $\text{Na}_{1.9}\text{Cu}_2\text{Se}_2\text{Cu}_2\text{O}$ with Their Estimated Standard Deviations in Parentheses

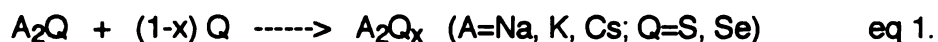
Atom	x	y	z	B_{eq}^{a} , Å ²
Se	0	0	0.1793(2)	1.45(9)
Cu(1)	1/2	0	1/4	2.0(1)
Cu(2)	0	-1/2	0	6.1(2)
Na	1/2	-1/2	0.118(1)	2.9(5) ^b
O	0	0	0	0.7(7)

^a B values for anisotropically refined atoms are given in the form of the isotropic equivalent displacement parameter defined as $B_{\text{eq}} = (4/3)[a^2B_{11} + b^2B_{22} + c^2B_{33} + ab(\cos \gamma)B_{12} + ac(\cos \beta)B_{13} + bc(\cos \alpha)B_{23}]$. ^b The refined occupancy of Na site is 96 (5) %.

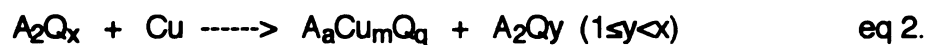
3. Results and Discussion

3.1. Synthesis and Spectroscopy

The synthesis of all compounds has been readily accomplished at the intermediate temperature range (215 °C - 400 °C) using alkali metal polychalcogenide fluxes as solvents and reagents. Each reaction formed a complete melt at the temperature employed. Alkali metal polychalcogenide flux is easily prepared by fusing alkali metal monochalcogenide with stoichiometric amounts of elemental chalcogen as shown in eq 1.



The highly reactive and corrosive A_2Q_x fluxes at the employed temperatures oxidize Cu metal and are reduced to shorter polychalcogenides as shown in eq 2.



After reaction, excess alkali metal polychalcogenides are easily removed from the product by washing with water and/or DMF. All compounds are relatively stable in moist air for several days.

Our initial synthesis attempts in the ternary A/Cu/Q system concentrated on temperatures below 400 °C which are relatively lower than those typically required for solid state reactions ($T > 500$ °C). The reaction of Cu in polysulfide fluxes (e.g. K_2S_x , Na_2S_x) at 375 °C or above yielded several known compounds such as KCu_4S_3 ⁶¹, CuS ⁶², and $Na_3Cu_4S_4$ ⁶³ which had been

prepared at relatively higher temperatures. This was disappointing, but it suggested that these temperatures were still too high to stabilize any new phases in this system. Therefore, we lowered the reaction temperature to 250 °C and isolated a novel polychalcogenide phase, β -KCuS₄, using polychalcogenide flux (e.g. K₂S₅). When we used a polysulfide flux with shorter chains (e.g. K₂S₃) the thermodynamically stable phase, KCu₄S₃⁶¹, was still isolated at 250 °C. This is probably due to the higher reactivity of this more basic shorter chain flux. When the reaction temperature was lowered to 215 °C, surprisingly, another polychalcogenide phase, α -KCuS₄, was obtained using the same reactant ratio K₂S/Cu/S of 2/1/8 (e.g. in K₂S₅ flux) as that of β -KCuS₄. Since the α - and β -phase are formed from the same reactant ratio but at slightly different temperatures, they are expected to originate from the same solution precursor. The β -phase, which requires a slightly higher temperature to form, is probably more thermodynamically stable than the α -phase. The α - to β -transformation is not reversible and was only observed in the polysulfide flux (K₂S₅). Attempts to effect an α - to β -conversion by heating crystals of α -KCuS₄ at 250 °C in the absence of K₂S₅ flux resulted in decomposition to CuS and K₂S_x. These observations underscore the importance of the nature of the polychalcogenide flux and the reaction temperature in stabilizing new metastable phases. They emphasize the validity of the intermediate temperature approach that we have undertaken.

The extension of the above reaction into polyselenide systems showed chemistry similar to that seen in polysulfide system. α -KCuSe₄ was obtained in the polyselenide fluxes (K₂Se₃–K₂Se₉) at 250 °C. Since β -KCuS₄ was formed at slightly higher temperature compared to the low-temperature α -polymorph, we increased the reaction temperature to 390 °C to obtain the Se-analogue of β -KCuS₄. However, α -KCuSe₄ is the only phase we have seen in the entire

temperature region (250-390 °C). The expected β -KCuSe₄ perhaps requires a higher temperature to overcome the activation barrier of the α - to β -conversion or it can not exist as a stable lattice.

During this study we saw another promising phase in the reactant ratio K₂Se/Cu/Se of 1/1/8 at 250 °C, but we could not reproduce it for sometime. It has the approximate composition of KCuSe₇ as determined by the EDS/SEM analysis. Since this phase has a composition more selenium-rich than α -KCuSe₄, we increased the selenium ratio from 1/1/8 to 1/1/16. Of these, 1/1/12~13 ratios yielded better crystals at 350 °C. The preliminary X-ray single crystal study was unsuccessful due to poor crystallinity and hair-like morphology. We were unsuccessful in refining the structure, but preliminary refinements showed highly disordered Se₆²⁻ and Se₄²⁻ units. Recollection of the data is necessary to complete the structural refinement. The cell parameters of this new phase are: a=12.560(4) Å, b=5.449(6) Å, c=22.949(4) Å, and β =92.95(2) deg. Work to obtain better single crystals is in progress.

The use of cesium polyselenide fluxes (Cs₂Se₃~Cs₂Se₉) yielded results similar to those seen in potassium polyselenide flux. α -CsCuSe₄ was the only product obtained in the Cs/Cu/Se system in the temperature range of 250-350 °C.

The use of Na₂Se_x flux, which requires a slightly higher reaction temperature to form melt, did not afford any polychalcogenide compounds. Two competing phases, Na₃Cu₄Se₄ and Na_{1.9}Cu₂Se₂·Cu₂O, were isolated. Even though we suspected that either Na₂Se or Cu metal had become contaminated with oxygen, isolation of oxygen containing phase was quite surprising to us because of the well known Cu chalcophilicity. The Na₂Se is likely the oxygen source in the reaction due to the surface oxidation of sodium metal producing NaOH during the period of its preparation. Many variations in the reaction

conditions were made to obtain pure $\text{Na}_3\text{Cu}_4\text{Se}_4$ and $\text{Na}_{1.9}\text{Cu}_2\text{Se}_2\cdot\text{Cu}_2\text{O}$ phases. We used fresh Na_2Se every time and varied reactant ratios and reaction temperatures, but $\text{Na}_2\text{Cu}_2\text{Se}_2\cdot\text{Cu}_2\text{O}$ was always present as a coexisting phase. Among them, only the reactant ratio $\text{Na}_2\text{Se}/\text{Cu}/\text{Se}$ of 4/1.5/8 at 330 °C gave a relatively homogeneous product of $\text{Na}_3\text{Cu}_4\text{Se}_4$. The rest of the reactions yielded $\text{Na}_{1.9}\text{Cu}_2\text{Se}_2\cdot\text{Cu}_2\text{O}$ as the major product with a small amount of $\text{Na}_3\text{Cu}_4\text{Se}_4$ which can be identified by its X-ray powder diffraction (XRD) pattern. Especially the 3/1/8 ratio at 340 °C yielded a relatively pure phase of $\text{Na}_{1.9}\text{Cu}_2\text{Se}_2\cdot\text{Cu}_2\text{O}$ with large (1 mm) single crystals, but it was still contaminated with $\text{Na}_3\text{Cu}_4\text{Se}_4$. When we increased the reaction temperature to 450 °C, increased amounts of the $\text{Na}_{1.9}\text{Cu}_2\text{Se}_2\cdot\text{Cu}_2\text{O}$ phase were observed, implying that it is thermodynamically the more stable phase. Preparation of $\text{Na}_{1.9}\text{Cu}_2\text{Se}_2\cdot\text{Cu}_2\text{O}$ using Cu_2O instead of Cu metal at 330 °C gave almost the same results we had seen in the $\text{Na}_2\text{Se}/\text{Cu}/\text{Se}$ system. The reactant ratio $\text{Na}_2\text{Se}/\text{Cu}_2\text{O}/\text{Se}$ of 3/2/8 yielded fairly pure $\text{Na}_{1.9}\text{Cu}_2\text{Se}_2\cdot\text{Cu}_2\text{O}$ with small contamination of $\text{Na}_3\text{Cu}_4\text{Se}_4$. We also used a different source of Na_2Se , purchased from CERAC. However, it yielded discouraging results. The reaction mixtures did not form melts even at 450 °C and selenium simply evaporated into the colder regions of the reaction tubes, probably because the particle size (-100 mesh) of Na_2Se purchased was larger than that which we prepared or, more likely, the Na_2Se was grossly impure. Further work is in progress to obtain homogeneous phases and large size single crystals suitable for charge transport property measurements.

In the far-IR region (I), (II), (III), and (IV) exhibit spectral absorptions due to Q-Q and/or Cu-Q stretching vibrations as shown in Figure 5. Observed absorption frequencies are given in Table 17.

Figure 5. Far-IR spectra of (A) α -KCuS₄, (B) β -KCuS₄, (C) α -KCuSe₄, and (D) α -CsCuSe₄.

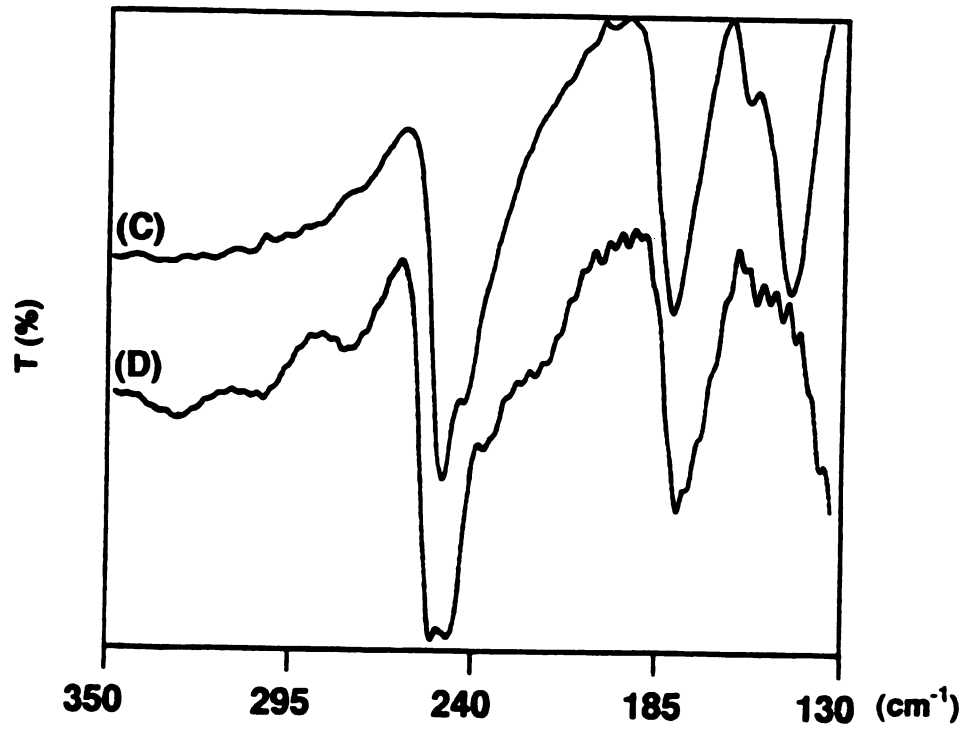
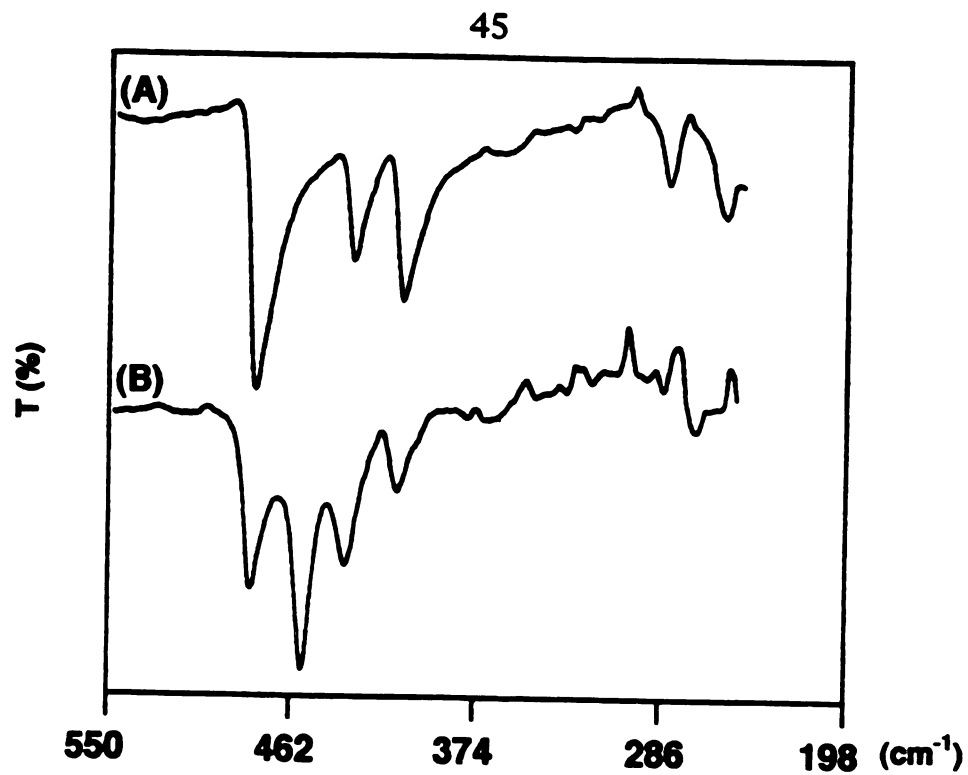


Figure 5.

Table 17. Frequencies (cm^{-1}) of Spectral Absorptions of (I), (II), (III), and (IV) due to Q-Q and M-Q Stretching Vibrations

(I)	(II)	(III)	(IV)
$\alpha\text{-KCuS}_4$	$\beta\text{-KCuS}_4$	$\alpha\text{-KCuSe}_4$	$\alpha\text{-CsCuSe}_4$
481 (s) ^a	481 (m)	249 (s)	252 (s)
435 (m)	456 (s)	241 (w)	246 (s)
412 (m)	436 (m)	180 (m)	236 (w)
286 (m)	412 (m)	158 (w)	179 (m)
259 (m)	269 (w)	145 (m)	175 (w)

^a (s) strong; (m) medium; (w) weak

The polysulfide compounds in this study, α - and β - KCuS_4 , show a common absorption at 481 cm^{-1} which is attributed to a S-S stretching vibration by comparison with the spectra of other known polysulfide compounds.⁶⁴ The $\nu_{\text{S-S}}$ vibrational frequencies are observed in the range of $446\sim 500 \text{ cm}^{-1}$. The additional common peak at 435 cm^{-1} can be attributed to a Cu-S stretching vibration. For Cu/Se_4^{2-} polyselenide compounds, a spectral absorption is observed in the range of $246\sim 252 \text{ cm}^{-1}$. This band can be assigned to Se-Se stretching vibrations by comparison with the spectra of other known polyselenide complexes and with that of the unbound ligand $(\text{Ph}_4\text{P})_2\text{Se}_5^{26(\text{b})}$ ($\nu_{\text{Se-Se}}$ 267 cm^{-1}). In addition, the $\nu_{\text{Se-Se}}$ absorption in this region has been observed previously in various compounds, e.g. Se_x^{2-65} ($x=1-6$) at 258 cm^{-1} , C-Se_6^{66} at 253 cm^{-1} , $[\text{Fe}_2\text{Se}_{12}]^{2-24}$ at 258 cm^{-1} , and $[\text{Pd}(\text{Se}_4)_2]^{2-67}$ at 274 cm^{-1} .

In Cu/Se_4^{2-} compounds an additional absorption band was found in the vicinity of 240 cm^{-1} . This can be a possible candidate for a Cu-Se stretching vibration. It is usually difficult to interpret the IR spectra of metal polyselenide compounds unambiguously because M-Se and Se-Se stretching frequencies fall in the same low-frequency IR region ($200\text{-}340\text{ cm}^{-1}$ for Se) and systematic IR spectroscopic data for the various free ligands (Q_x^{2-} , $x=2\text{-}6$) and metal chalcogenide complexes are still lacking.

3.2. Description of Structures

3.2.1. Structure of $\alpha\text{-KCuS}_4$ (I), $\alpha\text{-KCuSe}_4$ (III), and $\alpha\text{-CsCuSe}_4$ (IV)

(I), (II), and (III) possess one-dimensional structures as shown in Figure 6. They are isostructural with the known $(\text{NH}_4)\text{CuS}_4$ ³⁶ and contain tetrachalcogenide ligands (S_4^{2-} or Se_4^{2-}) chelating and also bridging Cu atoms. The infinite noncentrosymmetric $[\text{CuQ}_4]_n^{n-}$ (hereafter $\text{Q}=\text{S, Se}$) chains are running parallel to the crystallographic *a*-axis. The chains are composed of condensed CuQ_4 five-membered rings related to each other by a crystallographic 2-fold screw axis, parallel to the chain direction as shown in Figure 7. The whole $\alpha\text{-}[\text{Cu}(\text{Q}_4)]_n^{n-}$ chain can be viewed as an array of fused CuQ_4 and Cu_2Q_3 five-membered rings. The Q_4^{2-} ligand features an asymmetric bridging mode bound to three Cu^+ centers. It chelates one Cu atom via its terminal atoms (Q(1) and (Q(4))) and bridges two neighboring copper atoms via a terminal atom (Q(1)) and an adjacent internal atom (Q(2)). The Cu atoms are all crystallographically equivalent and feature a distorted tetrahedral geometry. The average Cu-Q bond distances are $2.34(6)\text{ \AA}$, $2.45(6)\text{ \AA}$, and $2.47(8)\text{ \AA}$ in (I), (II), and (III) respectively. However, the Cu-Q bridging bond of the internal chalcogenide atom (Q(1)) is slightly elongated compared to the

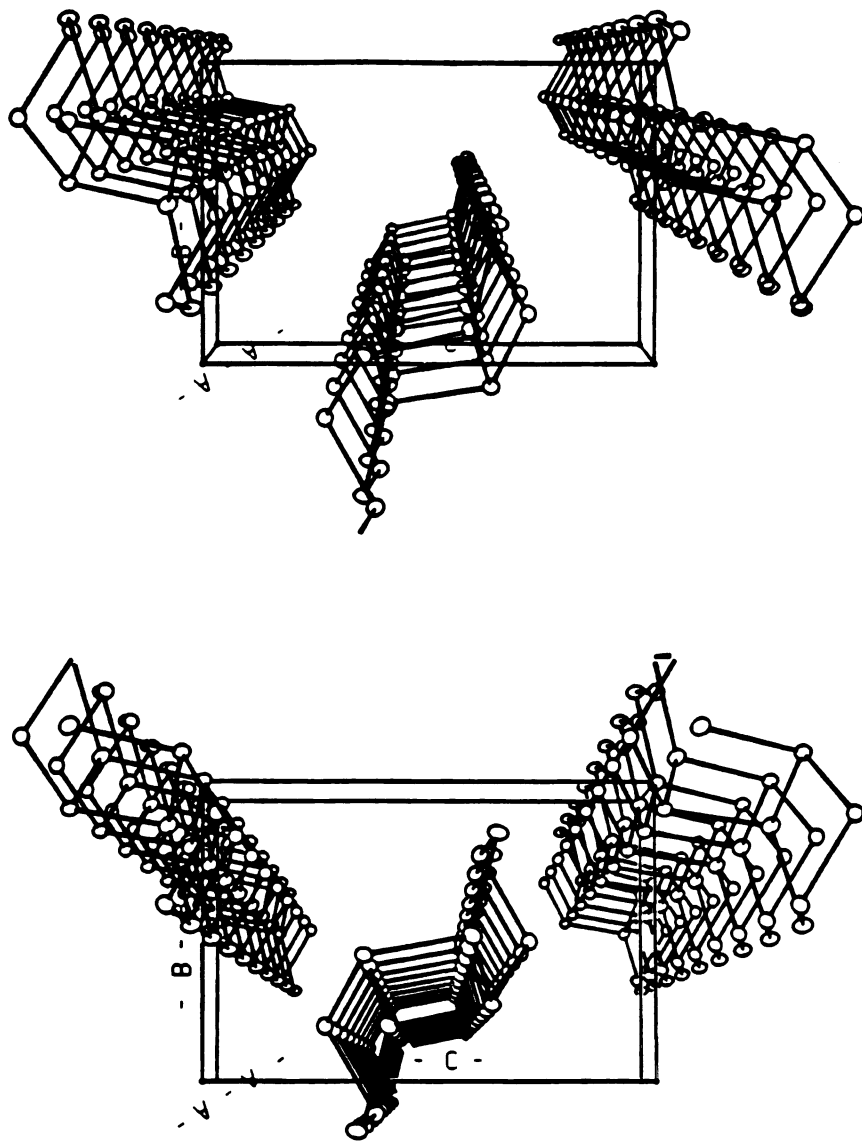


Figure 6. Stereoview of the unit cell of α -ACuQ₄ (A=K, Cs; Q=S, Se). The alkali atoms have been omitted for clarity.

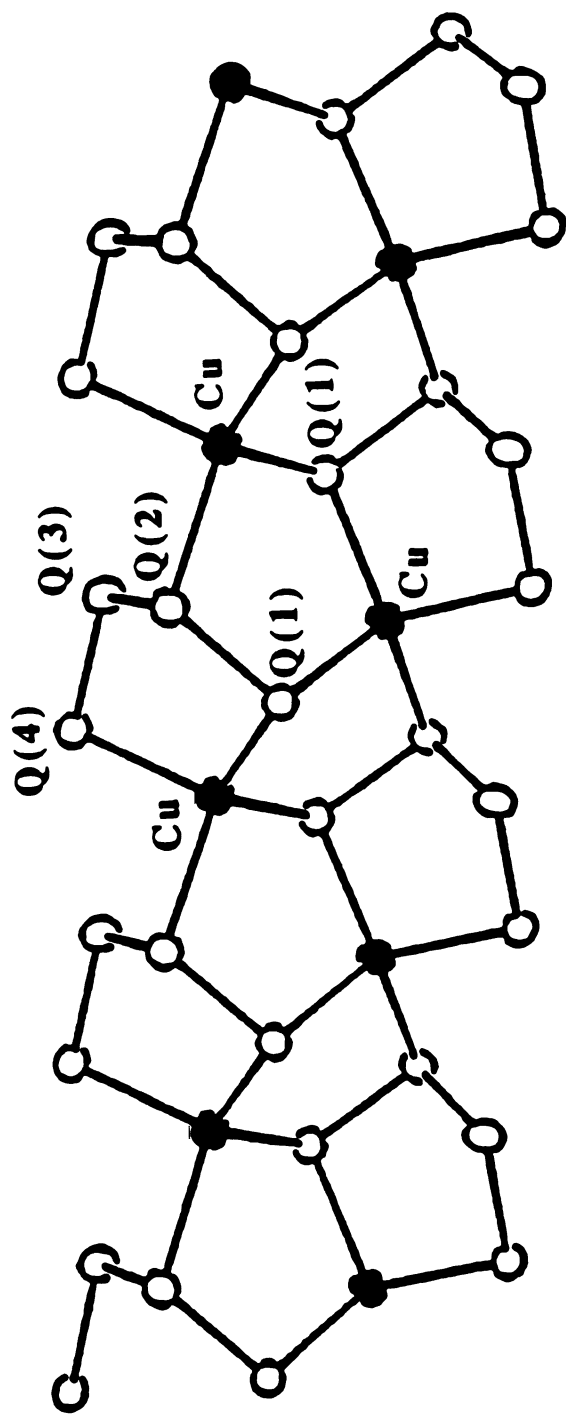


Figure 7. ORTEP representation of the one-dimensional infinite α -[CuQ₄]_nⁿ⁻ chain with labeling scheme.

other three Cu-Q bonds of tetrahedral Cu atoms. They are 2.428(3) Å, 2.528(3) Å, and 2.592(2) Å for (I), (II), and (III) respectively. Selected bond distances and angles are given in Tables 18-20. There is one crystallographically distinct alkali metal in the asymmetric unit of α -ACuQ₄ (A=K, Cs). The alkali ions are distributed between the chains. The environments of alkali ions in each compound vary from 5-coordination to 8-coordination depending on the criteria used to determine their ionic interaction limits. The shortest distances are K-S(3) at 3.218(4) Å, K-Se(3) at 3.322(4) Å, and Cs-Se(3) at 3.620(2) Å.

Table 18. Selected Bond Distances (Å) and Angles (deg) in α -KCuS₄ with Standard Deviations in Parentheses

Cu-S(1)	2.321(3)	S(1)-Cu-S(1)	109.8(1)
Cu-S(1)	2.298(3)	S(1)-Cu-S(2)	100.3(1)
Cu-S(2)	2.428(3)	S(1)-Cu-S(4)	120.0(1)
Cu-S(4)	2.305(3)	S(1)-Cu-S(2)	126.5(1)
Cu-S (mean)	2.34(6)	S(1)-Cu-S(4)	103.4(1)
		S(2)-Cu-S(4)	98.1(1)
S(1)-S(2)	2.091(4)	Cu-S(1)-Cu	102.1(1)
S(2)-S(3)	2.096(4)	Cu-S(1)-S(2)	105.1(1)
S(3)-S(4)	2.061(4)	Cu-S(1)-S(2)	101.4(1)
S-S (mean)	2.08(2)	Cu-S(2)-S(1)	109.7(1)
		Cu-S(2)-S(3)	85.8(1)
K-S(1)	3.337(4)	S(1)-S(2)-S(3)	104.1(2)
K-S(2)	3.308(4)	S(2)-S(3)-S(4)	103.2(2)
K-S(3)	3.424(4)	Cu-S(4)-S(3)	98.7(1)
K-S(3)	3.218(4)		
K-S(4)	3.252(4)		
K-S(4)	3.458(4)		
K-S(4)	3.294(4)		
K-S (mean)	3.33(9)	Cu-Cu	3.592(2)

Table 19. Selected Bond Distances (Å) and Angles (deg) in α -KCuSe₄ with Standard Deviations in Parentheses

Cu-Se(1)	2.431(2)	Se(1)-Cu-Se(1)	110.83(9)
Cu-Se(1)	2.397(3)	Se(1)-Cu-Se(2)	122.9(1)
Cu-Se(2)	2.528(3)	Se(1)-Cu-Se(2)	100.54(9)
Cu-Se(4)	2.428(2)	Se(1)-Cu-Se(4)	115.98(9)
Cu-Se (mean)	2.45(6)	Se(1)-Cu-Se(4)	108.86(9)
		Se(2)-Cu-Se(4)	97.48(9)
Se(1)-Se(2)	2.382(2)	Cu-Se(1)-Cu	103.06(9)
Se(2)-Se(3)	2.381(2)	Se(1)-Se(2)-Se(3)	100.85(8)
Se(3)-Se(4)	2.351(2)	Se(2)-Se(3)-Se(4)	99.81(8)
Se-Se (mean)	2.37(2)	Se(2)-Se(1)-Cu	102.47(9)
		Se(2)-Se(1)-Cu	100.36(8)
K-Se(1)	3.373(4)	Se(1)-Se(2)-Cu	108.91(8)
K-Se(3)	3.533(4)	Se(3)-Se(2)-Cu	80.75(7)
K-Se(3)	3.322(4)	Se(3)-Se(4)-Cu	97.58(8)
K-Se(4)	3.413(4)		
K-Se(4)	3.562(4)		
K-Se (mean)	3.44(10)	Cu-Cu	3.781(3)

Table 20. Selected Bond Distances (Å) and Angles (deg) in α -CsCuSe₄ with Standard Deviations in Parentheses

Cu-Se(1)	2.439(2)	Se(1)-Cu-Se(1)	110.99(8)
Cu-Se(1)	2.405(2)	Se(1)-Cu-Se(2)	98.94(7)
Cu-Se(2)	2.592(2)	Se(1)-Cu-Se(4)	119.83(8)
Cu-Se(4)	2.426(2)	Se(1)-Cu-Se(2)	119.82(8)
Cu-Se (mean)	2.47(9)	Se(1)-Cu-Se(4)	108.56(8)
		Se(2)-Cu-Se(4)	98.64(7)
Se(1)-Se(2)	2.374(2)		
Se(2)-Se(3)	2.379(2)	Se(2)-Se(1)-Cu	101.84(7)
Se(3)-Se(4)	2.350(2)	Se(2)-Se(1)-Cu	101.64(7)
Se-Se (mean)	2.37(2)	Cu-Se(1)-Cu	104.24(7)
		Se(1)-Se(2)-Se(3)	101.71(6)
Cs-Se(1)	3.632(2)	Se(1)-Se(2)-Cu	110.90(7)
Cs-Se(2)	3.662(2)	Se(3)-Se(2)-Cu	80.11(6)
Cs-Se(2)	3.767(2)	Se(2)-Se(3)-Se(4)	101.44(6)
Cs-Se(3)	3.783(2)	Se(3)-Se(4)-Cu	98.22(7)
Cs-Se(3)	3.620(2)		
Cs-Se(4)	3.643(1)		
Cs-Se(4)	3.777(2)		
Cs-Se(4)	3.686(1)		
Cs-Se (mean)	3.70(7)	Cu-Cu	3.824(2)

3.2.2. Structure of β -KCuS₄ (II)

The structure of β -KCuS₄ is composed of centrosymmetric one-dimensional chains as shown in Figure 8. The chains are running parallel to the crystallographic *a*-axis and feature an almost linear array (Cu-Cu-Cu angle is 173.5°) of Cu atoms bridged by S₄²⁻ ligands. This bridging occurs via the terminal sulfur atoms of the chelating tetrasulfide units and is distinct from that in the α -polymorph, resulting in an entirely new one-dimensional chain structure. It is the first example of a single tetrasulfide ligand holding on to three almost collinear metal centers. The chains can be viewed as being composed of fused five-membered CuS₄ and four-membered Cu₂S₂ rings as shown in Figure 9. The center of symmetry in the chain lies at the center of the Cu₂S₂ rhombus. The Cu atoms are all crystallographically equivalent and feature a distorted tetrahedral geometry. The average Cu-S distance is 2.370(7) Å. There are short Cu-Cu distances at 2.607(1) Å and 2.661(1) Å. The presence of sulfide bridging ligands complicates any attempts to characterize these short distances as bonding, although they may be considered as d¹⁰-d¹⁰ "attractive interactions"⁶⁸. Short Cu-Cu contacts are not uncommon in either discrete⁶⁹ or solid state structures, some examples of which include KCu₃S₂⁷⁰, K₃Cu₈S₆⁷¹, and KCuS⁷². There is one crystallographically distinct K atom in the asymmetric unit. The K⁺ atoms are distributed between the chains. They are surrounded by seven sulfur atoms in the range of 3.237(2)-3.370(2) Å. Selected bond distances and angles are given in the Table 21.

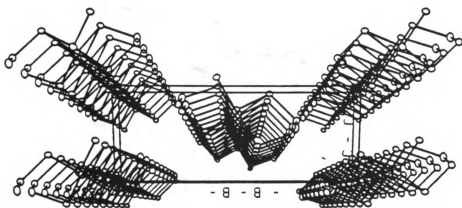
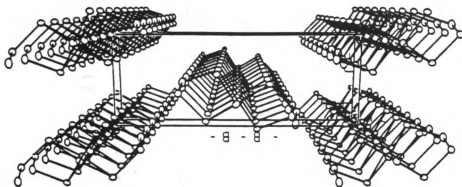


Figure 8. Stereoview of the unit cell of β - KCuS_4 . The alkali atoms have been omitted for clarity.

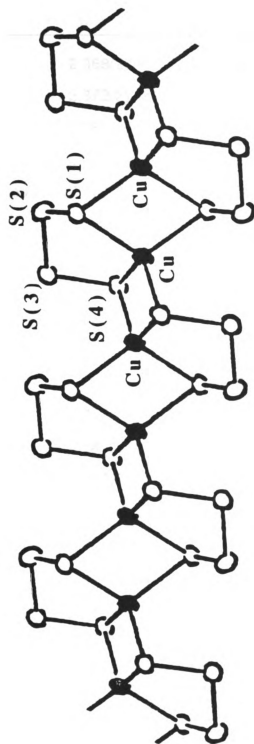


Figure 9. ORTEP representation of the one-dimensional infinite β - $[\text{CuS}_4]_n$ chain with labeling scheme.

Table 21. Selected Bond Distances (Å) and Angles (deg) in β -KCuS₄ with Standard Deviations in Parentheses

Cu-S(1)	2.368(2)	S(1)-Cu-S(1)	113.28(5)
Cu-S(1)	2.372(2)	S(1)-Cu-S(4)	110.33(6)
Cu-S(4)	2.360(2)	S(1)-Cu-S(4)	109.65(6)
Cu-S(4)	2.378(2)	S(1)-Cu-S(4)	109.95(6)
Cu-S (mean)	2.370(7)	S(1)-Cu-S(4)	101.75(6)
		S(4)-Cu-S(4)	111.65(5)
S(1)-S(2)	2.078(2)	Cu--S(1)-Cu	66.73(5)
S(2)-S(3)	2.060(2)	Cu--S(1)-S(2)	104.32(8)
S(3)-S(4)	2.080(2)	Cu--S(1)-S(2)	99.74(8)
S-S (mean)	2.07(1)	S(1)-S(2)-S(3)	103.94(9)
		S(2)-S(3)-S(4)	104.69(9)
K-S(1)	3.237(2)	Cu-S(4)-Cu	68.35(5)
K-S(1)	3.243(2)	Cu-S(4)-S(3)	104.02(8)
K-S(2)	3.370(2)	Cu-S(4)-S(3)	99.20(8)
K-S(2)	3.259(2)		
K-S(4)	3.326(2)		
K-S(4)	3.347(2)	Cu-Cu	2.607(1)
K-S(4)	3.342(2)	Cu-Cu	2.661(1)
K-S (mean)	3.30(6)		

3.2.3. Structure of $\text{Na}_3\text{Cu}_4\text{Se}_4$ (V)

The compound $\text{Na}_3\text{Cu}_4\text{Se}_4$ possesses a one-dimensional structure as shown in Figure 10. It is isostructural to the known mixed-valence compound $\text{Na}_3\text{Cu}_4\text{S}_4$ ⁶³. The structure of $\text{Na}_3\text{Cu}_4\text{Se}_4$ consists of infinite centrosymmetric $[\text{Cu}_4\text{Se}_4]_n^{3n-}$ columns running parallel to the crystallographic *c*-axis. The center of symmetry is lying at the center of the column. The columns are composed of parallel Cu_4Se_4 eight-membered rings which are connected to each other by the inter-ring Cu-Se bonds as shown in Figure 11. Alternatively, this can be viewed as an array of fused Cu_3Se_3 six-membered rings.

$\text{Na}_3\text{Cu}_4\text{Se}_4$ is formally a mixed-valence compound. Based on the formula $\text{Na}_3\text{Cu}_4\text{Se}_4$ and the assumption that the formal oxidation state on each Se atom is -2, the formal oxidation state on Cu atoms is +1 (three atoms) and +2 (one atom). However, the coexistence of Cu^{2+} and Se^{2-} is thermodynamically unstable with respect to electron transfer from the reducing Se^{2-} to the oxidizing Cu^{2+} . If one then considers all copper atoms in the +1 oxidation state, one electron vacancy exists per four Se atoms. In $\text{Na}_3\text{Cu}_4\text{Se}_4$ there are two crystallographically distinct Cu atoms in the asymmetric unit. They feature slightly distorted trigonal planar geometry. The average Cu-Se bond distances, 2.38(2) Å for Cu(1) and 2.443(1) Å for Cu(2), are similar to those of three-coordinated Cu^{1+} atoms in TlCu_3Se_2 ⁷³ at 2.46(1)~2.47(8) Å. There are two crystallographically distinct Se atoms in the asymmetric unit. They are bonded to three Cu atoms with trigonal pyramidal geometry. The average Cu-Se(1) distance of 2.43(2) Å is very similar to that of Cu-Se(2) of 2.39(5) Å. Therefore, these two crystallographically distinct selenium atoms are expected to have indistinguishable oxidation states. Since there is no short Se-Se contacts, we can expect one electron deficiency (hole) to be delocalized on the valence

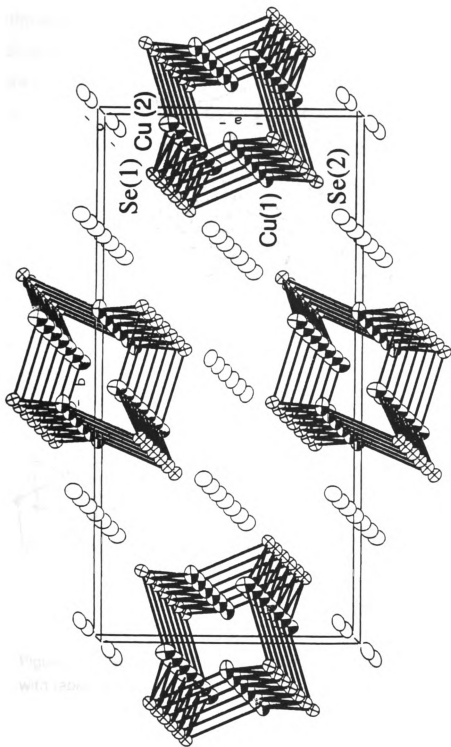


Figure 10. ORTEP representation of the unit cell of $\text{Na}_3\text{Cu}_4\text{Se}_4$.

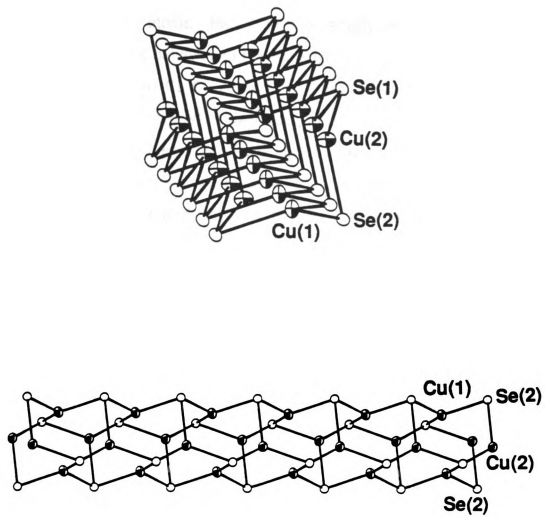


Figure 11. Two views of the one-dimensional structure of $[\text{Cu}_4\text{Se}_4]_n^{3-}$ with labeling scheme.

band, consisting mainly of p orbitals of four atoms. This gives rise to -1.75 average formal charge on Se. Therefore, $\text{Na}_3\text{Cu}_4\text{Se}_4$ can be reasonably formulated as $(\text{Na}^+)_3(\text{Cu}^+)_4(\text{Se}^{1.75-})_4$. These are only formal charges; the actual description is more complex due to the small electronegativity difference between Cu and Se atoms. Based on this partially empty valence band, we expect p-type metallic behavior for this material.

There are short Cu-Cu contacts at 2.593(2) Å in the column, slightly shorter than those observed in $\text{Na}_3\text{Cu}_4\text{S}_4$ at 2.619(1) Å. These short Cu-Cu contacts can be considered as $d^{10}\text{-}d^{10}$ attractive interactions⁶⁸. Selected bond distances and angles are given in Table 22. There are two crystallographically distinct Na atoms located between the chains. They participate in ionic interactions with Se atoms and have distorted octahedral geometry with 6 adjacent Se atoms. The shortest Na-Se bond distances are 3.033(2) Å for Na(1)-Se(2) and 2.971(5) Å for Na(2)-Se(2).

Table 22. Selected Bond Distances (Å) and Angles (deg) in Na₃Cu₄Se₄ with Standard Deviations in Parentheses

Cu(1)-Se(1)	2.402(2)	Se(1)-Cu(1)-Se(2)	120.73(5) (x2)
Cu(1)-Se(2)	2.362(2) (x2)	Se(2)-Cu(1)-Se(2)	112.36(9)
Cu-Se (mean)	2.38(2)	Se(1)-Cu(2)-Se(1)	106.89(9)
		Se(1)-Cu(2)-Se(2)	117.77(5) (x2)
Cu(2)-Se(1)	2.443(2) (x2)	Cu(1)-Se(1)-Cu(2)	64.73(5) (x2)
Cu(2)-Se(2)	2.444(2)	Cu(2)-Se(1)-Cu(2)	106.89(9)
Cu-Se (mean)	2.443(6)	Cu(1)-Se(2)-Cu(1)	112.36(9)
		Cu(1)-Se(2)-Cu(2)	81.14(5) (x2)
Na(1)-Se(2)	3.033(2) (x4)	Na(2)-Se(1)	3.120(4) (x2)
Na(1)-Se(1)	3.080(1) (x2)	Na(2)-Se(1)	3.036(4) (x2)
Na(1)-Se (mean)	3.05(2)	Na(2)-Se(2)	2.971(5)
		Na(2)-Se(2)	3.167(5)
Cu(2)-Cu(1)	2.593(2)	Na(2)-Se (mean)	3.08(7)
Cu(1)-Cu(1)	2.922(3)		
Cu(2)-Cu(2)	3.009(3)		
Cu(1)-Cu(2)	3.126(2)		

3.2.4. Structure of Na_{1.9}Cu₂Se₂-Cu₂O (VI)

The structure of Na_{1.9}Cu₂Se₂-Cu₂O is intriguing and consists of two independent layers of [CuSe]_nⁿ⁻ and [Cu₂O] as shown in Figure 12. It can be considered an intergrowth of NaCuSe⁷⁴ with a Cu₂O layer. Figure 13 shows views of the two individual layers. The [CuSe]_nⁿ⁻ in the NaCuSe fragment is an anti PbO-type layer, where Cu (on -4m2 site) has tetrahedral geometry and Se (on 4mm site) has square pyramidal geometry. The average Cu-Se bond distance of 2.484 (3) is slightly smaller than that found in NaCuSe (2.55 Å), but is very similar to those found in α-ACuSe₄ (A=K, Cs) (see Tables 19 and 20). The Cu₂O layer is a new structural type. In this layer Cu, situated on a crystallographic mmm site, has linear coordination and oxygen on the crystallographic 4/mmm site are bonded to four linear Cu atoms with square planar geometry. Thus, the Cu₂O layer can be considered as an anti CuO₂-type layer, common in high T_c cuprate superconductors⁷⁵. Square planar geometry of oxygen is rare in metal oxide chemistry. One known example is NbO⁷⁶, which contains square planar Nb and O atoms in the framework. The average Cu-O bond distance of linear Cu atoms of 1.957 (1) Å is in the normal range found in known Cu/O compounds (1.85~1.98 Å). There are short Cu--Cu contacts in the layers in the range of 2.768(2) Å, but no Cu--Cu contacts between the layers. Selected bond distances and angles are given in Table 23. Na_{1.9}Cu₂Se₂-Cu₂O is the first example of cocrystallization of a Cu/O layer with Cu/Q layer. It is interesting to see the similarity in lattice size of two independent layers; this could be the driving force to stabilize the whole lattice.

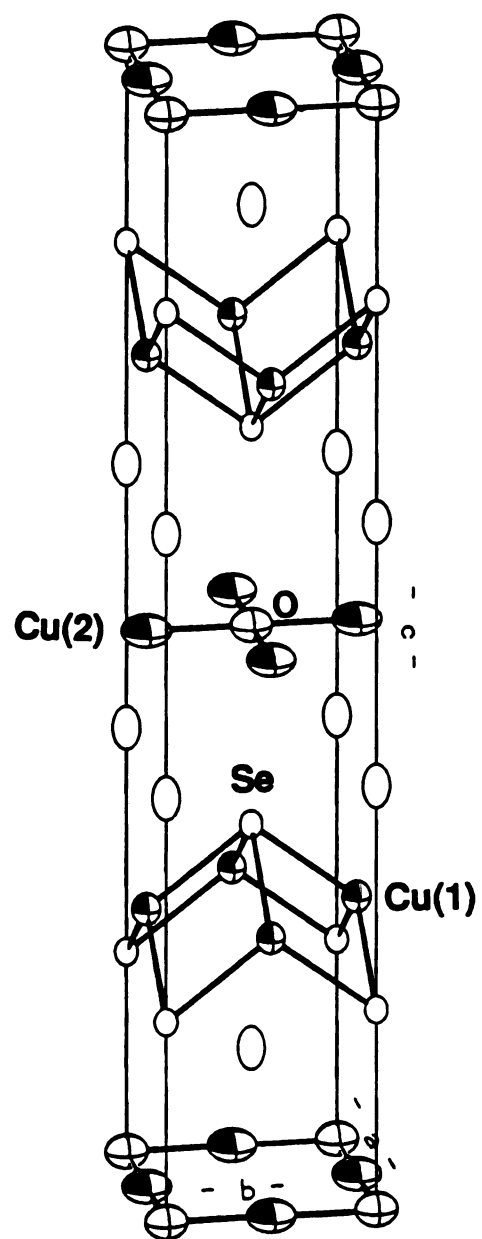


Figure 12. ORTEP representation of the unit cell of $\text{Na}_{1.9}\text{Cu}_2\text{Se}_2 \cdot \text{Cu}_2\text{O}$ with labeling scheme.

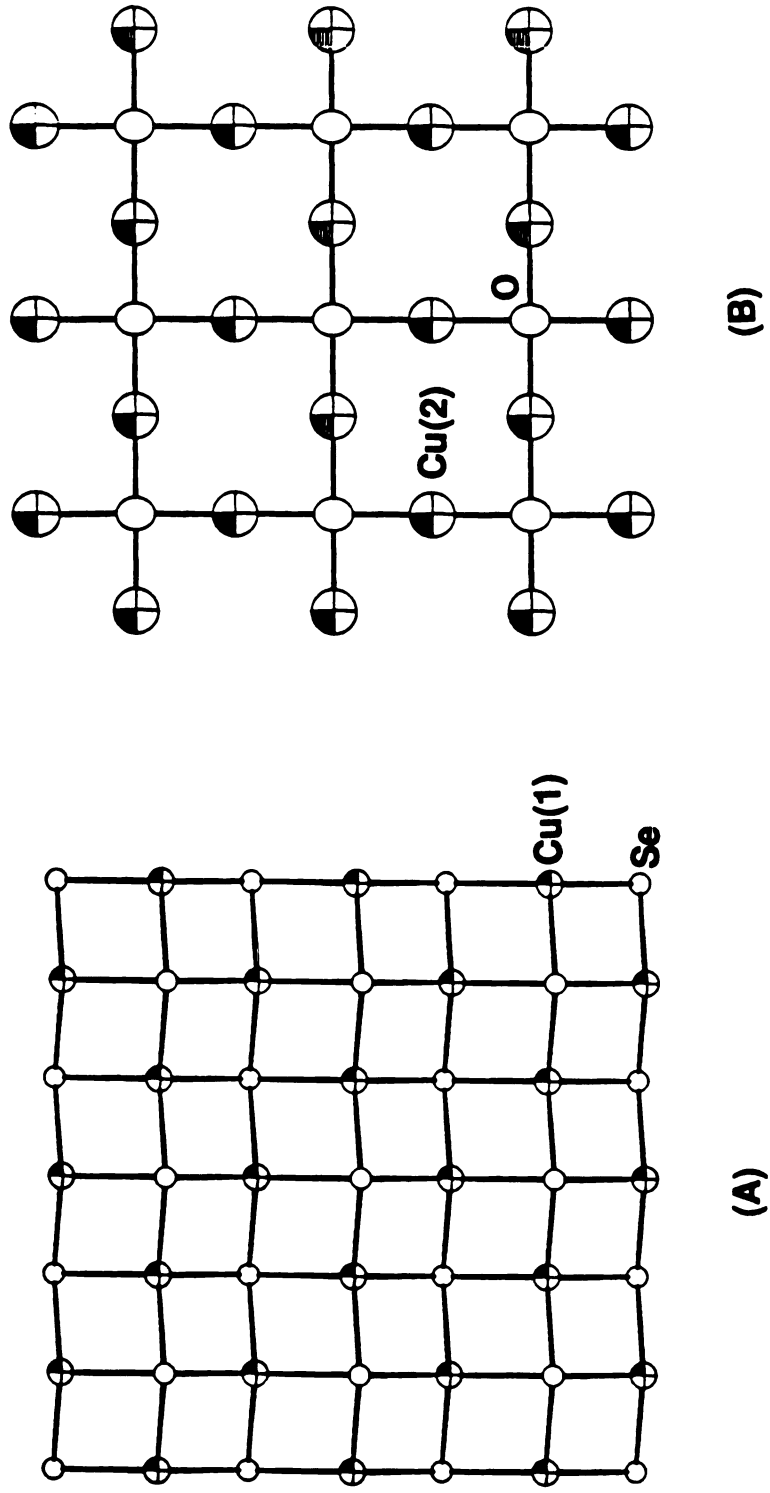
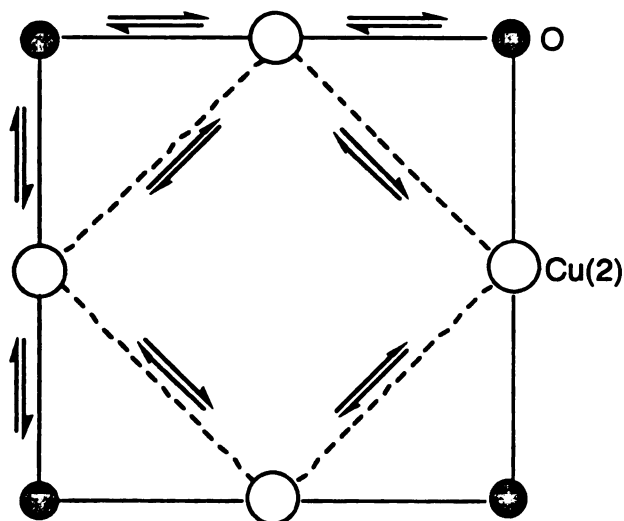


Figure 13. ORTEP representation of (A) [CuSe]_n⁻ layer (B) Cu₂O layer viewed down [001] direction. Octant-shaded ellipsoids are Cu atoms and open circles are Se and O atoms.

Table 23. Selected Bond Distances (Å) and Angles (deg) in Na_{1.9}Cu₂Se₂Cu₂O with Standard Deviations in Parentheses

Cu(1)-Se	2.484(3) (x4)	Se-Cu(1)-Se	104.0(2) (x3)
Cu(1)-Cu(1)	2.768(2)	Se-Cu(1)-Se	112.29(9)(x3)
		Cu(1)-Se-Cu(1)	67.71(9) (x4)
		Cu(1)-Se-Cu(1)	104.0(2) (x2)
Cu(2)-O	1.957(1)	O-Cu(2)-O	180.00
Cu(2)-Cu(2)	2.768(2)	Cu(2)-O-Cu(2)	90.00 (x4)
		Cu(2)-O-Cu(2)	180.00 (x2)
Cu-Cu			
Na-Se	3.070(9) (x4)		
Cu(1)-Cu(1)	3.914(2)		
Cu(2)-Cu(2)	3.914(2)		

It should be noted that the temperature factor of the Cu(2) atom in the Cu₂O layer is very large (see Table 16). This may suggest positional disorder of this atom on the (0,1/2,0) position. Cu atoms may move back and forth along *a*- and *b*-axis to make Cu-O and Cu-Cu distances short and long as shown in the following Scheme 1. This could occur randomly in the lattice and would not be detectable by an X-ray single crystal study, but could be manifested as higher temperature factors for Cu.



Scheme 1

Based on the structural formula $\text{Na}_{1.9}\text{Cu}_2\text{Se}_2\text{Cu}_2\text{O}$, one could expect p-type metallic behavior for this material. Partial removal of electropositive elements from the lattice is accompanied with the creation of electron vacancies in the framework (e.g. oxidation of the framework), resulting in a partially empty valence band. This p-type metallic behavior is consistent with the measured charge transport properties (see below). Alternatively, the removal of Cu atoms from the framework also creates electron holes, resulting p-type metallic behavior. However, based on the refinement result, this does not appear to occur to a significant extent.

There is only one crystallographically distinct Na atom situated on a crystallographic 4mm site. Na atoms interact ionically only with Se atoms at 3.070 (9) Å. They have square pyramidal geometry.

3.3. Close Structural Relationships between α - and β - $[\text{Cu}(\text{S}_4)]_n^{n-}$ Chains.

The α - $[\text{Cu}(\text{S}_4)]_n^{n-}$ chain is quite distinct from the β - $[\text{Cu}(\text{S}_4)]_n^{n-}$ chain in binding mode of the tetrasulfide ligand, even though the two have a very close structural relationship. For instance, both chains are composed of tetrasulfide ligands and CuS_4 five-membered rings. Yet, the bridging mode of tetrasulfide ligand and the Cu atom arrangement in both chains exhibit a significant difference. In the α - $[\text{Cu}(\text{S}_4)]_n^{n-}$ chain, the bridging atoms of tetrasulfide ligand are one a terminal atom and the other an internal atom, which lead to the zigzag array of Cu atoms along the chain direction. The bridging atoms in the β - $[\text{Cu}(\text{S}_4)]_n^{n-}$ chain are terminal sulfur atoms of the tetrasulfide. This leads to formation of Cu_2S_2 four-membered rings with a linear array of Cu atoms along the chain direction.

If α - and β - $[\text{Cu}(\text{S}_4)]_n^{n-}$ chains are to be formed by the same solution precursor, one can easily visualize the α - to β -phase conversion as shown in Figure 14. The long Cu-S(2) bond of bridging internal sulfur atoms in α - $[\text{Cu}(\text{S}_4)]_n^{n-}$ chain can be easily broken by thermal activation to form the hypothetical intermediate $[\text{Cu}(\text{S}_4)]_n^{n-}$ chain. This hypothetical $[\text{Cu}(\text{S}_4)]_n^{n-}$ chain is similar in structure to the known $[\text{AgSe}_4]_n^{n-26(b),39}$ in which Ag^+ is trigonal planar. This $[\text{AgSe}_4]_n^{n-}$ chain is also shown in Figure 14 (C), for the comparison with hypothetical intermediate $[\text{Cu}(\text{S}_4)]_n^{n-}$ chain. From this hypothetical $[\text{Cu}(\text{S}_4)]_n^{n-}$ chain, if S(4) atoms and three-coordinate Cu atoms are brought close to each other, β - $[\text{Cu}(\text{S}_4)]_n^{n-}$ chain can be formed.

Figure 14. Schematic representation of structural transformation of (A) the α - $[\text{CuS}_4]_n^{n-}$ chain to (D) the β - $[\text{CuS}_4]_n^{n-}$ chain (bottom) via (B) hypothetical $[\text{CuS}_4]_n^{n-}$ intermediate which is similar in structure to (C) the known $[\text{AgSe}_4]_n^{n-}$ chain.

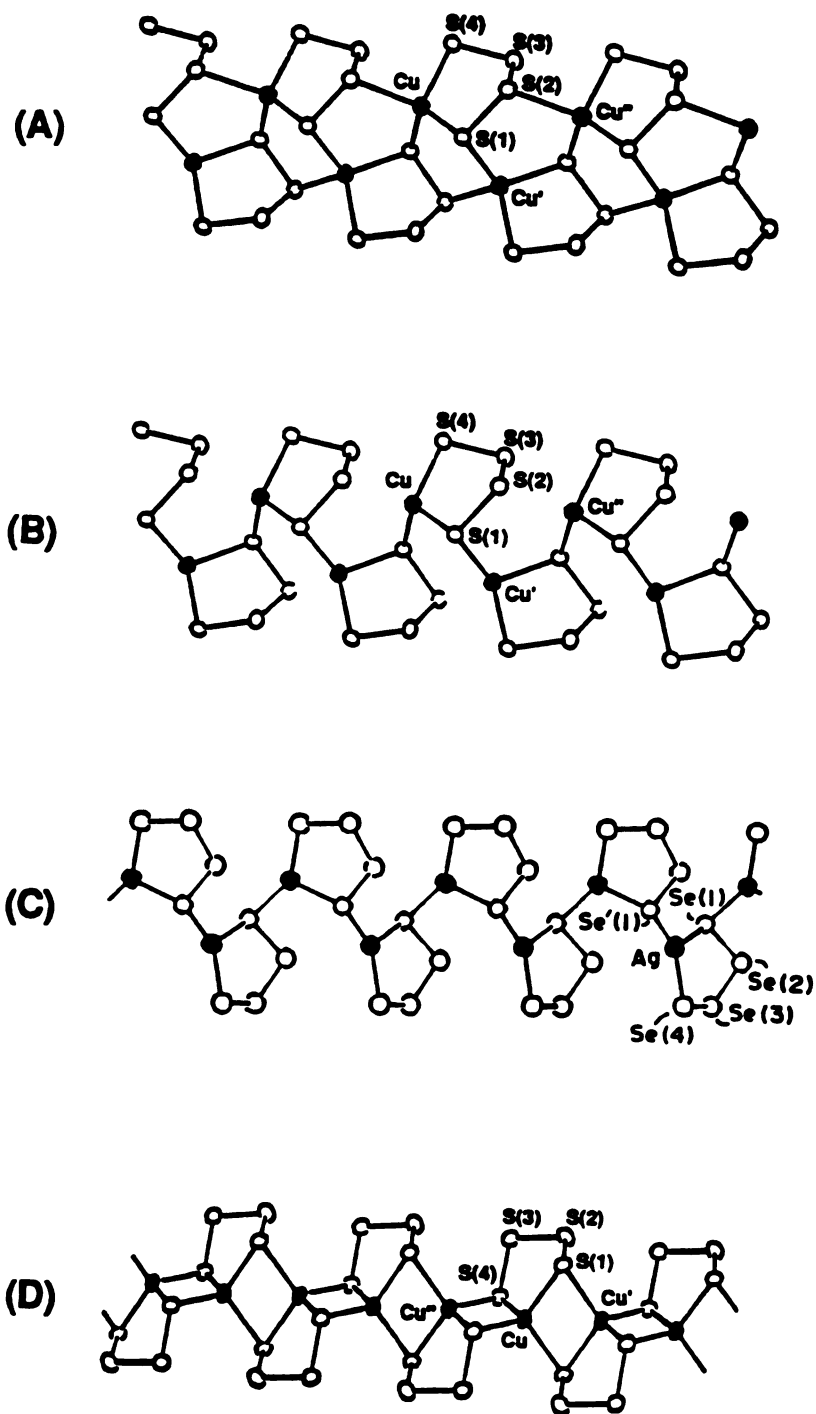


Figure 14.

3.4. Charge Transport Properties of α -KCuSe₄ (III) and Na_{1.9}Cu₂Se₂·Cu₂O (VI)

Based on the completely filled valence band of α -KCuSe₄ due to the d¹⁰ electronic configuration of Cu atoms, one could expect semiconducting behavior of this material. The conductivity data of its single crystal over the temperature range of 80-330 K shows increasing conductivity with increasing temperature, which is typical behavior of semiconductors, as shown in Figure 15. However, its values are relatively small and reach 10⁻⁶ S/cm at 330 K. These materials are expected to have narrow band width due to their low dimensionality and poor overlaps between Cu and Se atoms between chains.

Based on the partial cation vacancy, Na_{1.9}Cu₂Se₂·Cu₂O is expected to be a p-type metallic conductor. The charge transport measurements on single crystals of Na_{1.9}Cu₂Se₂·Cu₂O along the (001) plane show that the resistivity at first decreases linearly with decreasing temperature and at low temperatures levels off to a constant value (so called residual resistivity) over the temperature range 5-300 K as shown in Figure 16. This is typical metallic behavior. The resistivity increases from 5×10⁻⁶ Ω·cm at 5 K to 1.1×10⁻⁴ Ω·cm at room temperature. There is a little jump in the resistivity around 270 K. Since the compound contains Na ions which are easily hydrolyzed, this may originate from the melting of the water vapor which must have been condensed during the period of measurements. The temperature dependence of the thermoelectric power (Seebeck coefficient) shows a very small positive value of 0.5~3 μV/K in the temperature range of 100~330 K as shown in Figure 17. The small and linearly increasing Seebeck coefficient with rising temperature indicates that Na_{1.9}Cu₂Se₂·Cu₂O is a p-type metal.

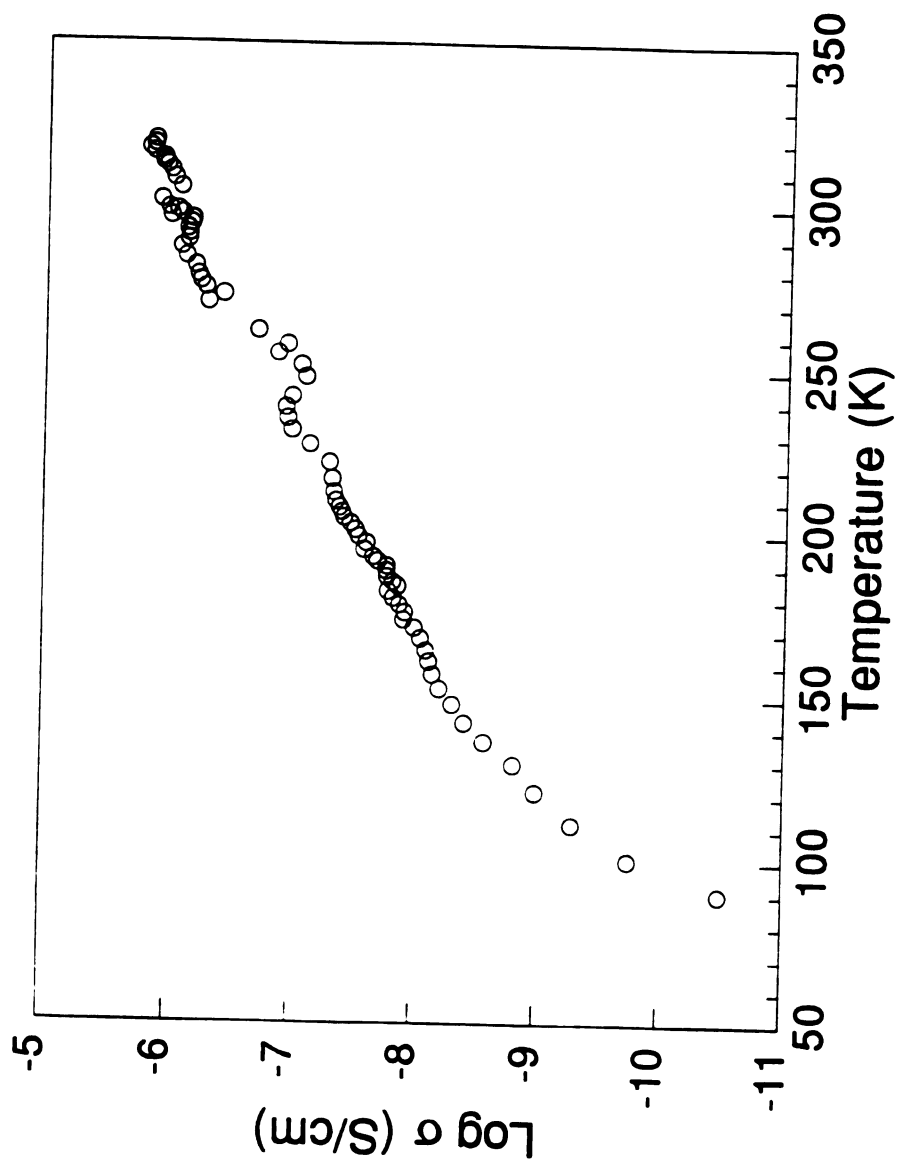


Figure 15. Four probe electrical conductivity (Scm^{-1}) data as a function of temperature for a single crystal α - KCuSe_4 .

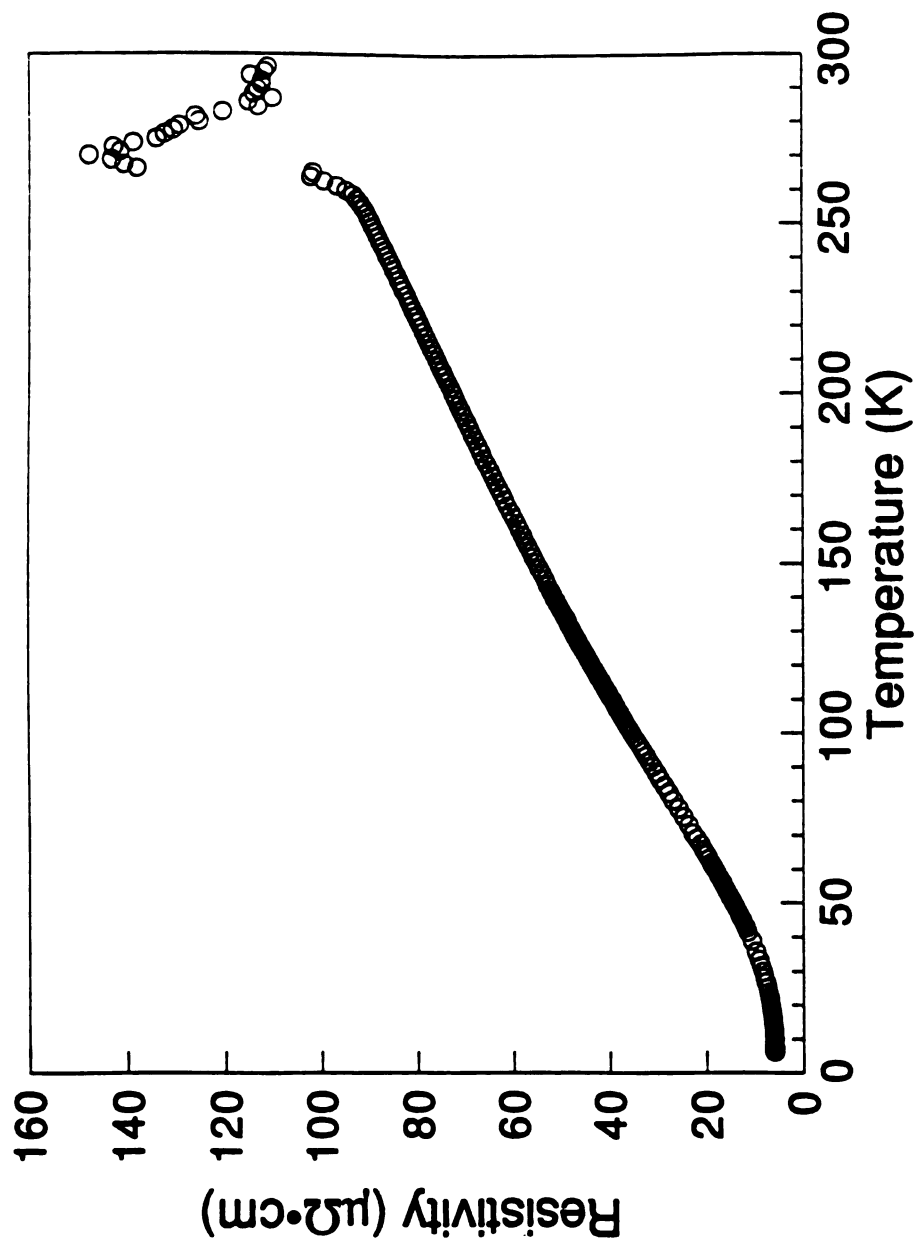


Figure 16. Four probe resistivity ($\mu\Omega\cdot\text{cm}$) data as a function of temperature for a single crystal of $\text{Na}_{1.9}\text{Cu}_2\text{Se}_2\cdot\text{Cu}_2\text{O}$.

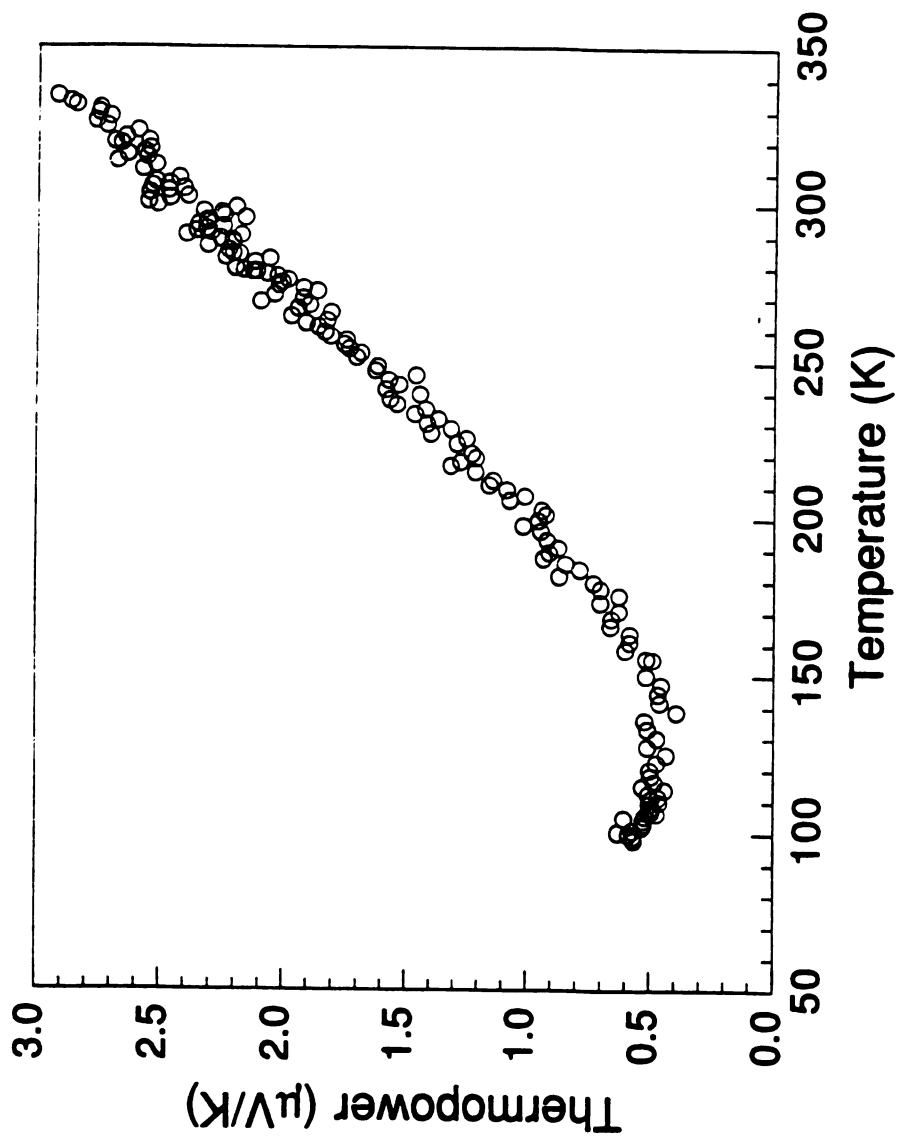


Figure 17. Thermoelectric power ($\mu\text{V/K}$) data as a function of temperature for a single crystal of $\text{Na}_{1.9}\text{Cu}_2\text{Se}_2\cdot\text{Cu}_2\text{O}$.

The mixed-valence compound $\text{Na}_3\text{Cu}_4\text{Se}_4$ is also expected to have interesting electronic properties because one- and two-dimensional metallic conductors are often subject to metal-insulator transitions due to their electronic instability⁷⁷. Furthermore, a recent theoretical study^{63(c)} on the sulfide analogue of $\text{Na}_3\text{Cu}_4\text{Se}_4$ suggested it might be electronically unstable to show as charge density waves (CDW) or spin density waves (SDW). However, $\text{Na}_3\text{Cu}_4\text{S}_4$ is a normal metallic conductor without any anomalies in resistivity and charge transport properties^{63(b)}. Therefore, it would be quite interesting to study electronic properties of $\text{Na}_3\text{Cu}_4\text{Se}_4$ to look for such anomalies. Unfortunately, due to the sample inhomogeneity and small size of single crystals, we have not been able to pursue further investigations on its electronic properties. Work to obtain pure materials and large crystals is still in progress.⁷⁸

We have demonstrated that synthesis at intermediate temperatures (215 to 350 °C) can provide an avenue to metastable polychalcogenide materials and low-dimensional chalcogenide compounds with interesting electrical properties. The structural diversity of Q_4^{2-} ligands, which is pervasive in discrete molecular polychalcogenide compounds, highlighted the potential use of polychalcogenide fluxes at intermediate temperatures in the study of the polychalcogenide ligation and structural diversity in extended structures.

CHAPTER 3

Low-Dimensional Compounds Incorporating (Poly)chalcogenide Ligands In the A/Au/Q (A=Na, K, Cs; Q=S, Se) Systems

1. Introduction

Solid state compounds incorporating the versatile polychalcogenide ligands (Q_x^{2-}) are rare. These ligands are thermally unstable and release chalcogen at the high temperatures commonly used in solid state reactions. We believe that an enormous number of interesting polychalcogenide compounds occur at intermediate (e.g. 150-500 °C) temperatures and could be discovered, provided suitable solvents (e.g. molten salts) were available. These temperatures do not support the conventional (non)aqueous solvents commonly used near room temperature, nor do they favor true solid state reactions due to exceedingly slow diffusion rate. This has been particularly true in chalcogenide chemistry.⁷⁹

We have been successful in synthesizing new polychalcogenide compounds of α - and β -ACuQ₄ using alkali metal polychalcogenide fluxes as solvents and reagents at intermediate temperatures.^{53(a)} (see chapter 2) They contain polychalcogenide ligands (S_4^{2-} and Se_4^{2-}) with one-dimensional chain structures. We also have initiated investigations of ternary A/Au/Q systems (A=alkali metal; Q=S, Se) using alkali metal polychalcogenide (A_2Q_x)

fluxes as solvents and reagents at intermediate temperatures. In the ternary A/Au/Q systems (A= alkali metal) there are only three known compounds of KAuQ^{80} (Q=S, Se), $\text{Na}_3\text{AuS}_2^{81}$, and $\text{K}_4\text{Au}_6\text{S}_5^{82}$, containing monochalcogenide ligands. In this chapter, we illustrate the structural diversity associated with various polychalcogenides from Se_3^{2-} to Se_5^{2-} and the interesting $\text{Au}^{1+/3+}$ redox chemistry in A_2Se_x flux. Novel low-dimensional (poly)chalcogenide compounds of KAuQ_5 (Q=S, $\text{Se}^{53(c)}$), CsAuSe_3 , $\text{K}_3\text{AuSe}_{13}^{53(c)}$, Na_3AuSe_8 , and AAuQ_2 (A=Na, K) are readily obtained in A_2Q_x fluxes at 250-350 °C.

2. Experimental Section

2.1 Reagents

Chemicals in this work were used as obtained: gold powder, -325 mesh, 99.95% purity, Cerac, Milwaukee, WI; selenium powder, -100 mesh, 99.95% purity, Aldrich Chemical Co., Milwaukee, WI; sulfur powder, sublimed, J. T. Baker Chemical Co., Phillipsburg, NJ; potassium and sodium metal, analytical reagent, Mallinckrodt Inc., Paris, KY; cesium metal, 99.98% purity, AESAR, Johnson Matthey, Seabrook, NH.

2.2. Physical Measurements

FT-IR spectra were determined as a pellet in a CsI matrix. Each sample was ground with dry CsI into a fine powder and a pressure of about 6 tons was applied to the mixture to make a translucent pellet. Spectra were recorded in

the far IR region (600 to 100 cm^{-1}) with the use of a Nicolet 740 FT-IR spectrometer.

Quantitative microprobe analysis was performed on a Jeol 35CF scanning electron microscopy equipped with Tracor Northern TN5500 X-ray microanalysis attachment. Single crystals of each sample were carefully picked and mounted on an aluminum stub using conducting silver paint to help dissipate charges that develop on the sample surface during measurements. Energy Dispersive Spectra (EDS) were obtained using the following experimental set-up:

X-ray detector position : 55mm

Working distance : 39mm

Accelerating voltage : 20 KV

Take-off angle : 27 deg

Beam current : 200 picoamps

Accumulation time : 100 seconds

Window : Be

A standardless quantitative analysis (SQ) program was used to analyze the X-ray spectra obtained. Since the selenium ratio is always underestimated due to artifact of the program, a correction factor (x1.86), which has been calibrated using known K/Au/Se ternary compounds, was used to evaluate selenium percentage. The analyses reported are the average of four to six individual measurements on different crystals.

2.3. Synthesis

Chemicals were measured and loaded in Pyrex tubes under a dry nitrogen atmosphere in a Vacuum Atmospheres Dri-Lab glovebox. Potassium

monosulfide (K_2S) and alkali metal monoselenide (A_2Se ; $A=Na, K, Cs$) were prepared in liquid ammonia from alkali metal and elemental sulfur (or selenium) in a 2:1 ratio.

Potassium (1,5- μ_2 -pentasulfido)aurate(I), $KAuS_5$ (I) 0.198 g (1.8 mmol) of K_2S , 0.196 g (1.0 mmol) of Au powder, and 0.256 g (8.0 mmol) of S powder were mixed together and loaded in a Pyrex tube which was flame-sealed under vacuum ($\sim 10^{-3}$ torr). The tube was placed in a computer-controlled Furnace and heated at 250 °C for 99 hrs and cooled slowly to 50 °C at a rate of 2 °C/hr. The pale yellow needle-like crystals were obtained by removing excess molten potassium polysulfides with water under a N_2 atmosphere (yield: 78 % based on the Au used). A quantitative analysis performed on a large number of crystals using scanning electron microscope/EDS gave an average composition of $K_{1.0}Au_{1.0}S_{5.4}$.

Potassium (1,5- μ_2 -pentaselenido)aurate(I), $KAuSe_5$ (II) 0.157 g (1.0 mmol) of K_2Se , 0.098 g (0.5 mmol) of Au powder, and 0.316 g (4.0 mmol) of Se powder were mixed together and loaded in a Pyrex tube which was flame-sealed under vacuum ($\sim 10^{-3}$ torr). The tube was placed in a computer-controlled Furnace and heated at 250 °C for 99 hrs and cooled slowly to 50 °C at a rate of 2 °C/hr. The reddish black needle-shaped crystals were obtained by removing excess potassium polyselenides with water under a N_2 atmosphere (yield: 74% based on the Au used). A quantitative analysis performed on a large number of crystals using scanning electron microscope/EDS gave an average composition of $K_{1.0}Au_{1.0}Se_{5.1}$.

Cesium (1,3- μ_2 -triselenido)aurate(I), $CsAuSe_3$ (III) 0.172 g (0.5 mmol) of Cs_2Se , 0.024 g (0.12 mmol) of Au powder, and 0.078 g (1.0

mmol) of Se powder were mixed together and loaded in a Pyrex tube which was flame-sealed under vacuum ($\sim 10^{-3}$ torr). The tube was placed in a computer-controlled Furnace and heated at 350 °C for 54 hrs and cooled slowly to 50 °C at a rate of 2 °C/hr. The purple colored needle-shaped crystals were obtained by removing excess cesium polyselenides with water under a N₂-atmosphere (yield: 63 % based on the Au used). A quantitative analysis performed on a large number of crystals using scanning electron microscope/EDS gave an average composition of Cs_{1.0}Au_{1.0}Se_{3.2}.

Tripotassium bis(pentaseleido)(1,3- μ_2 -triseleido)aurite(III), K₃AuSe₁₃ (IV). 0.140 g (0.9 mmol) of K₂Se, 0.098 g (0.5 mmol) of Au powder, and 0.316 g (4 mmol) of Se powder were mixed together and loaded in a Pyrex tube which was flame-sealed under vacuum ($\sim 10^{-3}$ torr). The tube was placed in a computer-controlled Furnace and heated at 250 °C for 99 hrs and cooled slowly to 50 °C at a rate of 2 °C/hr. The black needle-like crystals were obtained by removing excess molten potassium polyselenides with water under a N₂ atmosphere (yield: 57% based on the Au used). A quantitative analysis performed on a large number of crystals using scanning electron microscope/EDS gave an average composition of K_{3.0}Au_{1.1}Se₁₂.

Potassium bis(μ_2 -selenido)aurite(III), KAuSe₂ (V) 0.070 g (0.45 mmol) of K₂Se, 0.10 g (0.51 mmol) of Au powder, and 0.158 g (2.0 mmol) of Se powder were mixed together and loaded in a Pyrex tube which was flame-sealed under vacuum ($\sim 10^{-3}$ torr). The tube was placed in a computer-controlled Furnace and heated at 290 °C for 99 hrs and cooled slowly to 50 °C at a rate of 2 °C/hr. The metallic black needle-shaped crystals were obtained by removing excess potassium polyselenides with water under a N₂-atmosphere (yield: 78 % based on the Au used). A quantitative analysis

performed on a large number of crystals using scanning electron microscope/EDS gave an average composition of $K_{1.0}Au_{1.0}Se_{2.0}$.

Trisodium bis(triselenido)(μ_2 -diselenido)aurite(III), Na_3AuSe_8 (VI) 0.031 g (0.25 mmol) of Na_2Se , 0.049 g (0.25 mmol) of Au powder, and 0.158 g (2.0 mmol) of Se powder were mixed together and loaded in a Pyrex tube which was flame-sealed under vacuum ($\sim 10^{-3}$ torr). The tube was placed in a computer-controlled Furnace and heated at 310 °C for 99 hrs and cooled slowly to 50 °C at a rate of 2 °C/hr. The purple-colored, needle-shaped crystals were obtained by removing excess molten sodium polyselenides with water under a N_2 atmosphere (yield: 67 % based on the Au used). A quantitative analysis performed on a large number of crystals using scanning electron microscope/EDS gave an average composition of $Na_{3.0}Au_{0.94}Se_{7.9}$.

Potassium bis(μ_2 -selenido)aurite(III), $NaAuSe_2$ (VII) 0.093 g (0.75 mmol) of Na_2Se , 0.197 g (1.0 mmol) of Au powder, and 0.158 g (2.0 mmol) of Se powder were mixed together and loaded in a Pyrex tube which was flame-sealed under vacuum ($\sim 10^{-3}$ torr). The tube was placed in a computer-controlled Furnace and heated at 290 °C for 99 hrs and cooled slowly to 50 °C at a rate of 2 °C/hr. The black rectangular crystals were obtained by removing excess potassium polyselenides with water under a N_2 atmosphere (yield: 81 % based on the Au used). A quantitative analysis performed on a large number of crystals using scanning electron microscope/EDS gave an average composition of $Na_{1.0}Au_{1.0}Se_{2.0}$.

2.4. X-ray Crystallographic Studies

All compounds were examined by X-ray powder diffraction for the purpose of phase characterization and identification. The d-spacings for each compound were obtained from the powder patterns recorded on a Phillips XRG-3000 computer-controlled powder diffractometer, operating at 40KV, 35 mA. Graphite monochromated Cu-K α radiation was used. To verify product homogeneity, the d-spacings observed for the bulk materials were compared, and found to be in accord, with those calculated from the single crystal X-ray structure analysis data. The calculation of d-spacings was performed using the POWD10 program⁵⁶. The results are summarized in Tables 24-30.

Table 24. Calculated and Observed X-ray Powder Diffraction Pattern of KAuS_5

H K L	d_{calc} (Å)	d_{obs} (Å)	I/max (obs.)
0 0 2	7.73	7.92	22.7
1 1 0	6.57	6.72	55.1
0 2 0	5.37	5.47	10.6
1 1 2	5.00	5.07	27.3
2 0 0	4.15	4.21	25.4
0 0 4	3.86	3.91	7.4
2 1 1	3.75	3.80	13.7
2 0 2	3.66	3.70	28.9
1 3 0	3.29	3.32	37.6
1 3 2	3.02	3.05	100
2 0 4	2.83	2.85	63.2
0 4 0	2.68	2.71	50.1
0 4 2	2.540	2.557	23.5
1 3 4	2.506	2.526	12.9
2 4 0	2.257	2.273	4.8
3 1 4 (3 3 0)	2.204	2.207	18.0
2 4 2	2.167	2.181	17.6
3 3 2	2.109	2.123	23.8
4 0 0	2.077	2.090	22.1
1 3 6	2.029	2.053	13.7
1 5 2	2.011	2.021	16.1
2 4 4 (0 0 8)	1.9497	1.9594	17.4
3 3 4	1.9069	1.9070	8.2
0 4 6	1.8610	1.8696	6.2
4 0 4	1.8300	1.8391	4.5
0 6 0	1.7929	1.8024	10.6
2 4 6	1.6984	1.7085	6.3
3 3 6	1.6699	1.6772	14.6
4 4 2	1.6081	1.6146	11.6

Table 25. Calculated and Observed X-ray Powder Diffraction Pattern of KAuSe_5

H K L	d_{calc} (Å)	d_{obs} (Å)	I/I _{max} (obs.)
0 0 2	8.21	8.29	11.3
1 1 0	6.85	6.91	34.0
0 2 0	5.64	5.69	13.6
1 1 2	5.26	5.29	39.7
2 1 1	3.91	3.93	33.6
1 2 3	3.57	3.59	10.4
1 3 0	3.44	3.45	13.9
1 3 2	3.18	3.19	82.5
2 0 4	2.97	2.98	100
0 4 0	2.82	2.83	73.7
0 4 2	2.66	2.67	17.9
1 4 1	2.64	2.65	22.5
3 1 4	2.305	2.313	7.5
2 4 2	2.270	2.277	7.7
3 3 2	2.201	2.206	18.9
4 0 0	2.156	2.162	33.6
1 3 6	2.144		
1 5 2	2.111	2.116	11.3
0 0 8	2.053		
2 4 4	2.047	2.053	33.6
3 2 5	2.020	2.025	10.8
4 1 3	1.975		
3 1 6	1.952	1.956	7.2
0 6 0	1.8821	1.8858	10.8
3 3 6	1.7541	1.7581	12.8
4 4 0	1.7136	1.7182	11.3
1 2 9	1.7023		
4 4 2	1.6775	1.6815	7.9
2 6 4	1.5903	1.5925	6.8
1 7 2	1.5569	1.5588	5.2

Table 26. Calculated and Observed X-ray Powder Diffraction Pattern of CsAuSe₃

H K L	d_{calc} (Å)	d_{obs} (Å)	I/I _{max} (obs.)
0 2 0	6.89	7.07	9.5
0 2 1	4.94	4.99	29.3
1 1 1	3.76	3.86	38.9
1 3 0	3.64	3.67	80.0
0 4 0	3.44	3.47	78.7
0 4 1	3.09	3.12	67.2
2 0 0	3.00	3.03	63.5
1 3 1	2.97	2.99	100
-2 0 2	2.89	2.91	49.9
1 5 0	2.50	2.51	31.8
1 3 2	2.292	2.307	25.4
-1 3 3	2.229	2.258	25.4
-2 4 2 (-2 2 3)	2.214	2.196	39.9
-3 1 2	2.093	2.076	31.3
2 0 2 (-3 3 1)	1.955	1.957	32.6
-3 3 2	1.9236	1.9150	23.8
-1 1 4	1.8873	1.8817	22.4
-3 3 3 (0 0 4)	1.7771	1.7704	19.0
-3 5 2 (0 8 1)	1.6797	1.6821	38.9

Table 27. Calculated and Observed X-ray Powder Diffraction Pattern of K_3AuSe_{13}

H K L	d_{calc} (Å)	d_{obs} (Å)	I/I _{max} (obs.)
1 0 0	14.91	16.00	2.6
2 0 0	7.45	7.62	7.6
0 0 2	6.84	6.98	12.9
-1 0 2	6.38	6.52	6.1
-2 0 2	5.22	5.32	4.9
3 0 0	4.97	5.04	21.7
1 1 0	4.61	4.68	18.4
0 1 1	4.57	4.64	17.3
-1 1 1	4.40	4.46	32.5
1 1 1	4.34	4.40	17.8
2 1 0	4.07	4.12	14.9
0 1 2	3.96	4.00	10.6
-1 1 2 (2 1 1)	3.86	3.90	32.2
-2 1 2	3.55	3.59	6.3
3 1 0	3.47	3.51	17.0
2 1 2	3.44	3.48	21.7
0 0 4	3.42	3.44	31.0
-1 1 3	3.28	3.31	6.5
1 1 3	3.21	3.24	7.9
-3 1 2	3.15	3.18	100
-2 1 3	3.09	3.12	20.8
2 0 4	3.03	3.06	24.0
-4 1 1	2.92	2.94	31.7
3 0 4	2.73	2.75	45.0
3 1 3	2.70	2.72	22.4
-3 1 4	2.50	2.52	6.6
1 2 0	2.397	2.413	11.2
1 2 1	2.357	2.373	19.6

Table 27. (cont'd)

H K L	d_{calc} (Å)	d_{obs} (Å)	I/I _{max} (obs.)
5 1 2	2.339	2.353	13.8
2 2 0	2.309	2.323	6.2
-2 2 1	2.285	2.299	18.7
1 0 6	2.233	2.247	5.8
3 2 0	2.182	2.196	22.0
-6 1 2	2.143	2.156	13.8
-3 2 2	2.097	2.109	15.6
-6 0 4	2.078	2.091	27.4
6 1 2 (0 1 6)	2.069	2.079	45.0
-3 2 3	1.991	2.037	18.4
5 1 4	1.987	1.997	9.4
4 1 5	1.958	1.968	8.1
-3 1 6	1.9498	1.957	9.3
-4 2 3	1.8847	1.8943	12.4
-5 2 1	1.8767	1.8743	13.6
0 2 5	1.8170	1.8217	13.3
1 1 7	1.7877	1.7958	7.2
8 0 2	1.7690	1.7771	5.0
7 1 3	1.7555	1.7636	10.4
-3 1 7	1.7397	1.7475	9.5
4 2 4	1.7218	1.7301	11.7
-6 2 2	1.7031	1.7109	14.8
6 2 2	1.6653	1.6715	15.7
9 0 0	1.6572	1.6635	30.7
-3 0 8	1.6528	1.6588	26.7
4 2 5	1.6055	1.6091	9.5
8 0 4	1.5929	1.5996	12.6

Table 28. Calculated and Observed X-ray Powder Diffraction Pattern of KAuSe_2

H K L	$d_{\text{calc}} (\text{\AA})$	$d_{\text{obs}} (\text{\AA})$	I/I _{max} (obs.)
1 1 0	5.44	5.50	100
2 0 0	3.84	3.88	56.3
2 1 0	3.44	3.46	42.3
1 1 1	3.04	3.05	10.4
2 2 0	2.72	2.73	55.5
2 0 1	2.65	2.66	69.5
2 1 1	2.50	2.52	21.8
3 1 0	2.434	2.447	5.9
2 2 1	2.185	2.194	26.1
3 1 1	2.027	2.037	74.0
4 0 0	1.9247	1.9328	4.3
4 1 0	1.8672	1.8731	4.5
0 0 2	1.8325	1.8391	10.6
3 3 0	1.8146	1.8217	40.3
1 1 2	1.7367	1.7422	10.4
4 2 0	1.7215	1.7276	36.2
4 0 1	1.7040	1.7101	33.8
2 0 2	1.6545	1.6584	6.0
2 1 2	1.6176	1.6222	3.8
4 2 1	1.5582	1.5638	13.7

Table 29. Calculated and Observed X-ray Powder Diffraction Pattern of Na_3AuSe_8

H K L	d_{calc} (Å)	d_{obs} (Å)	I/I _{max} (obs.)
-1 1 1	7.32	7.46	39.4
-2 0 2	6.96	7.08	19.4
2 0 0	5.06	5.12	11.5
-3 1 2	4.72	4.78	47.5
1 1 1	4.19	4.24	14.6
-3 1 3	4.08	4.12	38.5
-4 0 2	4.03	4.07	18.4
-2 2 2	3.66	3.69	25.1
-1 1 3	3.22	3.25	16.6
3 1 0	3.14	3.16	19.7
-3 1 4	3.10	3.12	10.8
-4 2 3	2.99	3.02	25.2
-4 2 2	2.94	2.96	100
-2 0 4	2.91	2.93	45.5
1 3 0	2.76	2.77	15.7
-4 2 4	2.70	2.72	17.8
-5 1 5	2.64	2.66	17.2
2 2 1	2.62	2.64	7.3
1 3 1	2.464	2.478	14.6
-3 3 1	2.450	2.457	10.3
3 1 1	2.405	2.419	10.5
-6 2 4	2.361	2.374	24.1
-7 1 5	2.317	2.329	7.3
-7 1 4	2.296	2.307	12.0
-6 2 3	2.279	2.291	5.2
-1 3 3	2.213	2.225	12.5
1 1 3	2.180	2.187	8.3
0 4 0	2.152	2.163	23.7

Table 29. (cont'd)

H K L	d_{calc} (Å)	d_{obs} (Å)	I/I _{max} (obs.)
-4 0 6	2.136	2.147	23.1
2 2 2	2.099	2.109	30.1
0 4 1	2.083	2.092	30.1
-6 2 6	2.042	2.052	29.3
-8 0 4	2.015	2.025	14.9
-5 3 5	1.998	2.007	19.8
2 4 0	1.980	1.988	9.4
-7 1 7	1.9379	1.9453	11.7
-4 2 6	1.9139	1.9225	21.0
-5 3 1	1.8745	1.8819	25.2
-7 3 5	1.8438	1.8518	22.3
-8 2 4	1.8251	1.8344	20.6
-5 3 6	1.7845	1.7920	16.9
-7 3 6	1.7685	1.7758	18.1
-8 2 7	1.7683	1.7471	19.7
-8 0 8	1.7404	1.7129	8.1
-10 0 6	1.6826	1.6904	16.6
5 3 0	1.6544	1.6591	16.0
4 0 2	1.6525	1.6546	15.7
1 5 1	1.6212	1.6269	24.1
-3 5 3 (-8 2 8)	1.6144	1.6196	59.7
-6 4 2	1.5883	1.5931	12.5
-1 5 3 (-9 3 7)	1.5433	1.5479	23.7

Table 30. Calculated and Observed X-ray Powder Diffraction Pattern of NaAuSe₂

H K L	d _{calc} (Å)	d _{obs} (Å)	I/I _{max} (obs.)
1 0 0	6.74	6.86	4.3
1 1 0	5.25	5.32	58.6
0 1 1	5.12	5.19	30.7
1 1 1	3.72	3.76	6.5
1 2 0	3.55	3.58	9.3
2 0 0	3.37	3.40	9.3
-1 2 1	3.31	3.34	7.1
-2 1 1	3.13	3.15	6.8
1 2 1	2.95	2.97	100
-2 0 2	2.72	2.73	37.4
-2 1 2	2.58	2.60	27.2
1 1 2	2.537	2.55	7.7
-3 1 1	2.237	2.250	13.7
-3 0 2	2.128	2.140	11.6
0 1 3	2.093	2.104	15.3
0 4 0	2.093	2.097	31.4
2 0 2	2.080	2.089	24.3
-3 1 2	2.062	2.074	13.5
-3 2 1	2.030	2.041	31.1
0 4 1	1.992	2.001	5.9
-1 2 3	1.973	1.984	27.6
2 3 1	1.9461	1.956	16.3
1 3 2	1.9267	1.9370	7.3
-3 3 1	1.7849	1.7923	18.7
3 2 1	1.7828	1.7864	19.0
-1 3 3	1.7457	1.7530	8.2
0 3 3	1.7095	1.7164	6.5
-4 0 2	1.6888	1.6954	12.9
-2 3 3	1.6712	1.6765	7.8
-2 4 2	1.6595	1.6613	27.9
1 5 0	1.6254	1.6314	20.6
-4 2 1	1.6128	1.6196	17.0

The X-ray single crystal data of KAuS_5 , KAuSe_5 , $\text{K}_3\text{AuSe}_{13}$, Na_3AuSe_8 , NaAuSe_2 , and KAuSe_2 were collected on a Nicolet P3 four circle diffractometer with graphite monochromated Mo-K_α radiation using the θ - 2θ scan mode. The data for CsAuSe_3 were collected on a Rigaku AFC6S diffractometer with graphite monochromated Mo-K_α radiation using the ω - 2θ scan mode. Accurate unit cell parameters for all compounds were obtained from the least-squares refinement of the 2θ , ω , χ , and ϕ values of 20-25 machine-centered reflections. The stability of the experimental setup and crystal integrity were monitored by measuring three standard reflections periodically (every 100 reflections) during the data collection period. The intensities did not show any appreciable decay. An empirical absorption correction based on ψ scans for 3 reflections was applied to the KAuS_5 data. Two absorption corrections were applied to the data of KAuSe_5 , $\text{K}_3\text{AuSe}_{13}$, Na_3AuSe_8 , NaAuSe_2 , KAuSe_2 , and CsAuSe_3 : an empirical absorption correction based on ψ scans for 3 reflections followed by a DIFABS⁵⁷ correction. The structures of KAuS_5 , KAuSe_5 , $\text{K}_3\text{AuSe}_{13}$, Na_3AuSe_8 , NaAuSe_2 , and KAuSe_2 were solved with direct methods using SHELXS-86⁵⁸ and were refined with the SDP⁵⁹ package of crystallographic programs. Computations were performed on a VAXstation 2000 computer. The structure of CsAuSe_3 was solved with direct methods using SHELXS-86 and was refined with the TEXSAN⁶⁰ package of crystallographic programs on a VAXstation 3100 computer. All atoms were refined anisotropically. The complete data collection parameters and details of the structure solution and refinement for all compounds are given in Table 31. The final coordinates, temperature factors, and their estimated standard deviations of all atoms are shown in Tables 32-37.

Table 31. Summary of Crystallographic Data for KAuS_5 , KAuSe_5 , CsAuSe_3 , $\text{K}_3\text{AuSe}_{13}$, KAuSe_2 , Na_3AuSe_8 , and NaAuSe_2

	compound		
	I	II	III
Formula	KAuS_5	KAuSe_5	CsAuSe_3
Formula weight	396.39	630.87	566.75
space group	lbam	lbam	C2/c
a (Å)	8.310(2)	8.625(6)	6.483(3)
b (Å)	10.758(3)	11.293(9)	13.789(5)
c (Å)	15.468(4)	16.425(11)	7.651(3)
α (deg)	90.0	90.0	90.0
β (deg)	90.0	90.0	112.17(3)
γ (deg)	90.0	90.0	90.0
Vol (Å ³), Z	1382.7(6), 8	1600(2), 8	633.3(5), 4
Temperature (°C)	23	23	23
Crystal size (mm)	0.44x0.16x0.08	0.30x0.16x0.14	0.49x0.03x0.05
Radiation	Mo-K α	Mo-K α	Mo-K α
μ (Mo-K α , cm ⁻¹)	231.8	413.1	457.2
D_{calc} (g/cm ³)	3.81	5.24	5.94
$2\theta_{\text{max}}$ (deg)	50	46	50
Scan method	$\theta/2\theta$	$\theta/2\theta$	$\omega/2\theta$
No. of data collected	2829	744	1211
No. of unique data	639	536	581
No. of data used ($F_o^2 > 3\sigma(F_o^2)$)	519	382	390
No. of atoms	6	6	4
No. of variables	37	37	25
Phasing technique	Direct methods	Direct methods	Direct methods
Final R/R_w	5.1/6.3	5.7/7.1	4.0/4.7
Max. shift/esd (final cycle)	0.0	0.0	0.00
Extinction coefficient	4.22×10^{-7}	1.61×10^{-7}	N/A

Table 31. (cont'd)

	compound		
	IV	V	VI
Formula	K_3AuSe_{13}	$KAuSe_2$	Na_3AuSe_8
Formula weight	1340.75	393.99	897.62
space group	P2/c	P4/mbm	C2/c
<i>a</i> (Å)	14.949(6)	7.699(3)	16.948(8)
<i>b</i> (Å)	4.8589(2)	7.699(3)	8.610(3)
<i>c</i> (Å)	13.723(5)	3.665(1)	13.931(5)
α (deg)	90.0	90.0	90.0
β (deg)	93.86(3)	90.0	143.32(2)
γ (deg)	90.0	90.0	90.0
Vol (Å ³), <i>Z</i>	994.3(7), 2	217.2(2), 2	1214.3(8), 4
Temperature (°C)	23	23	23
Crystal size (mm)	0.42x0.10x0.07	0.18x0.18x0.05	0.38x0.20x0.04
Radiation	Mo-K α	Mo-K α	Mo-K α
μ (Mo-K α , cm ⁻¹)	315.6	511.4	359.0
<i>D</i> calc (g/cm ³)	4.48	6.02	4.91
$2\theta_{max}$ (deg)	48	48	46
Scan method	$\theta/2\theta$	$\theta/2\theta$	$\theta/2\theta$
No. of data collected	1918	460	1924
No. of unique data	1570	118	858
No. of data used ($F_o^2 > 3\sigma(F_o^2)$)	1167	111	698
No. of atoms	10	3	7
No. of variables	81	10	59
Phasing technique	Direct methods	Direct methods	Direct methods
Final R/R _w	4.4/5.0	3.2/3.7	5.9/6.8
Max. shift/esd (final cycle)	0.0	0.00	0.0
Extinction coefficient	2.72×10^{-7}	1.00×10^{-7}	5.22×10^{-7}

Table 31. (cont'd)

compound	
VII	
Formula	NaAuSe ₂
Formula weight	377.88
space group	P2 ₁ /c
<i>a</i> (Å)	6.991(8)
<i>b</i> (Å)	8.374(9)
<i>c</i> (Å)	6.724(8)
α (deg)	90.0
β (deg)	105.23(9)
γ (deg)	90.0
Vol (Å ³), <i>Z</i>	379.8(7), 4
Temperature (oC)	23
Crystal size (mm)	0.20X0.16X0.08
Radiation	Mo-K α
μ (Mo-K α , cm ⁻¹)	575.1
<i>D</i> _{calc} (g/cm ³)	6.61
2 θ _{max} (deg)	48
Scan method	$\theta/2\theta$
No. of data collected	1430
No. of unique data	604
No. of data used	510
($F_o^2 > 3\sigma(F_o^2)$)	
No. of atoms	4
No. of variables	38
Phasing technique	Direct methods
Final R/R _w	6.8/8.3
Max. shift/esd	0.00
(last cycle)	
Extinction coefficient	4.26 x10 ⁻⁷

Table 32. Fractional Atomic Coordinates and B_{eq} Values for KAuS_5 with Their Estimated Standard Deviations in Parentheses

Atom	x	y	z	$B_{\text{eq}}^{\text{a}}, \text{\AA}^2$
Au	0	0.13773(9)	1/4	1.74(2)
S(1)	0.2012(7)	0.1402(5)	0.3517(4)	2.1(1)
S(2)	0.2943(6)	0.1760(5)	0.1067(3)	1.87(9)
S(3)	0.9422(9)	0.3381(7)	0	2.1(1)
K(1)	1/2	0	1/4	2.3(2)
K(2)	0	0	0	2.5(2)

^a B values for anisotropically refined atoms are given in the form of the isotropic equivalent displacement parameter defined as $B_{\text{eq}} = (4/3)[a^2B_{11} + b^2B_{22} + c^2B_{33} + ab(\cos \gamma)B_{12} + ac(\cos \beta)B_{13} + bc(\cos \alpha)B_{23}]$.

Table 33. Fractional Atomic Coordinates and B_{eq} Values for KAuSe_5 with Their Estimated Standard Deviations in Parentheses

Atom	x	y	z	$B_{\text{eq}}^{\text{a}}, \text{\AA}^2$
Au	0	0.1306(2)	1/4	2.39(4)
Se(1)	0.2065(5)	0.1286(4)	0.3488(3)	2.55(8)
Se(2)	0.2837(5)	0.1701(4)	0.1125(3)	2.25(8)
Se(3)	0.9500(6)	0.3418(6)	0	2.5(1)
K(1)	1/2	0	1/4	2.4(4)
K(2)	0	0	0	3.1(4)

^a B values for anisotropically refined atoms are given in the form of the isotropic equivalent displacement parameter defined as $B_{\text{eq}} = (4/3)[a^2B_{11} + b^2B_{22} + c^2B_{33} + ab(\cos \gamma)B_{12} + ac(\cos \beta)B_{13} + bc(\cos \alpha)B_{23}]$.

Table 34. Fractional Atomic Coordinates and B_{eq} Values for CsAuSe_3 with Their Estimated Standard Deviations in Parentheses

Atom	x	y	z	B_{eq}^{a} , Å ²
Au	0	0.5780(1)	1/4	2.27(5)
Se(1)	0.2160(4)	0.5887(2)	0.0557(3)	2.7(1)
Se(2)	0.5	0.6950(2)	1/4	2.6(1)
Cs	-0.5	0.6476(2)	-1/4	3.34(9)

^a B values for anisotropically refined atoms are given in the form of the isotropic equivalent displacement parameter defined as $B_{\text{eq}} = (4/3)[a^2B_{11} + b^2B_{22} + c^2B_{33} + ab(\cos \gamma)B_{12} + ac(\cos \beta)B_{13} + bc(\cos \alpha)B_{23}]$.

Table 35. Fractional Atomic Coordinates and B_{eq} Values for $\text{K}_3\text{Au}(\text{Se}_5)_2(\text{Se}_3)$ with Their Estimated Standard Deviations in Parentheses

Atom	x	y	z	B_{eq}^{a} , Å ²
Au	1/2	0	0	1.71(2)
Se(1)	0.6198(1)	0.3099(4)	-0.0482(1)	2.15(4)
Se(2)	0.7325(1)	0.3674(5)	0.0779(2)	2.53(4)
Se(3)	0.1505(2)	0.0742(5)	0.4666(2)	2.99(5)
Se(4)	0.0730(1)	0.3259(5)	0.5803(2)	3.13(5)
Se(5)	0.1522(1)	0.3037(5)	0.7334(2)	2.56(4)
Se(6)	0.4140(1)	0.8955(5)	0.3431(1)	2.47(4)
Se(7)	1/2	0.3971(6)	0.750	2.31(5)
K(1)	0	0.172(1)	1/4	3.2(1)
K(2)	0.7180(3)	0.203(1)	0.3346(4)	3.2(1)

^a B values for anisotropically refined atoms are given in the form of the isotropic equivalent displacement parameter defined as $B_{\text{eq}} = (4/3)[a^2B_{11} + b^2B_{22} + c^2B_{33} + ab(\cos \gamma)B_{12} + ac(\cos \beta)B_{13} + bc(\cos \alpha)B_{23}]$.

Table 36. Fractional Atomic Coordinates and B_{eq} Values for KAuSe_2 with Their Estimated Standard Deviations in Parentheses

Atom	x	y	z	B_{eq}^{a} , Å ²
Au	1/2	0	0	0.20(1)
Se	0.347	0.1528(3)	1/2	0.49(3)
K	0	0	0	1.2(1)

^a B values for anisotropically refined atoms are given in the form of the isotropic equivalent displacement parameter defined as $B_{\text{eq}} = (4/3)[a^2B_{11} + b^2B_{22} + c^2B_{33} + ab(\cos \gamma)B_{12} + ac(\cos \beta)B_{13} + bc(\cos \alpha)B_{23}]$.

Table 37. Fractional Atomic Coordinates and B_{eq} Values for Na_3AuSe_8 with Their Estimated Standard Deviations in Parentheses

Atom	x	y	z	B_{eq}^{a} , Å ²
Au	1/4	1/4	1/2	0.72(3)
Se(1)	0.4086(2)	0.4569(3)	0.6091(2)	0.90(6)
Se(2)	0.1014(2)	0.3226(4)	0.2190(2)	1.17(6)
Se(3)	0.1966(2)	0.4691(4)	0.7269(2)	1.07(6)
Se(4)	0.3802(2)	0.7542(4)	0.7587(2)	1.51(6)
Na(1)	1/2	1/2	1/2	2.9(4)
Na(2)	0.1358(9)	0.602(2)	0.458(1)	3.1(4)

^a B values for anisotropically refined atoms are given in the form of the isotropic equivalent displacement parameter defined as $B_{\text{eq}} = (4/3)[a^2B_{11} + b^2B_{22} + c^2B_{33} + ab(\cos \gamma)B_{12} + ac(\cos \beta)B_{13} + bc(\cos \alpha)B_{23}]$.

Table 38. Fractional Atomic Coordinates and B_{eq} Values for NaAuSe₂ with Their Estimated Standard Deviations in Parentheses

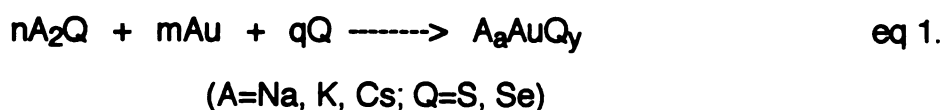
Atom	x	y	z	B_{eq}^{a} , Å ²
Au	0.2176(2)	0.6311(1)	0.0087(2)	0.40(2)
Se(1)	-0.0205(5)	0.5764(4)	0.2122(5)	0.86(6)
Se(2)	0.4157(5)	0.8314(4)	0.2506(5)	0.72(6)
Na	0.275(2)	0.366(2)	0.488(2)	1.9(3)

^a B values for anisotropically refined atoms are given in the form of the isotropic equivalent displacement parameter defined as $B_{\text{eq}} = (4/3)[a^2B_{11} + b^2B_{22} + c^2B_{33} + ab(\cos \gamma)B_{12} + ac(\cos \beta)B_{13} + bc(\cos \alpha)B_{23}]$.

3. Results and Discussion

3.1. Synthesis and Spectroscopy

The synthesis of all compounds has been accomplished at the intermediate temperature range (from 250 °C to 350 °C) using alkali metal polychalcogenide fluxes as solvents and reagents as shown in eq 1.

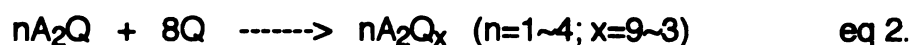


Each reaction formed a complete melt at the employed temperatures (250 °C~350 °C). The equation given above is not balanced and shows only reactants used (left-hand side) and product obtained (right-hand side). Since alkali metal polychalcogenide flux is very reactive and corrosive, it oxidizes Au metal while itself is reduced to shorter polychalcogenides. After reaction, excess alkali metal polychalcogenide flux is easily removed from the product by washing with water and/or dimethylformamide (DMF). All compounds are stable in the air and moisture for several days.

In this study we have seen profound redox chemistry associated with Au⁺³ ions and controlled by the chemical composition of alkali metal polychalcogenide fluxes. When we tried to optimize the reaction conditions for the Au⁺ compound of KAuSe₅, which was prepared from the reactant ratio K₂Se/Au/Se of 2/1/8 at 250 °C, a slight variation of K₂Se ratio from 2 to 1.8 yielded a surprising result: the novel Au³⁺ compound of K₃AuSe₁₃. The subsequent isolation and structural characterization of three more Au³⁺ compounds in K/Au/Se and Na/Au/Se systems and another Au⁺ compound in

the Cs/Au/Se system suggests that a variety of Au⁺ and Au³⁺ compounds may occur in these molten polychalcogenide fluxes which may undergo complex solution equilibria.

Various alkali metal polychalcogenide flux compositions A₂Q_x (x=3~9) are obtained by fusing A₂Q with stoichiometric amounts of chalcogenide atoms as shown in eq 2.



The reactivity of these fluxes varies according to their chemical compositions. Polychalcogenide fluxes with longer chains, A₂Q_x (x=9, 5), generally favored compounds with long polychalcogenide ligands (Q_x²⁻ x=5,3). For example, KAuSe₅, K₃AuSe₁₃, and Na₃AuSe₈ were prepared from K₂Se₅, K₂Se_{5.4} and Na₂Se₉ fluxes, respectively. The opposite is also true. Shorter chain fluxes generally favored monochalcogenide compound formation. For example, NaAuSe₂ was prepared from Na₂Se_{3.7}, but KAuSe₂ was prepared from the longer polychalcogenide flux (K₂Se_{5.4}), the composition used for preparation of K₃AuSe₁₃. However, the increased amounts of Au required for preparation of KAuSe₂ broke the starting K₂Se_{5.4} flux into a much shorter chain polychalcogenide flux during the reaction. Another interesting observation made during this study is the alkali metal cation size effect which could support new structural frameworks (e.g. one-dimensional KAuSe₂ vs layered NaAuSe₂) and various polychalcogenide ligands (e.g. Se₃²⁻ vs Se₅²⁻). Therefore, the systematic investigations with various size of alkali metals turned out to be quite valuable.

In the far-IR region all compounds exhibit spectral absorptions due to Q-Q and Au-Q stretching vibrations. The observed absorptions are given in Table 39 and their spectra are shown in Figures 18-20.

Table 39. Frequencies (cm^{-1}) of Spectral Absorptions of (I), (II), (III), (IV), (V), (VI), and (VII) due to Q-Q and M-Q stretching Vibrations

(I)	(II)	(III)	(IV)	(V)	(VI)	(VII)
KAuS ₅	KAuSe ₅	CsAuSe ₃	K ₃ AuSe ₁₃	Na ₃ AuSe ₈	KAuSe ₂	NaAuSe ₂
461 (s) ^a	257 (s)	243 (s)	264 (s)	259 (s)	231 (s)	236 (s)
317 (m)	244 (sh)	233 (m)	231 (s)	224 (m)	146 (m)	230 (m)
255 (m)	225 (s)	207 (w)	222 (w)	210 (m)	110 (m)	222 (sh)
212 (m)	213 (w)	163 (w)	214 (w)	194 (w)		191 (m)
	194 (w)			177(m)		134 (m)
						111(m)

^a (s) strong; (m) medium; (w) weak; (sh) shoulder

The only polysulfide compound in this study, KAuS₅, shows an absorption at 461 cm^{-1} which is attributed to a S-S stretching vibration by comparison with the spectra of other known polysulfide compounds.⁶⁴ (see also Table 17) The vs-s vibrational frequencies are observed in the range of 446~500 cm^{-1} . The additional peak at 317 cm^{-1} can be attributed to an Au-S stretching vibration. For the Au polyselenide compounds, a spectral absorption is observed in the range of 242~264 cm^{-1} . This band can be assigned to a Se-Se stretching

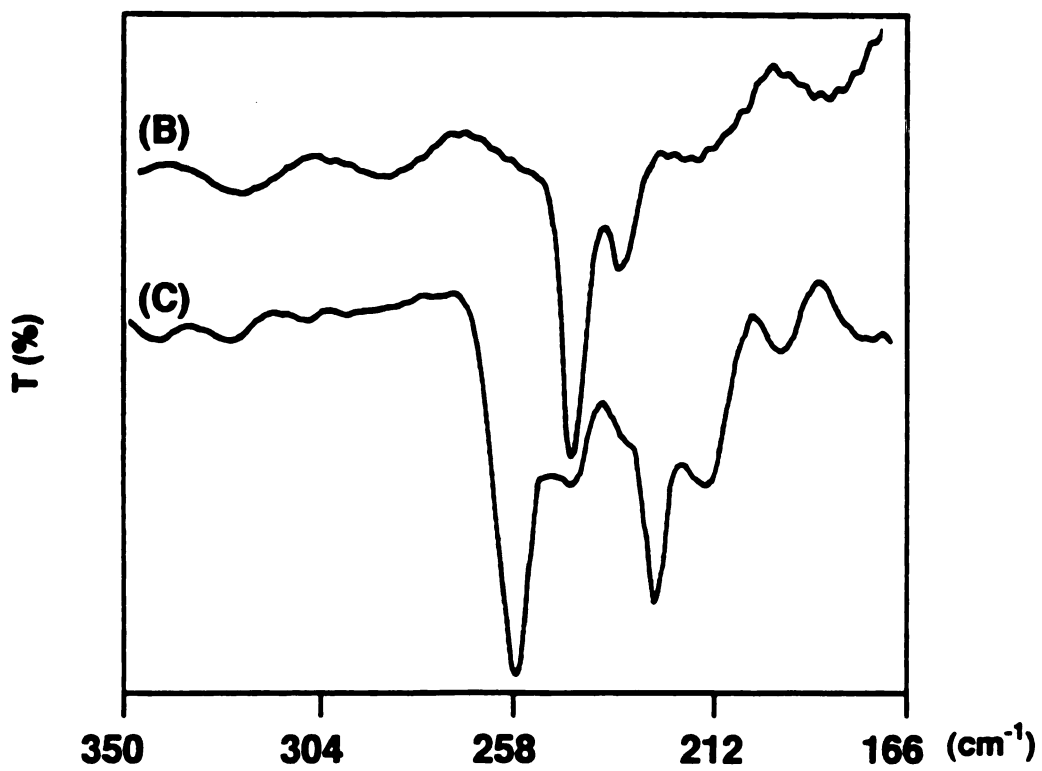
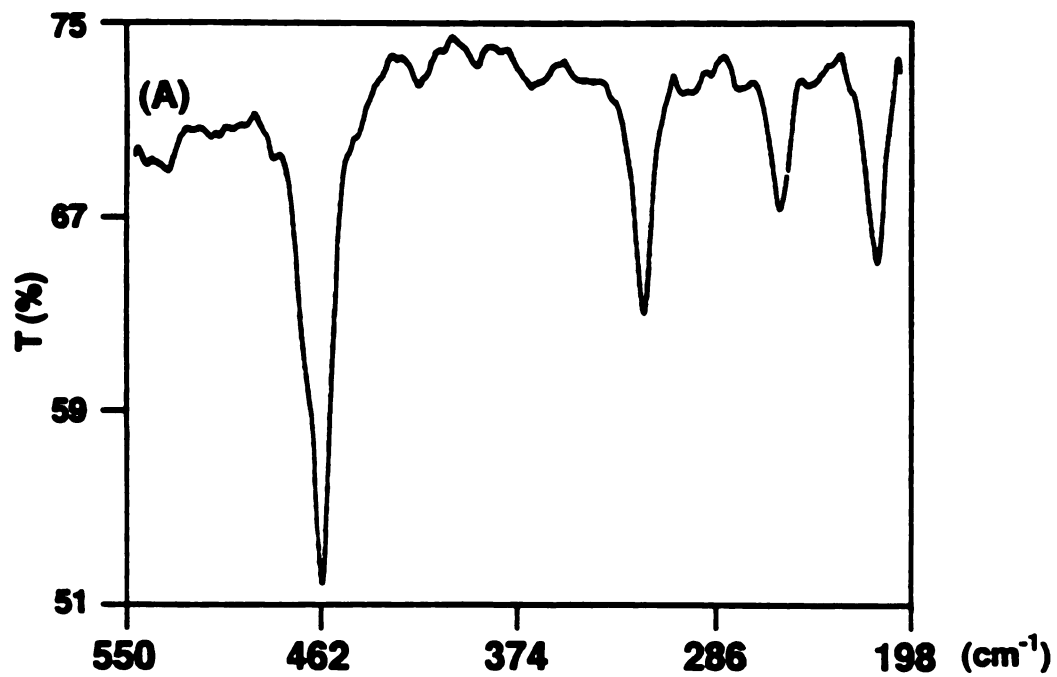


Figure 18. Far-IR spectra of (A) KAuS_5 , (B) CsAuSe_3 , and (C) KAuSe_5

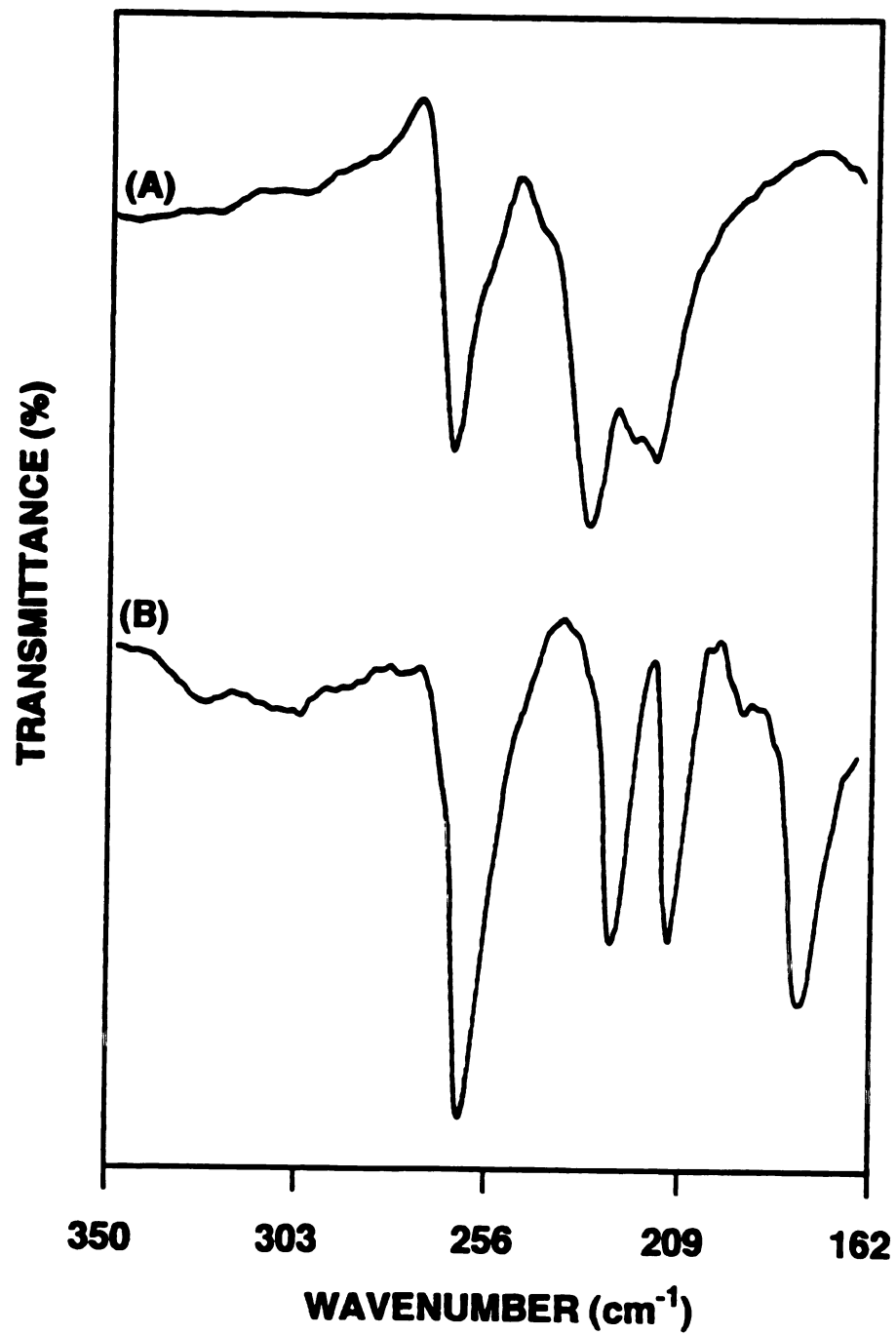


Figure 19. Far-IR spectra of (A) K_3AuSe_{13} and (B) Na_3AuSe_8

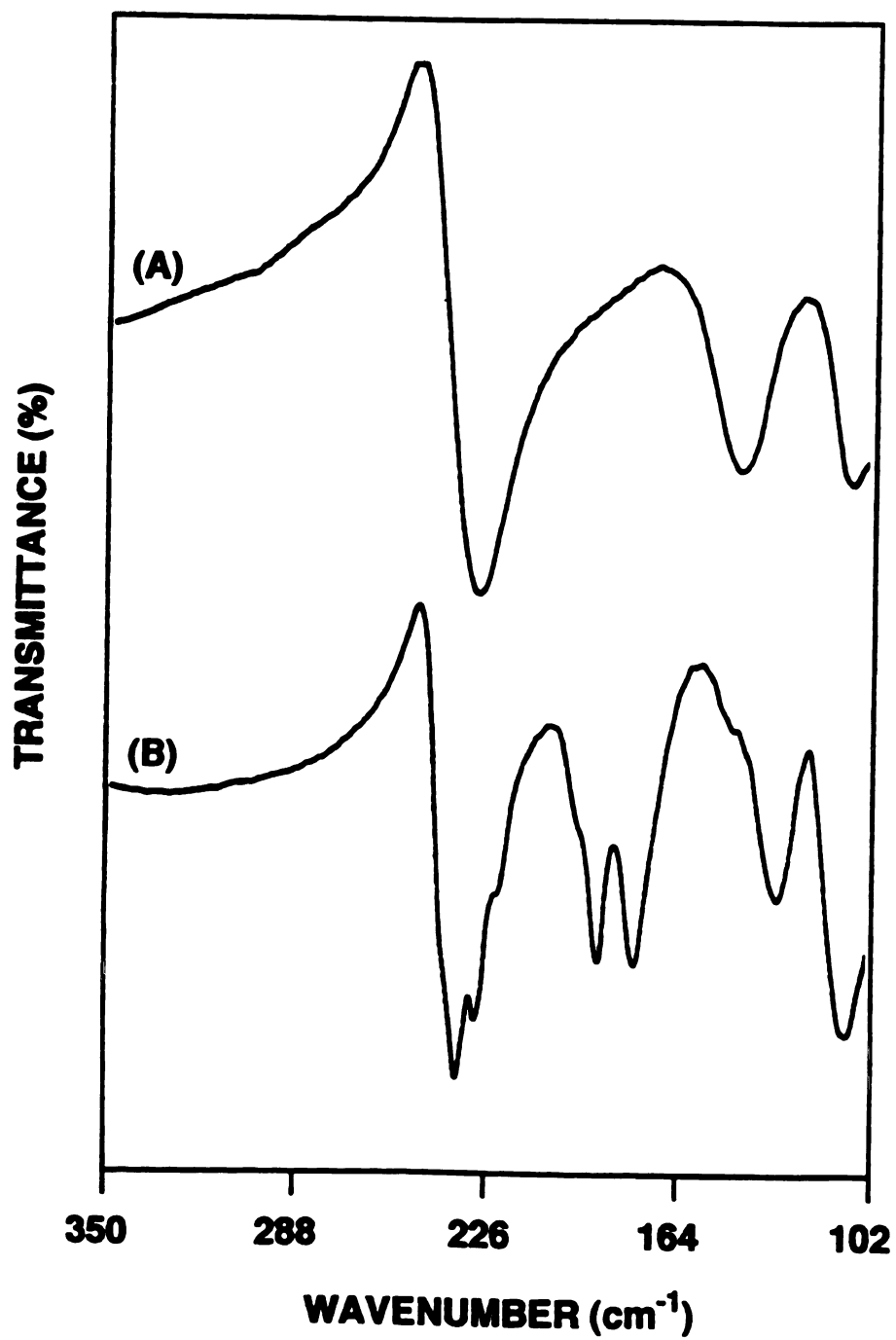


Figure 20. Far-IR spectra of (A) KAuSe_2 and (B) NaAuSe_2

vibration by comparison with the spectra of other known polyselenide complexes and with that of the unbound ligand $(\text{Ph}_4\text{P})_2\text{Se}_5$ ($\nu_{\text{Se-Se}}$ 267 cm^{-1}) 26(b). The $\nu_{\text{Se-Se}}$ absorption in this region has been observed previously in various compounds, e.g. Se_x^{2-65} ($x=1-6$) at 258 cm^{-1} , $\alpha\text{-Se}_6^{66}$ at 253 cm^{-1} , $[\text{Fe}_2\text{Se}_{12}]^{2-24}$ at 258 cm^{-1} , $[\text{Pd}(\text{Se}_4)_2]^{2-67}$ at 274 cm^{-1} , and $\alpha\text{-}[\text{CuSe}_4]_n^{n-}$ at 246~252 cm^{-1} (see Table 17). In addition, an absorption in the vicinity of 230 cm^{-1} found in all Au/Se_x^{2-} compounds may be attributed to an Au-Se stretching vibration. The monoselenide compounds of (V) and (VII) show common absorptions around 230 cm^{-1} and 110 cm^{-1} . Using simple group theory and assuming D_{4h} symmetry on the Au^{3+} center, we expect one IR-active Au-Se stretching vibration in KAuSe_2 . For the NaAuSe_2 compound there are 4 IR-active Au-Se stretching vibrations expected by assuming the C_{2h} symmetry on the Au^{3+} center. Thus, we can assign the 230 cm^{-1} band in KAuSe_2 and the 236 cm^{-1} , 230 cm^{-1} , and 222 cm^{-1} bands in NaAuSe_2 as Au-Se stretching vibrations. This interpretation must be an oversimplification on this complicated extended lattice system. It is usually difficult to interpret the IR spectra of metal polychalcogenide compounds without ambiguity. This is because of the fact that M-Se and Se-Se stretching frequencies fall in the same low-frequency IR region (200-340 cm^{-1}) and that systematic IR spectroscopic data for the various free ligands (Q_x^{2-} , $x=2-6$) and metal chalcogenide complexes are still lacking.

3.2. Description of Structures

3.2.1. Structure of KAuS_5 (I) and KAuSe_5 (II)

(I) and (II) are isostructural. They possess one-dimensional polymeric chains. Figure 21 shows the alternating planes of charge compensating K^+ ions and $[\text{AuQ}_5]_n^{n-}$ chains along the crystallographic b -axis in the unit cell.

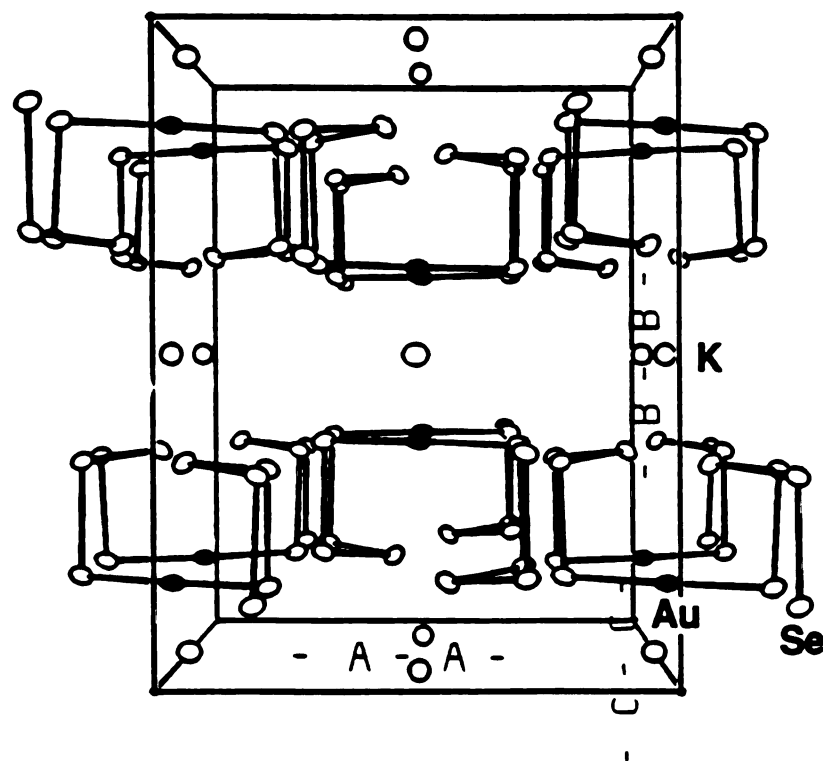


Figure 21. ORTEP representation of the unit cell of KAuQ_5 (Q=S, Se).

The anionic $[\text{AuQ}_5]_n^{n-}$ chains are composed of pentachalcogenide ligands (S_5^{2-} and Se_5^{2-} respectively) bridging Au^+ atoms via their terminal Q atoms. The chains lack a center of symmetry and run parallel to the crystallographic *c*-axis. The Au^+ centers, situated on a crystallographic 2-fold axis, show a linear coordination with a Q-Au-Q bond angles of 178.7(2) deg and 178.9(2) deg for (I) and (II), respectively. The observed Au-Q bond distances (Au-S; 2.296(6) Å and Au-Se; 2.410(4) Å) are similar to those found in KAuQ^{77} (Q=S, Se) at 2.305(6) and 2.414(1) Å, respectively. There are short Au-Au contacts at 2.963(1) Å and 2.950(3) Å for (I) and (II) respectively. These contacts are considerably shorter than those observed in KAuS^{77} (3.260 (1) Å) and $\alpha\text{-AuSe}^{83}$ (3.222 (6) Å) and comparable to that in Ag_3AuSe_2 (2.974 Å)^{68(a)}. These close Au-Au interactions occur between chains along the crystallographic *b*-axis, to form dimers as shown in figure 22. These close Au-Au contacts are considered as favorable $d^{10}\text{-}d^{10}$ interactions⁶⁸. There are no interactions between the chains along the crystallographic *a*-axis. Selected bond distances and angles for (I) and (II) are given in Table 40. The two crystallographically distinct K atoms in the asymmetric unit participate in ionic interactions with the Q_5^{2-} ligands. The K atoms are surrounded by eight chalcogen atoms. The shortest K-S distances in (I) are K(1)-S(1) 3.304(5) Å, and K(2)-S(1) 3.214(5) Å; the shortest K-Se distances in (II) are K(1)-Se(1) 3.339(4) Å, and K(2)-Se(1) 3.384(4) Å.

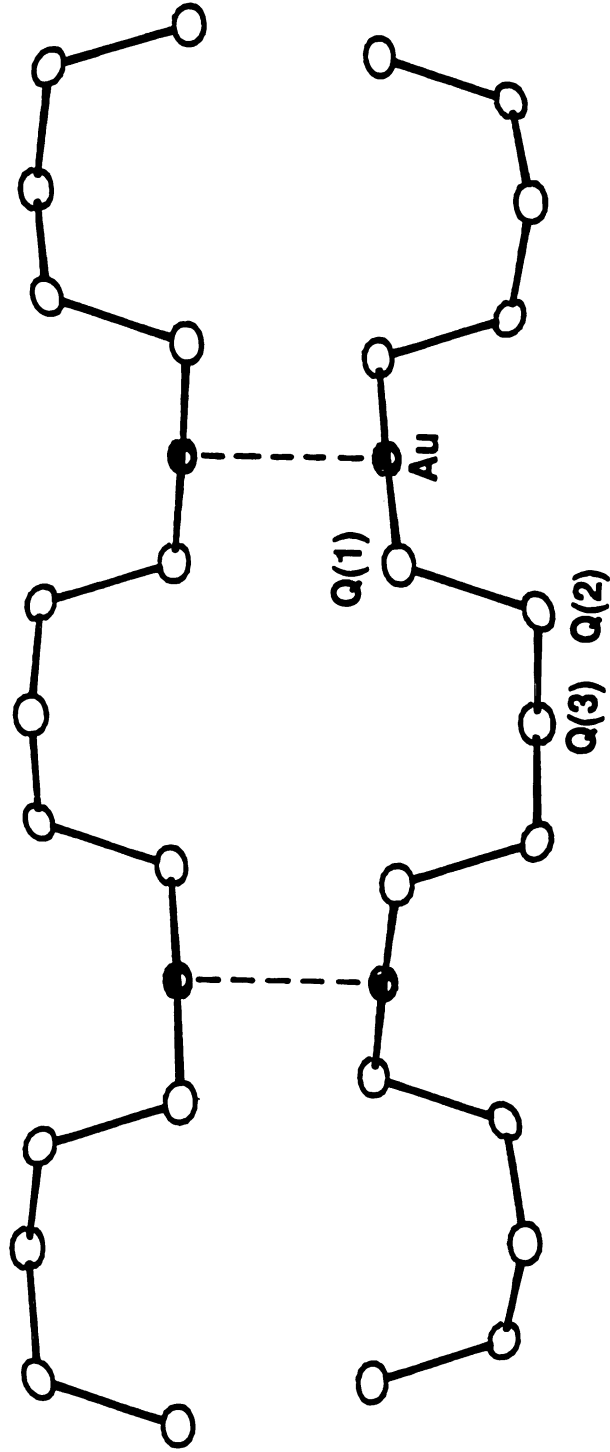


Figure 22. One-dimensional structure of $[\text{AuQ}_5]_n^-$ chains, showing the mode of dimerization.

Table 40. Selected Bond Distances (Å) and Angles (deg) in KAuS_5 and KAuSe_5 with Standard Deviations in Parentheses

KAuS_5			
Au-S(1)	2.296(6)	S(1)-Au-S(1)	178.7(2)
S(1)-S(2)	2.080(7)	Au-S(1)-S(2)	103.7(3)
S(2)-S(3)	2.063(7)	S(1)-S(2)-S(3)	107.9(3)
S-S (mean)	2.07	S(2)-S(3)-S(2)	106.3(4)
Au-Au	2.963(1)		
K(1)-S(1)	3.305(5) (x4)	K(2)-S(1)	3.214(5) (x4)
K(1)-S(2)	3.379(5) (x4)	K(2)-S(2)	3.506(5) (x4)
K(1)-S (mean)	3.34(4)	K(2)-S (mean)	3.36
KAuSe_5			
Au-Se(1)	2.410(4)	Se(1)-Au-Se(1)	179.0(2)
Se(1)-Se(2)	2.363(6)	Au-Se(1)-Se(2)	101.4(2)
Se(2)-Se(3)	2.343(5)	Se(1)-Se(2)-Se(3)	104.2(2)
Se-Se (mean)	2.35(1)	Se(2)-Se(3)-Se(2)	104.2(3)
Au-Au	2.950(3)		
K(1)-Se(1)	3.339(4) (x4)	K(2)-Se(1)	3.384(4) (x4)
K(1)-Se(2)	3.503(4) (x4)	K(2)-Se(2)	3.619(4)(x4)
K(1)-Se (mean)	3.42(9)	K(2)-Se (mean)	3.50(13)

3.2.2. Structure of CsAuSe₃ (III)

The anion of this compound also has a one-dimensional polymeric structure, as shown in Figure 23. Like the homologous [Au(Se₅)]_nⁿ⁻ in (II), the anionic [Au(Se₃)]_nⁿ⁻ chains are composed of Se₃²⁻ ligands bridging adjacent Au atoms via terminal Se atoms. The chains lack a center of symmetry and run parallel to the crystallographic *a*-axis in a helical fashion. The Au atoms, situated on a crystallographic 2-fold axis, have a slightly distorted linear geometry with a Se-Au-Se bond angle of 172.9 (1) deg. Since there are no close Au--Au or interchain Au--Se contacts observed in this compound, this distortion may be due to close Au-Cs contacts which are in the range of 3.784(3) ~ 4.087(2) Å. The sum of their van der Waals radii is approximately 4.99 Å (The van der Waals radius of Cs was estimated using the linear correlation between known ionic and van der Waals radii of alkali metals). The Au-Se distance is 2.401(2) Å which is similar to that found in (II). Selected bond distances and angles are given in Table 41. There is one crystallographically distinct Cs atom in the asymmetric unit. The Cs atoms participate in ionic interactions with the Se₃²⁻ ligands. Within the limit of 3.9 Å, the Cs atom has eight Se atoms around it. The shortest Cs-Se distance in (III) is with terminal Se atoms (Cs-Se(1)) at 3.573(2) Å.

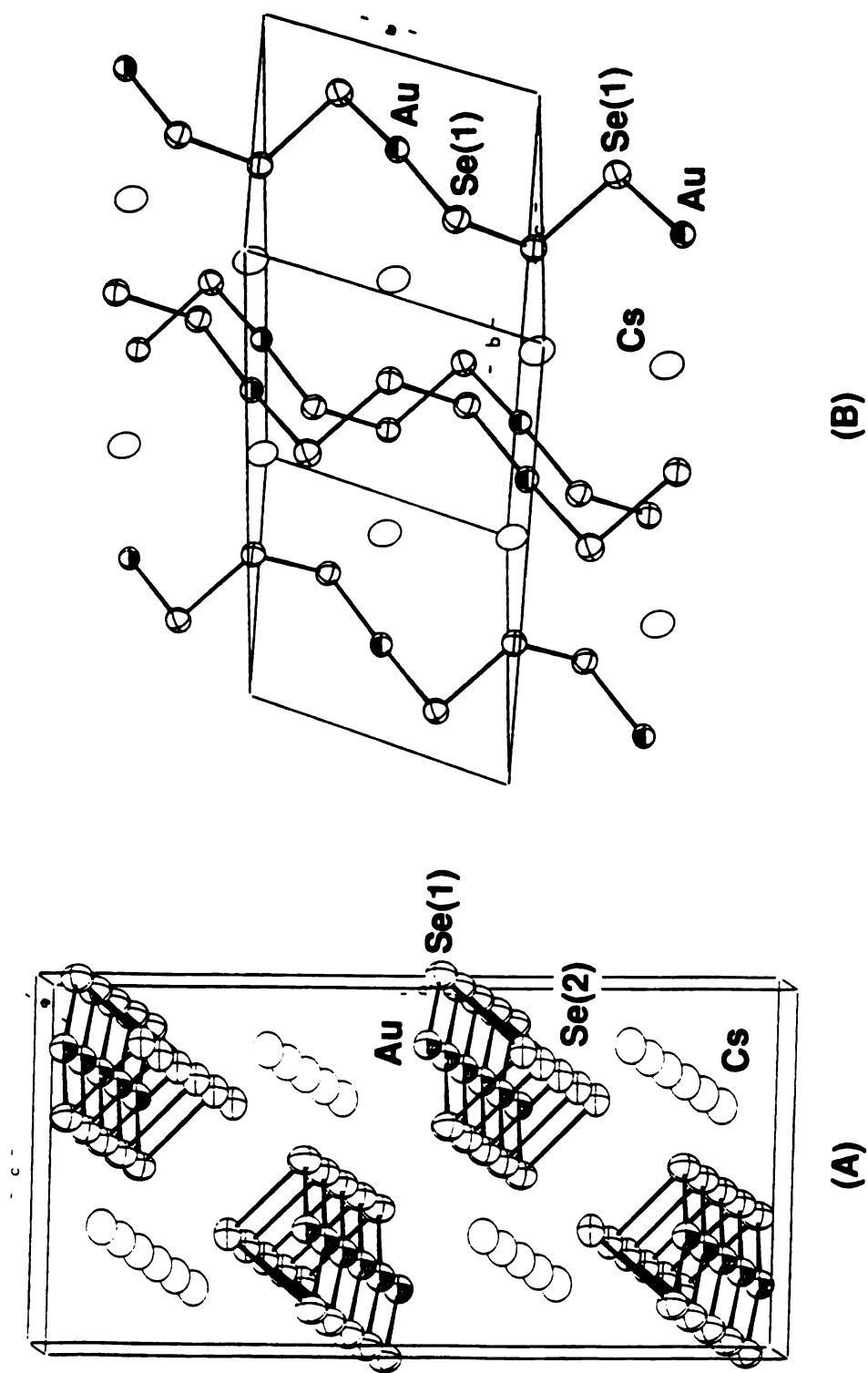


Figure 23. ORTEP representation of two axial views of CsAuSe₃: (A) viewed down [100] direction, (B) viewed down [011] direction.

Table 41. Selected Bond Distances (Å) and Angles (deg) in CsAuSe₃ with Standard Deviations in Parentheses

Au-Se(1)	2.401(2) (x2)	Se(1)-Au-Se(1)	172.9(1)
Au-Cs	3.784(3)	Au(1)-Se(1)-Se(2)	98.4(1)
Se(1)-Se(2)	2.384(3) (x2)	Se(1)-Se(2)-Se(1)	104.1(2)
Cs-Se(1)	3.573(2) (x2)	Cs-Se(2)	3.881(2) (x2)
Cs-Se(1)	3.763(3) (x2)	Cs-Se(2)	3.900(2) (x2)
Cs-Se (mean)	3.78(14)		

3.2.3. Structure of $\text{K}_3\text{AuSe}_{13}$ (IV)

The compound of $\text{K}_3\text{AuSe}_{13}$ is very intriguing and the most Se rich Au compound yet characterized to the best of our knowledge. The structure is shown in Figure 24. This is a Au^{3+} compound composed of centrosymmetric one-dimensional $[\text{Au}(\text{Se}_3)(\text{Se}_5)_2]_n^{3n-}$ chains and charge balancing K^+ ions. The chains are composed of Se_3^{2-} ligands bridging adjacent Au atoms to which two Se_5^{2-} ligands are coordinated in a trans fashion via one of their terminal Se atoms. The Au atoms are situated on a crystallographic inversion center. The chains run parallel to the crystallographic c -axis. Two views of one-dimensional $[\text{Au}(\text{Se}_3)(\text{Se}_5)_2]_n^{3n-}$ chains are shown in Figure 25. The geometry around Au atoms is square planar as expected for Au^{3+} . No short Au-Au interactions are observed in the structure. The average Au-Se distance of 2.48(1) Å is comparable to the corresponding distances in $\alpha\text{-AuSe}^{83}$ (2.48Å) and in the molecular $[\text{Au}_2\text{Se}_{10}]^{2-}$,²³ (2.45Å), both of which are formally Au^{3+} compounds. Selected bond distances and angles are given in Table 42. The unusual dangling monodentate Se_5^{2-} ligands are stabilized by ionic interactions with two crystallographically distinct K^+ ions. Figure 26 shows the coordination environments of the K atoms. K(1) atoms are surrounded by 10 Se atoms of which four sets of Se(4)-Se(5) bonds of monodentate Se_5^{2-} ligands belong to four different chains. The shortest K-Se interactions are those with unbound Se(5) atoms at 3.262(6) and 3.432(6) Å. The K(2) atoms are located in the pockets created by two monodentate Se_5^{2-} ligands which belong to two different chains. The shortest interactions are with unbound terminal Se(5) atoms at 3.261(6) Å and 3.306(6) Å.

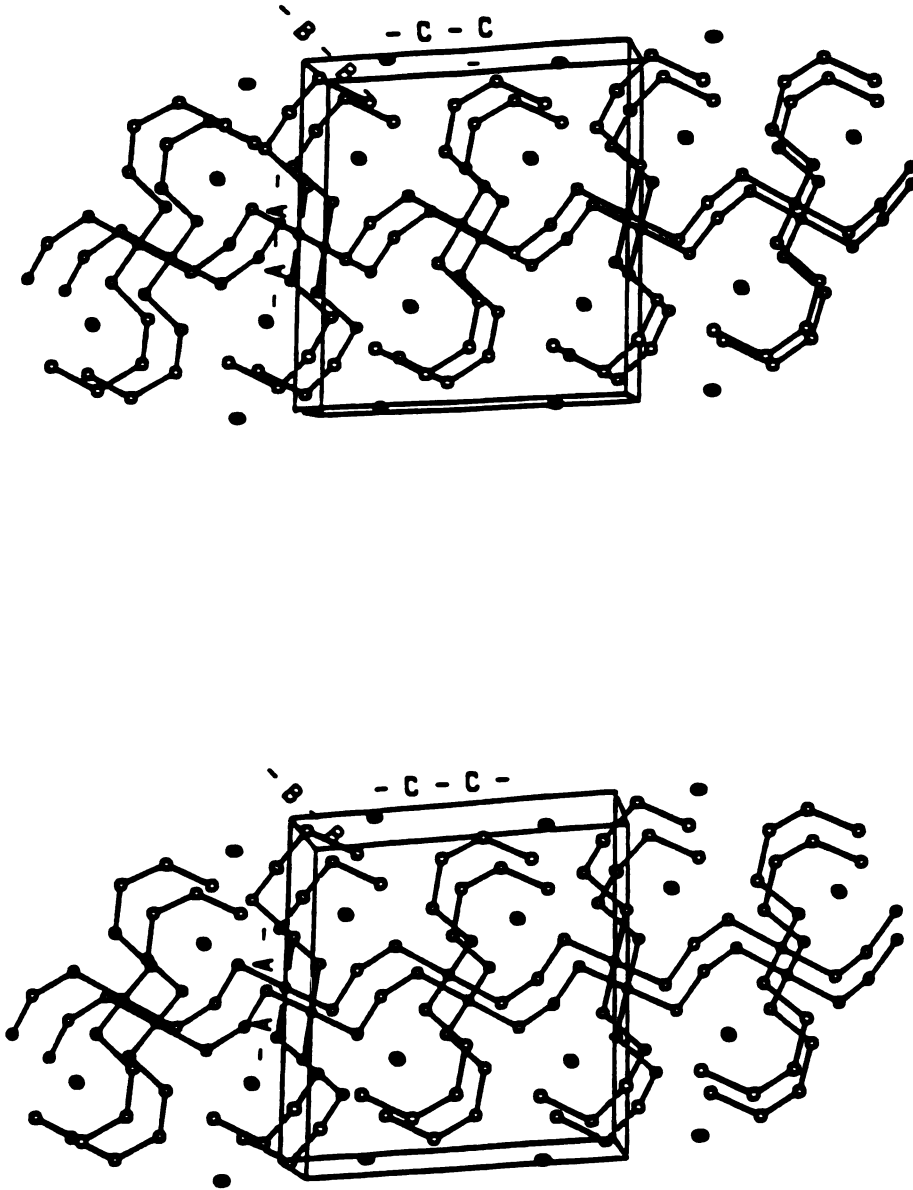


Figure 24. Stereoview of the unit cell of K_3AuSe_{13} .

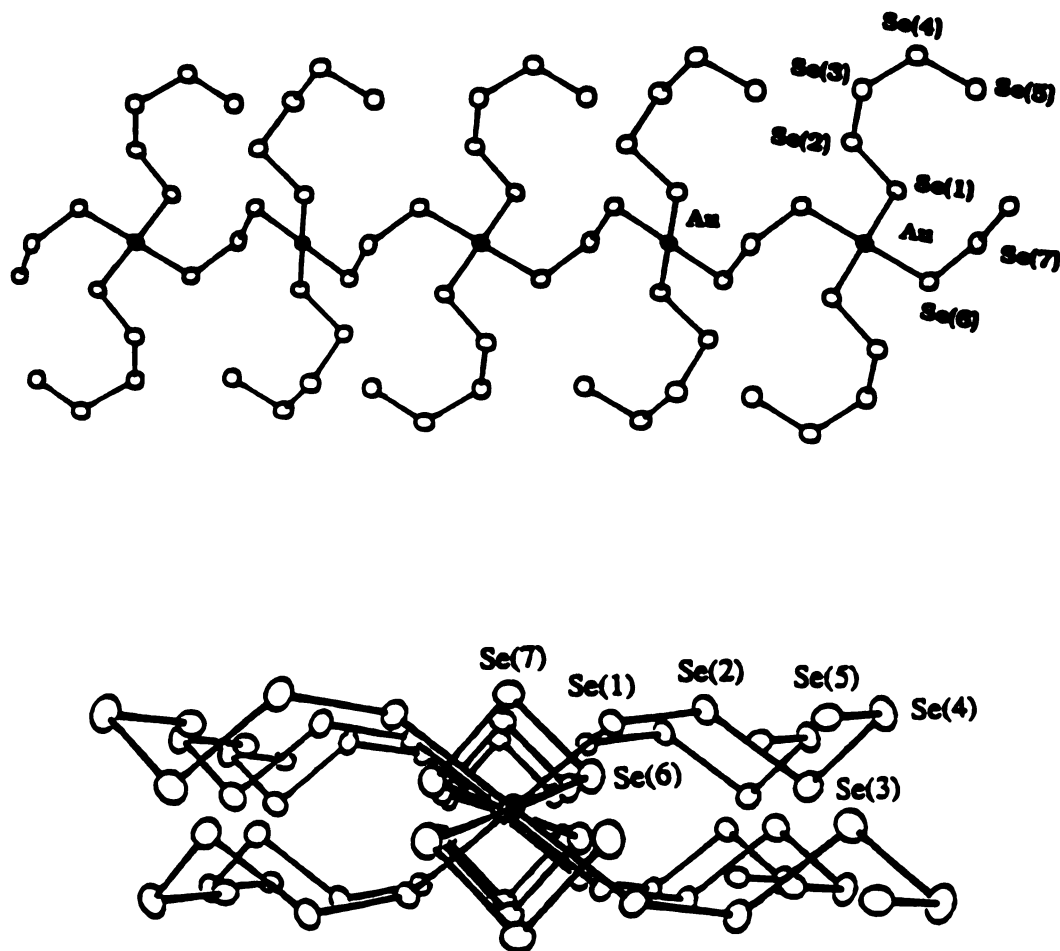


Figure 25. ORTEP representation of two views of the one-dimensional $[\text{AuSe}_{13}]_n^{3n-}$ chain.

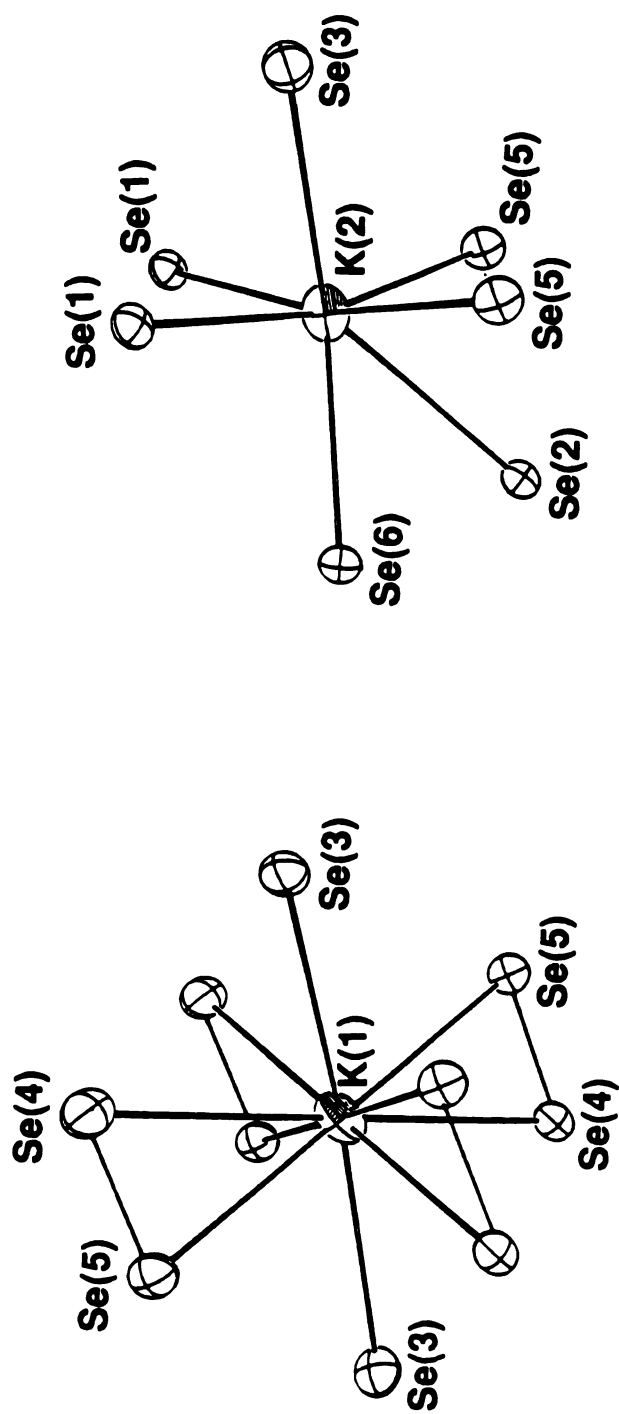


Figure 26. Coordination environments of K atoms with labeling scheme.

Table 42. Selected Bond Distances (Å) and Angles (deg) in K_3AuSe_{13} with Standard Deviations in Parentheses

Au-Se(1)	2.465(2) (x2)	Se(1)-Au-Se(1)	180.0(0)
Au-Se(6)	2.485(2) (x2)	Se(1)-Au-Se(6)	90.8(1)
Au-Se (mean)	2.48(1)	Se(6)-Au-Se(6)	180.0(0)
		Se(1)-Au-Se(6)	89.2(1)
Se(1)-Se(2)	2.349(3)	Au-Se(1)-Se(2)	111.9(1)
Se(2)-Se(3)	2.368(3)	Se(1)-Se(2)-Se(3)	104.1(1)
Se(3)-Se(4)	2.348(3)	Se(2)-Se(3)-Se(4)	105.3(1)
Se(4)-Se(5)	2.343(3)	Se(3)-Se(4)-Se(5)	109.2(1)
Se-Se (mean)	2.35(1)	Au-Se(6)-Se(7)	108.9(1)
		Se(6)-Se(7)-Se(6)	105.6(1)
Se(6)-Se(7)	2.351(3) (x2)		
K(2)-Se(1)	3.356(6)	K(2)-Se(1)	3.266(6)
K(1)-Se(3)	3.637(2) (x2)	K(2)-Se(2)	3.632(6)
K(1)-Se(4)	3.579(5) (x2)	K(2)-Se(3)	3.521(5)
K(1)-Se(4)	3.592(5) (x2)	K(2)-Se(5)	3.306(6)
K(1)-Se(5)	3.262(6) (x2)	K(2)-Se(5)	3.261(6)
K(1)-Se(5)	3.432(6) (x2)	K(2)-Se(6)	3.378(5)
K(1)-Se (mean)	3.50(15)	K(2)-Se (mean)	3.38(15)

3.2.4. Structure of KAuSe_2 (V)

The structure of KAuSe_2 is one-dimensional and contains only monoselenide ligands. It is composed of centrosymmetric one-dimensional $[\text{AuSe}_2]_n^{n-}$ chains and charge balancing K^+ ions as shown in Figure 27. The one-dimensional $[\text{AuSe}_2]_n^{n-}$ chain has a PdCl_2 -type⁸⁴ structure and is isostructural to $[\text{PtS}_2]_n^{2n-}$ ⁸⁵ chain. The flat ribbons of $[\text{AuSe}_2]_n^{n-}$ are made of edge-sharing AuSe_4 square planes. The Au^{3+} center, situated on a crystallographic mmm site, is strictly square planar as expected for a d^8 configuration. The Au-Au distance in the $[\text{AuSe}_2]_n^{n-}$ chain is 3.665(1) Å, indicating no Au-Au interaction. The Au-Se distance at 2.475(1) Å is similar to that in (IV). Selected bond distances and angles are given in Table 43. The charge balancing K^+ ions participate in ionic interactions with Se atoms at 3.448(1) Å. The geometry around the K atoms is square prismatic.

Table 43. Selected Bond Distances (Å) and Angles (deg) in KAuSe_2 with Standard Deviations in Parentheses

Au-Se	2.476(1) (x4)	Se-Au-Se	180.0(0) (x2)
		Se-Au-Se	84.48(4) (x2)
		Se-Au-Se	95.52(4) (x2)
		Au-Se-Au	95.52(5)
K-Se	3.448(2) (x8)		

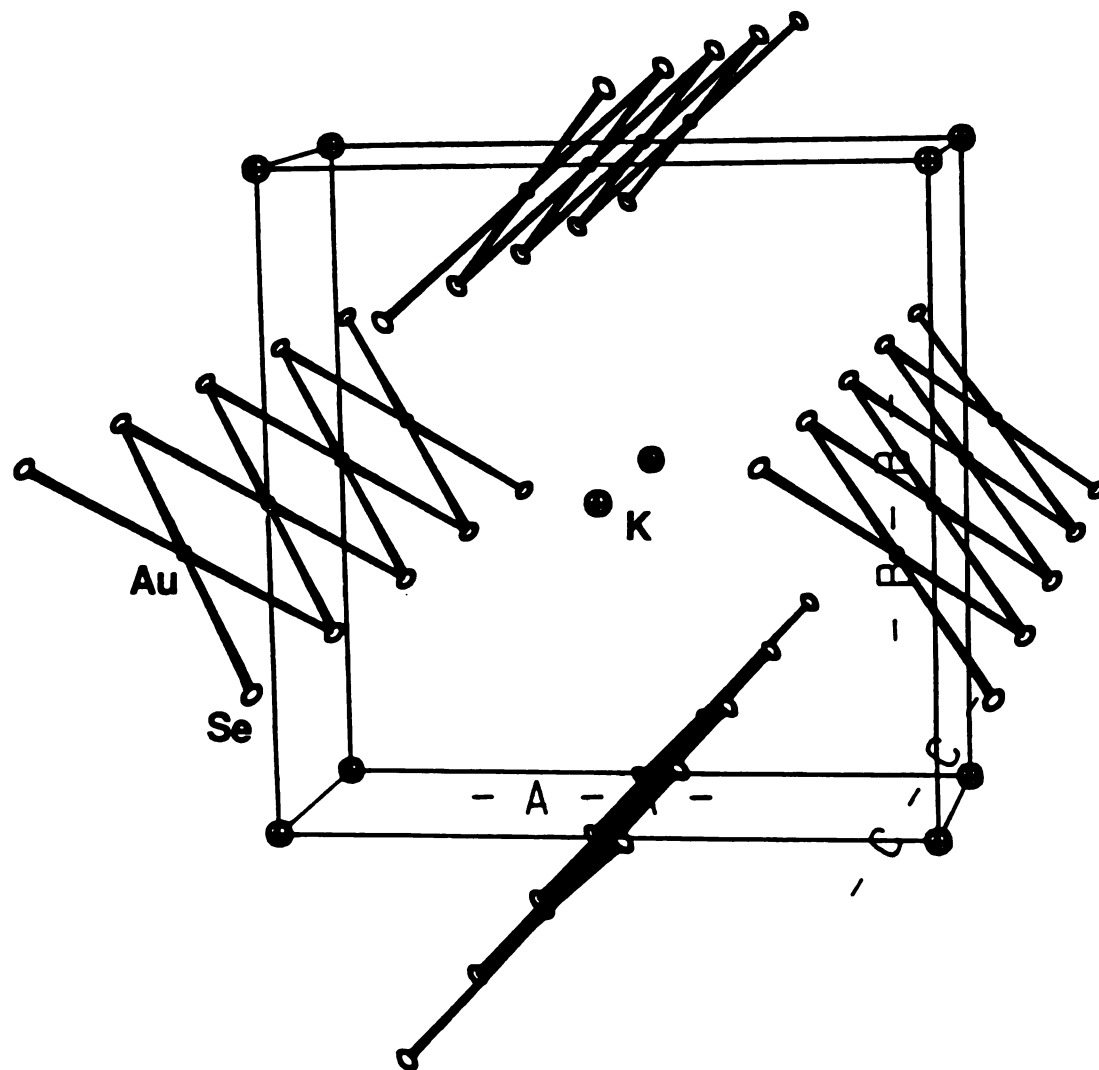


Figure 27. ORTEP representation of the unit cell of KAuSe_2 .

3.2.5. Structure of Na₃AuSe₈ (VI)

This compound is homologous to K₃AuSe₁₃. It is composed of centrosymmetric one-dimensional [Au(Se₂)(Se₃)₂]_n³ⁿ⁻ chains and charge balancing Na⁺ ions. Two views of one-dimensional [Au(Se₂)(Se₃)₂]_n³ⁿ⁻ chains are shown in Figure 28. The chains are composed of Se₂²⁻ ligands bridging adjacent Au atoms to which two Se₃²⁻ ligands are coordinated in a trans fashion via one of their terminal Se atoms. The Au atoms are sitting on a crystallographic inversion center. Like [Au(Se₃)(Se₅)₂]_n³ⁿ⁻ in (IV), [Au(Se₂)(Se₃)₂]_n³ⁿ⁻ represents another remarkable example of a monodentate long polyselenide (Se₃²⁻), where one terminal atom is coordinated to a metal while the other is loose, ionically interacting with alkali ions. The geometry around Au³⁺ centers is square planar as expected for a d⁸ configuration. The average Au-Se distance is 2.49(1) Å, similar to those found in Au³⁺ compounds of (IV) and (V). Selected bond distances and angles are given in Table 44. The coordination environments of two crystallographically distinct Na atoms are shown in Figure 29. Na(1) has distorted octahedral geometry with ionic interactions with selenium atoms in the range of 2.937(4)-3.099(2)Å. Na(2) has distorted tetrahedral geometry with ionic interactions with four selenium atoms in the range of 2.94(1)-3.20(2)Å.

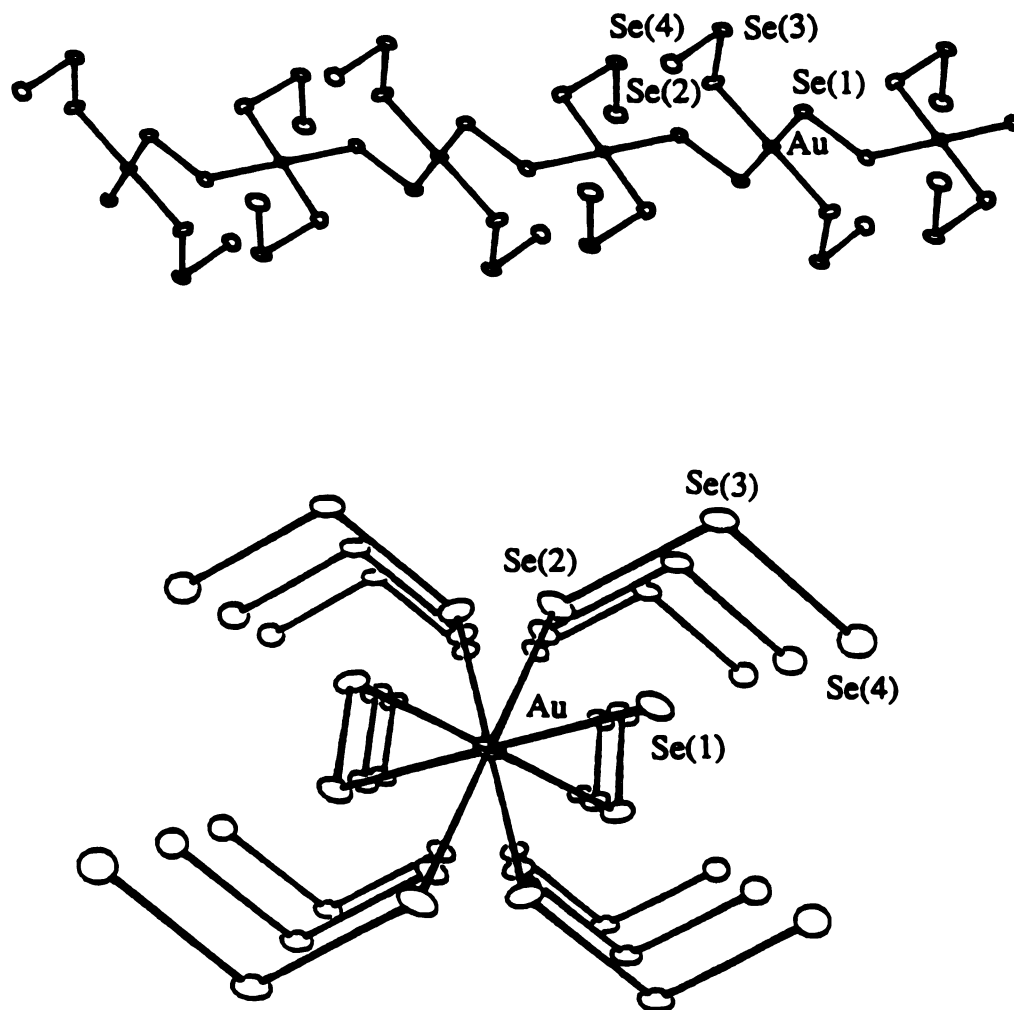


Figure 28. ORTEP representation of two views of the one-dimensional $[\text{AuSe}_8]_n^{3n-}$ chain.

Table 44. Selected Bond Distances (Å) and Angles (deg) in Na₃AuSe₈ with Standard Deviations in Parentheses

Au-Se(1)	2.481(3) (x2)	Se(1)-Au-Se(1)	180.0(0)
Au-Se(2)	2.499(3) (X2)	Se(2)-Au-Se(2)	180.0(0)
Au-Se (mean)	2.49(1)	Se(1)-Au-Se(2)	90.9(1) (x2)
		Se(1)-Au-Se(2)	89.1(1) (x2)
Se(1)-Se(1)	2.345(2)	Au-Se(1)-Se(1)	110.7(1)
		Au-Se(2)-Se(3)	109.0(1)
Se(2)-Se(3)	2.354(5)	Se(2)-Se(3)-Se(4)	101.4(2)
Se(3)-Se(4)	2.361(5)		
Se-Se (mean)	2.358(5)		
Na(1)-Se(1)	2.937(4) (x2)	Na(2)-Se(3)	3.20(2)
Na(1)-Se(3)	3.099(2) (x2)	Na(2)-Se(4)	2.94(1)
Na(1)-Se(4)	3.043(3) (x2)	Na(2)-Se(4)	3.06(2)
		Na(2)-Se(4)	2.95(1)
Na(1)-Se (mean)	3.03(8)	Na(2)-Se (mean)	3.04(12)

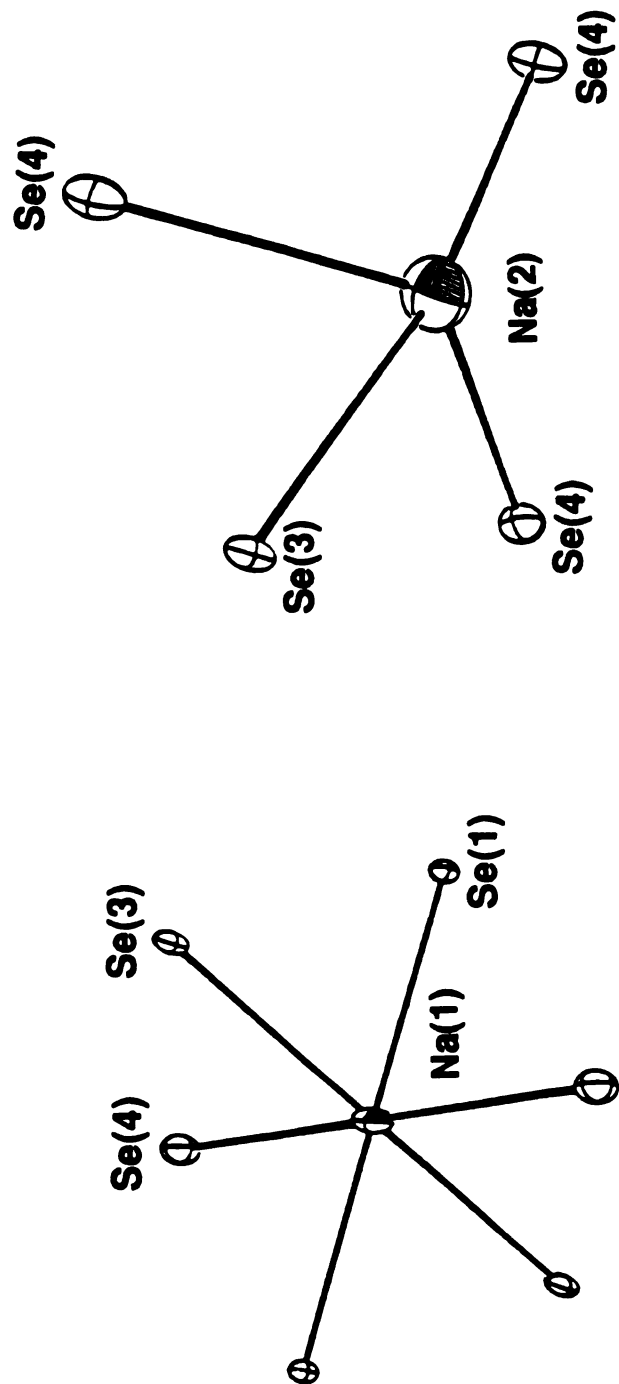


Figure 29. Coordination environments of Na atoms with labeling scheme.

3.2.6. Structure of NaAuSe₂ (VII)

The structure of NaAuSe₂ possess a covalently bonded [AuSe₂]_nⁿ⁻ anionic layered network instead of the one-dimensional chain of [AuSe₂]_nⁿ⁻ even though its stoichiometry in formula units is same as that of KAuSe₂. The structure of one layer of [AuSe₂]_nⁿ⁻ is shown in Figure 30. The anionic [AuSe₂]_nⁿ⁻ layer represents a new structure type for an MX₂ stoichiometry. The layers are made of polymerized [Au₂Se₂]Se_{4/2} dimeric units with a central rhombic [Au₂Se₂]²⁺ core. The Au--Au distance at 3.730(2) Å does not imply any significant Au--Au interactions in the layer. The geometry of the Au³⁺ center is slightly distorted square planar. Two Au-Se distances are observed; Au-Se(1) inside the central [Au₂Se₂]²⁺ core is short at 2.460(4) while Au-Se(2) outside the central core is slightly longer at 2.498(4) Å. Selected bond distances and angles are given in Table 45. The [AuSe₂]_nⁿ⁻ layers form corrugated sheets that stack in phase in the crystallographic *a*-axis direction, as shown in Figure 31. The interlayer spacing is 6.745 Å. There is one crystallographically distinct Na atom in the asymmetric unit. Charge balancing Na⁺ ions are distributed between layers with ionic interactions with Se atoms. The Na atom has distorted octahedral geometry. The shortest Na-Se distance is 2.92(1) Å.

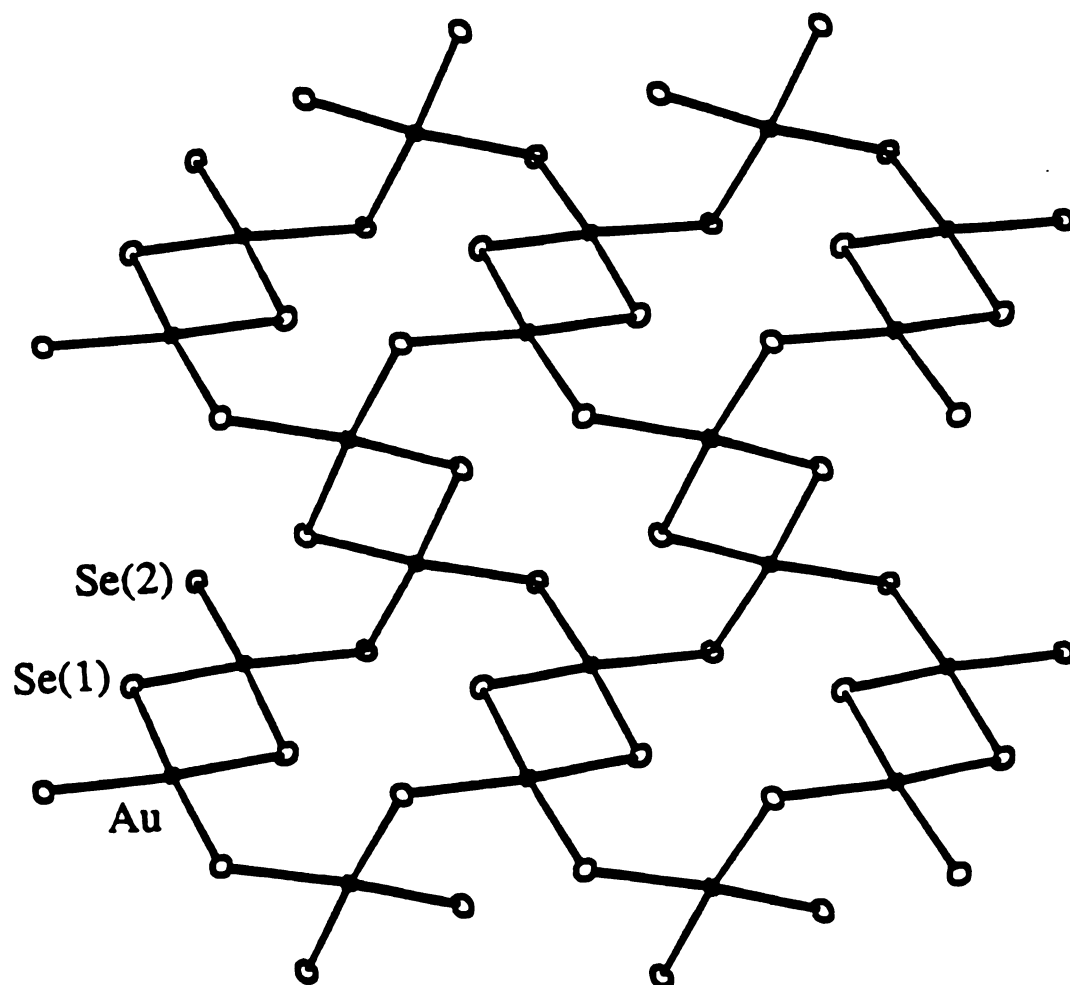


Figure 30. ORTEP representation of the layered structure of $[\text{AuSe}_2]_n^-$, looking perpendicular to the layer.

Table 45. Selected Bond Distances (Å) and Angles (deg) in NaAuSe₂ with Standard Deviations in Parentheses

Au-Se(1)	2.460(4)	Se(1)-Au-Se(1)	81.4(1)
Au-Se(1)	2.459(3)	Se(2)-Au-Se(2)	93.1(1)
Au-Se(2)	2.508(4)	Se(1)-Au-Se(2)	96.0(1)
Au-Se(2)	2.489(3)	Se(1)-Au-Se(2)	170.3(1)
Au-Se (mean)	2.48(2)	Se(1)-Au-Se(2)	176.6(1)
		Se(1)-Au-Se(2)	89.6(1)
		Au-Se(1)-Au	98.6(1)
		Au-Se(2)-Au	102.9(1)
Na-Se(1)	3.04(7) (x3)		
Na-Se(2)	3.01(9) (x3)		
Na-Se (mean)	3.03(2)		

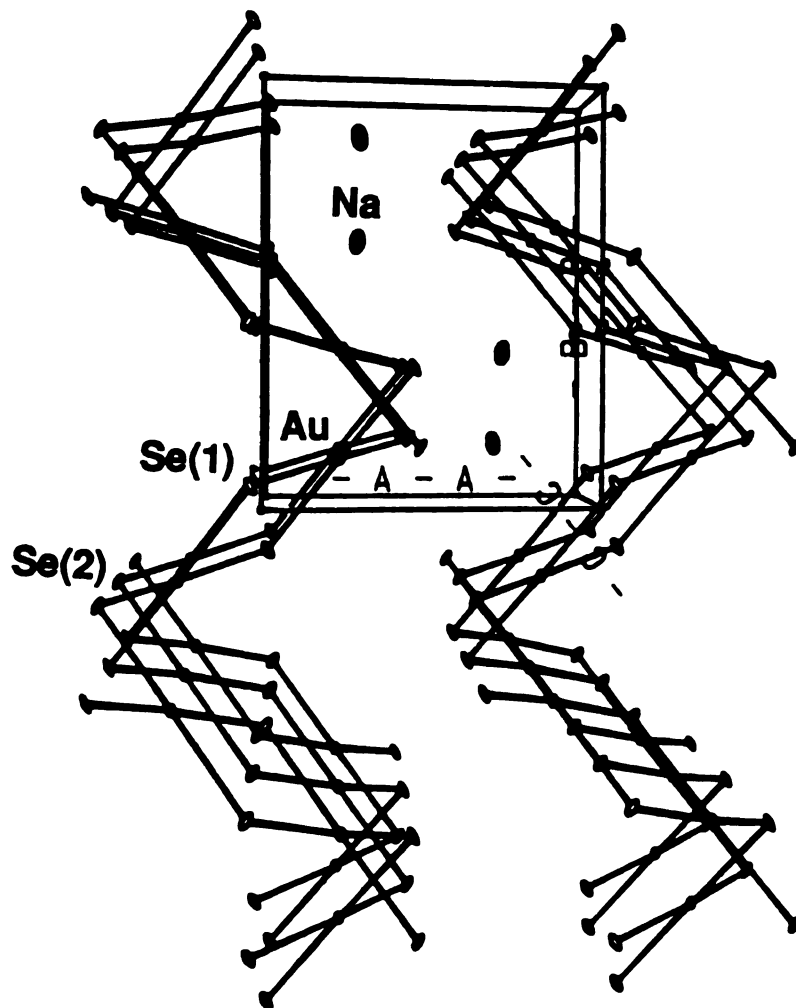
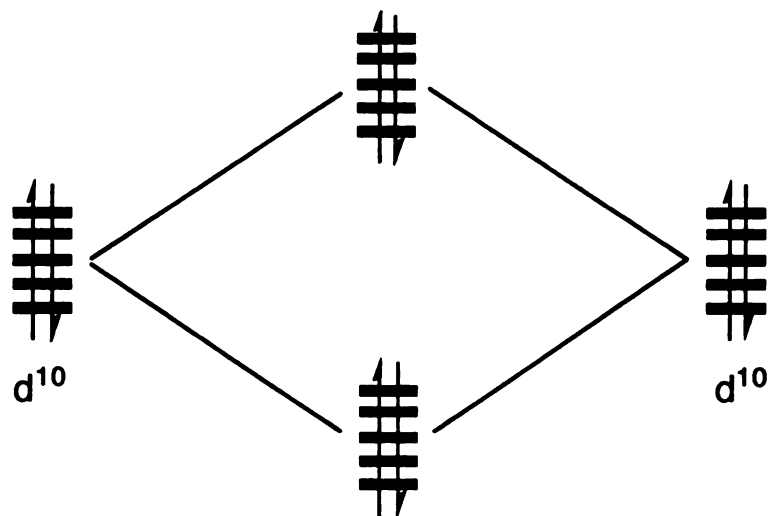


Figure 31. ORTEP representation of the unit cell of NaAuSe₂.

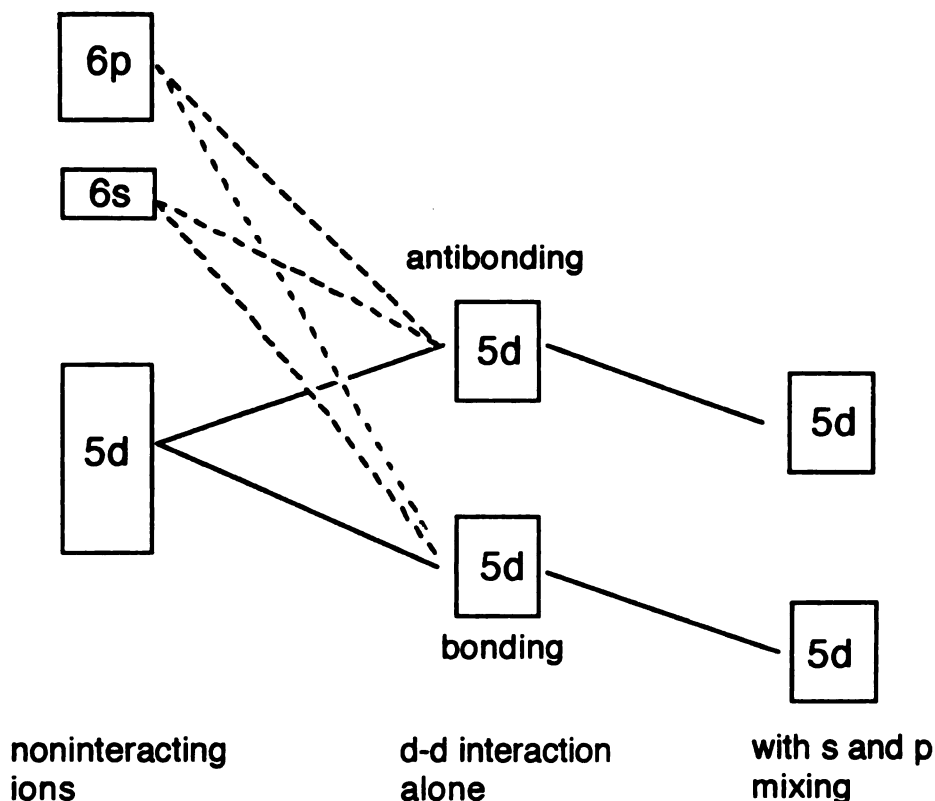
3.3. Structures

The compounds isolated in this system show a rich structural chemistry involving the various polychalcogenide ligands. All compounds obtained in the ternary A/Au/Q (A=alkali metal) system can be grouped into two different categories based on the oxidation state of the central metal: (i) Au⁺ polychalcogenide compounds, and (ii) Au³⁺ (poly)chalcogenide compounds. The Au⁺ compounds, KAuS₅, KAuSe₅, and CsAuSe₃, are homologous to known zigzag chain compounds of KAuQ (Q=S, Se)⁸⁰. The anionic chains of these polychalcogenide compounds are viewed as derivatives of [AuQ]_nⁿ⁻ chains⁸⁰ in which Q²⁻ ligands have been replaced with polychalcogenides (S₅²⁻, Se₅²⁻, and Se₃²⁻ respectively). Alternatively, the structures of these compounds can be viewed as being derived from helical polymeric chains of sulfur (S_x) or selenium (Se_x) by substitution of linear Au⁺ atoms for every sixth sulfur (or selenium) atom for (I) and (II) and every fourth atom for (III). However, the helical character of the Se chain is maintained only in the CsAuSe₃ structure.

In the KAuQ₅ compounds short Au-Au contacts are observed at 2.963(1) Å and 2.950(3) Å for (I) and (II), respectively. This is a beautiful example of a well defined, isolated d¹⁰-d¹⁰ interactions⁶⁸ in the solid state. In general, d¹⁰-d¹⁰ bonding contacts are not fully understood. Normally, the interaction of two-filled metal orbitals results in a nonbonding situation due to formation of a bonding and an equally antibonding state as shown in the following scheme. Of course, the result of such interaction is zero.



However, recent theoretical investigations into this issue have invoked a significant admixture of s and p character (from the empty s and p orbitals) into predominantly d metal orbitals.⁸⁶ This hybridization gives rise simultaneously to a more bonding and a less antibonding M-M interaction and therefore an overall stabilization as shown in the following scheme.



Two sets of intriguing Au^{3+} compounds, (i) $\text{K}_3\text{AuSe}_{13}$ and Na_3AuSe_8 , and (ii) KAuSe_2 and NaAuSe_2 , exhibit cation size effect on structures and interesting redox chemistry associated with $\text{Au}^+/\text{Au}^{3+}$ ion in the alkali metal polyselenide fluxes. The anionic chains of $[\text{Au}(\text{Se}_3)(\text{Se}_5)_2]_n^{3n-}$ and $[\text{Au}(\text{Se}_2)(\text{Se}_3)_2]_n^{3n-}$ in (IV) and (VI), respectively, can be viewed as the oxidative addition product of Se_x^{2-} ($x=10, 6$) ligands to the Au^+ atoms of one-dimensional $[\text{AuSe}_y]_n^{n-}$ ($y=3,2$) chains as shown in eq 3.



Yet, the hypothetical anionic chain of $[\text{AuSe}_2]_n^{n-}$ in eq 3 (b) is not known. It is, however, another possible phase in the homologous series of compounds of $[\text{AuSe}_x]_n^{n-}$ ($x=1, 3, 5$ known) chain. (IV) and (VI) show very unusual binding modes such as monodentate ligation for the long polychalcogenide ligands. The usual binding mode of polychalcogenides (Se_x^{2-} $x \geq 2$) known to date is at least bidentate, either bridging or chelating as shown in the previous chapter (see Table 2). Another example of these unusual monodentate ligation of Se_5^{2-} have been found in $\text{Cs}_4[\text{Se}_{16}]$.⁸⁷ In this compound a square planar Se^{2+} atom is bonded by three Se_5^{2-} chains, of which one act as bidentate chelate, while the other two act as monodentate ligands. In the structure of (IV) and (VI) alkali metal cations interact ionically with those monodentate polyselenide ligands to stabilize the unusual monodentate ligation.

A second set of Au^{3+} compounds, (V) and (VII) with the same formula unit stoichiometry $[\text{AuSe}_2]_n^{n-}$ gives an excellent example of counterion size effect on structure (one-dimensional vs. two-dimensional). Substitution of Na^+ for K^+ in (V) would result in a significant decrease in cation partial volume and would bring the $[\text{AuSe}]_n^{n-}$ chains close enough that considerable coulombic interchain repulsions might develop, thus destabilizing the structure. These repulsions could be overcome and converted to attractive forces by combining the chains into layers through interchain Au-Se bonding. This structural relationship is shown in Figure 32. One can visualize Au-Se(2) bond breakage along the dotted line in the layer to form $[\text{Au}_2\text{Se}_2]\text{Se}_2\text{Se}_{2/2}$ units and flexible $[\text{Au}_2\text{Se}_2]\text{Se}_{2/2}$ units.

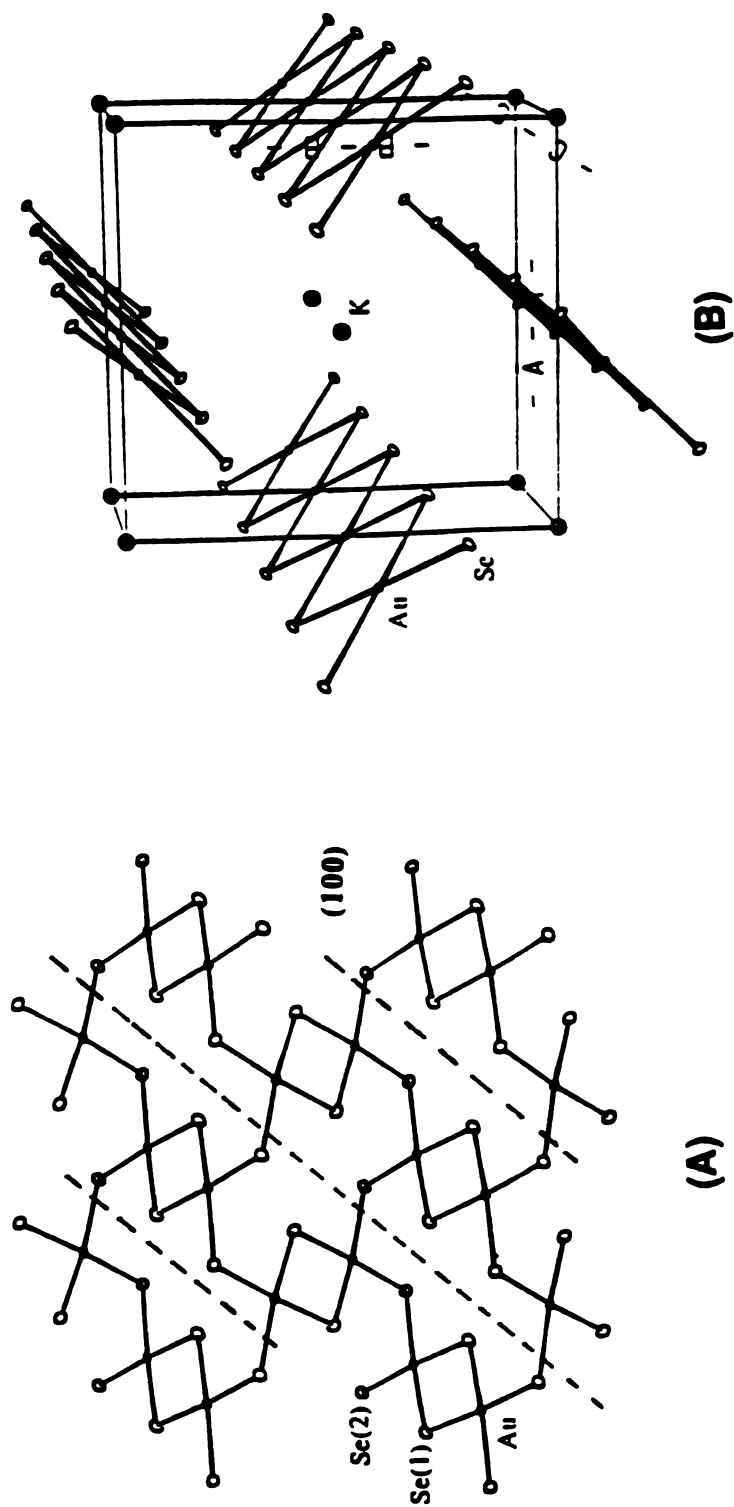


Figure 32. Schematic representation of the counter cation size effect on structures of $[\text{AuSe}_2]_n^-$: (A) layer structure of $[\text{AuSe}_2]_n^-$ in (VII) vs (B) chain structure of $[\text{AuSe}_2]_n^-$ in (V).

These $[\text{Au}_2\text{Se}_2]\text{Se}_{2/2}$ units can rotate to complete square planar coordination of the Au^{3+} ion by sharing Se atoms of $[\text{Au}_2\text{Se}_2]\text{Se}_2\text{Se}_{2/2}$ and produce one-dimensional chains of (VI).

It will be interesting to determine any structural changes that occur in the $[\text{AuSe}_2]_n^{n-}$ unit with even smaller Li^+ or larger Cs^+ counter ions. These compounds have not been synthesized yet. However, one could predict a three-dimensional structure of a Li^+ salt because the smaller Li^+ would bring the layers in the Na^+ salt closer together and rearrange the two-dimensional framework into a three-dimensional structure to overcome the coulombic repulsions between the layers. Since one-dimensional chains are more flexible in accepting a larger cation, similar chain structure of KAuSe_2 should remain unchanged for the Cs^+ salt.

The investigation of ternary $A/\text{Au}/\text{Q}$ systems yields an intriguing set of new compounds with novel structural architectures and underscores the significance of the polychalcogenide molten salt method for new materials synthesis. The slight but significant variation in the polyselenide melt composition and the isolation of both Au^{1+} and Au^{3+} polyselenide compounds highlight the complexity of these reaction mixtures and the delicate coordination and redox equilibria present among various Au^{m+} ($m=1, 3$) and Se_x^{2-} species.

CHAPTER 4

Molten Salt Synthesis of Low-Dimensional Ternary Chalcogenides. Novel Structure Types in the A/Hg/Q System (A=K, Cs; Q=S, Se)

1. Introduction

We have demonstrated in previous chapters that by using alkali metal polychalcogenide fluxes as solvents and reagents at intermediate temperatures (e.g. 210-350 °C), novel, low-dimensional solid compounds can be isolated in crystalline form. We believe that an enormous number of interesting and perhaps metastable compounds with low-dimensional structures occur at these temperatures (150~500 °C). Solid chalcogenides are of intense interest due to their useful electronic⁵⁵ and catalytic²⁷ properties. Therefore, new such materials are highly desirable. Ternary A/Hg/Q compounds (A= alkali metal) have been rarely explored. Prior to this work there was only one known structural class of compounds, A_6HgQ_4 (A=K, Rb; Q=S, Se)⁸⁸. Therefore, we initiated the investigation of ternary A/Hg/Q systems using alkali metal polychalcogenide fluxes (A_2Q_x) at intermediate temperatures. In this chapter, we illustrate that alkali metal polychalcogenide fluxes at 210~370 °C promote synthesis and crystal growth of new ternary compounds, $A_2Hg_3Q_4$ (A=Na, K,

Cs; Q=S, Se) and $A_2Hg_6Q_7$ (A=K, Cs; Q=S, Se), which feature novel structure types.

2. Experimental Section

2.1 Reagents

Chemicals in this work were used as obtained: mercury sulfide (HgS) powder, analytical reagent, J. T. Baker Chemical Co., Phillipsburg, NJ; mercury selenide (HgSe) powder, -100 mesh, 99.9% purity, Cerac, Milwaukee, WI; sulfur powder, sublimed, J. T. Baker Chemical Co., Phillipsburg, NJ; selenium powder, -100 mesh, 99.95% purity, Aldrich Chemical Co., Milwaukee, WI; potassium metal, analytical reagent, Mallinckrodt Inc., Paris, KY; cesium metal, 99.98% purity, AESAR, Johnson Matthey, Seabrook, NH.

2.2. Physical Measurements

Quantitative microprobe analysis was performed on a Jeol 35CF scanning electron microscopy equipped with Tracor Northern TN5500 X-ray microanalysis attachment. Single crystals of each sample were carefully picked and mounted on an aluminum stub using conducting silver paint to help dissipate charges that develop on the sample surface during measurements. Energy Dispersive Spectra (EDS) were obtained using the following experimental set-up:

X-ray detector position : 55 mm

Working distance : 39 mm

Accelerating voltage : 20 KV

Take-off angle : 27 deg

Beam current : 200 picoamps

Accumulation time : 100 seconds

Window : Be

A standardless quantitative analysis (SQ) program was used to analyze the X-ray spectra obtained. Since the selenium ratio is always underestimated due to an artifact of the program, a correction factor (x1.83), which was determined with a known HgSe compound, was used to evaluate the selenium percentage. The analysis reported is the average of four to six individual measurements on different crystals.

2.3. Synthesis

Chemicals were measured and loaded in Pyrex tubes under a dry nitrogen atmosphere in a Vacuum Atmospheres Dri-Lab glovebox. Potassium monosulfide (K_2S) and alkali metal monoselenide (A_2Se ; $A=K, Cs$) were prepared in liquid ammonia from alkali metal and elemental sulfur (or selenium) in a 2:1 ratio.

Dipotassium tetra(μ_2 -sulfido)trimercurate(II), $K_2Hg_3S_4$ (I)
0.165 g (1.5 mmol) of K_2S , 0.116 g (0.5 mmol) of HgS , and 0.128 g (4.0 mmol) of S were mixed together and loaded in a Pyrex tube which was flame-sealed under vacuum ($\sim 10^{-3}$ torr). The tube was placed in a computer-controlled furnace and heated at 220 °C for 99 hrs and cooled slowly to 50 °C at a rate of 2 °C/hr. Pale yellow transparent hexagonal crystals were obtained with small contamination of HgS by removing excess potassium polysulfides with

degassed dimethylformamide (DMF) under a N₂ atmosphere (yield: 46 % based on the amount of Hg used). The product is not stable in water and decompose rapidly. The presence of K and Hg and S atoms in a large number of crystals was confirmed using the EDS/SEM system.

Dipotassium tetra(μ_2 -selenido)trimercurate(II), K₂Hg₃Se₄ (II)
0.118 g (1.75 mmol) of K₂Se, 0.070 g (0.25 mmol) of HgSe, and 0.158 g (2.0 mmol) of Se were mixed together and loaded in a Pyrex tube which was flame-sealed under vacuum ($\sim 10^{-3}$ torr). The tube was placed in a computer-controlled furnace and heated at 250 °C for 99 hrs and cooled slowly to 50 °C at a rate of 2 °C/hr. Red hexagonal crystals were obtained with small contamination of HgSe by removing excess potassium polyselenides with degassed DMF under a N₂ atmosphere (yield: 53 % based on Hg used). The product is not stable in water and decompose rapidly. The presence of K and Hg and Se atoms in a large number of crystals was confirmed using the EDS/SEM system.

Dicesium tetra(μ_2 -selenido)trimercurate(II), Cs₂Hg₃Se₄ (III)
0.115 g (0.33 mmol) of Cs₂Se, 0.047 g (0.17 mmol) of HgSe, and 0.105 g (1.33 mmol) of Se were mixed together and loaded in a Pyrex tube which was flame-sealed under vacuum ($\sim 10^{-3}$ torr). The tube was placed in a computer-controlled furnace and heated at 250 °C for 99 hrs and cooled slowly to 50 °C at a rate of 2 °C/hr. Orange-yellow hexagonal crystals were obtained, with small contamination of HgSe, by removing excess cesium polyselenides with degassed DMF under a N₂ atmosphere (yield: 58 % based on Hg used). The product is relatively stable in water in a short time of period, but decomposes in an hour. A quantitative microprobe analysis performed on a large number of

crystals with the EDS/SEM system gave an average composition of $\text{Cs}_{1.9}\text{Hg}_{3.0}\text{Se}_{3.8}$.

Dipotassium hepta(μ_2 -sulfido)hexamercurate(II), $\text{K}_2\text{Hg}_6\text{S}_7$ (IV) 0.055 g (0.5 mmol) of K_2S , 0.203 g (0.87 mmol) of HgS , and 0.064 g (2.0 mmol) of S were mixed together and loaded in a Pyrex tube which was flame-sealed under vacuum ($\sim 10^{-3}$ torr). The tube was placed in a computer-controlled furnace and heated at 370 °C for 99 hrs and cooled slowly to 50 °C at a rate of 2 °C/hr. Black needle-like crystals were obtained, with little contamination of red HgS crystals, by removing excess molten potassium polysulfides with water under a N_2 atmosphere (yield: 72 % based on Hg used). The product was washed with ethanol and ether and vacuum dried. The product is not soluble in water and any common organic solvents. A quantitative microprobe analysis performed on a large number of crystals with the EDS/SEM system gave an average composition of $\text{K}_{2.0}\text{Hg}_{5.8}\text{S}_{7.1}$.

This compound can also be prepared by direct synthesis: 0.110 g (1.0 mmol) of K_2S and 1.396 g (6 mmol) of HgS were mixed together and loaded in a Pyrex tube which was flame-sealed under vacuum ($\sim 10^{-3}$ torr). The tube was placed in a computer-controlled furnace and heated at 375 °C for 7 days and cooled slowly to 50 °C at a rate of 2 °C/hr. Black powder of $\text{K}_2\text{Hg}_6\text{S}_7$ were obtained with little contamination of red HgS . It was identified with X-ray powder diffraction pattern.

Dicesium hepta(μ_2 -selenido)hexamercurate(II), $\text{Cs}_2\text{Hg}_6\text{Se}_7$ (V) This compound could be prepared only by direct synthesis: 0.086 g (0.25 mmol) of Cs_2Se and 0.420 g (1.50 mmol) of HgSe were mixed together and loaded in a Pyrex tube which was flame-sealed under vacuum ($\sim 10^{-3}$ torr). The

tube was placed in a computer-controlled furnace and heated at 375 °C for 72 hrs and cooled slowly to 50 °C at a rate of 3 °C/hr. Black needle-shaped crystals were obtained. The product is not soluble in water and any common organic solvents. A quantitative microprobe analysis performed on a large number of crystals with the EDS/SEM system gave an average composition of $\text{Cs}_{2.1}\text{Hg}_{6.0}\text{Se}_{7.3}$.

2.4. X-ray Crystallographic Studies

All compounds were examined by X-ray powder diffraction for the purpose of phase characterization and identification. The d-spacings for each compound were obtained from the powder pattern recorded on a Phillips XRG-3000 computer-controlled powder diffractometer, operating at 40KV, 35 mA. Graphite monochromated Cu radiation was used. The d-spacings observed for the bulk materials of (I) and (II) matched well with those calculated from the single crystal X-ray structure analysis data. However, they showed extra peaks which correspond to small impurities of HgS and HgSe, respectively. The d-spacings observed for manually selected single crystals of (III), (IV), and (V) were compared, and found to be in accord, with the calculated d-spacings from the single crystal X-ray structure analysis data. The calculation of d-spacings were performed using the POWD10 program⁵⁶. The results are summarized in Tables 46-50.

Table 46. Calculated and Observed X-ray Powder Diffraction Pattern of $K_2Hg_3S_4$

H K L	d_{calc} (Å)	d_{obs} (Å)	I/I _{max} (obs.)
0 0 2	6.85	6.90	33.1
0 0 4	3.42	3.43	100
0 2 1	3.17	3.18	5.6
3 1 0	3.09	3.10	7.2
2 1 3	3.05	3.06	4.5
3 1 1	3.02	3.03	4.0
0 2 2	2.94	2.95	2.5
3 1 2	2.82	2.82	12.5
0 2 3	2.65	2.67	10.4
3 1 3	2.56	2.57	4.4
0 2 4	2.364	2.366	3.1
3 1 4	2.298	2.301	12.7
0 0 6	2.284	2.285	29.9
0 2 5	2.099	2.104	8.3
3 1 5	2.053	2.057	4.7
0 2 6	1.8720	1.8747	2.4
3 1 6	1.8388	1.8425	13.1
3 3 1	1.8354	1.8384	11.6
3 3 3	1.7164	1.7169	40.4
0 0 8	1.7132	1.7166	22.4
6 0 2	1.7048		
0 4 1	1.6220	1.6265	3.2
0 4 2	1.5889	1.5848	1.7
6 0 4	1.5656	1.5694	1.8

Table 47. Calculated and Observed X-ray Powder Diffraction Pattern of $K_2Hg_3Se_4$

H K L	d_{calc} (Å)	d_{obs} (Å)	I/I _{max} (obs.)
0 0 2	7.02	7.22	100
3 1 0	3.18	3.20	34.2
0 2 2	3.05	3.09	14.6
3 1 2	2.90	2.90	30.4
0 2 3	2.74	2.77	28.1
0 2 4	2.43	2.43	8.0
3 1 4	2.358	2.373	52.4
0 2 5	2.163	2.181	31.1
3 1 5	2.106	2.137	13.1
2 3 2	1.999	2.007	10.7
0 2 6	1.926	1.939	11.8
3 3 1	1.8981	1.914	28.6
3 1 6	1.8858		
3 3 3	1.7729	1.780	34.8
0 0 8	1.7552		
0 4 1	1.6835	1.687	5.0
0 4 2	1.6483	1.661	9.7
3 3 5 (6 2 1)	1.5825	1.590	13.1

Table 48. Calculated and Observed X-ray Powder Diffraction Pattern of $\text{Cs}_2\text{Hg}_3\text{Se}_4$

H K L	d_{calc} (Å)	d_{obs} (Å)	I/I _{max} (obs.)
0 0 2	7.38	7.51	78.9
0 0 4	3.69	3.72	94.2
3 1 0	3.41	3.44	36.7
2 1 3	3.28	3.31	100
3 1 2	3.09	3.12	46.6
4 0 0	3.01	3.03	18.4
0 2 2	2.96	2.98	56.7
3 1 4	2.50	2.52	37.4
2 1 5	2.453	2.469	31.2
0 2 4	2.432	2.445	29.3
4 2 0	2.203	2.215	14.2
3 1 6	1.996	2.004	21.1
0 2 6	1.958	1.967	49.0
6 0 2	1.9374	1.9396	11.6
4 0 6	1.9060	1.9093	16.5
0 0 8	1.8463	1.8541	77.9
6 1 3	1.7867	1.7934	10.9
3 1 8	1.6237	1.6284	10.5

Table 49. Calculated and Observed X-ray Powder Diffraction Pattern of $K_2Hg_6S_7$

H K L	d_{calc} (Å)	d_{obs} (Å)	I/I _{max} (obs.)
2 0 0	6.90	6.99	7.5
2 1 0	6.17	6.24	42.8
3 1 0	4.36	4.40	16.6
4 0 0	3.45	3.47	45.1
2 1 1	3.40	3.43	54.6
4 1 0	3.34	3.37	100
3 3 0	3.25	3.27	43.0
2 2 1	3.13	3.14	88.2
4 2 0	3.08	3.10	13.1
3 0 1	3.05	3.06	14.4
3 2 1	2.79	2.80	21.9
4 3 0	2.76	2.77	67.9
5 1 0	2.70	2.72	18.2
5 2 0	2.56	2.57	36.0
4 2 1	2.461	2.470	16.3
4 4 0	2.440	2.448	11.5
4 4 1	2.094	2.099	16.0
5 3 1	2.047	2.048	23.5
0 0 2	2.040	2.044	18.0
6 1 1	1.983	1.988	47.4
5 5 0	1.952	1.957	15.2
6 4 0	1.9144	1.9191	16.4
6 3 1	1.8374	1.8413	13.7
7 1 1 (5 5 1)	1.7610	1.7651	51.1
8 1 0	1.7123	1.7156	17.9
7 3 1	1.6565	1.6602	14.7
4 3 2	1.6407	1.6435	8.5
8 3 0	1.6157	1.6188	20.9
5 2 2	1.5962	1.5968	4.0

Table 50. Calculated and Observed X-ray Powder Diffraction Pattern of $\text{Cs}_2\text{Hg}_6\text{Se}_7$

H K L	d_{calc} (Å)	d_{obs} (Å)	I/I _{max} (obs.)
2 1 0	6.48	6.58	9.5
4 0 0	3.62	3.66	21.4
2 1 1	3.58	3.61	16.0
4 1 0	3.51	3.54	42.9
3 3 0	3.41	3.44	43.9
2 2 1	3.29	3.32	100
3 1 1	3.14	3.16	11.6
3 2 1	2.94	2.96	29.2
4 3 0	2.90	2.92	27.3
5 2 0	2.69	2.71	10.4
4 2 1	2.59	2.60	11.1
4 4 0	2.56	2.58	14.8
5 3 0	2.487	2.50	8.4
5 0 1 (4 3 1)	2.406	2.419	16.6
5 4 0	2.265	2.295	7.7
0 0 2	2.154	2.162	42.0
6 1 1	2.086	2.097	42.0
6 3 1	1.9325	1.9405	31.3
7 0 1	1.8673	1.8770	13.7
7 1 1 (5 5 1)	1.8520	1.8600	28.8
(4 0 2)			
6 4 1 (3 3 2)	1.8226	1.8426	21.1
8 1 0	1.7991	1.8081	23.9
7 3 1	1.7419	1.7492	7.7
4 3 2	1.7294	1.7358	11.1
8 3 0	1.6976	1.7048	13.4
5 2 2	1.6822	1.6899	7.9
5 3 2	1.6283	1.6345	10.6

The X-ray single crystal data of $K_2Hg_3S_4$, $Cs_2Hg_3Se_4$, $K_2Hg_6S_7$, and $Cs_2Hg_6Se_7$ were collected on a Nicolet P3 four-circle diffractometer with graphite monochromated Mo- K_α radiation using the θ - 2θ scan mode. The data for $K_2Hg_3Se_4$ were collected on an Enraf-Nonius CAD4 diffractometer with Mo- K_α radiation using the ω - 2θ scan mode by Dr. M. Sabat at Northwestern University. Accurate unit cell parameters for all compounds were obtained from the least-squares refinement on the 2θ , ω , χ , and ϕ values of several (20-25) machine-centered reflections. The stability of the experimental setup and crystal integrity were monitored by measuring three standard reflections periodically (every 100 reflections) during the data collection period. The data of (I) showed appreciable decay (34.3 % decay) due to decomposition of the crystal. The color of the crystal changed from yellow to light black during the data collection period. The data of (II), (III), (IV), and (V) did not show any appreciable decay. Two absorption corrections were applied to all data: an empirical absorption correction based on ψ scans for 3 reflections followed by a DIFABS⁵⁷ correction. The structures were solved with direct methods using SHELXS-86⁵⁸ and were refined with the SDP⁵⁹ package of crystallographic programs on a VAXstation 2000 computer. The effect of secondary extinction was considered in the least-square refinement as an additional parameter due to the heavy atomic constituents of the crystals. All atoms except the sulfur atoms in $K_2Hg_3S_4$ were refined anisotropically. Due to decomposition of the crystal during the data collection the sulfur atoms of $K_2Hg_3S_4$ could not be refined anisotropically. The complete data collection parameters and details of the structure solution and refinement for all compounds are given in Table 51. The final atomic coordinates, temperature factors and their estimated standard deviations are given in Tables 52-56.

Table 51. Summary of Crystallographic Data for $K_2Hg_3S_4$, $K_2Hg_3Se_4$, $Cs_2Hg_3Se_4$, $K_2Hg_6S_7$, and $Cs_2Hg_6Se_7$

	compound		
	I	II	III
Formula	$K_2Hg_3S_4$	$K_2Hg_3Se_4$	$Cs_2Hg_3Se_4$
Formula weight	808.23	995.81	1183.42
space group	Pbcn	Pbcn	Pbcn
<i>a</i> (Å)	10.561(5)	10.820(2)	12.047(4)
<i>b</i> (Å)	6.534(3)	6.783(1)	6.465(2)
<i>c</i> (Å)	13.706(2)	14.042(2)	14.771(6)
α (deg)	90.0	90.0	90.0
β (deg)	90.0	90.0	90.0
γ (deg)	90.0	90.0	90.0
Vol (Å ³), <i>Z</i>	945.8(7), 4	1030.6(5), 4	1150.4(7), 4
Temperature (°C)	23	-120	23
Crystal size (mm)	0.15x0.10x0.01	0.17x0.12x0.02	0.22x0.18x0.02
Radiation	Mo-K α	Mo-K α	Mo-K α
μ (Mo-K α , cm ⁻¹)	502.3	593.2	586.1
<i>D</i> _{calc} (g/cm ³)	5.68	6.42	6.83
$2\theta_{max}$ (deg)	50	50	48
Scan method	$\theta/2\theta$	$\theta/2\theta$	$\theta/2\theta$
No. of data collected	2829	1088	1058
No. of unique data	831	903	900
No. of data used ($F_o^2 > 3\sigma(F_o^2)$)	326	567	319
No. of atoms	5	5	5
No. of variables	33	43	43
Phasing technique	Direct methods	Direct methods	Direct methods
Final R/Rw	5.7/6.3	7.73/8.36	5.5/6.2
Max. shift/esd (last cycle)	0.00	0.00	0.00
Extinction coefficient	1.58×10^{-8}	2.06×10^{-8}	3.15×10^{-8}

Table 51. (cont'd)

	compound	
	IV	V
Formula	$K_2Hg_6S_7$	$Cs_2Hg_6Se_7$
Formula weight	1506.19	2022.07
space group	P-42 ₁ m	P4 ₂ nm
<i>a</i> (Å)	13.805(8)	14.505(7)
<i>b</i> (Å)	13.805(8)	14.505(7)
<i>c</i> (Å)	4.080(3)	4.308(2)
α (deg)	90.0	90.0
β (deg)	90.0	90.0
γ (deg)	90.0	90.0
Vol (Å ³), <i>Z</i>	778(1), 2	906(1), 2
Temperature (°C)	23	23
Crystal size (mm)	0.46x0.04x0.04	0.76x0.02x0.04
Radiation	Mo-K α	Mo-K α
μ (Mo-K α , cm ⁻¹)	604.2	684.7
<i>D</i> _{calc} (g/cm ³)	6.43	7.41
2 θ _{max} (deg)	50	44
Scan method	$\theta/2\theta$	$\theta/2\theta$
No. of data collected	1614	1440
No. of unique data	453	604
No. of data used ($F_o^2 > 3\sigma(F_o^2)$)	402	530
No. of atoms	6	6
No. of variables	42	41
Phasing technique	Direct methods	Direct methods
Final R/Rw	3.1/3.6	3.6/4.0
Max. shift/esd (last cycle)	0.00	0.00
Extinction coefficient	1.50×10^{-7}	1.11×10^{-7}

Table 52. Fractional Atomic Coordinates and B_{eq} Values for $\text{K}_2\text{Hg}_3\text{S}_4$ with Their Estimated Standard Deviations in Parentheses

Atom	x	y	z	B_{eq}^{a} , Å ²
Hg(1)	0.34148(9)	0.0852(3)	0.2582(1)	1.48(3)
Hg(2)	0	0.0837(5)	1/4	1.77(5)
K	0.3788(6)	0.766(3)	0.5018(8)	1.8(2)
S(1)	0.3674(7)	0.175(2)	0.6416(8)	0.8(2)*
S(2)	0.3710(7)	0.362(2)	0.3678(8)	1.1(2)*

^a B values for anisotropically refined atoms are given in the form of the isotropic equivalent displacement parameter defined as $B_{\text{eq}} = (4/3)[a^2B_{11} + b^2B_{22} + c^2B_{33} + ab(\cos \gamma)B_{12} + ac(\cos \beta)B_{13} + bc(\cos \alpha)B_{23}]$. Starred atoms were refined isotropically.

Table 53. Fractional Atomic Coordinates and B_{eq} Values for $\text{K}_2\text{Hg}_3\text{Se}_4$ with Their Estimated Standard Deviations in Parentheses

Atom	x	y	z	B_{eq}^{a} , Å ²
Hg(1)	0.3383(2)	0.0889(3)	0.2586(2)	2.74(4)
Hg(2)	0	0.0874(6)	1/4	2.77(6)
Se(1)	0.1338(5)	0.3239(9)	0.1382(4)	2.2(1)
Se(2)	0.3723(6)	0.3649(8)	0.3707(4)	2.3(1)
K	0.118(1)	0.270(2)	0.501(1)	2.6(2)

^a B values for anisotropically refined atoms are given in the form of the isotropic equivalent displacement parameter defined as $B_{\text{eq}} = (4/3)[a^2B_{11} + b^2B_{22} + c^2B_{33} + ab(\cos \gamma)B_{12} + ac(\cos \beta)B_{13} + bc(\cos \alpha)B_{23}]$.

Table 54. Fractional Atomic Coordinates and B_{eq} Values for $\text{Cs}_2\text{Hg}_3\text{Se}_4$ with Their Estimated Standard Deviations in Parentheses

Atom	x	y	z	B_{eq}^{a} , Å ²
Hg(1)	0.3309(2)	0.0051(6)	0.2416(3)	3.66(4)
Hg(2)	0	-0.0123(9)	1/4	3.40(6)
Cs	0.1203(3)	0.2656(4)	0.5105(3)	2.94(6)
Se(1)	0.1234(5)	0.2316(7)	0.1353(4)	2.5(1)
Se(2)	0.3604(4)	0.2918(7)	0.3541(5)	2.2(1)

^a B values for anisotropically refined atoms are given in the form of the isotropic equivalent displacement parameter defined as $B_{\text{eq}} = (4/3)[a^2B_{11} + b^2B_{22} + c^2B_{33} + ab(\cos \gamma)B_{12} + ac(\cos \beta)B_{13} + bc(\cos \alpha)B_{23}]$.

Table 55. Fractional Atomic Coordinates and B_{eq} Values for $\text{K}_2\text{Hg}_6\text{S}_7$ with Their Estimated Standard Deviations in Parentheses

Atom	x	y	z	B_{eq}^{a} , Å ²
Hg(1)	0.56782(6)	0.34115(7)	0.7608(4)	2.64(2)
Hg(2)	0.90144(6)	0.599	0.7238(4)	2.14(2)
K	0.6713(4)	0.829	0.764(3)	3.5(1)
S(1)	0.6965(4)	0.4650(4)	0.743(2)	1.8(1)
S(2)	0	1/2	0.061(4)	2.8(2)
S(3)	0.8139(4)	0.686	0.330(2)	2.0(1)

^a B values for anisotropically refined atoms are given in the form of the isotropic equivalent displacement parameter defined as $B_{\text{eq}} = (4/3)[a^2B_{11} + b^2B_{22} + c^2B_{33} + ab(\cos \gamma)B_{12} + ac(\cos \beta)B_{13} + bc(\cos \alpha)B_{23}]$.

Table 56. Fractional Atomic Coordinates and B_{eq} Values for $\text{Cs}_2\text{Hg}_6\text{Se}_7$ with Their Estimated Standard Deviations in Parentheses

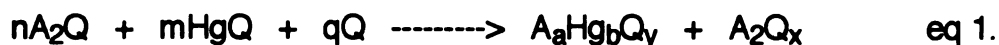
Atom	x	y	z	B_{eq}^{a} , Å ²
Hg(1)	0.07503(9)	0.3488(1)	0.058	2.71(2)
Hg(2)	0.10077(9)	0.101	0.4687(5)	2.42(2)
Cs	-0.1686(2)	0.169	0.063(1)	2.68(4)
Se(1)	0.0200(2)	0.6935(2)	0.556(1)	1.68(6)
Se(2)	1/2	1/2	0.285(2)	2.28(9)
Se(3)	0.3168(2)	0.683	0.548(1)	1.66(5)

^a B values for anisotropically refined atoms are given in the form of the isotropic equivalent displacement parameter defined as $B_{\text{eq}} = (4/3)[a^2B_{11} + b^2B_{22} + c^2B_{33} + ab(\cos \gamma)B_{12} + ac(\cos \beta)B_{13} + bc(\cos \alpha)B_{23}]$.

3. Results and Discussion

3.1. Synthesis

The synthesis of $K_2Hg_3S_4$, $K_2Hg_3Se_4$, $Cs_2Hg_3Se_4$, and $K_2Hg_6S_7$ has been readily accomplished at the intermediate temperature range (220~370 °C) using alkali metal polychalcogenide fluxes as solvent and reagents as shown in eq 1.



In eq 1 A represents an alkali metal (K or Cs) and Q a chalcogen atom (S or Se). Each mixture formed a complete melt at the temperature employed. After reaction, excess alkali metal polychalcogenide flux was easily removed from the product by washing with water or DMF. (I) and (II) are not stable in water and decompose rapidly in moist air and light to form black HgQ. Although (III), (IV), and (V) are relatively stable in the air and moisture for several days, (III) decomposes slowly to form black HgQ.

Preparation of $Cs_2Hg_6Se_7$ was unsuccessful in polychalcogenide flux (Cs_2Se_x). However, direct synthesis at 375 °C using stoichiometric amounts of Cs_2Se and HgSe in a 1:6 ratio yielded black crystals of $Cs_2Hg_6Se_7$ as shown in eq 2.



An attempt to synthesize $K_2Hg_6S_7$ by direct combinations of K_2S and HgS in a 1:6 ratio at 375 °C yielded only microcrystalline $K_2Hg_6S_7$.

In our initial investigations of the A/Hg/Q (A=alkali metal; Q=S, Se) systems, we used Hg metal as a reactant. However, elemental mercury did not react completely. A surface-only reaction cover the Hg bead with "crust" of product which prevented further reaction. When we substituted finely powdered HgQ for mercury metal we obtained more homogeneous mixing and complete reaction.

The compounds of $A_2Hg_3Q_4$ (A=K, Cs; Q=S, Se) were isolated in every reactant ratio from 2/1/8 to 5/1/8 ($A_2Q/HgQ/Q$). Among them, the 3/1/8 ratio for (I) and (II), and the 2/1/8 ratio for (III) gave better yield with larger single crystals suitable for a X-ray single crystal study. However, contamination of the HgQ phase seen in every reactant ratio could not be avoided even by changing the reaction temperatures from 220 °C to 350 °C. Use of higher temperatures gave more HgQ. The amount of HgQ impurity is estimated roughly to be 10 % in (I), 20 % in (II), and 10 % in (III).

During the preparation of $K_2Hg_3S_4$ we found a few black needle crystals of a new phase in the higher ratio of K_2S (4~5/1/8). This phase was found to be $K_2Hg_6S_7$ and was also observed in the preliminary reaction with mercury metal. Subsequently, $K_2Hg_6S_7$ was prepared at 370 °C in better yield and as large single crystals, up to 5 mm, by increasing the HgS ratio to 2/3.5/8. Even though $K_2Hg_3S_4$ formation could be completely suppressed using this reactant ratio, HgS was always present in small amounts. We were not successful in preparing the Se-analogue of $K_2Hg_6S_7$ either in K_2Se_x flux or by direct reaction of K_2Se with HgSe. This is probably because of the smaller size of the K^+ ions compared to enlarged size of Hg-Se tunnels created by the Se substitution. The size of the tunnel is too big for the smaller K^+ ions and requires larger cations such as Cs^+ ions. In fact, the Cs salt of Se-analogue, $Cs_2Hg_6Se_7$ was prepared from the direct synthetic method.

During this study we wondered why no polychalcogenide compounds were obtained. We do not have a clear answer to this, but it may be explained in terms of the comparable charges on Hg^{2+} ions and monochalcogenide Q^{2-} ions which would form more energetically favorable lattice. However, one possible approach to obtain polychalcogenide compounds could be to provide polychalcogenide fluxes with much longer chains in combination with lower reaction temperature. This could increase the concentration of polychalcogenide species vs monochalcogenide species in the flux and possibly force the reaction equilibrium towards formation of polychalcogenide compounds.

3.2. Description of Structures

3.2.1. Structure of $\text{K}_2\text{Hg}_3\text{S}_4$ (I), $\text{K}_2\text{Hg}_3\text{Se}_4$ (II), and $\text{Cs}_2\text{Hg}_3\text{Se}_4$ (III)

(I), (II), and (III) are isostructural. They possess centrosymmetric one-dimensional $[\text{Hg}_3\text{Q}_4]_n^{2n-}$ chains. Two views of the unit cell of $\text{A}_2\text{Hg}_3\text{Q}_4$ are shown in Figure 33. The $[\text{Hg}_3\text{Q}_4]_n^{2n-}$ chains run parallel to the crystallographic *b*-axis. The make-up of this chain can be regarded as a one-dimensional assembly of distorted tetrahedral $[\text{HgQ}_4]^{6-}$ building blocks connected by two-coordinate Hg^{2+} ions as shown in Figure 34. Alternatively, it can be viewed as a one-dimensional spiro-polymer of eight-membered Hg_4Q_4 rings. There are two crystallographically distinct Hg atoms in the asymmetric unit. The Hg(1) atom has linear geometry, while Hg(2) atom, situated on a crystallographic 2-fold axis, has distorted tetrahedral geometry. The angles of the linear Hg(1) atoms at 165.3(3), and 164.2(2), and 158.8(2) deg for (I), (II), and (III),

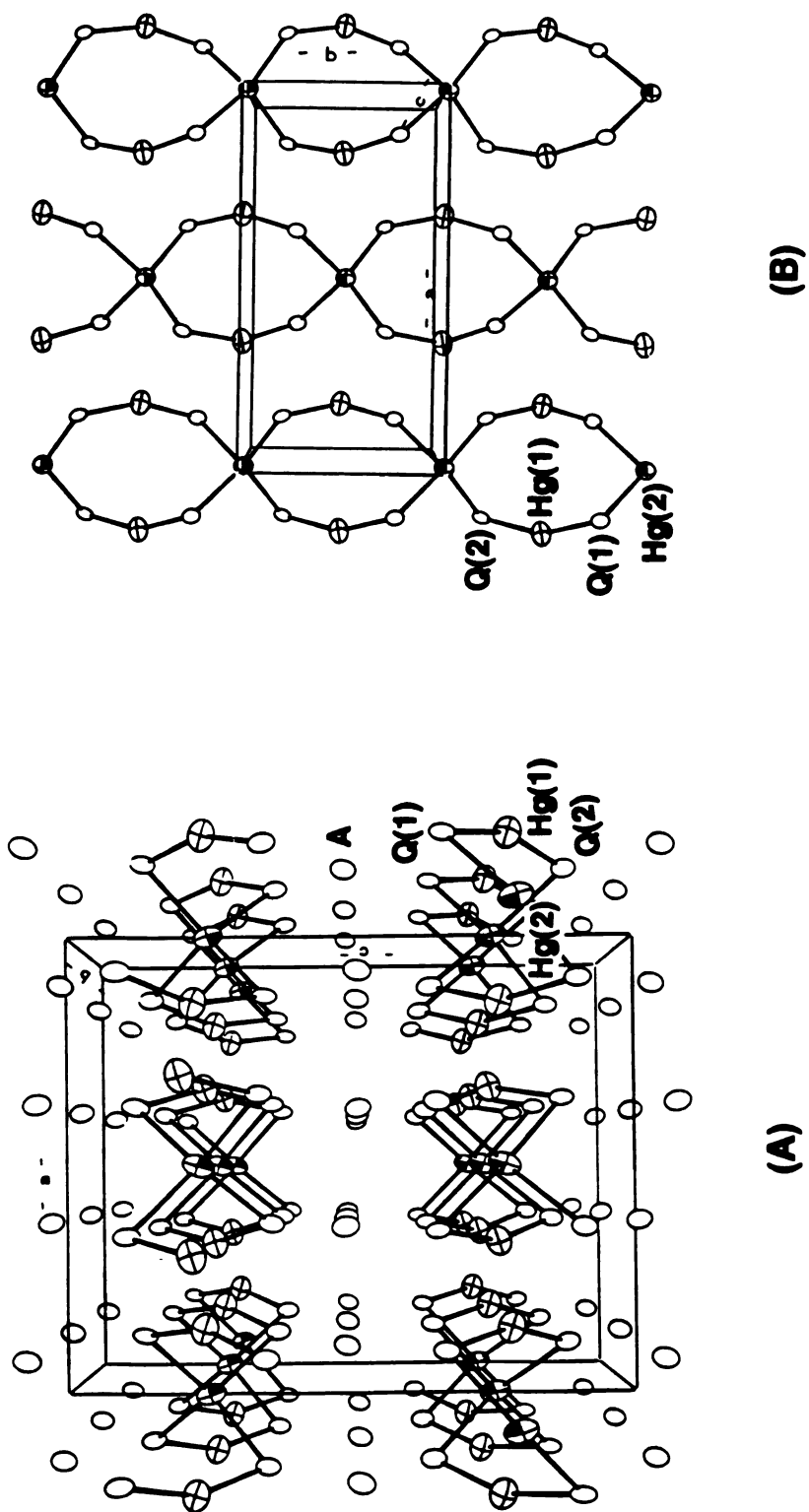


Figure 33. Two axial views of the unit cell of $A_2Hg_3Q_4$ ($A=K, Cs$; $Q=S, Se$):
 (A) b-axial view and (B) projection view along (001) plane.

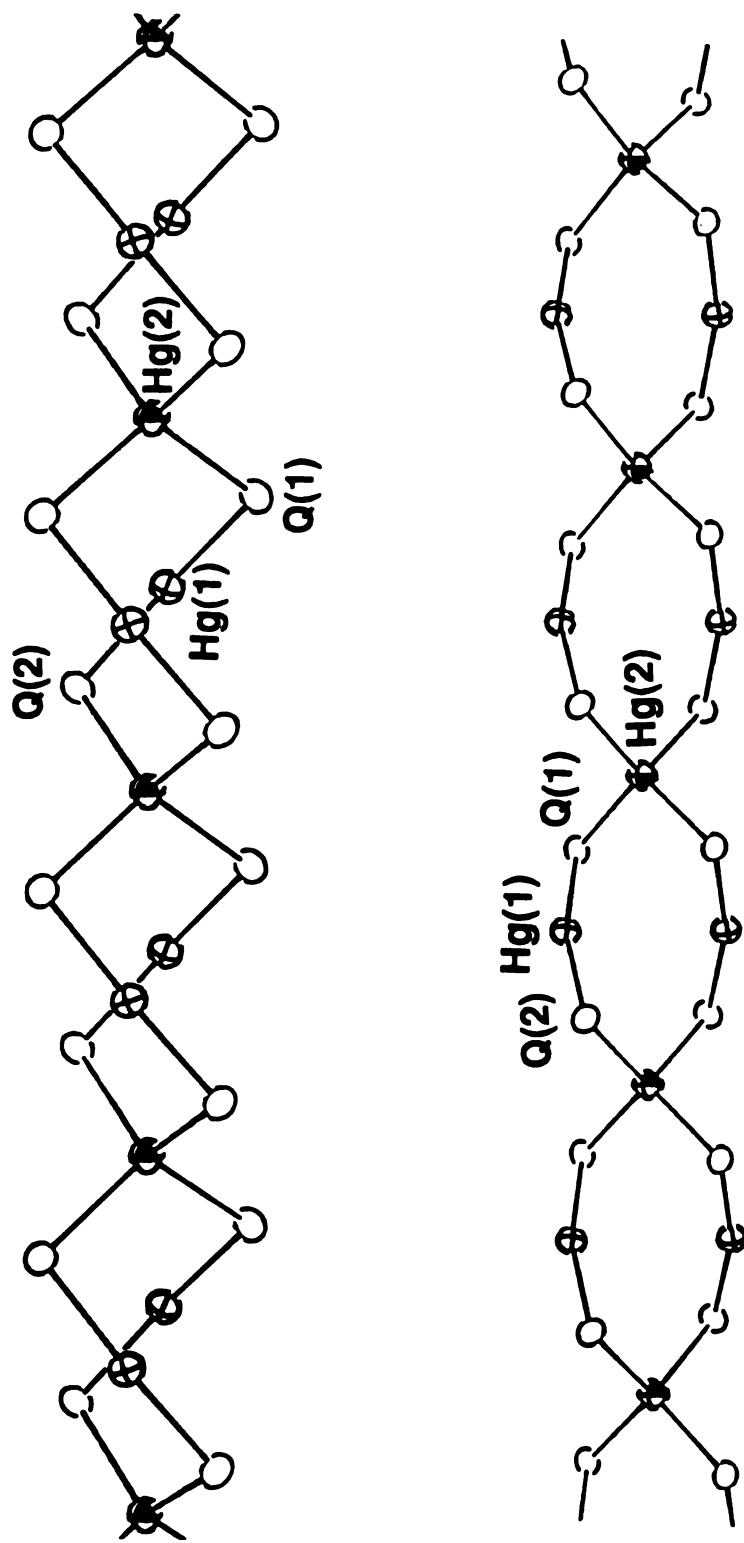


Figure 34. Two views of the one-dimensional structure of $[\text{Hg}_3\text{Q}_4]_n^{2n-}$ with labeling scheme.

respectively, are smaller than that found in the linear Hg atoms (172 deg) in HgS⁸⁹. These are due to the short Hg(1)-Q(2) contacts between the chains along (001) plane at 3.08 (1) Å, 3.159 (6) Å, and 3.158(6) Å for (I), (II), and (III), respectively. There are two sets of long and short Hg-Q bonds in this structure type associated with tetrahedral and quasi-linear Hg²⁺ centers. The average Hg-Q bond distances are (a) for quasi-linear Hg(1) atom: 2.37(1) Å, 2.48(1) Å, and 2.47(6) Å in (I), (II), and (III), respectively; (b) for tetrahedral Hg(2) atom: 2.57(1)Å, 2.66(1)Å, and 2.68(8)Å in (I), (II), and (III), respectively . Selected bond distances and angles are given in tables 57-59 for (I), (II), and (III) respectively. There is one crystallographically distinct alkali metal in the asymmetric unit of each compound. The charge balancing alkali metal cations, A⁺ ions (A=K, Cs) are distributed between the chains. They participate in ionic interactions with the chalcogenides. The K⁺ ions are surrounded by six chalcogen atoms in the range of 3.22(2)-3.35(1) Å and 3.30(2)-3.37(1) Å in (I) and (II) respectively, while Cs⁺ ions in (III) are surrounded by seven selenium atoms in the range of 3.596(7)-3.844(7) Å.

Table 57. Selected Bond Distances (Å) and Angles (deg) in K₂Hg₃S₄ with Standard Deviations in Parentheses

Hg(1)-S(1)	2.36(1)	S(1)-Hg(1)-S(2)	165.3(3)
Hg(1)-S(2)	2.38(1)	S(1)-Hg(2)-S(1)	104.7(3)
Hg(1)-S (mean)	2.37(1)	S(1)-Hg(2)-S(2)	105.7(3) (x2)
		S(1)-Hg(2)-S(2)	114.9(3) (x2)
Hg(2)-S(1)	2.58(1) (x2)	S(2)-Hg(2)-S(2)	111.0(4)
Hg(2)-S(2)	2.56(1) (x2)	Hg(1)-S(1)-Hg(2)	96.5(4)
Hg(1)-S (mean)	2.57(1)	Hg(1)-S(2)-Hg(2)	95.8(4)
Hg(1)-S(1)	3.08 (1)		
Hg(1)-S(1)	3.15 (2)		
K-S(1)	3.29(2)	K-S(2)	3.22(2)
K-S(1)	3.35(1)	K-S(2)	3.30(1)
K-S(1)	3.28(1)	K-S(2)	3.27(1)
K-S (mean)	3.29(4)		

Table 58. Selected Bond Distances (Å) and Angles (deg) in $K_2Hg_3Se_4$ with Standard Deviations in Parentheses

Hg(1)-Se(1)	2.486(6)	Se(1)-Hg(1)-Se(2)	164.2(2)
Hg(1)-Se(2)	2.473(6)	Se(1)-Hg(2)-Se(2)	115.7(2) (x2)
Hg(1)-Se (mean)	2.480(9)	Se(1)-Hg(2)-Se(2)	104.4(2) (x2)
		Se(2)-Hg(2)-Se(2)	110.7(2)
Hg(2)-Se(1)	2.671(6) (x2)	Se(1)-Hg(2)-Se(1)	106.2(2)
Hg(2)-Se(2)	2.657(6) (x2)	Hg(1)-Se(1)-Hg(2)	95.7(2)
Hg(2)-Se (mean)	2.664(8)	Hg(1)-Se(2)-Hg(2)	95.8(2)
Hg(1)-Se(1)	3.159(6)		
Hg(1)-Se(1)	3.210(6)		
K-Se(1)	3.37(1) (x3)	K-Se(2)	3.36(1)
K-Se(2)	3.30(2)	K-Se(2)	3.35(1)
K-Se (mean)	3.35(3)		

Table 59. Selected Bond Distances (Å) and Angles (deg) in Cs₂Hg₃Se₄ with Standard Deviations in Parentheses

Hg(1)-Se(1)	2.429(7)	Se(1)-Hg(1)-Se(2)	158.8(2)
Hg(1)-Se(2)	2.515(7)	Se(1)-Hg(2)-Se(1)	110.1(2)
Hg(1)-Se (mean)	2.47(6)	Se(1)-Hg(2)-Se(2)	105.3(2) (x2)
		Se(1)-Hg(2)-Se(2)	107.0(2) (x2)
Hg(2)-Se(1)	2.751(6) (x2)	Se(2)-Hg(2)-Se(2)	121.9(3)
Hg(2)-Se(2)	2.608(6) (x2)	Hg(1)-Se(1)-Hg(2)	98.2(2)
Hg(2)-Se (mean)	2.68(8)	Hg(1)-Se(2)-Hg(2)	93.5(2)
Hg(1)-Se(1)	3.158 (6)		
Hg(1)-Se(2)	3.295 (6)		
Cs-Se(1)	3.596 (7)	Cs-Se(2)	3.706 (5)
Cs-Se(1)	3.647 (7)	Cs-Se(2)	3.734 (7)
Cs-Se(1)	3.706 (6)	Cs-Se(2)	3.844 (7)
Cs-Se(1)	3.737 (6)	Cs-Se (mean)	3.66(16)

3.2.2. Structures of $\text{K}_2\text{Hg}_6\text{S}_7$ (IV) and $\text{Cs}_2\text{Hg}_6\text{Se}_7$ (V)

The structures of $\text{K}_2\text{Hg}_6\text{S}_7$ and $\text{Cs}_2\text{Hg}_6\text{Se}_7$ are unique and possess three-dimensional frameworks with one-dimensional tunnels. The stereoviews of the unit cells of (IV) and (V) are shown in Figures 35 and 36, respectively. They are composed of two crystallographically distinct linear and tetrahedral Hg^{2+} ions bridged by three crystallographically distinct Q^{2-} ions. Even though they crystallized with different space groups ($P-42_1m$ for (IV), $P4_2nm$ for (V)), the basic make-up of the three-dimensional framework of both compounds is the same. Every asymmetric atom has same point symmetry in both space group. Figure 37 shows the unit cells of (IV) and (V). The major difference between the two structures is the existing symmetry element, four-fold inversion axis (-4) in (IV) vs four-fold screw axis (4_2) in (V), at the center of the 8-membered empty channel.

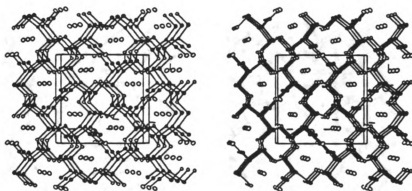


Figure 35. Stereoview of the unit cell of $K_2Hg_6S_7$.

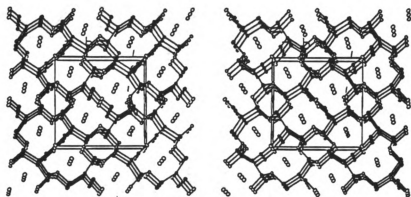


Figure 36. Stereoview of the unit cell of $\text{Cs}_2\text{Hg}_6\text{Se}_7$.

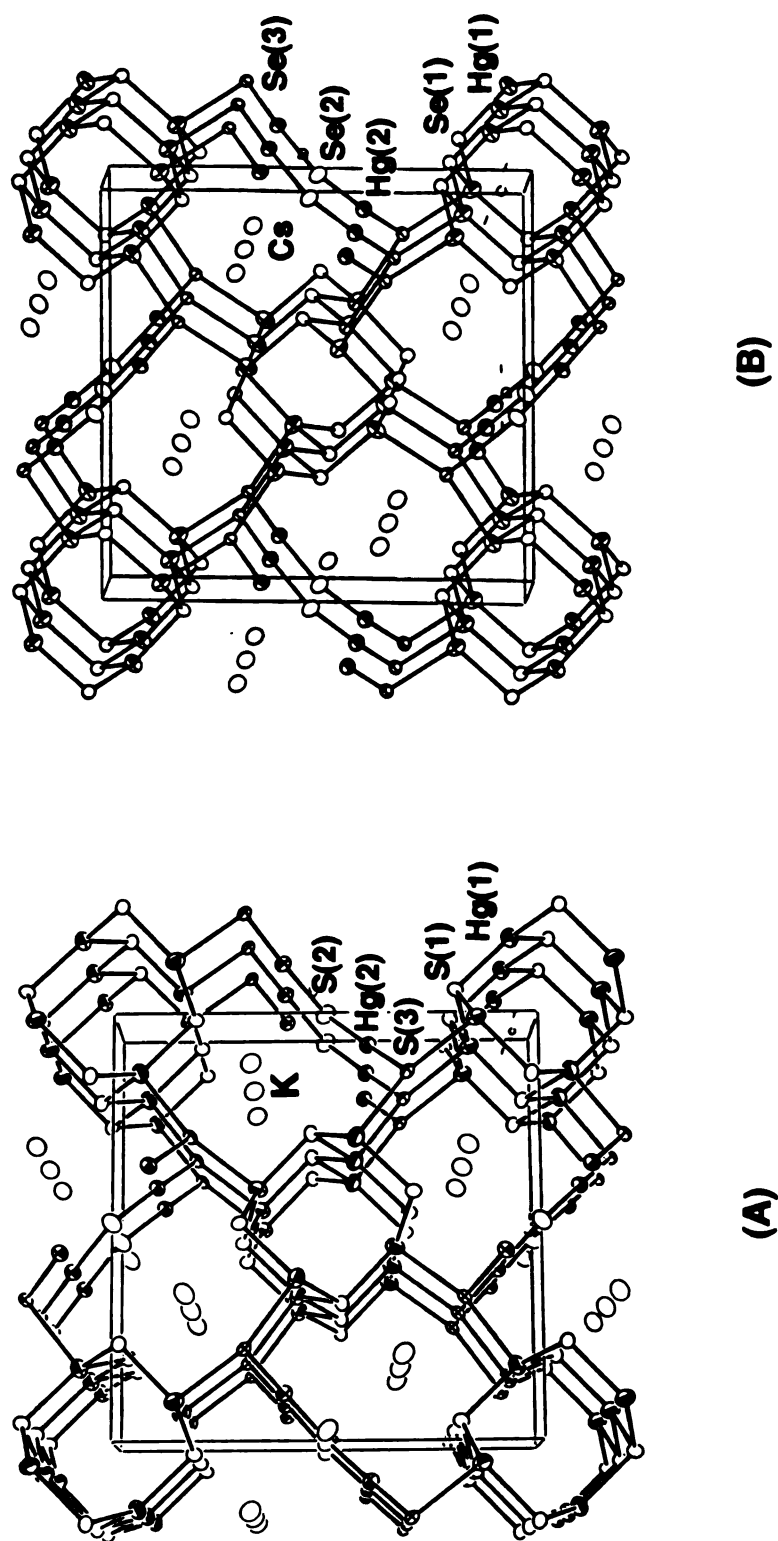
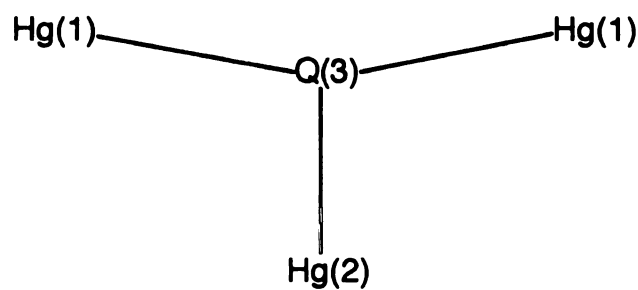


Figure 37. ORTEP representation of (A) the unit cell of $K_2Hg_6S_7$ and (B) the unit cell of $Cs_2Hg_6Se_7$. The origin of the unit cell of (B) has been moved to $(1/2, 0, 0)$ for clear comparison.

There are two sets of easily recognizable one-dimensional tunnels running parallel to the crystallographic *c*-axis. A set of empty, narrow tunnels with an octagonal cross section is composed of distorted tetrahedral Hg(1) and trigonal pyramidal Q(1) ions. The diameters of these tunnels are ca. 4.769(1) Å and 4.896(2) Å, corresponding to Hg(1)--Hg(1) distance, for (IV) and (V) respectively. A second set of "stuffed", wider tunnels has a 12-membered ring cross section in which both tetrahedral Hg(2) and linear Hg(1) atoms are held together by triply and doubly bridging Q²⁻ ions. The geometry of doubly bridging Q(2) and triply bridging Q(1) atoms are V-shaped and trigonal pyramidal, respectively. However, the other triply bridging Q(3) ion has an unusual T-type coordination as shown below:



A mirror plane passes through the Hg(2)-Q(3) bond, bisecting the Hg(1)-Q(3)-Hg(1) angle. In (IV) the S(3) atom is on the trigonal plane of the three Hg atoms, but in (V) Se(3) atoms are slightly displaced from the plane. This displacement imposes lower symmetry on the framework of (V). The Hg(1)-S(3)-Hg(1) and Hg(1)-S(3)-Hg(2) angles in (IV) are 158.1(3)° and 100.9(2)° respectively. The Hg(1)-Se(3)-Hg(1) and Hg(1)-Se(3)-Hg(2) angles in (V) are 156.2(1)° and 97.5(1)° respectively. The Hg(1)-Q(3) bonds are unusually long at 2.718(4) Å, and 2.879(2) Å in (IV) and (V), respectively, while the Hg(2)-Q(3) bonds are

normal (for two-coordinated Hg^{2+} ion) at 2.345(8) Å, and 2.477(5) Å for (IV) and (V), respectively. As a result, there are two kinds of Hg-Q bond distances associated with tetrahedral or linear coordination. The average Hg-Q bond distances of tetrahedral Hg(1) centers are long at 2.57 (10) Å and 2.67 (13) Å and those of linear Hg(2) centers are short at 2.36 (1) Å and 2.477(1) Å in (IV) and (V) respectively. These are similar to those observed in (I), (II), and (III). The angles of linear Hg(2) atom in (IV) and (V) are 172.4(4)°, and 166.4(2)° respectively. Selected bond distances and angles are given in Tables 60 and 61 for (IV) and (V), respectively. There is one crystallographically distinct alkali metal in the asymmetric units of (IV) and (V). The alkali ions (K^+ , Cs^+) are found inserted in the center of the large 12-membered tunnels, interacting with the chalcogenide lone pairs of electrons that are directed toward the tunnel center. The alkali ions are surrounded by seven chalcogen atoms in the range of 3.30(1)-3.62(1) Å for K^+ in (IV) and 3.626(4)-3.764(5) Å for Cs^+ in (V).

Table 60. Selected Bond Distances (Å) and Angles (deg) in K₂Hg₆S₇ with Standard Deviations in Parentheses

Hg(1)-S(1)	2.467(5)	S(1)-Hg(1)-S(1)	121.2(2)
Hg(1)-S(1)	2.552(8)	S(1)-Hg(1)-S(1)	124.8(3)
Hg(1)-S(1)	2.527(8)	S(1)-Hg(1)-S(1)	106.9(2)
Hg(1)-S(3)	2.718(4)	S(1)-Hg(1)-S(3)	96.3(2)
Hg(1)-S (mean)	2.57(11)	S(1)-Hg(1)-S(3)	93.7(2)
		S(1)-Hg(1)-S(3)	106.5(2)
Hg(2)-S(2)	2.366(9)	S(2)-Hg(2)-S(3)	172.4(4)
Hg(2)-S(3)	2.345(8)	Hg(1)-S(1)-Hg(1)	105.2(2)
Hg(2)-S (mean)	2.36(15)	Hg(1)-S(1)-Hg(1)	106.9(2)
		Hg(1)-S(1)-Hg(1)	102.6(3)
		Hg(2)-S(2)-Hg(2)	108.8(6)
		Hg(1)-S(3)-Hg(1)	158.1(3)
		Hg(1)-S(3)-Hg(2)	100.9(2) (x2)
K-S(1)	3.34(1) (x2)	K-S(3)	3.30(1)
K-S(1)	3.30(1) (x2)	K-S(3)	3.62(1)
K-S(2)	3.420(6)	K-S (mean)	3.39(12)

Table 61. Selected Bond Distances (Å) and Angles (deg) in Cs₂Hg₆Se₇ with Standard Deviations in Parentheses

Hg(1)-Se(1)	2.637(4)	Se(1)-Hg(1)-Se(1)	121.3(1)
Hg(1)-Se(1)	2.622(4)	Se(1)-Hg(1)-Se(1)	121.9(1)
Hg(1)-Se(1)	2.564(3)	Se(1)-Hg(1)-Se(1)	110.0(1)
Hg(1)-Se(3)	2.870(2)	Se(1)-Hg(1)-Se(3)	94.5(1)
Hg(1)-Se (mean)	2.67(13)	Se(1)-Hg(1)-Se(3)	95.9(1)
		Se(1)-Hg(1)-Se(3)	104.8(1)
Hg(2)-Se(2)	2.476(4)	Se(2)-Hg(2)-Se(3)	166.4(2)
Hg(2)-Se(3)	2.477(5)	Hg(1)-Se(1)-Hg(1)	110.0(1)
Hg(2)-Se (mean)	2.477(1)	Hg(1)-Se(1)-Hg(1)	103.7(1)
		Hg(1)-Se(1)-Hg(1)	103.2(1)
		Hg(2)-Se(2)-Hg(2)	113.2(3)
		Hg(1)-Se(3)-Hg(1)	156.2(1)
		Hg(1)-Se(3)-Hg(2)	97.5(1) (x2)
Cs-Se(1)	3.664 (4) (x2)	Cs-Se(3)	3.764 (5)
Cs-Se(1)	3.626 (4) (x2)	Cs-Se(3)	3.690 (5)
Cs-Se(2)	3.660 (3)	Cs-Se (mean)	3.67(5)

3.3. Structure

The compounds prepared in ternary A/Hg/Q systems (A= K, Cs; Q=S, Se) , $A_2Hg_3Q_4$ and $A_2Hg_6Q_7$ can be regarded as members of a new general family with the chemical formula $(A_2Q)_n(HgQ)_m$ ($n=1, m=3$ in (I), (II), and (III); $n=1, m=6$ in (IV) and (V)). These structures can be viewed as deriving from the successive dismantling of the three-dimensional zinc-blende structure of HgQ (Q=S, Se) by the various amounts of added A_2Q . The three-dimensional zinc-blende structure (see Figure 1) of HgQ contains tetrahedral Hg^{2+} centers and tetrahedral μ_4-Q^{2-} atoms with Hg-Q bond distances at 2.53 Å and 2.63 Å in HgS^{89} and $HgSe^{90}$, respectively. This three-dimensional framework of HgQ is broken up as it tries to accommodate added A_2Q . The μ_4 -coordination of Q^{2-} atoms is reduced to μ_3 - and μ_2 -coordination in $[Hg_6Q_7]_n^{2n-}$ and to only μ_2 -coordination in $[Hg_3Q_4]_n^{2n-}$. Another phase that also belongs to this homologous family is $A_6HgQ_4^{88}$, $(A_2Q)_3(HgQ)_1$, which features discrete tetrahedral $[HgQ_4]^{6-}$ units. This compound can be considered as a complete breakup of the three dimensional framework of HgQ into individual $[HgQ_4]^{6-}$ units. This is very similar to the successive breakup of the structures of the main group elements (e.g., Si, P) that ensues upon reduction with electro-positive metals to form the familiar Zintl phases⁹¹. Recently some more examples of successive dismantling of the three-dimensional zinc-blende framework of CdS has been discovered in our group⁹². The compounds $K_2Cd_2S_3$ and $K_2Cd_3S_4$, which feature tetrahedral $[CdS_4]^{6-}$ units and μ_3 - and μ_2 -coordination of S^{2-} , make the whole new family of $(K_2S)_n(CdS)_m$ ($n=1, m=2$ and $n=1, m=3$ respectively). They are reminiscent of what we have seen in the A/Hg/Q system. However, isostructural compounds in both systems are not yet available even though the stoichiometry of the formula unit of $K_2Cd_3S_4$ is the same as that of

$A_2Hg_3Q_4$. This is probably because the Hg^{2+} atoms can afford two favorable coordination environments (linear and tetrahedral) while Cd^{2+} can afford only one favorable tetrahedral environment. In fact, the compound $K_2Cd_3S_4$ shows the structural similarity to $A_2Hg_3Q_4$. In $K_2Cd_3S_4$, the tetrahedral Cd^{2+} atoms occupying the linear Hg^{2+} site of the $[Hg_3Q_4]_n^{2n-}$ chain extend its linear coordination into tetrahedral coordination through an interchain Cd-S bond, producing a two-dimensional layer.

Based on the +2 formal charges on Hg atoms, and assuming -2 formal charges on sulfide atoms, all compounds are expected to have a completely filled valence band due to the d^{10} electronic configuration of Hg^{2+} and should exhibit semiconducting behavior. Among them, three-dimensional compounds $K_2Hg_6S_7$ and $Cs_2Hg_6Se_7$ are expected to have smaller band gaps than the one-dimensional compounds of (I), (II), and (III) because its three-dimensional characteristics increases overlap of the band orbitals. We tried to measure the band gaps of (IV) and (V) using FT-IR spectroscopy in the mid- and near-IR region. However, in preliminary measurements we did not observe any spectral absorptions in those regions. Work to study their charge transport properties is in progress.

This study in the $A/Hg/Q$ systems showed that the three-dimensional structure of HgQ is tractable and can accommodate various amounts of alkali metal monochalcogenides. It is likely that the A_2Q/HgQ system constitutes an infinitely adaptive pair similar to the $(ZnS)_n(In_2S_3)_m$ ⁹³ and $(BaS)_n(FeS)_m$ ⁹⁴ systems. Work to identify other members of this family is in progress.

CHAPTER 5

Synthesis and Characterization of Layered Compounds of $K_2Cu_5Te_5$ and $NaCuTe$

1. Introduction

Since the discovery of high temperature superconductivity, mixed-valence Cu compounds have received considerable attention in the hope of discovering related materials with even higher transition temperatures. Although mixed-valence solid Cu-chalcogenide compounds have been known for some time, they remain relatively rare. For example, the only mixed-valence compounds known so far are $Na_3Cu_4S_4$ ⁶³, ACu_4Q_3 (A=K, Rb, Cs, Tl; Q=S, Se)⁶¹, $A_3Cu_8S_6$ (A=K, Rb)⁷¹, $A_3Cu_8Se_6$ (A=Rb, Cs)⁹⁵, $Cs_2Cu_5Se_4$ ⁹⁶, $TlCu_2Q_2$ (Q=S, Se)⁹⁷, $TlCu_6S_4$ ⁹⁸, and $Tl_5Cu_{14}Se_{10}$ ⁹⁹. Even though the *a-priori* design of a high- T_c superconducting material is not yet possible, it is still worthwhile to pursue the synthesis of mixed valence Cu compounds since such electronic features generally play an important role for high electrical conductivity. Furthermore, compared to ternary sulfides and selenides, tellurides are even more rare.^{6,7,79(d),100} To the best of our knowledge, there are only four known phases $NaCu_3Te_2$ ¹⁰¹, KCu_3Te_2 ¹⁰², and $ACuTe$ (A=Na, K)⁷⁴ in the ternary A/Cu/Te (A=alkali metal) systems, none of which have a mixed Cu oxidation state. With this rationale in mind, we decided to use the now

proven polychalcogenide flux method⁵⁰⁻⁵⁴ to explore new such compounds. In our hands, this synthetic method has been quite successful in preparing novel structural types of (poly)sulfides and (poly)selenides of various transition-metals.^{50,53,54} (see previous chapters) Thus, we extended it to the telluride systems where we were able to synthesize the layered materials, $K_2Cu_5Te_5$ and $NaCuTe$. The first is a novel mixed-valence Cu/Te compound which possesses high metallic conductivity. The latter has been synthesized earlier at 800 °C by direct combination of the elements.⁷⁴ Here we demonstrate a more convenient lower temperature synthetic method and its accurate crystal structure.

2. Experimental Section

2.1 Reagents

Chemicals in this work were used as obtained: copper powder, -325 mesh, 99.95% purity, Cerac, Milwaukee, WI; tellurium powder, -100 mesh, 99.95% purity, Aldrich Chemical Co., Milwaukee, WI; potassium and sodium metal, analytical reagent, Mallinckrodt Inc., Paris, KY.

2.2. Physical Measurements

Magnetic susceptibility measurements in the temperature range from 2 K to 300 K at 5 kG were performed on a MPMS Quantum Design SQUID magnetometer. Single crystals of $K_2Cu_5Te_5$ were manually selected for measurements. They were used without grinding as random oriented single crystals. The data were corrected for diamagnetic contributions of the sample

holder. To obtain molar susceptibility the corrections for ion-core diamagnetic contributions from atomic constituents were made using the values tabulated by Mulay¹⁰³. The magnetization of $K_2Cu_5Te_5$ was examined at 5 K as a function of applied field from 250 G to 7 kG and was found to vary linearly with the applied field.

Four-probe dc resistivity and thermoelectric power data for $K_2Cu_5Te_5$ were provided by Prof. Carl C. Kanneurf (Northwestern University) over the temperature range 5 K to 300 K. A computer automated measurement system was employed to obtain thermopower and resistivity data with both the current and thermal gradient applied along the needle axis. For all measurements electrode connections to the small single crystals were made with the use of 25 and 60 μm gold wires and gold bonding paste.

Quantitative microprobe analysis of the compounds were performed on a Jeol 35CF scanning electron microscope equipped with Tracor Northern TN 5500 X-ray microanalysis attachment. Single crystals of each sample were carefully picked and mounted on an aluminum stub using conducting silver paint to help dissipate charges that developed on the sample surface during measurements. Energy Dispersive Spectra (EDS) were obtained using the following experimental set-up:

X-ray detector position : 55 mm

Working distance : 39 mm

Accelerating voltage : 20 KV

Take-off angle : 27 deg

Beam current : 200 picoamps

Accumulation time : 100 seconds

Window : Be

A standardless quantitative analysis (SQ) program was used to analyze the X-ray spectra obtained. Since the Cu ratio is always overestimated due to the contribution of system Cu peaks, a correction factor ($\times 0.73$), which was determined by calibrating with known K/Cu/Te compounds, was used to evaluate the Cu percentage.

2.3. Synthesis

Chemicals were measured and loaded in Pyrex tubes under a dry nitrogen atmosphere in a Vacuum Atmospheres Dri-Lab glovebox. Potassium monotelluride (K_2Te) and sodium monotelluride (Na_2Te) were prepared in liquid ammonia from alkali metal and elemental tellurium in a 2:1 ratio.

Dipotassium (μ_8 -ditelluro)tris(μ_4 -telluro)pentacuprate(I,II), $K_2Cu_5Te_5$ (I) 0.309 g (1.5 mmol) of K_2Te , 0.032 g (0.5 mmol) of Cu and 0.508 g (4.0 mmol) of Te were mixed together and loaded in a Pyrex tube which was flame-sealed under vacuum ($\sim 10^{-3}$ torr). The tube was placed in a computer-controlled furnace and heated at 350 °C for 3 days and cooled slowly to 50 °C at a rate of 2 °C/hr. Black parallelepiped crystals were obtained by removing excess molten potassium polytellurides (K_2Te_x) with dimethylformamide (DMF) under a N_2 atmosphere (yield: 77 % based on the Cu metal used). A quantitative microprobe analysis performed on a large number of crystals with the EDS/SEM system gave an average composition of $KCu_{2.4}Te_{2.6}$.

Sodium (μ_4 -telluro)cuprate(I), $NaCuTe$ (II) 0.434 g (2.5 mmol) of Na_2Te , 0.032 g (0.5 mmol) of Cu and 0.508 g (4.0 mmol) of Te were mixed together and loaded in a Pyrex tube which was flame-sealed under vacuum

($\sim 10^{-3}$ torr). The tube was placed in a computer-controlled furnace and heated at 400 °C for 5 days and slowly cooled to 260 °C at a rate of 2 °C/hr, then to 140 °C at a rate 3 °/hr, and to 50 °C at a rate of 10 °C/hr. Black plate-like crystals were obtained by removing excess molten potassium polytellurides (Na_2Te_x) with DMF under a N_2 atmosphere (yield: 43 % based on the Cu metal used). A quantitative microprobe analysis performed on a large number of crystals with the EDS/SEM system gave an average composition of $\text{Na}_{1.0}\text{Cu}_{1.0}\text{Te}_{1.1}$.

2.4. X-ray Crystallographic Studies

Each compound was examined by X-ray powder diffraction for the purpose of phase characterization and identification. The d-spacings for each compound were obtained from the powder pattern recorded on a Phillips XRG-3000 computer-controlled powder diffractometer, operating at 40KV, 35 mA. Graphite monochromated Cu radiation was used. To verify product homogeneity, the d-spacings observed for the bulk materials were compared, and found to be in accord, with those calculated from the single crystal X-ray structure analysis data. The calculation of d-spacings was performed using the POWD10 program⁵⁶. The results are summarized in Tables 62 and 63.

Table 62. Calculated and Observed X-ray Powder Diffraction Pattern of $K_2Cu_5Te_5$

H K L	d_{calc} (Å)	d_{obs} (Å)	I/I _{max} (obs.)
0 2 0	8.00	8.06	44.9
0 2 1	7.35	7.41	7.5
0 0 4	4.63	4.67	8.1
1 1 0	4.00	4.02	22.5
1 1 1	3.90	3.93	15.3
0 4 2	3.67	3.71	8.1
0 2 5	3.36	3.38	56.0
1 3 0	3.27	3.27	44.2
1 3 1	3.22	3.23	31.8
0 0 6	3.09	3.10	17.6
0 4 4 (1 1 4)	3.03	3.04	46.4
0 2 6	2.88	2.89	24.2
1 3 4	2.67	2.68	16.2
1 3 5	2.45	2.450	32.5
1 5 2	2.440		
1 5 3	2.341	2.350	15.3
1 3 6	2.244	2.251	34.4
1 5 4	2.220	2.228	44.2
2 0 0	2.065	2.069	26.9
2 2 0 (0 2 9)	2.000	2.000	33.7
1 7 2	1.955	1.962	100
1 5 7	1.8291	1.8346	26.9
2 2 5	1.7597	1.7635	14.4
1 5 8	1.7085	1.7095	16.1
2 4 4	1.7060	1.6967	6.6
1 7 7	1.5959	1.6007	10.5
1 9 3	1.5790	1.5800	9.4

Table 63. Calculated and Observed X-ray Powder Diffraction Pattern of NaCuTe

H K L	d_{calc} (Å)	d_{obs} (Å)	I/I _{max} (obs.)
0 0 1	7.13	7.03	54.7
1 0 1	3.73	3.73	100
0 0 2	3.56	3.56	41.4
1 0 2	2.76	2.76	22.9
1 1 2	2.341	2.333	72.1
2 0 0	2.195		
1 0 3	2.090	2.086	65.3
1 1 3	1.8874	1.8887	45.0
0 0 4	1.7827	1.7810	79.2
1 0 4	1.6518	1.6502	39.7

The X-ray single crystal data of $\text{K}_2\text{Cu}_5\text{Te}_5$ and NaCuTe were collected on a Rigaku AFC6S diffractometer with graphite monochromated Mo-K_α radiation using the ω - 2θ scan mode. Accurate unit cell parameters for all compounds were obtained from the least-squares refinement of the 2θ , ω , χ , and ϕ values of 20-25 machine-centered reflections. The stability of the experimental setup and crystal integrity were monitored by measuring three standard reflections periodically (every 100 reflections) during data collection. The intensities did not show any appreciable decay. Two absorption corrections were applied to the data of $\text{K}_2\text{Cu}_5\text{Te}_5$ and NaCuTe : an empirical absorption correction based on ψ scans for 3 reflections followed by a DIFABS⁵⁷ correction. The structures of both compounds were solved with direct methods using SHELXS-86⁵⁸ and were refined with the TEXSAN⁶⁰ package of crystallographic programs. All calculations were performed on a VAXstation 3100 computer. All atoms were refined anisotropically. The complete data collection parameters and details of the structure solution and refinement for (I) and (II) are given in Table 64. The final atomic coordinates, temperature factors and their estimated standard deviations are given in Tables 65 and 66.

Table 64. Summary of Crystallographic Data for $K_2Cu_5Te_5$ and $NaCuTe$

	compound	
	I	II
Formula	$K_2Cu_5Te_5$	$NaCuTe$
Formula weight	1033.93	214.14
space group	Cmcm	P4/nmm (2nd. setting)
a (Å)	4.130(3)	4.3913(9)
b (Å)	16.004(2)	4.3913(9)
c (Å)	18.533(3)	7.131(2)
α (deg)	90.0	90.0
β (deg)	90.0	90.0
γ (deg)	90.0	90.0
Vol (Å ³), Z	1225.0(9), 4	137.5(1), 2
Temperature (°C)	23	23
Crystal size (mm)	0.70x0.13x0.10	0.39x0.13x0.03
Radiation	Mo-K α	Mo-K α
μ (Mo-K α , cm ⁻¹)	209.2	181.9
D_{calc} (g/cm ³)	5.61	5.17
$2\theta_{max}$ (deg)	50	60
Scan method	$\omega/2\theta$	$\omega/2\theta$
No. of data collected	2238	495
No. of unique data	663	154
No. of data used ($F_o^2 > 3\sigma(F_o^2)$)	569	134
No. of atoms	7	3
No. of variables	40	9
Phasing technique	Direct methods	Direct methods
Final R/R_w	2.5/3.4	2.8/3.4
Max. shift/esd (last cycle)	0.00	0.00
Extinction coefficient	6.43×10^{-7}	N/A

Table 65. Fractional Atomic Coordinates and B_{eq} Values for $\text{K}_2\text{Cu}_5\text{Te}_5$ with Their Estimated Standard Deviations in Parentheses

Atom	x	y	z	B_{eq}^{a} , Å ²
Te(1)	0	0.12811(3)	0.51974(4)	1.30(3)
Te(2)	1/2	0.30524(3)	0.67015(4)	1.44(3)
Te(3)	0	0.07738(5)	3/4	1.32(4)
Cu(1)	0	0.19941(7)	0.64842(8)	1.96(6)
Cu(2)	0	0.27787(7)	0.46035(8)	2.26(6)
Cu(3)	1/2	0.1698(1)	3/4	1.80(7)
K(1)	1/2	-0.0186(1)	0.6172(1)	2.2(1)

^a B values for anisotropically refined atoms are given in the form of the isotropic equivalent displacement parameter defined as $B_{\text{eq}} = (4/3)[a^2B_{11} + b^2B_{22} + c^2B_{33} + ab(\cos \gamma)B_{12} + ac(\cos \beta)B_{13} + bc(\cos \alpha)B_{23}]$.

Table 66. Fractional Atomic Coordinates and B_{eq} Values for NaCuTe with Their Estimated Standard Deviations in Parentheses

Atom	x	y	z	B_{eq}^{a} , Å ²
Te	1/4	1/4	0.7224(1)	1.24(2)
Cu	-1/4	1/4	1/2	2.46(4)
Na	1/4	1/4	1.172(1)	1.9(1)

^a B values for anisotropically refined atoms are given in the form of the isotropic equivalent displacement parameter defined as $B_{\text{eq}} = (4/3)[a^2B_{11} + b^2B_{22} + c^2B_{33} + ab(\cos \gamma)B_{12} + ac(\cos \beta)B_{13} + bc(\cos \alpha)B_{23}]$.

3. Results and Discussion

3.1. Synthesis

The synthesis of two novel layer compounds of $K_2Cu_5Te_5$ and $NaCuTe$ has been achieved using polytelluride fluxes as solvents and reagents at 300-400 °C as shown in eq 1.



where A is K or Na metal and n is 3 or 5, respectively. They form complete melts at the temperature employed (350 °C for (I) and 450 °C for (II)). The equation given above is not balanced and only shows the reactants used (left-hand side) and product obtained (right-hand side). After reaction, excess polytelluride flux was removed from the product with extra caution by washing with degassed DMF. During washing, we have often seen decomposition of the polytelluride flux into elemental tellurium in the presence of oxygen or water. Therefore, isolation has to be done carefully under an inert atmosphere using degassed DMF. Both compounds are stable in the air and moisture for several days.

The preparation of $K_2Cu_5Te_5$ and $NaCuTe$ was carried on without difficulty. They were readily obtained from the K_2Te_x and Na_2Te_x fluxes as pure phases. However, $K_2Cu_5Te_5$ caused some difficulties in obtaining pure another ternary K/Cu/Te compound, $K_4Cu_8Te_{11}$ (see the synthesis section in chapter 6 for detail), since the former was a competing phase in the preparation of the latter. When we used a polytelluride flux with shorter chains (e.g. K_2Te_3) the known compound, KCu_3Te_2 ¹⁰² was obtained at 350 °C. The $NaCuTe$

phase, which had been prepared at 800 °C by direct combination of the elements⁷⁴, was isolated with every reactant ratio Na₂Te/Cu/Te of 1/1/8 to 5/1/8 at lower temperature (400 °C). Among them, higher Na₂Te ratio of 5/1/8 gave better yield and crystallinity. The rest of the ratios showed relatively poor crystallinity and had elemental tellurium as coexisting phase.

3.2. Description of Structures

3.2.1. Structure of K₂Cu₅Te₅ (I)

The structure of K₂Cu₅Te₅ is anisotropic and is shown in Figure 38. Anionic [Cu₅Te₅]_n²ⁿ⁻ corrugated layers alternate with charge compensating K⁺ ions. The [Cu₅Te₅]_n²ⁿ⁻ layers are formed by edge-sharing (fused) rhombic [Cu₂Te₂] units to form a *distorted* anti-PbO like structure as shown in Figure 39. The structure of K₂Cu₅Te₅ can be viewed as deriving from the anti-PbO like structure of CuTe¹⁰⁴ into which K⁺ ions are reductively inserted. The two-dimensional layered structure of CuTe is shown in Figure 40. It contains unusual infinite straight Te chains along the *a*-axis with a Te-Te bond distance of 3.10 Å. In this structure Cu atoms occupy the O sites and Te occupy the Pb sites of the PbO structure. Based on the formula K₂Cu₅Te₅ and on the assumption that the oxidation state on each Te atom is -2, the formal oxidation state on copper is +1 (two atoms) and +2 (three atoms). However, the coexistence of Cu²⁺ and Te²⁻ is thermodynamically unstable with respect to electron transfer from the reducing Te²⁻ to the oxidizing Cu²⁺. If one then considers all copper atoms in the +1 oxidation state, it follows that the average oxidation state of Te is -1.4. This electron deficiency (holes) on Te can be either delocalized in the valence band or localized as ditelluride via a structural distortion or both. This situation is reminiscent of that found in CuS⁶², a known

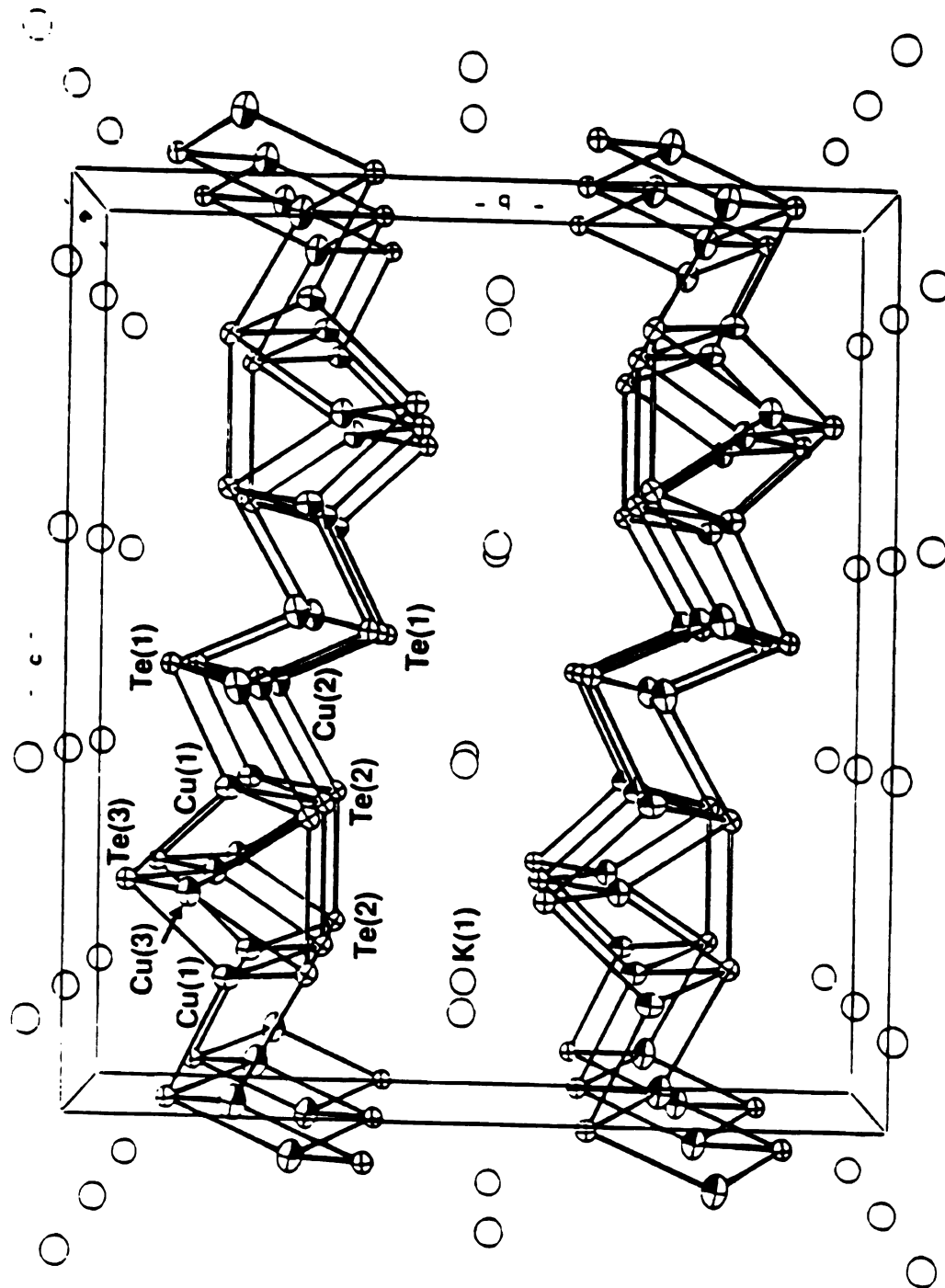


Figure 38. ORTEP representation and labeling scheme of the unit cell of $K_2Cu_5Te_5$.

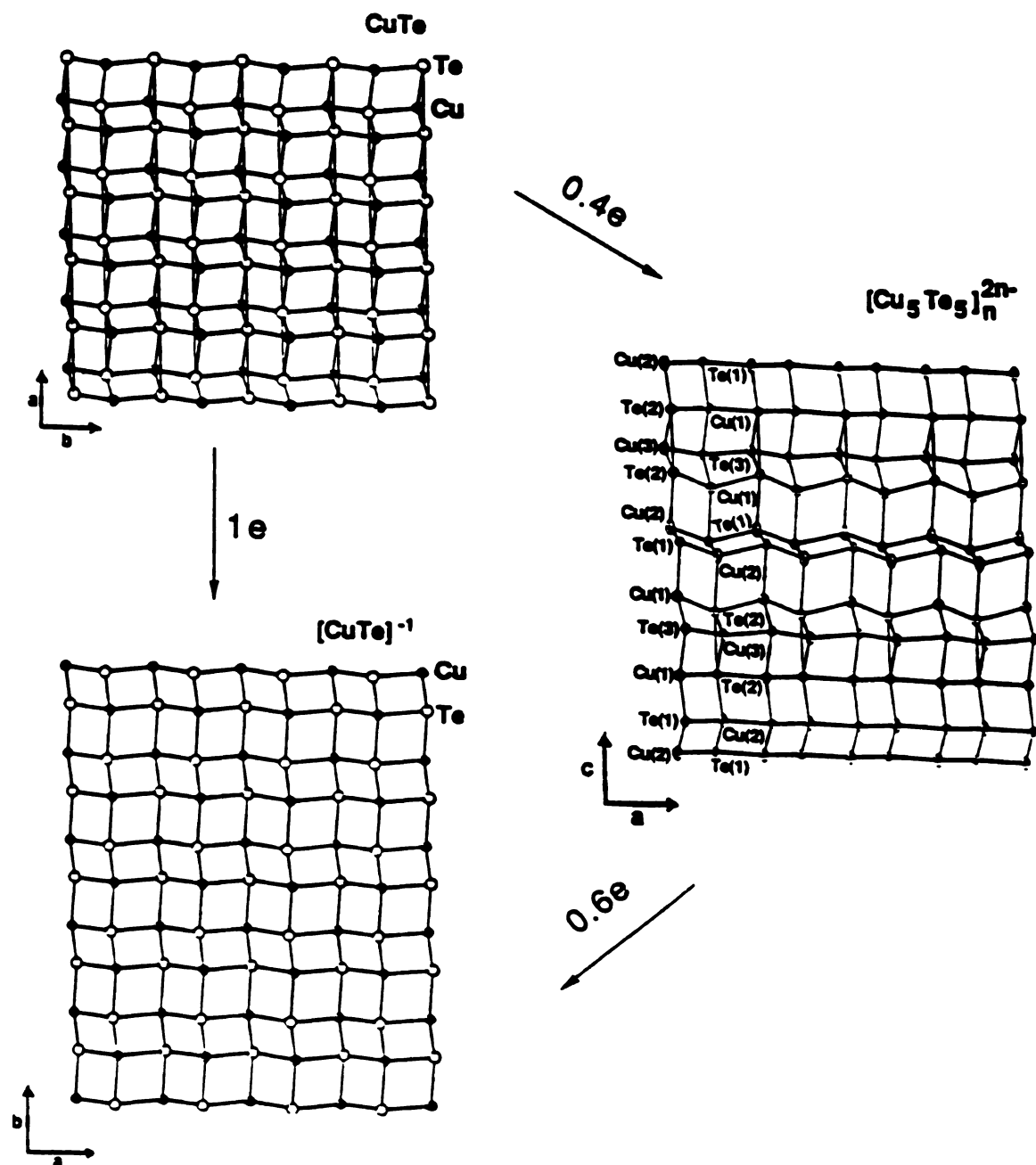


Figure 39. Structural relationship of the $[\text{Cu}_5\text{Te}_5]_n^{2n-}$ layer to those of CuTe (above) and $[\text{CuTe}]_n^{-1}$ (below) as a function of oxidation state.

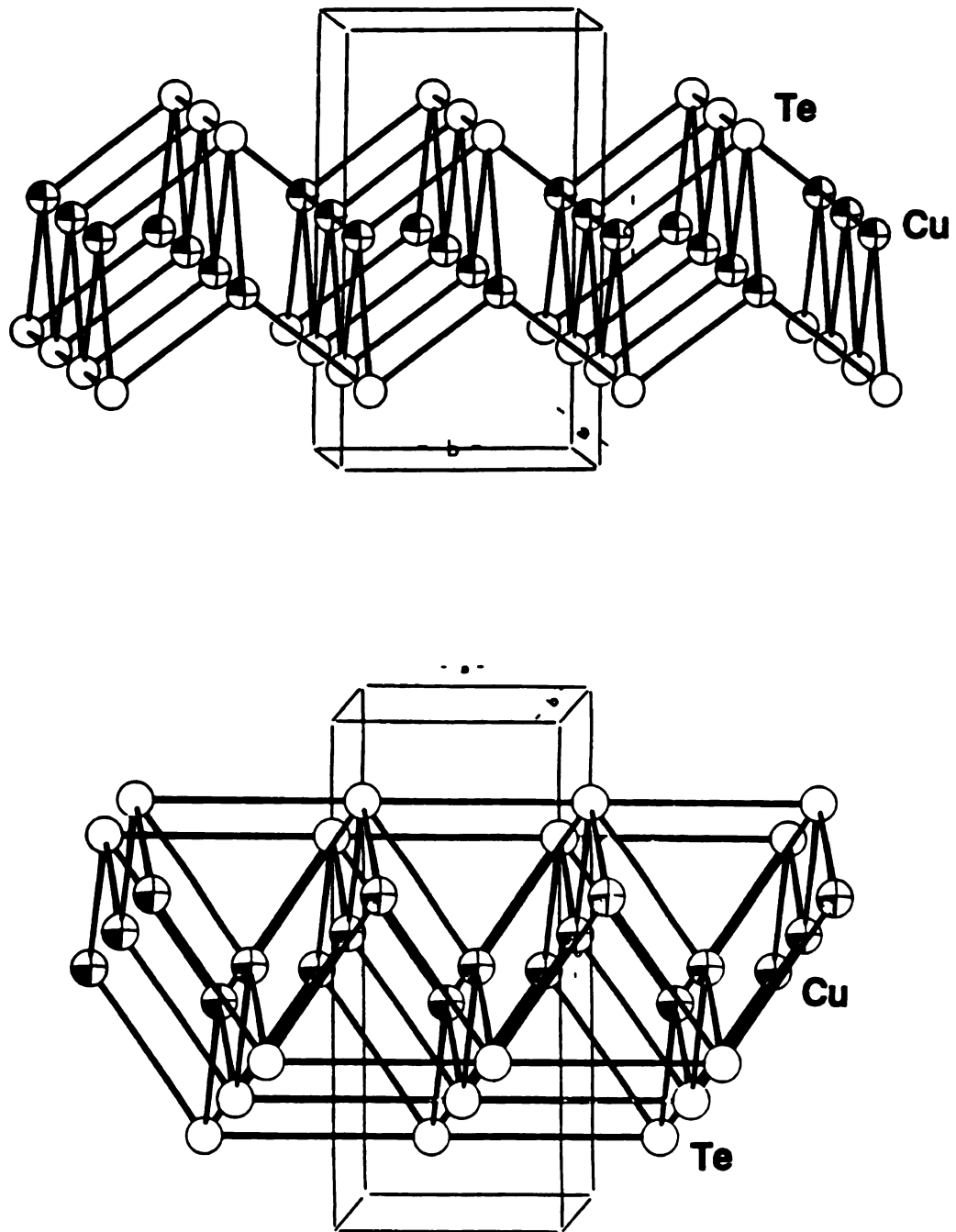


Figure 40. Two axial views of the layered structure of CuTe: (A) *a*-axial view and (B) *b*-axial view.

metallic mixed-valence compound formulated as $\text{Cu}_2^+\text{Cu}^{2+}(\text{S}_2^{2-})(\text{S}^{2-})$ or as $\text{Cu}_3^+(\text{S}_2^{2-})(\text{S}^-)^{105}$. In $\text{K}_2\text{Cu}_5\text{Te}_5$ there are three crystallographically independent copper atoms which possess a distorted tetrahedral geometry. The average Cu-Te distances for Cu(1), Cu(2) and Cu(3) are in the range of 2.69(3) Å, 2.64(7) Å and 2.58(4)Å respectively, and compare favorably with those found in CuTe^{104} . However, the Cu(2)-Te(1) and Cu(3)-Te(3) distances (along the crystallographic *a*-axis) are short at 2.582(1) Å and 2.540(2) Å, respectively, suggesting that the hole might be constrained but delocalized on rows made from these atoms parallel to the *a*-axis. Based on the +1 oxidation state for Cu, there are three electron vacancies per five Te. As a result, a structural distortion from the ideal anti-PbO structure occurs in which two vicinal Te(2) atoms move closer together along the *c*-axis to form a bond. Structural distortions in the electronegative element network as a response to changes in the electronic structure of the electropositive metal are at the core of the Zintl concept⁹¹ and are found in other ternary chalcogenide and pnictide systems¹⁰⁶.

There are three crystallographically distinct Te atoms in the asymmetric unit of $\text{K}_2\text{Cu}_5\text{Te}_5$. Among them, Te(2) atoms form Te(2)-Te(2) bonds of 2.960(1)Å by localizing 2 holes. In the absence of an additional distortion we can expect the remaining electron vacancy to be delocalized on the valence band, consisting mainly of p orbitals of the remaining three Te atoms. This gives rise to a partially empty band. The Te(2)-Te(2) bond is longer than the normal Te-Te single bonds found in known polytelluride compounds¹⁰⁷ by ~0.20 Å due to the multidentate nature of the Te(2)-Te(2) ligand. Each Te(2) atom binds four Cu atoms which pull a significant fraction of the electron density from the Te-Te bond. The next shortest Te-Te distance is in the non-bonding range of 3.667(1) Å. The square pyramidal geometry around Te(1) and Te(3)

and their comparable average Cu-Te distances (2.61(3) Å for Te(1) and 2.63(9) Å for Te(3)) suggest indistinguishable oxidation states on Te(1) and Te(3) even though they are crystallographically distinct. $K_2Cu_5Te_5$ can be reasonably formulated as $K_2^+Cu_5^+(Te_2^{2-})Te_3^{1.67-}$. The Cu atoms in the $[Cu_5Te_5]_n^{2n-}$ layer make short Cu-Cu contacts with each other in the range of 2.687(2) Å-2.909(2) Å. Short Cu-Cu contacts are not uncommon in the copper chalcogenide compounds. Selected bond distances and angles are given in Table 67. Charge balancing K^+ ions are distributed between the layers, making ionic interactions with 10 Te atoms. The shortest K-Te distance is 3.561(2) Å.

Table 67. Selected Bond Distances (Å) and Angles (deg) in $K_2Cu_5Te_5$ with Standard Deviations in Parentheses

Cu(1)-Te(1)	2.644(2)	Cu(1)-Te(1)-Cu(2)	89.10(5)
Cu(2)-Te(1)	2.637(1)	Cu(1)-Te(1)-Cu(2)	67.63(4) (x2)
Cu(2)-Te(1)	2.582(1) (x2)	Cu(2)-Te(1)-Cu(2)	61.96(4) (x2)
		Cu(2)-Te(1)-Cu(2)	106.24(6)
Cu(1)-Te(2)	2.701(1) (x2)	Cu(1)-Te(2)-Cu(1)	99.74(6)
Cu(2)-Te(2)	2.760(2)	Cu(1)-Te(2)-Cu(2)	64.35(4) (x2)
Cu(3)-Te(2)	2.625(1)	Cu(1)-Te(2)-Cu(3)	64.29(3) (x2)
		Cu(2)-Te(2)-Cu(3)	95.51(4)
Te(2)-Te(2)	2.960(1)	Te(2)-Te(2)-Cu(1)	98.57(3) (x2)
		Te(2)-Te(2)-Cu(2)	151.19(3)
		Te(2)-Te(2)-Cu(3)	55.68(2)
Cu(1)-Te(3)	2.713(1)	Cu(1)-Te(3)-Cu(3)	65.22(3) (x4)
Cu(3)-Te(3)	2.540(2) (x2)	Cu(3)-Te(3)-Cu(3)	108.79(7) (x2)
Cu(1)-Cu(3)	2.834(2)	Te(1)-Cu(1)-Te(2)	113.90(4) (x2)
Cu(1)-Cu(2)	2.909(2)	Te(1)-Cu(1)-Te(3)	108.38(4)
Cu(2)-Cu(2)	2.687(2)	Te(2)-Cu(1)-Te(2)	99.74(6)
Cu(2)-Cu(2)	2.687(2)	Te(2)-Cu(1)-Te(3)	110.37(4) (x2)
		Te(1)-Cu(2)-Te(1)	118.04(4) (x2)
Cu(1)-Te (mean)	2.69(3)	Te(1)-Cu(2)-Te(1)	106.24(6)
Cu(2)-Te (mean)	2.64(7)	Te(1)-Cu(2)-Te(2)	85.86(4)
Cu(3)-Te (mean)	2.58(4)	Te(1)-Cu(2)-Te(2)	113.96(4) (x2)
		Te(2)-Cu(3)-Te(2)	68.63(5)
		Te(2)-Cu(3)-Te(3)	118.74(2) (x4)
		Te(3)-Cu(3)-Te(3)	108.79(7)
K-Te(1)	3.611(2) (x2)	K-Te(2)	3.630(2) (x2)
K-Te(1)	3.712(2) (x2)	K-Te(3)	3.561(2) (x4)

3.2.2. Structure of NaCuTe (II)

The structure of NaCuTe has been known for a while.⁷⁴ However, its poor characterization of the structure and quite important structural relationship with the $K_2Cu_5Te_5$ and CuTe renders us to redetermine its structural details with high accuracy. NaCuTe possesses an *ideal* anti-PbO-type layer and isostructural to NaCuSe. The structure is shown in Figure 41. The anionic $[CuTe]_n^{n-}$ layer (shown in Figure 39) is made of edge-sharing rhombic $[Cu_2Te_2]$ units. The structure of NaCuTe can also be viewed as being derived from the *distorted* anti-PbO-type structure of CuTe into which Na^+ ions are reductively inserted. The Cu-Te bond distance of 2.709(1)Å compares well with that of $NaCu_3Te_2$ ¹⁰¹. The tellurium atoms have μ_4 -type coordination with square pyramidal geometry. Selected bond distances and angles are given in Table 68. Charge balancing Na^+ atoms are distributed between the layer, making ionic interactions with Te atoms. The average Na-Te distance is 3.197(3)Å. The geometry of the 5 coordinate Na^+ ions is square pyramidal.

Table 68. Selected Bond Distances (Å) and Angles (deg) in NaCuTe with Standard Deviations in Parentheses

Te-Cu	2.7086(6)	Cu-Te-Cu	69.95(2) (x4)
		Cu-Te-Cu	108.31(3) (x2)
Te-Na	3.203(7)	Te-Cu-Te	108.31(3) (x2)

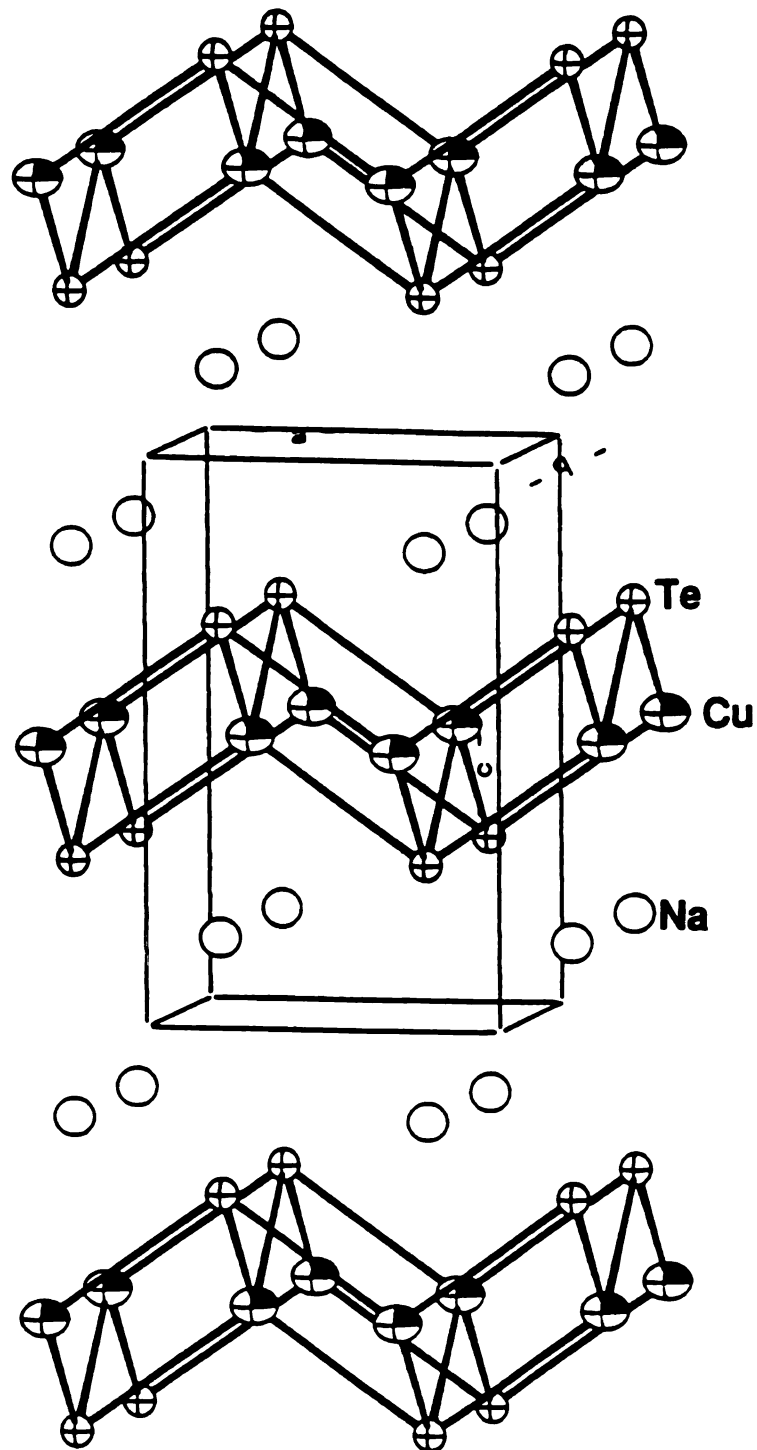
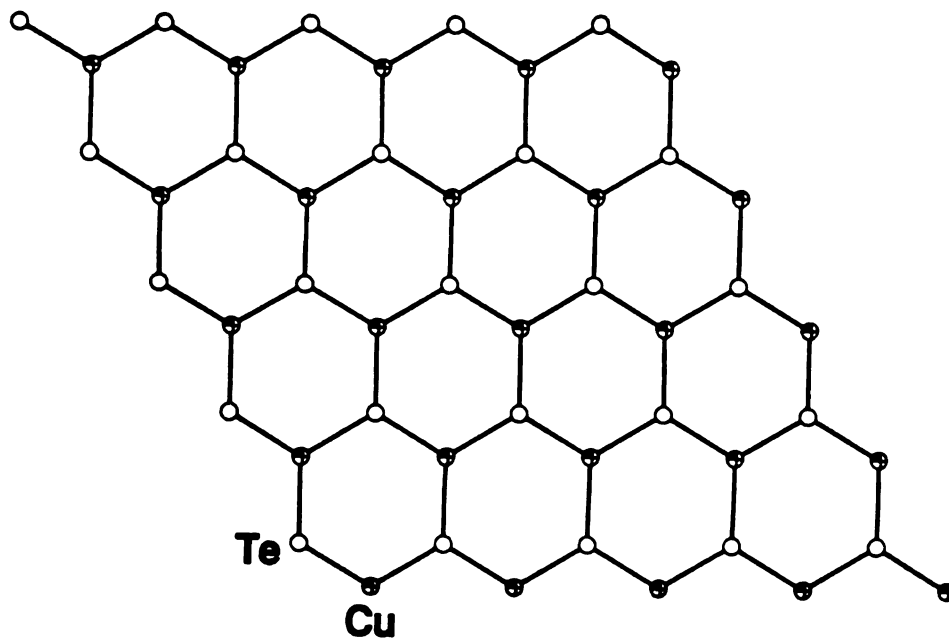


Figure 41. ORTEP representation of the layered structure of NaCuTe.

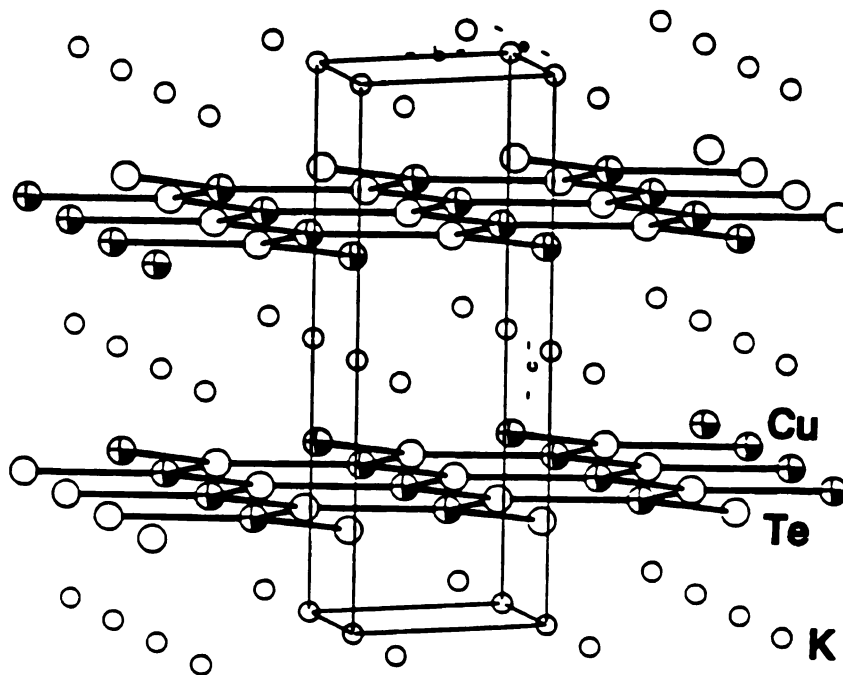
3.3. Structural Relationship of the $[\text{Cu}_5\text{Te}_5]_n^{2n-}$ layers in (I) to those of $[\text{CuTe}]_n^{n-}$ in (II) and CuTe

The layered compound CuTe, which is formally better described as $(\text{Cu}^+)_n(\text{Te}_n^{n-})$ rather than $(\text{Cu}^{2+})(\text{Te}^{2-})$, contains unusual, straight Te_n^{n-} chains. The long Te-Te bonds at 3.10 Å are considered half bonds and are subject to reduction by accepting electrons from the electropositive elements. Thus, the structure of the $[\text{Cu}_5\text{Te}_5]_n^{2n-}$ layer can be rationalized as being derived from that of CuTe by addition of 0.4 electrons. This reduction breaks some of the Te-Te bonds in CuTe. One electron per CuTe unit is required to reduce all Te-Te bonds of the infinite Te_n^{n-} chain as is found in NaCuTe. The Te-Te bonds of the infinite, straight Te_n^{n-} chains are broken by accepting electrons from the electropositive Na atoms to give the *ideal* anti-PbO-type layered structure of $[\text{CuTe}]_n^{n-}$. Thus, $\text{K}_2\text{Cu}_5\text{Te}_5$ can be considered as a true intermediate oxidation state compound between completely oxidized CuTe^{104} and completely reduced NaCuTe as illustrated in Figure 39.

The known layered compound KCuTe^{73} can also be considered as being derived from the CuTe framework by reduction with 1 electron. Surprisingly, the structure of KCuTe differs from that of NaCuTe. It forms the boron-nitride honeycomb layer structure shown in Figure 42. The structure change of the anionic framework from Na to K is purely an electrostatic effect. The larger K^+ ion requires a larger area and volume than does the Na^+ ions. This destabilizes the PbO structure which requires that the closest $\text{K}^+ \cdots \text{K}^+$ distances be the same as the $\text{Na}^+ \cdots \text{Na}^+$ distances. For the same number of formula units of $[\text{CuTe}]^-$, the boron-nitride structure type covers more area than the PbO structure type. Thus, enough space is created to accommodate the K^+ ions. Based on these observations, it is possible to predict the CsCuTe



(A)



(B)

Figure 42. ORTEP representation of (A) the $[\text{CuTe}]_n^-$ layer and (B) the unit cell of KCuTe .

structure which is not identified yet. Since ionic radius of Cs^+ is much larger than that of K^+ ion, much larger areas and volume would be required for the Cs^+ ion. This would destabilize the boron-nitride framework of $[\text{CuTe}]_n^{n-}$ and form one-dimensional structure which is similar to that of KCuS_2 .

3.4. Charge Transport Properties of $\text{K}_2\text{Cu}_5\text{Te}_5$ (I)

Based on the band filling arguments advanced above, $\text{K}_2\text{Cu}_5\text{Te}_5$ is expected to be a p-type metallic conductor. Charge transport measurements over the temperature range 5-300 K on the single crystals of $\text{K}_2\text{Cu}_5\text{Te}_5$ along the needle axis show that the resistivity first decreases linearly with decreasing temperature and at low temperatures levels off to a constant value (so called residual resistance due to scattering by impurities). The data are shown in Figure 43. The resistivity increases from $3.1 \times 10^{-6} \Omega\text{cm}$ at 5 K to $6.7 \times 10^{-5} \Omega\text{cm}$ at room temperature. The conductivity values of $\text{K}_2\text{Cu}_5\text{Te}_5$ are among the highest for known copper chalcogenide compounds. The residual resistance ratio (r_{H}/r_0), which is often used to determine the purity of the metal, is 21.3 in $\text{K}_2\text{Cu}_5\text{Te}_5$. In some of high purity metals such as copper and aluminum, the ratio can be ~ 200 . The temperature dependence of the thermoelectric power (Seebeck coefficient) shows a very small positive value of $1\sim 3 \mu\text{V/K}$ in the temperature range of 25 \sim 300 K as shown in Figure 44. The small and almost constant Seebeck coefficient indicate that $\text{K}_2\text{Cu}_5\text{Te}_5$ is a p-type metal. The small increase of the thermopower at low temperature (onset at 50K) is probably due to scattering by impurities.

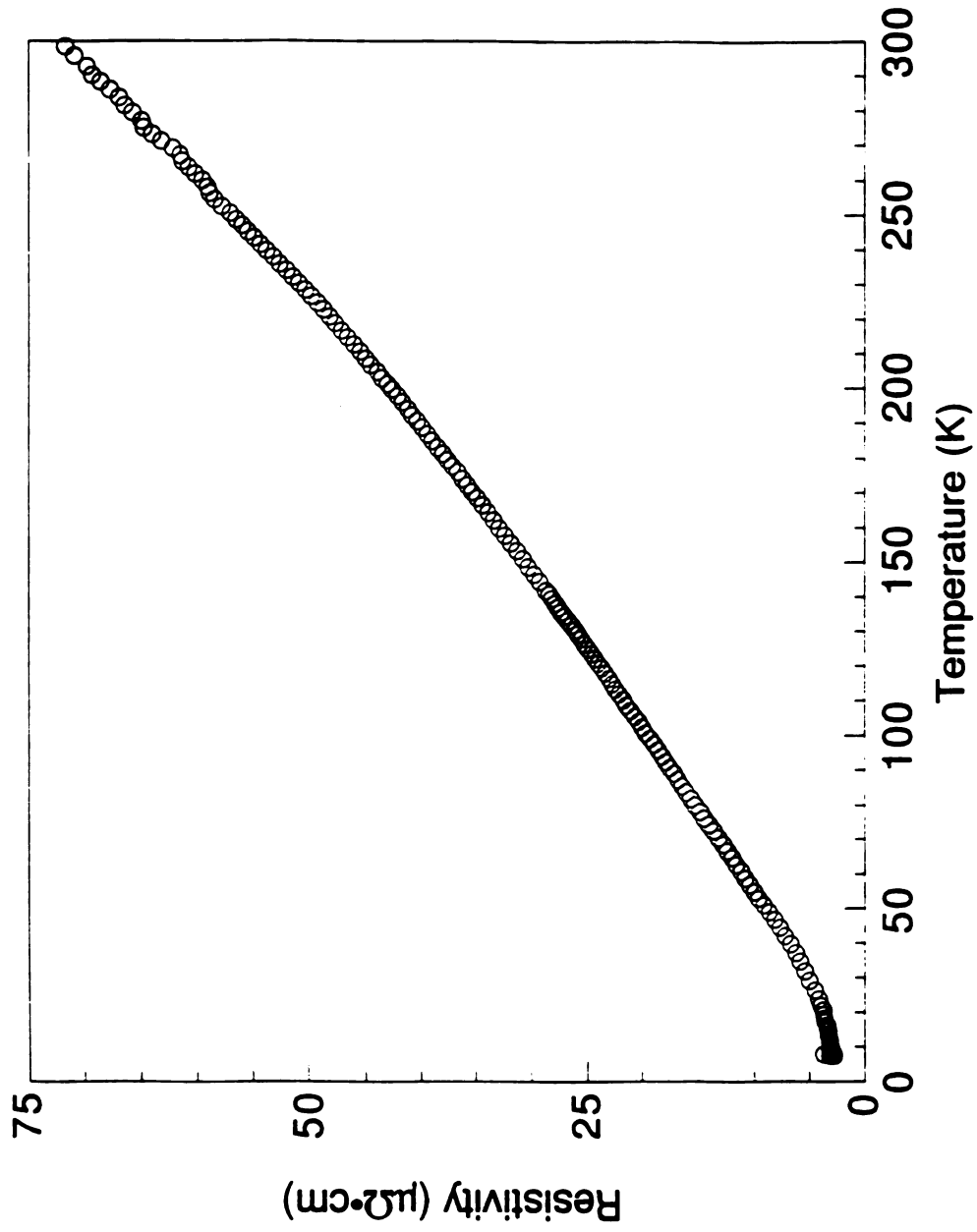


Figure 43. Four probe resistivity ($\mu\Omega\cdot cm$) data as a function of temperature for a single crystal of $K_2Cu_5Te_5$.

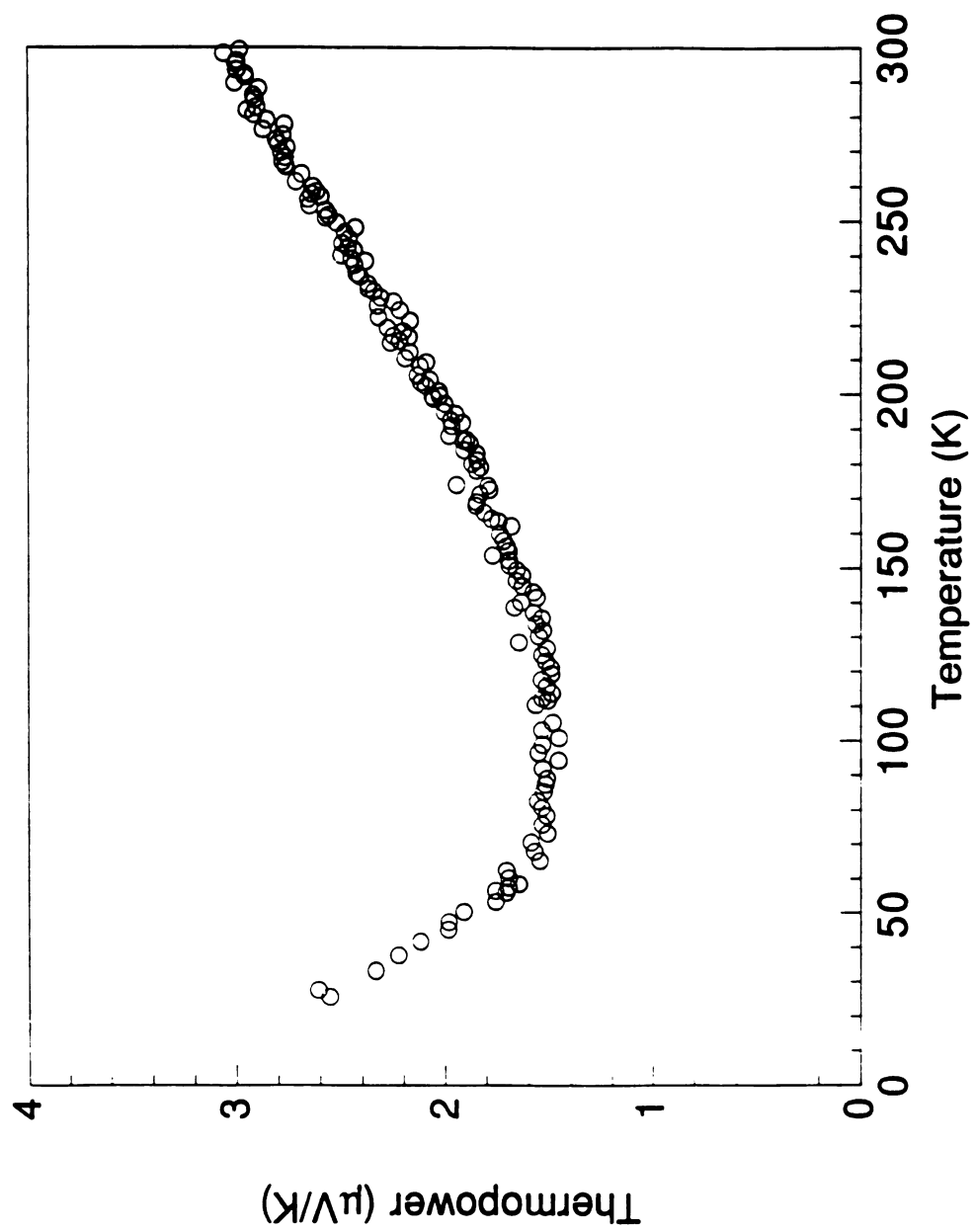


Figure 44. Variable-temperature thermoelectric power ($\mu\text{V/K}$) data for a single crystal of $\text{K}_2\text{Cu}_5\text{Te}_5$.

3.5. Magnetic Susceptibility of $K_2Cu_5Te_5$ (I)

Magnetic susceptibility data for $K_2Cu_5Te_5$ in the temperature range 2-300 K at 5 kG are shown in Figure 45. When plotted as χ^{-1} vs temperature, the data above 30 K show temperature-independent paramagnetism while below 30 K the data follow a Curie-Weiss Law. This behavior is characteristic of metals (Pauli paramagnetism) containing a low concentration of paramagnetic impurities.

In the free electron gas metal, the Pauli spin magnetization of the conduction electrons is given by eq 2.¹⁰⁸

$$M = \frac{3N\mu^2}{2K_B T_F} \times B \quad \text{eq 2.}$$

Where μ is Bohr magneton (0.921×10^{-20} erg/Oe), B is the magnetic field intensity, K_B is the Boltzman constant, N is number of carriers, and T_F is the Fermi temperature. Landau has shown that for free electrons the magnetic field induces a diamagnetic moment equal to -1/3 of the paramagnetic moment. Thus, the total magnetization of a free electron gas is given by eq 3.

$$M = \frac{N\mu^2}{K_B T_F} B = \frac{N\mu^2 B}{E_F} \quad \text{eq 3.}$$

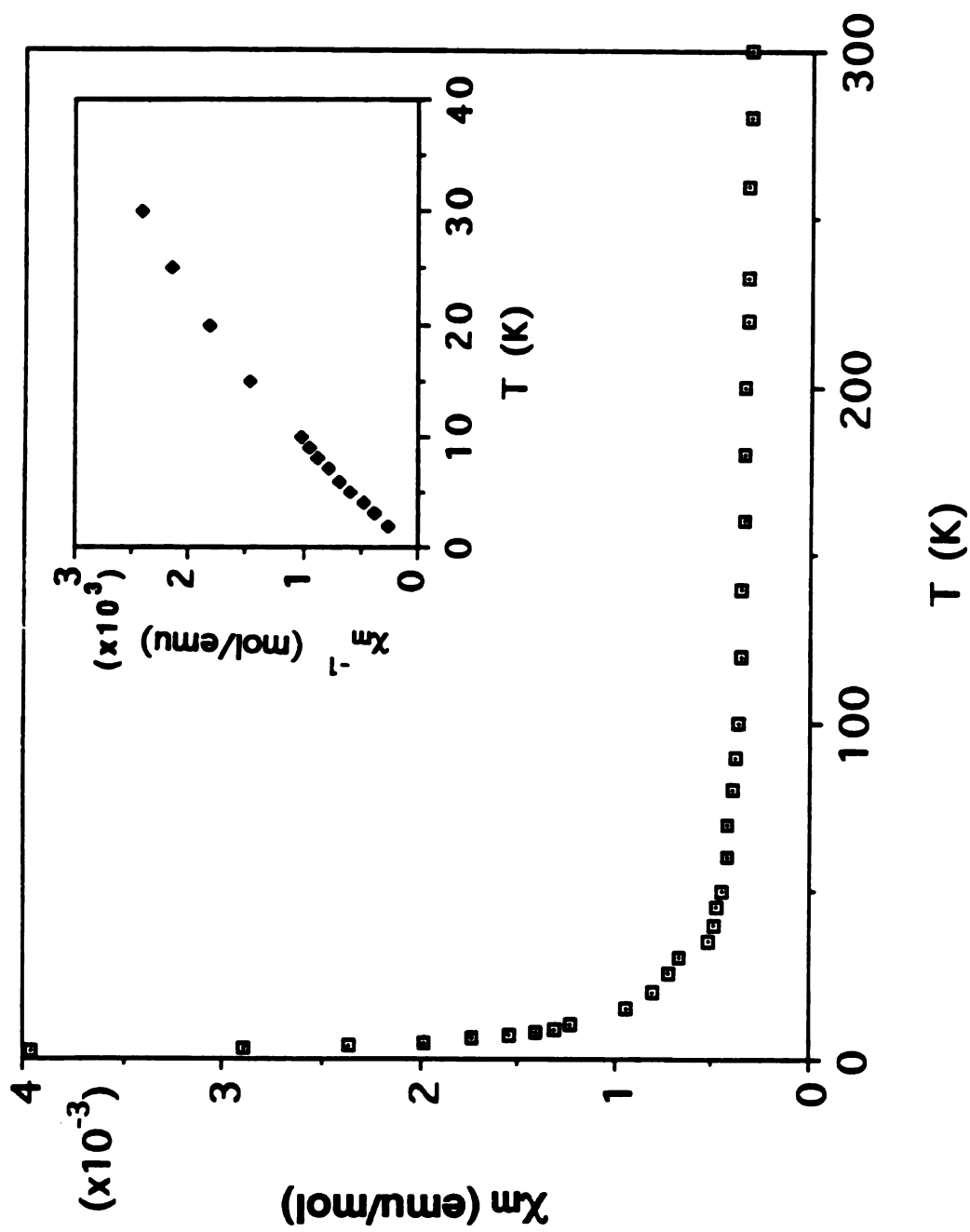


Figure 45. Variable-temperature magnetic susceptibility (emu/mol) data for polycrystalline $K_2Cu_5Te_5$. Inset: χ_m^{-1} (mol/emu) vs T .

E_F is the Fermi energy which may be estimated from the eq 4 where m is the mass of the electron, N is the number of carriers, and the V is the molar volume. Thus N/V is the conduction electron concentration.

$$E_F = \frac{h^2}{2m} \times \left(\frac{3\pi^2 N}{V} \right)^{2/3} \quad \text{eq 4.}$$

For $K_2Cu_5Te_5$, we expect one carrier per formula unit. Knowing the molar volume (184.4 cm^3), N/V is then $3.265 \times 10^{21} \text{ cm}^{-3}$ and the Fermi energy is calculated as $E_F = 1.286 \times 10^{-12} \text{ erg}$. The predicted magnetic susceptibility is then $\chi_p = 39.7 \times 10^{-5} \text{ emu/mol}$. The temperature independent Pauli paramagnetism of the sample ($\chi_p = 25.6 \times 10^{-5} \text{ emu/mol}$) has been obtained by subtracting the Curie-Weiss portion of the paramagnetism from the measured magnetic susceptibility. This value compares reasonably well with the predicted value of $39.7 \times 10^{-5} \text{ emu/mol}$.

CHAPTER 6

Synthesis and Characterization of $K_4Cu_8Te_{11}$ and $Cs_3Cu_8Te_{10}$: Novel Solid State Chalcogenide Compounds with a Dodecahedral Cluster as a Building Block

1. Introduction

In the last decade there have been great efforts to search for new materials with interesting electrical, optical and catalytic properties. We have been pursuing this goal by exploring new ternary solid metal chalcogenide compounds using molten salt synthetic methods. Particularly, the use of alkali metal polychalcogenide fluxes as solvents and reagents has been quite successful in synthesizing novel structural types of (poly)sulfides and (poly)selenides of various transition-metals at intermediate temperatures ($150 < T < 500$ °C)^{50,53} (see previous chapters 1-4). We also have initiated investigations into polytelluride melts and have discovered several new compounds with unusual structures (see chapter 5). A new mixed-valence compound $K_2Cu_5Te_5$ discovered in our laboratory was reported earlier.^{54(b)} Metal tellurides have rarely been investigated compared to the corresponding metal sulfides and metal selenides^{6,7,79(d),100}. In this chapter, two novel Cu/Te cluster compounds, $K_4Cu_8Te_{11}$ and $Cs_3Cu_8Te_{10}$, with complicated structures will be illustrated. Prior to our work in the A/Cu/Te (A=alkali metal) system there

were only four known phases, NaCu_3Te_2 ¹⁰¹, KCu_3Te_2 ¹⁰², NaCuTe (see page 190), and KCuTe ⁷⁴, all of which contain only mono-telluride ligands.

2. Experimental Section

2.1 Reagents

Chemicals were used as obtained: copper powder, -325 mesh, 99.95% purity, Cerac, Milwaukee, WI; tellurium powder, -100 mesh, 99.95% purity, Aldrich Chemical Co., Milwaukee, WI; potassium metal, analytical reagent, Mallinckrodt Inc., Paris, KY; cesium metal, 99.98% purity, AESAR, Johnson Matthey, Seabrook, NH.

2.2. Physical Measurements

Magnetic susceptibility measurements for $\text{Cs}_3\text{Cu}_8\text{Te}_{10}$ over the temperature range from 5 K to 300 K at 5 kG were performed on a MPMS Quantum Design SQUID magnetometer. Single crystals of $\text{Cs}_3\text{Cu}_8\text{Te}_{10}$ were manually selected for measurements. They were used without grinding as random oriented single crystals. The data were corrected for diamagnetic contributions of the sample holder. To obtain molar susceptibility the corrections for ion-core diamagnetic contributions from atomic constituents were made using the values tabulated by Mulay¹⁰³. The magnetization of $\text{Cs}_3\text{Cu}_8\text{Te}_{10}$ was examined at 5 K as a function of applied field from 500 G to 7 kG and was found to vary linearly with the applied field.

Four-probe dc resistivity data for $\text{K}_4\text{Cu}_8\text{Te}_{11}$ and thermoelectric power data for $\text{Cs}_3\text{Cu}_8\text{Te}_{10}$ over the temperature range 5 K to 300 K were provided by

Prof. C. R. Kannewurf (Northwestern University). A computer automated measurement system was employed to obtain thermopower and resistivity data with both the current and thermal gradient applied along the needle axis of $K_4Cu_8Te_{11}$ and (010) plane of $Cs_3Cu_8Te_{10}$. For all measurements electrode connections to the small single crystals were made with the use of 25 and 60 μm gold wires and gold bonding paste.

Quantitative microprobe analysis of the compounds were performed on a Jeol 35CF scanning electron microscope equipped with Tracor Northern TN 5500 X-ray microanalysis attachment. Single crystals of each sample were carefully picked and mounted on an aluminum stub using conducting silver paint to help dissipate charges that developed on the sample surface during measurements. Energy Dispersive Spectra (EDS) were obtained using the following experimental set-up:

X-ray detector position : 55 mm

Working distance : 39 mm

Accelerating voltage : 20 KV

Take-off angle : 27 deg

Beam current : 200 picoamps

Accumulation time : 100 seconds

Window : Be

A standardless quantitative analysis (SQ) program was used to analyze the X-ray spectra obtained. Since the Cu ratio is always overestimated because of the contribution of system Cu peaks, a correction factor ($\times 0.73$), determined by calibrating with known K/Cu/Te compounds, was used to better evaluate the Cu percentage.

2.3. Synthesis

Chemicals were measured and loaded in Pyrex tubes under a dry nitrogen atmosphere in a Vacuum Atmospheres Dri-Lab glovebox. Potassium monotelluride (K_2Te) and sodium monotelluride (Cs_2Te) were prepared in liquid ammonia from alkali metal and elemental tellurium in a 2:1 ratio.

Tetrapotassium bis(μ_4 -ditelluro)tris(μ_8 -ditelluro)(μ_4 -telluro) octacuprate(I), $K_4Cu_8Te_{11}$ (I) 0.309 g (1.5 mmol) of K_2Te , 0.064 g (1.0 mmol) of Cu and 0.765 g (6.0 mmol) of Te were mixed together and loaded in a Pyrex tube which was flame-sealed under vacuum ($\sim 10^{-3}$ torr). The tube was placed in a computer-controlled furnace and heated at 350 °C for 3 days and cooled slowly to 100 °C at a rate of 2 °C/hr. Black needle-like crystals, sometimes with small contamination of elemental tellurium, were obtained by removing excess molten potassium polytellurides (K_2Te_x) with DMF under a N_2 atmosphere (yield: 57% based on copper used). A quantitative microprobe analysis performed on a large number of crystals with the EDS/SEM system gave an average composition of $KCu_{2.1}Te_{2.7}$.

Tricesium bis(μ_4 -ditelluro)bis(μ_8 -ditelluro)bis(μ_4 -telluro) octacuprate(I,II), $Cs_3Cu_8Te_{10}$ (II) 0.197 g (0.5 mmol) of Cs_2Te , 0.032 g (0.5 mmol) of Cu and 0.383 g (3.0 mmol) of Te were mixed together and loaded in a Pyrex tube which was flame-sealed under vacuum ($\sim 10^{-3}$ torr). The tube was placed in a computer-controlled furnace and heated at 450 °C for 4 days and cooled slowly to 100 °C at a rate of 2 °C/hr and then to 50 °C at a rate of 10 °C/hr. Small amounts of black, plate-like crystals were obtained as a minor phase with large amounts of powder material including elemental tellurium. The matrix, a hard mass, does not dissolve easily in DMF and water or any

other common organic solvent. Thus, we have crushed the matrix to manually isolate single crystals. A quantitative microprobe analysis performed on a large number of single crystals with the EDS/SEM system gave an average composition of $\text{CsCu}_{2.6}\text{Te}_{3.3}$.

2.4. X-ray Crystallographic Studies

Both compounds were examined by X-ray powder diffraction for the purpose of phase characterization and identification. The d-spacings for each compound were obtained from the powder pattern recorded on a Phillips XRG-3000 computer-controlled powder diffractometer, operating at 40KV, 35 mA. Graphite monochromated Cu radiation was used. To verify product homogeneity, the d-spacings observed for the bulk materials of $\text{K}_4\text{Cu}_8\text{Te}_{11}$ were compared, and found to be in accord, with those calculated from the single crystal X-ray structure analysis data. The d-spacings observed for single crystals of $\text{Cs}_3\text{Cu}_8\text{Te}_{10}$, which were manually selected, are also in accord with those calculated from the single crystal X-ray structure analysis data. The calculation of d-spacings was performed using the POWD10 program⁵⁶. The results are summarized in Tables 69 and 70.

Table 69. Calculated and Observed X-ray Powder Diffraction Pattern of $K_4Cu_8Te_{11}$

H K L	d_{calc} (Å)	d_{obs} (Å)	I/I _{max} (obs.)
-2 0 1	11.97	12.08	21.3
2 0 0	9.93	10.0	6.7
-4 0 1	5.78	5.82	55.5
-4 0 3	5.38	5.42	7.3
-3 1 3	4.50	4.53	11.3
4 0 1	4.09	4.11	8.3
-4 0 5	3.69	3.71	18.3
-2 0 5	3.52	3.54	21.3
6 0 0	3.31	3.33	36.7
-3 1 5	3.23	3.25	26.0
0 2 2	3.11	3.08	35.0
5 1 1 (1 1 4)	3.04	3.06	44.7
-4 2 1	2.94	2.95	18.7
6 0 1	2.91	2.92	35.5
-8 0 5 (-4 2 3)	2.88	2.89	100
4 0 3	2.84	2.85	20.9
2 2 2	2.79	2.80	12.7
-8 0 6	2.69	2.70	18.3
8 0 0	2.483	2.485	8.9
-10 0 7	2.219	2.228	36.7
8 0 2 (6 2 2)	2.044	2.050	65.2

Table 69. (cont'd)

H K L	d_{calc} (Å)	d_{obs} (Å)	I/I _{max} (obs.)
-5 3 1	2.031	2.032	23.1
8 2 0 (-8 2 7)	2.007	2.004	24.5
-2 2 7	1.980	1.985	37.3
-7 1 9 (-10 2 5)	1.963	1.963	24.5
-9 1 9	1.9130	1.9195	23.1
1 3 4 (-12 0 8)	1.8899	1.8886	54.1
-2 0 9	1.8496	1.8541	28.0
-5 3 6	1.8261	1.8330	16.3
-10 0 10	1.7937	1.7972	10.0
-4 0 10	1.7612	1.7643	14.2
0 4 0	1.7053	1.7244	8.6
-14 0 4	1.6752	1.6788	15.5
-2 0 10	1.6511	1.6556	6.0

Table 70. Calculated and Observed X-ray Powder Diffraction Pattern of $\text{Cs}_3\text{Cu}_8\text{Te}_{10}$

H K L	d_{calc} (Å)	d_{obs} (Å)	I/max (obs.)
0 2 0	12.07	12.40	8.3
0 4 0	6.03	6.01	24.2
1 4 1	3.82	3.88	21.7
0 0 2	3.46	3.50	20.1
1 6 1 (0 7 1)	3.12	3.12	100
(1 1 2)	3.08		
(2 4 0)	3.04		
2 3 1	2.92	2.94	29.4
3 0 1	2.226	2.238	17.9
2 6 2 (1 11 0)	2.106	2.111	41.4
1 9 2	2.032	2.027	38.2
0 10 2	1.982	1.984	33.2
1 6 3 (2 1 3)	1.9283	1.9350	27.6
3 5 2	1.8050	1.8094	16.5
0 0 4	1.7337	1.7359	41.5
3 9 2 (4 0 2)	1.5754	1.5773	21.7

The X-ray single crystal data of $K_4Cu_8Te_{11}$ and $Cs_3Cu_8Te_{10}$ were collected on a Rigaku AFC6S diffractometer with graphite monochromated Mo- K_α radiation using the ω - 2θ scan mode. Accurate unit cell parameters for both compounds were obtained from the least-squares refinement of the 2θ , ω , χ , and ϕ values of 20-25 machine-centered reflections. The stability of the experimental setup and crystal integrity were monitored by measuring three standard reflections periodically (every 100 reflections) during data collection. The intensities did not show any appreciable decay. Two absorption corrections were applied to the data of $K_4Cu_8Te_{11}$ and $Cs_3Cu_8Te_{10}$: an empirical absorption correction based on ψ scans for three reflections followed by a DIFABS⁵⁷ correction. The structures were solved by direct methods with SHELXS-86⁵⁸ program and were refined with the TEXSAN⁶⁰ package of crystallographic programs. All calculations were performed on a VAXstation 3100 computer. All atoms were refined anisotropically. The complete data collection parameters and details of the structure solution and refinement for (I) and (II) are given in Table 71. The final atomic coordinates, temperature factors and their estimated standard deviations are given in Tables 72 and 73.

Table 71. Summary of Crystallographic Data for $K_4Cu_8Te_{11}$ and $Cs_3Cu_8Te_{10}$

	compound	
	I	II
Formula	$K_4Cu_8Te_{11}$	$Cs_3Cu_8Te_{10}$
Formula weight	2068.36	2183.08
space group	C2/m	Immm
a (Å)	24.086(3)	7.053(2)
b (Å)	6.821(6)	24.159(3)
c (Å)	18.461(3)	6.935(3)
α (deg)	90.0	90.0
β (deg)	124.45(1)	90.0
γ (deg)	90.0	90.0
Vol (Å ³), Z	2501(3), 4	1182(1), 2
Temperature (°C)	23	23
Crystal size (mm)	0.60x0.06x0.06	0.39x0.18x0.08
Radiation	Mo-K α	Mo-K α
μ (Mo-K α , cm ⁻¹)	199.8	237.4
D_{calc} (g/cm ³)	5.49	6.14
$2\theta_{max}$ (deg)	50	60
Scan method	$\omega/2\theta$	$\omega/2\theta$
No. of data collected	2535	1014
No. of unique data	2480	1014
No. of data used ($F_o^2 > 3\sigma(F_o^2)$)	2029	839
No. of atoms	17	7
No. of variables	121	36
Phasing technique	Direct methods	Direct methods
Final R/R _w	2.5/3.7	3.2/5.0
Max. shift/esd (last cycle)	0.00	0.00
Extinction coefficient	3.50×10^{-7}	2.05×10^{-7}

Table 72. Fractional Atomic Coordinates and B_{eq} Values for $\text{K}_4\text{Cu}_8\text{Te}_{11}$ with Their Estimated Standard Deviations in Parentheses

Atom	x	y	z	$B_{\text{eq}}^a, \text{\AA}^2$
Te(1)	0.03755(4)	0	0.13004(5)	1.12(3)
Te(2)	0.09026(4)	0	0.31031(5)	1.14(3)
Te(3)	-0.06544(4)	-1/2	-0.01854(5)	1.14(3)
Te(4)	-0.09455(3)	-0.29501(9)	0.18119(3)	1.36(2)
Te(5)	0.07121(4)	-1/2	0.44196(5)	1.45(3)
Te(6)	0.19740(4)	-1/2	0.46792(5)	1.19(3)
Te(7)	0.22861(3)	0.29496(9)	0.27474(4)	1.44(2)
Te(8)	-0.04266(4)	0	0.40721(5)	1.47(3)
Te(9)	-0.18848(4)	0	-0.05765(5)	1.30(3)
Cu(1)	0.00740(5)	-0.2060(2)	0.33673(7)	1.81(4)
Cu(2)	0.20463(6)	0.1924(2)	0.38766(7)	1.90(4)
Cu(3)	-0.07933(6)	-0.1939(2)	0.05821(7)	1.68(4)
Cu(4)	0.12886(5)	-0.1932(2)	0.11857(7)	1.65(4)
K(1)	0.0640(1)	-1/2	0.2222(2)	1.9(1)
K(2)	-0.1274(2)	1/2	0.3299(2)	2.7(1)
K(3)	0.3541(1)	1/2	0.4743(2)	2.1(1)
K(4)	-0.2499	0	0.0867(2)	3.8(2)

^a B values for anisotropically refined atoms are given in the form of the isotropic equivalent displacement parameter defined as $B_{\text{eq}} = (4/3)[a^2B_{11} + b^2B_{22} + c^2B_{33} + ab(\cos \gamma)B_{12} + ac(\cos \beta)B_{13} + bc(\cos \alpha)B_{23}]$.

Table 73. Fractional Atomic Coordinates and B_{eq} Values for $\text{Cs}_3\text{Cu}_8\text{Te}_{10}$ with Their Estimated Standard Deviations in Parentheses

Atom	x	y	z	B_{eq}^{a} , \AA^2
Cs(1)	1/2	0.22267(6)	0	2.98(6)
Cs(2)	1/2	0	1/2	0.98(5)
Te(1)	1/2	0.05808(4)	0	0.99(4)
Te(2)	0	0	0.2962(1)	1.02(4)
Te(3)	0.3026(1)	0.14514(3)	1/2	1.37(3)
Te(4)	0	0.16360(5)	0	1.27(4)
Cu(1)	0.1946(2)	0.09123(5)	1.1958(1)	1.62(4)

^a B values for anisotropically refined atoms are given in the form of the isotropic equivalent displacement parameter defined as $B_{\text{eq}} = (4/3)[a^2B_{11} + b^2B_{22} + c^2B_{33} + ab(\cos \gamma)B_{12} + ac(\cos \beta)B_{13} + bc(\cos \alpha)B_{23}]$.

3. Results and Discussion

3.1. Synthesis

The synthesis of two novel cluster-containing compounds, $K_4Cu_8Te_{11}$ and $Cs_3Cu_8Te_{10}$, has been achieved using polytelluride fluxes as solvents and reagents as shown in eq 1.



where A is K or Cs metal and n is 1.5 or 1, respectively. They form complete melts at the temperatures employed (350 °C for (I) and 450 °C for (II)). The equation given above is not balanced and only shows the reactants used (left-hand side) and product obtained (right-hand side). After reaction, excess polytelluride flux was removed from the product with extra caution by washing with degassed DMF. The polytelluride flux may decompose to elemental tellurium if water or oxygen are present. Therefore, isolation has to be done carefully under a inert atmosphere with degassed dry DMF. Both compounds are stable in the air and moisture for several days.

$K_4Cu_8Te_{11}$ was prepared at 350 °C using the reactant ratio $K_2Te/Cu/Te$ of 1/1/8. The product contained $K_2Cu_5Te_5$ (see page 183) and some amounts of tellurium as coexisting phases, as judged by X-ray powder diffraction pattern. In order to suppress the $K_2Cu_5Te_5$ and elemental tellurium phase, we made several variations in the reaction conditions. First, upon changing the Cu ratio from 1 to 2.5 in the $K_2Te/Cu/Te$ system at 350 °C, we obtained more or less the same results with elemental tellurium as the major phase. However, the 1/2/8 ratio yielded slightly more $K_4Cu_8Te_{11}$. Then we increased the K_2Te ratio from 1

to 4 to optimize the metal to flux ratio. The 4/2/8 ratio gave KCu_3Te_2 ⁹⁸ with tellurium contamination while the 2/2/8 ratio gave only $\text{K}_2\text{Cu}_5\text{Te}_5$. Only the 3/2/8 ratio gave $\text{K}_4\text{Cu}_8\text{Te}_{11}$ phase as the major product at 350 °C. This result seemed reasonable because the K/Cu ratio of $\text{K}_4\text{Cu}_8\text{Te}_{11}$ is slightly higher than that of $\text{K}_2\text{Cu}_5\text{Te}_5$. However, the product was still contaminated with minor $\text{K}_2\text{Cu}_5\text{Te}_5$ and Te phases. An additional variation in the reaction condition was made by increasing Te from 3/2/8 to 3/2/12 based on the fact that $\text{K}_4\text{Cu}_8\text{Te}_{11}$ has a higher Te/Cu ratio than $\text{K}_2\text{Cu}_5\text{Te}_5$. Indeed, the 3/2/12 ratio yielded $\text{K}_4\text{Cu}_8\text{Te}_{11}$ as the major product with complete suppression of $\text{K}_2\text{Cu}_5\text{Te}_5$. However, it is still contaminated with small amounts of tellurium. A parallel approach, made by increasing the temperature (400 °C and 450 °C) with the reaction ratios mentioned above, was unsuccessful. At these high temperatures $\text{K}_4\text{Cu}_8\text{Te}_{11}$ was suppressed while the competing $\text{K}_2\text{Cu}_5\text{Te}_5$ phase is stabilized. This is consistent with the known property of decomposition of polychalcogenides to monochalcogenides at high temperature.

In the $\text{Cs}_2\text{Te}/\text{Cu}/\text{Te}$ system, we have seen at least two new phases. The reaction has been carried out using reactant ratios $\text{Cs}_2\text{Te}/\text{Cu}/\text{Te}$ of 1/1/8 to 4/1/8 at 330 °C. The 1/1/8 to 2/1/8 ratios gave a few large single crystals of $\text{Cs}_3\text{Cu}_8\text{Te}_{10}$. The majority of the product was elemental tellurium. The ratio of 3/1/8 to 4/1/8 gave another new ternary compound which has approximate composition of CsCuTe_4 given by EDS/SEM quantitative analysis. However, so far, we have been able to isolate single crystals of this compound. Its thin, hair-like morphology was identified using scanning electron microscope. The yield of $\text{Cs}_3\text{Cu}_8\text{Te}_{10}$, a minor phase in the preliminary trial, was improved slightly by changing reaction conditions. We increased the Cu ratio from 1/1/8 to 1/3/8 at 380 °C and then reduced the Te ratio from 1/1/8 to 1/1/4 and increase the temperature (450 °C). The $\text{Cs}_3\text{Cu}_8\text{Te}_{10}$ phase isolated from fluxes with these

ratios was still only a minor phase, but the crystal sizes were as large as 3mm. Only the 1/1/6 ratio gave a better yield but still more work is required to improve the overall yield and homogeneity. Isolation of the homogeneous $\text{Cs}_3\text{Cu}_8\text{Te}_{10}$ phase and single crystals of the new CsCuTe_4 phase is currently under investigation.

3.2. Description of Structures

3.2.1. Structure of $\text{K}_4\text{Cu}_8\text{Te}_{11}$ (I)

The structure of $\text{K}_4\text{Cu}_8\text{Te}_{11}$ is a unique three-dimensional Cu/Te framework with large tunnels running parallel to the crystallographic *b*-axis, as shown in Figure 46. The tunnels are filled with K^+ ions. The framework contains tetrahedral Cu^+ centers bonded to Te^{2-} and Te_2^{2-} ligands. The formula unit can be represented as $\text{K}_4\text{Cu}_8(\text{Te}_2)_5\text{Te}$. The structure is somewhat complicated with its three-dimensionality, but is tailored from fused and linked recognizable Cu/Te clusters. The basic building block of this framework is the remarkable pentagonal dodecahedral cluster, $\text{Cu}_8(\text{Te}_2)_6$, as shown in Figure 47(A). A remarkable feature of the dodecahedral $\text{Cu}_8(\text{Te}_2)_6$ cluster is the encapsulation of a K^+ ion in its center. This dodecahedral cluster is made of fused Cu_2Te_3 pentagonal planar five-membered rings each with one ditelluride edge. These $\text{Cu}_8(\text{Te}_2)_6$ clusters contain three mutually perpendicular sets of ditelluride units. Two dodecahedral $\text{Cu}_8(\text{Te}_2)_6$ clusters share one Te-Te edge to form a "Siamese twin" type double cluster shown in Figure 47(B). These double clusters then share opposite Te-Te edges to form a straight one-dimensional column with oval cross-section, as shown in Figure 47(C). The Cu atoms in these columns are bridged by quadruply bonded $\mu_4\text{-Te}^{2-}$ ions above and below the columns. This results in another unusual Cu/Te cluster as shown in Figure

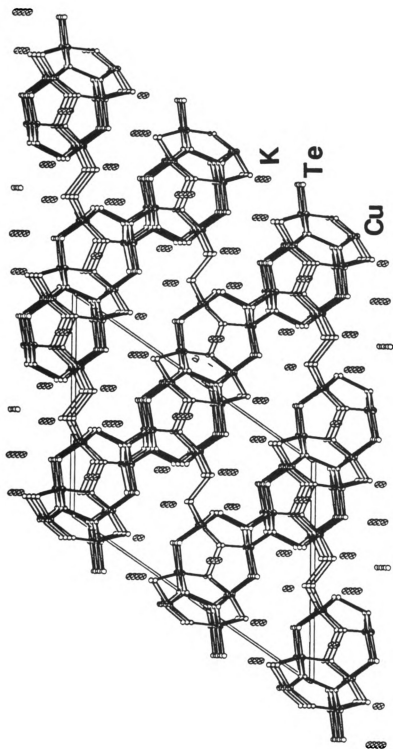


Figure 46. ORTEP representation of the unit cell of $K_4Cu_8Te_{11}$ viewed down $[010]$ direction.

Figure 47. ORTEP representation and labeling scheme of (A) the $[\text{KCu}_8\text{Te}_{12}]$ dodecahedral cluster, (B) two edge-shared $[\text{KCu}_8\text{Te}_{12}]$ units with capping Te^{2-} ions, (C) a one-dimensional column of edge-shared double clusters, and (D) the empty Cu_8Te_8 cluster.

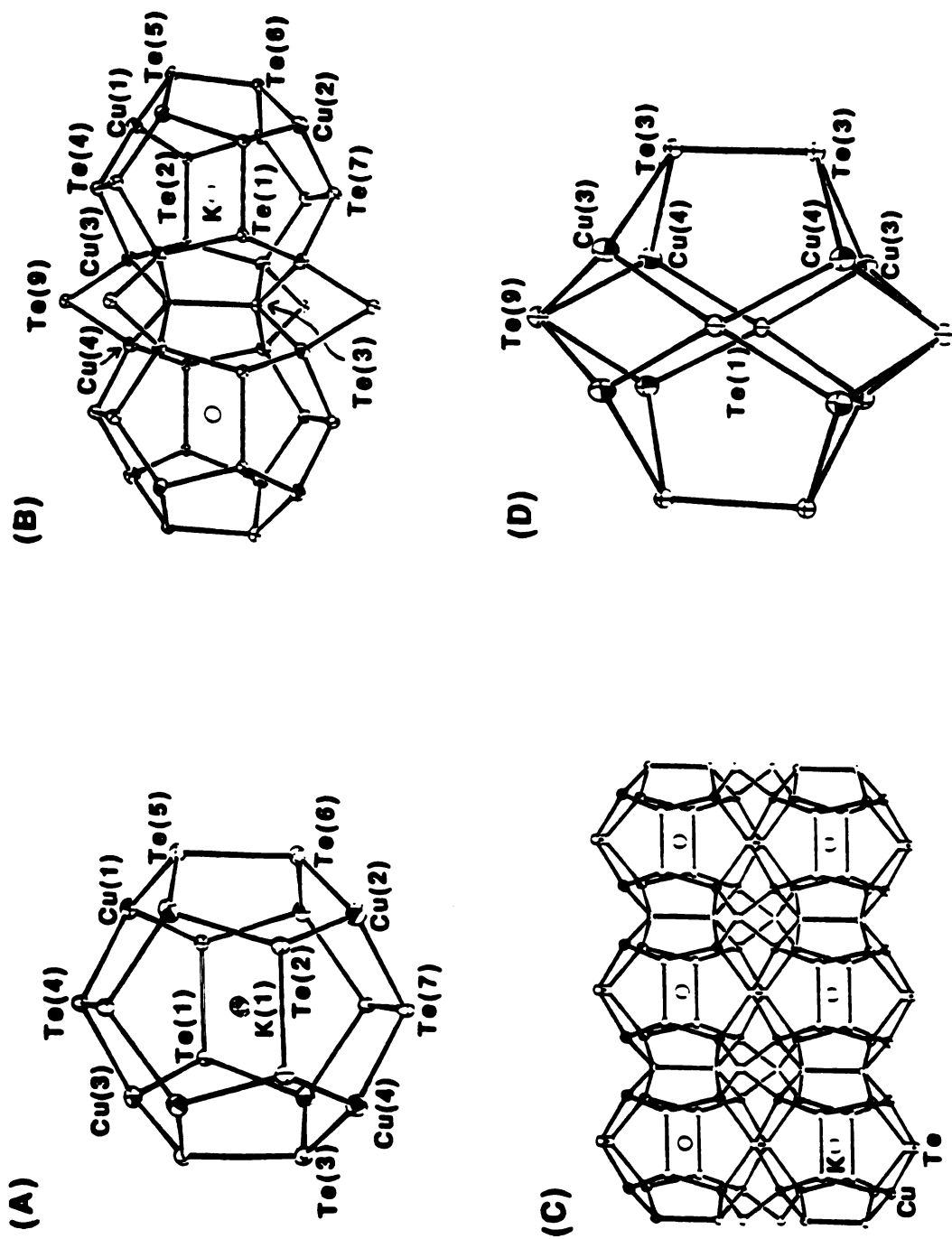
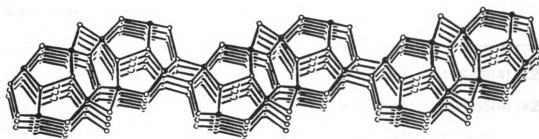


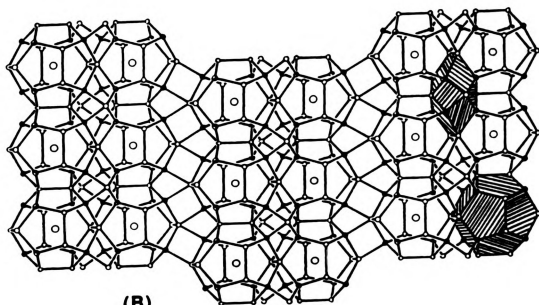
Figure 47.

47(D). This smaller cluster is made of four pentagonal Cu_2Te_3 five-membered rings and eight puckered Cu_2Te_2 four-membered rings. The inside of this Cu_8Te_8 cluster is completely empty with dimensions of $4.062\text{\AA} \times 6.821\text{\AA} \times 8.068\text{\AA}$ corresponding to the distances of $\text{Te}(1)\text{-Te}(1)$, $\text{Te}(3)\text{-Te}(3)$ and $\text{Te}(9)\text{-Te}(9)$, respectively. The one-dimensional columns of $\text{Cu}_8(\text{Te}_2)_6$ clusters are then assembled side by side through intercolumn $\text{Te}\rightarrow\text{Cu}$ bonding interactions to form Cu/Te layers as shown in Figure 48. The $\text{Te}(6)$ atoms that participate in these interactions are from one of the non-edge-shared ditelluride units (i.e. $\text{Te}(5)\text{-Te}(6)$) in the dodecahedral $\text{Cu}_8(\text{Te}_2)_6$ cluster. The Cu/Te layers are then connected to each other via bridging ditellurides (i.e. $\text{Te}(8)\text{-Te}(8)$) that act as pillars between the layers, producing the large channels as shown in Figure 46. The cross section of the channels is a 24 membered ring which is roughly rectangular-shaped; its short dimension is $4.581(1)\text{\AA}$. The geometry around the Cu atoms is distorted tetrahedral. The average Cu-Te distance is $2.63(4)\text{\AA}$ which is in the normal range of Cu-Te distances. Short Cu-Cu contacts are also observed in this compound, ranging from $2.625(3)\text{\AA}$ for $\text{Cu}(2)\text{-Cu}(2)$ to $2.810(4)\text{\AA}$ for $\text{Cu}(1)\text{-Cu}(1)$.

The coordination environments of Te atoms vary. The $\mu_4\text{-Te}(9)$ atoms have a square pyramidal geometry. The tellurium atoms ($\text{Te}(1)$, $\text{Te}(2)$, $\text{Te}(3)$, $\text{Te}(6)$) of ditellurides are bonded to four Cu atoms and one Te atom with a square pyramidal geometry, while the tellurium atoms ($\text{Te}(4)$, $\text{Te}(5)$, $\text{Te}(7)$ and $\text{Te}(8)$) of ditellurides are bonded to two Cu atoms and one Te atom with a trigonal pyramidal geometry. Higher coordination numbers of Te atoms are not uncommon in the binary or ternary compounds, some examples of which include $\text{KCu}_4\text{S}_2\text{Te}$ (see page 255), NaCu_3Te_2 ¹⁰¹, KCu_3Te_2 ¹⁰², and TiCu_3Te_2 ¹⁰⁹. The average Te-Te distance of ditellurides is normal at $2.81(1)\text{\AA}$.¹⁰³ Selected bond distances and angles are given Table 74.



(A)



(B)

Figure 48. ORTEP representation of (A) sideview and (B) top view of one Cu/Te layer. The $\text{Cu}_8(\text{Te}_2)_6$ and Cu_8Te_8 clusters are shaded for emphasis.

Table 74. Selected Bond Distances (Å) and Angles (deg) in $K_4Cu_8Te_{11}$ with Standard Deviations in Parentheses

Te(1)-Te(2)	2.812(1)	Te(2)-Te(1)-Cu(3)	103.29(4) (x2)
Te(1)-Cu(3)	2.685(2) (x2)	Te(2)-Te(1)-Cu(4)	104.65(4) (x2)
Te(1)-Cu(4)	2.673(2) (x2)	Cu(3)-Te(1)-Cu(3)	59.01(7)
Te(2)-Cu(1)	2.701(2) (x2)	Cu(3)-Te(1)-Cu(4)	113.45(5) (x2)
Te(2)-Cu(2)	2.627(2) (x2)	Cu(3)-Te(1)-Cu(4)	152.06(5) (x2)
		Cu(4)-Te(1)-Cu(4)	59.07(7)
		Te(1)-Te(2)-Cu(1)	109.19(4) (x2)
		Te(1)-Te(2)-Cu(2)	106.02(4) (x2)
		Cu(1)-Te(2)-Cu(1)	62.69(7)
		Cu(1)-Te(2)-Cu(2)	107.25(5) (x2)
		Cu(1)-Te(2)-Cu(2)	144.73(5) (x2)
		Cu(2)-Te(2)-Cu(2)	59.96(7)
Te(4)-Cu(3)	2.590(1)	Te(3)-Te(3)-Cu(3)	109.39(4) (x2)
Te(3)-Te(3)	2.822(2)	Te(3)-Te(3)-Cu(4)	107.18(4) (x2)
Te(3)-Cu(3)	2.649(2) (x2)	Cu(3)-Te(3)-Cu(3)	104.07(7)
Te(3)-Cu(4)	2.633(2) (x2)	Cu(3)-Te(3)-Cu(4)	63.24(5) (x2)
Te(4)-Te(4)	2.797(3)	Cu(3)-Te(3)-Cu(4)	143.43(5) (x2)
Te(4)-Cu(1)	2.582(1)	Cu(4)-Te(3)-Cu(4)	105.30(7)
		Te(4)-Te(4)-Cu(1)	103.60(3)
		Te(4)-Te(4)-Cu(3)	105.45(3)
		Cu(1)-Te(4)-Cu(3)	113.27(4)
Te(5)-Te(6)	2.796(1)	Te(6)-Te(5)-Cu(1)	104.68(4) (x2)
Te(5)-Cu(1)	2.604(2) (x2)	Cu(1)-Te(5)-Cu(1)	100.75(8)

Table 74. (cont'd)

Te(6)-Cu(2)	2.631(2) (x2)	Te(5)-Te(6)-Cu(2)	108.38(4) (x2)
Te(6)-Cu(2)	2.699(1) (x2)	Te(5)-Te(6)-Cu(2)	115.31(4) (x2)
		Cu(2)-Te(6)-Cu(2)	105.80(8)
		Cu(2)-Te(6)-Cu(2)	130.16(4)
		Cu(2)-Te(6)-Cu(2)	58.21(7)
		Cu(2)-Te(6)-Cu(2)	130.16(4)
		Cu(2)-Te(6)-Cu(2)	82.48(5) (x2)
Te(7)-Te(7)	2.797(3)	Te(7)-Te(7)-Cu(2)	105.88(3)
Te(7)-Cu(2)	2.556(1)	Te(7)-Te(7)-Cu(4)	105.53(3)
Te(7)-Cu(4)	2.594(1)	Cu(2)-Te(7)-Cu(4)	109.80(4)
Te(8)-Te(8)	2.828(2)	Te(8)-Te(8)-Cu(1)	112.19(5) (x2)
Te(8)-Cu(1)	2.626(2) (x2)	Cu(1)-Te(8)-Cu(1)	64.69(7)
Te(9)-Cu(3)	2.622(1) (x2)	Cu(3)-Te(9)-Cu(3)	60.58(7)
Te(9)-Cu(4)	2.625(1) (x2)	Cu(3)-Te(9)-Cu(4)	93.65(5) (x2)
		Cu(3)-Te(9)-Cu(4)	63.72(4) (x2)
		Cu(4)-Te(9)-Cu(4)	60.26(7)
Cu(1)-Cu(1)	2.810(4)	Te(2)-Cu(1)-Te(4)	104.86(4)
Cu(2)-Cu(2)	2.625(3)	Te(2)-Cu(1)-Te(5)	110.54(5)
Cu(3)-Cu(3)	2.645(3)	Te(2)-Cu(1)-Te(8)	113.85(6)
Cu(3)-Cu(4)	2.769(2)	Te(4)-Cu(1)-Te(5)	115.92(6)
Cu(4)-Cu(4)	2.635(3)	Te(4)-Cu(1)-Te(8)	105.22(5)
K(1)-Te(1)	3.703(3) (x2)	Te(5)-Cu(1)-Te(8)	106.56(5)

Table 74. (cont'd)

K(1)-Te(2)	3.676(3) (x2)	Te(2)-Cu(2)-Te(6)	110.86(6)
K(1)-Te(3)	3.715(3)	Te(2)-Cu(2)-Te(6)	108.76(5)
K(1)-Te(3)	3.781(3)	Te(2)-Cu(2)-Te(7)	110.17(5)
K(1)-Te(4)	3.719(3) (x2)	Te(6)-Cu(2)-Te(6)	97.52(5)
K(1)-Te(5)	3.960(3)	Te(6)-Cu(2)-Te(7)	117.66(5)
K(1)-Te(6)	3.796(3)	Te(6)-Cu(2)-Te(7)	111.02(6)
K(1)-Te(7)	3.778(3) (x2)	Te(1)-Cu(3)-Te(3)	103.78(5)
K(2)-Te(4)	2.546(3) (x2)	Te(1)-Cu(3)-Te(4)	109.09(4)
K(2)-Te(5)	2.623(3)	Te(1)-Cu(3)-Te(9)	116.22(6)
K(2)-Te(5)	2.996(4)	Te(3)-Cu(3)-Te(4)	112.47(6)
K(2)-Te(7)	3.622(3) (x2)	Te(3)-Cu(3)-Te(9)	109.45(5)
K(2)-Te(8)	3.813(3) (x2)	Te(4)-Cu(3)-Te(9)	106.00(5)
K(3)-Te(2)	3.402(3)	Te(1)-Cu(4)-Te(3)	105.69(5)
K(3)-Te(5)	3.756(3) (x2)	Te(1)-Cu(4)-Te(7)	109.28(4)
K(3)-Te(6)	3.709(3)	Te(1)-Cu(4)-Te(9)	117.42(6)
K(3)-Te(6)	3.976(3) (x2)	Te(3)-Cu(4)-Te(7)	111.82(6)
K(3)-Te(7)	3.474(3) (x2)	Te(3)-Cu(4)-Te(9)	109.85(5)
K(3)-Te(8)	3.347(3)	Te(7)-Cu(4)-Te(9)	102.91(5)
K(3)-Te(8)	3.764(3)		
K(4)-Te(3)	3.877(2)		
K(4)-Te(4)	3.703(1) (x2)		
K(4)-Te(9)	3.636(3) (x2)		
K(4)-Te(9)	3.709(4)		

There are four crystallographically distinct K atoms in the unit cell of (I). The encapsulated K(1) atom is slightly off-centered on a rectangular plane defined by two opposite ditellurides in the dodecahedral cluster. The K(1)-Te distances range from 3.676 (3) Å to 3.960(3) Å (average 3.75(8) Å). The remaining three K atoms are sitting in the large tunnels with various coordination environments {8 C.N. for K(2), 10 C.N. for K(3), 6 C.N. for K(4)}. The average K-Te distances are 3.70(16) Å for K(2), 3.66(23) Å for K(3), and 3.71(9) Å for K(4).

3.2.2. Structure of $\text{Cs}_3\text{Cu}_8\text{Te}_{10}$ (I)

The structure of $\text{Cs}_3\text{Cu}_8\text{Te}_{10}$, an intriguing two-dimensional Cu/Te framework, is shown in Figure 49. Interestingly, the two-dimensional Cu/Te layer is composed of the fused dodecahedral $\text{Cu}_8(\text{Te}_2)_6$ clusters found in $\text{K}_4\text{Cu}_8\text{Te}_{11}$. In this Cu/Te layer each dodecahedral cluster shares two sets of ditelluride edges out of three mutually perpendicular sets of ditellurides to form a layer as shown in Figure 50. The framework contains tetrahedral Cu^+ centers bonded to Te_2^{2-} and Te^{2-} . The Cu atoms in this layer are capped by quadruply bonded $\mu_4\text{-Te}^{2-}$ ions above and below the layer. Based on the formula $\text{Cs}_3\text{Cu}_8\text{Te}_{10}$ and on the assumption that the formal oxidation state on each ditelluride and telluride unit is -2, the formal oxidation state on Cu atoms is +1 (seven atoms) and +2 (one atom). In $\text{Cs}_3\text{Cu}_8\text{Te}_{10}$ all the copper atoms are crystallographically equivalent, implying complete delocalization of the one-electron vacancy (hole) on eight Cu atoms. This would result in the average formal oxidation state of copper being +1.125. However, in mixed-valence copper chalcogenide compounds, it is generally accepted that the formal oxidation state on the copper atom is +1. This is because coexistence of Cu^{2+} and Te^{2-} ions is thermodynamically unstable with respect to the electron

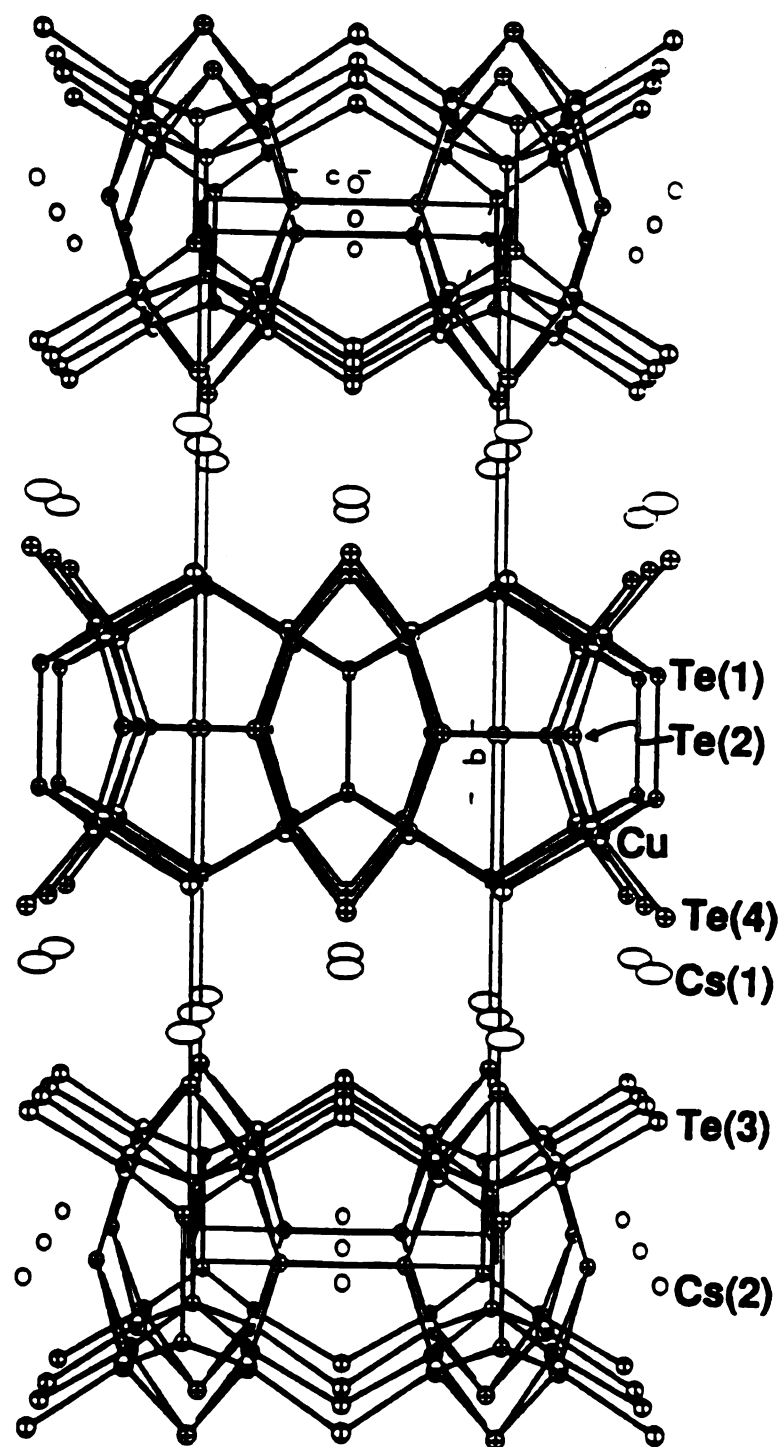
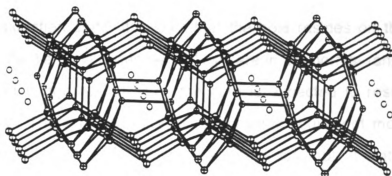
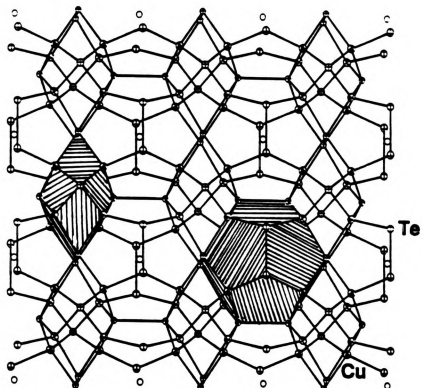


Figure 49. ORTEP representation of the unit cell of $\text{Cs}_3\text{Cu}_8\text{Te}_{10}$.



(A)



(B)

Figure 50. ORTEP representation of (A) sideview and (B) top view of one $[\text{Cu}_8\text{Te}_{10}]_n^{3n-}$ layer. The $\text{Cu}_8(\text{Te}_2)_6$ and Cu_8Te_8 clusters are shaded for emphasis.

transfer from the reducing Q^{2-} to the oxidizing Cu^{2+} . If one then consider Cu atoms in +1 oxidation state, it follows that the hole resides on the tellurium atoms. Since Te-Te bond distances of Te_2^{2-} are in the normal range of single bond observed in the $\text{K}_4\text{Cu}_8\text{Te}_{11}$, the hole is expected to reside on the monotellurides. There are two crystallographically equivalent monotelluride atoms in the asymmetric unit. Making the simple assumption that the hole is delocalized on two monotelluride atoms, the resulting average formal oxidation state of monotelluride atoms is -1.5. This situation gives rise to a partially empty valence band consisting mainly of p orbitals of the two monotelluride atoms. As a result, this material should be a p-type metallic conductor. Based on this formal charge assignment, the structural formula can be better represented as $\text{Cs}_3^+\text{Cu}_8^+(\text{Te}_2^{2-})_4\text{Te}^{1.5-}$. Certainly, these are only the formal oxidation states. The actual description is more complicated due to the small electronegativity difference between Cu (1.90) and Te (2.10) atoms.

The geometry around the Cu atom is slightly distorted tetrahedral. The average Cu-Te distance is 2.63(5) Å which is similar to that in (I). Short Cu-Cu contacts are also observed in this compound, ranging from 2.716(2) Å to 2.744(2) Å. The coordination environments of Te atoms are square pyramidal for $\text{Te}(1)_2^{2-}$, $\text{Te}(2)_2^{2-}$, and $\text{Te}(4)_2^{2-}$ and trigonal pyramidal for $\text{Te}(3)_2^{2-}$. The average Te-Te distance of ditellurides is in the normal range of 2.81(2) Å which is very close to that found in (I). The average Cu-Te bond distance of monotellurides ($\text{Te}(4)$) at 2.605(1) Å, which is slightly shorter than that found at 2.624(2) Å in (I). Even though the difference is quite small, it is consistent with the reduced effective ionic radius of $\text{Te}^{1.5-}$. Selected bond distances and angles are given in Table 75.

Table 75. Selected Bond Distances (Å) and Angles (deg) in $\text{Cs}_3\text{Cu}_8\text{Te}_{10}$ with Standard Deviations in Parentheses

Te(1)-Cu	2.670(1) (x4)	Te(1)-Cu-Te(2)	107.33 (5)
Te(2)-Cu	2.688(1) (x4)	Te(1)-Cu-Te(3)	109.10 (5)
Te(3)-Cu	2.594(1) (x2)	Te(1)-Cu-Te(4)	111.18 (5)
Te(4)-Cu	2.605(1) (x4)	Te(2)-Cu-Te(3)	110.54 (5)
		Te(2)-Cu-Te(4)	114.62 (5)
		Te(3)-Cu-Te(4)	103.99 (5)
Te(1)-Te(1)	2.806(2)	Te(1)-Te(1)-Cu	107.46(3) (x4)
Te(2)-Te(2)	2.826(2)	Te(2)-Te(2)-Cu	105.02(3) (x4)
Te(3)-Te(3)	2.785(2)	Te(3)-Te(3)-Cu	107.08(3) (x2)
		Cu-Te(1)-Cu	61.15(5) (x2)
Cs(1)-Te(1)	3.976(2)	Cu-Te(1)-Cu	107.61(6) (x2)
Cs(1)-Te(3)	4.180(1) (x4)	Cu-Te(1)-Cu	145.08(7) (x2)
Cs(1)-Te(3)	3.841(2) (x2)	Cu-Te(2)-Cu	61.39(5) (x2)
Cs(1)-Te(4)	3.804(1) (x2)	Cu-Te(2)-Cu	110.15(5) (x2)
		Cu-Te(2)-Cu	149.96(6) (x2)
Cs(2)-Te(1)	3.741(1) (x4)	Cu-Te(3)-Cu	108.85(6)
Cs(2)-Te(2)	3.799(1) (x4)	Cu-Te(4)-Cu	63.58(6) (x2)
Cs(2)-Te(3)	3.773(1) (x4)	Cu-Te(4)-Cu	95.66(7) (x2)
		Cu-Te(4)-Cu	62.85(6) (x2)
Cu-Cu	2.744(2)	Cu-Cu	2.716(2)

There are two crystallographically distinct Cs atoms in the asymmetric unit. The encapsulated Cs(2) atom, situated on the crystallographic mmm site, is in the center of dodecahedral cluster and is surrounded by 12 Te atoms. The Cs(2)-Te distances range from 3.741(1) Å to 3.779(1) Å (average 3.77(3) Å). The Cs(1) atoms are distributed between the $[\text{CsCu}_8\text{Te}_{10}]^{2-}$ layers. Within a radius of 4.0 Å, Cs(1) has 5 Te atoms around it, whereas within a radius of 4.2 Å it has 9 Te atoms around it. The Cs(1)-Te distances range from 3.804(2) Å to 4.180(1) Å, which is slightly longer than those of Cs(2)-Te.

3.3. Comparison of $\text{Cu}_8(\text{Te}_2)_6$ Cluster Size in $\text{K}_4\text{Cu}_8\text{Te}_{11}$ (I) and $\text{Cs}_3\text{Cu}_8\text{Te}_{10}$ (II)

Two novel Cu/Te compounds of $\text{K}_4\text{Cu}_8\text{Te}_{11}$ and $\text{Cs}_3\text{Cu}_8\text{Te}_{10}$ contain a common structural building unit, the dodecahedral $\text{Cu}_8(\text{Te}_2)_6$ cluster. At first glance, it is quite surprising that the Cs^+ ion, whose ionic radius (2.02 Å) is much larger than that of K^+ ion (1.78 Å), is encapsulated in the same dodecahedral cluster. Since the spatial requirements of the K^+ and Cs^+ ions are expected to be very different, a change in volume of the cluster would be expected based on the volume of the cation encapsulated. However, a close comparison of the two $\text{Cu}_8(\text{Te}_2)_6$ dodecahedral clusters does not show appreciable differences in size and volume. Selected metric data for the two dodecahedral clusters are given in Table 76.

Table 76. Selected Metric Data for the $\text{KCu}_8(\text{Te}_2)_6$ Cluster (A) and the $\text{CsCu}_8(\text{Te}_2)_6$ Cluster (B)

	(A)	(B)
	$\text{KCu}_8(\text{Te}_2)_6$	$\text{CsCu}_8(\text{Te}_2)_6$
Dimensions(Å) (Based on Te_2^{2-} edge)	6.822x6.955x7.091	6.936x7.013x7.053
$d_{\text{av}}(\text{Te-Te})$ (Å)	2.806(11)	2.806(19)
$d_{\text{max}}(\text{A-Te})$ (Å)	3.960(3)	3.779(1)
$d_{\text{min}}(\text{A-Te})$ (Å)	3.676(3)	3.741(1)
$d_{\text{av}}(\text{A-Te})$ (Å)	3.75(8)	3.77(3)
$d_{\text{av}}(\text{Cu-A})$ (Å)	3.689(25)	3.735(1)
$d_{\text{av}}(\text{Cu-Te})$ (Å)	2.63(4)	2.65(5)
Volume (Å ³) of Cluster	145.9	150.8
of alkali ion	23.6	34.5

The average Te-Te, A-Te (A=K, Cs) and Cu-Te distances in both clusters do not show any appreciable differences. If we consider the interactions between alkali metal ions and tellurium atoms as ionic, the average K-Te distance of 3.75 Å in (A) is very similar to the average Cs-Te distance of 3.77(3) Å in (B). However, these K-Te and Cs-Te distances are not unusual and are in the normal range. These similar distances lead to almost negligible change in volume of the Cs-encapsulated dodecahedral cluster. Calculation of the entire volume of each cluster indicated a 4.9 Å³ increase in (B). However, this volume change is still small compared to the increased volume (10.9 Å³) of Cs⁺ ion compared to K⁺. If we assume that Cs⁺ ion fills completely the Cu/Te cluster then the K⁺ analogue should be slightly empty. This may be explained in terms of packing efficiency of the atoms in the cluster. Cluster (B), which contains three mutually perpendicular mirror planes, is more symmetric than cluster (A), which contains only one mirror plane, lying on atoms Te(3), Te(5), Te(6), and K(1). Therefore, cluster (B) is more close packed than cluster (A), giving the small volume change.

Since K⁺ and Cs⁺ ions are easily encapsulated inside the dodecahedral cluster, Rb⁺, whose ionic radius is in between them, should also be easily encapsulated. Indeed, Rb₃Cu₈Te₁₀ containing an Rb-encapsulated dodecahedral cluster, was obtained recently in our laboratory¹¹⁰.

The 20-vertex dodecahedral Cu₈(Te₂)₆ cluster and 16-vertex Cu₈Te₈ cluster observed in this study are unique and, to the best of our knowledge, have no analogues in metal cluster chemistry. However, there is a 20-vertex dodecahedral cluster known in organic chemistry, the dodecahedrane, C₂₀H₂₀¹¹¹. One can envision the possibility of building up novel extended structures in two or three dimensions based on this dodecahedral Cu₈(Te₂)₆ cluster by sharing more or all the ditelluride edges. The two novel structural

compounds, (I) and (II), containing $\text{Cu}_8(\text{Te}_2)_6$ clusters as building units highlighted the potential use of this dodecahedral cluster as a building unit for novel structural compounds. We expect to find more compounds based on this structural motif in the Cu/Te system and further exploration on the $\text{A}_2\text{Te}_x/\text{Cu}$ systems is under way.

3.4. Charge transport properties of $\text{K}_4\text{Cu}_8\text{Te}_{11}$ (I) and $\text{Cs}_3\text{Cu}_8\text{Te}_{10}$ (II)

Based on -2 formal oxidation states on ditelluride units and monotelluride atoms, each Cu atom has a formal oxidation state of +1. This gives rise to a completely filled valence band due to the d^{10} electronic configuration of Cu^+ , suggesting that $\text{K}_4\text{Cu}_8\text{Te}_{11}$ should be a semiconductor. Preliminary conductivity measurements on several single crystals of $\text{K}_4\text{Cu}_8\text{Te}_{11}$ show semiconducting behavior over the temperature range 30-300 K as shown in Figure 51. The conductivity increases from ~ 50 S/cm at 30K to ~ 160 S/cm at room temperature. However, the strong deviations from linearity of the $\log \sigma$ vs. $1/T$ plot show a departure from classical semiconductor charge transport suggesting that the charge transport is dominated by defects.

The charge transport measurements on single crystals of $\text{Cs}_3\text{Cu}_8\text{Te}_{10}$ along the (010) plane show that the resistivity at first decreases linearly with decreasing temperature and at low temperatures levels off to a constant value over the temperature range 5-300 K, as shown in Figure 52. The resistivity increases from 1.2×10^{-6} Ωcm at 5 K to 1.1×10^{-3} Ωcm at room temperature. We note that the resistivity at 5 K is the smallest among the known ternary Cu chalcogenide compounds. It would be interesting to search for superconducting transition under pressure in this material.

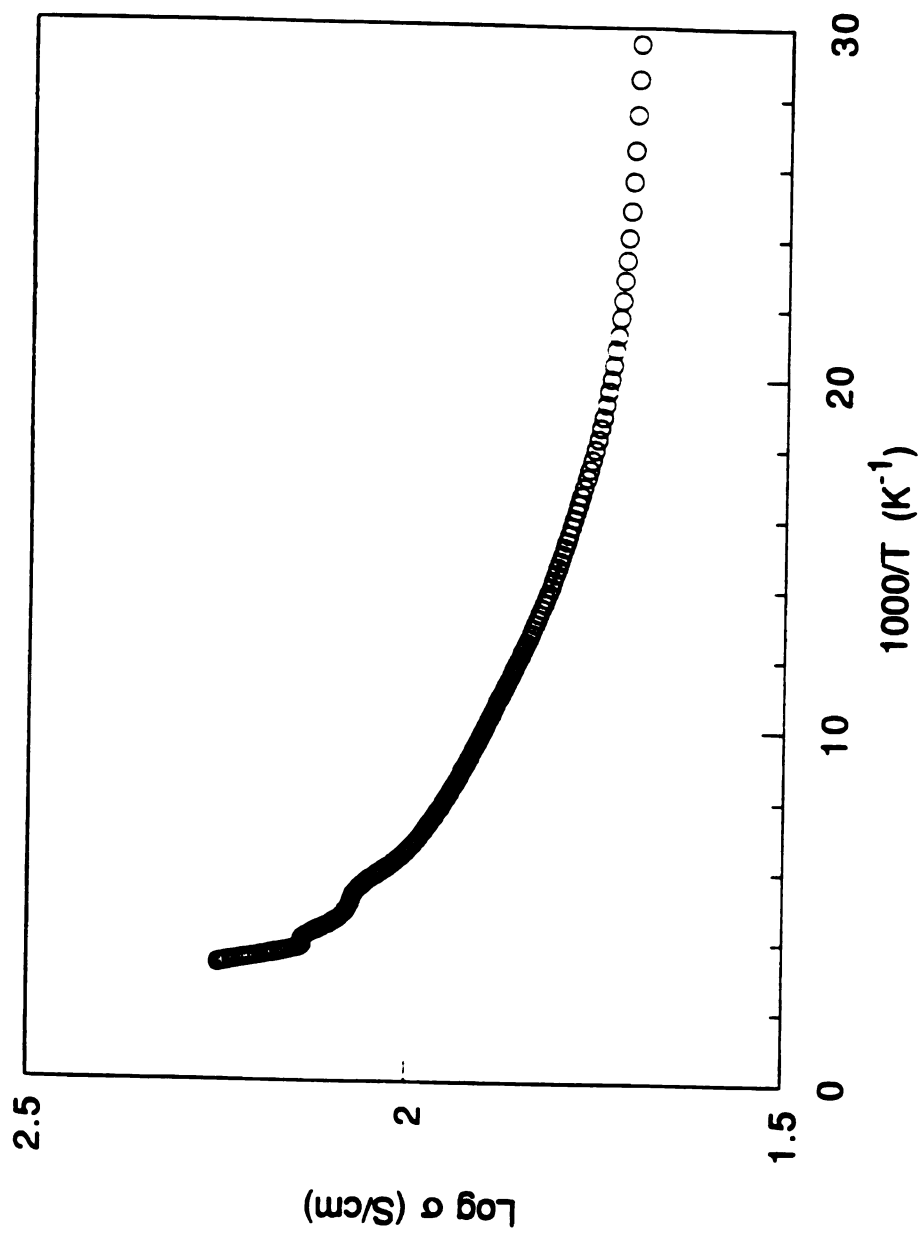


Figure 51. Four probe electrical conductivity (Scm^{-1}) data as a function of temperature for a single crystal of $\text{K}_4\text{Cu}_8\text{Te}_{11}$.

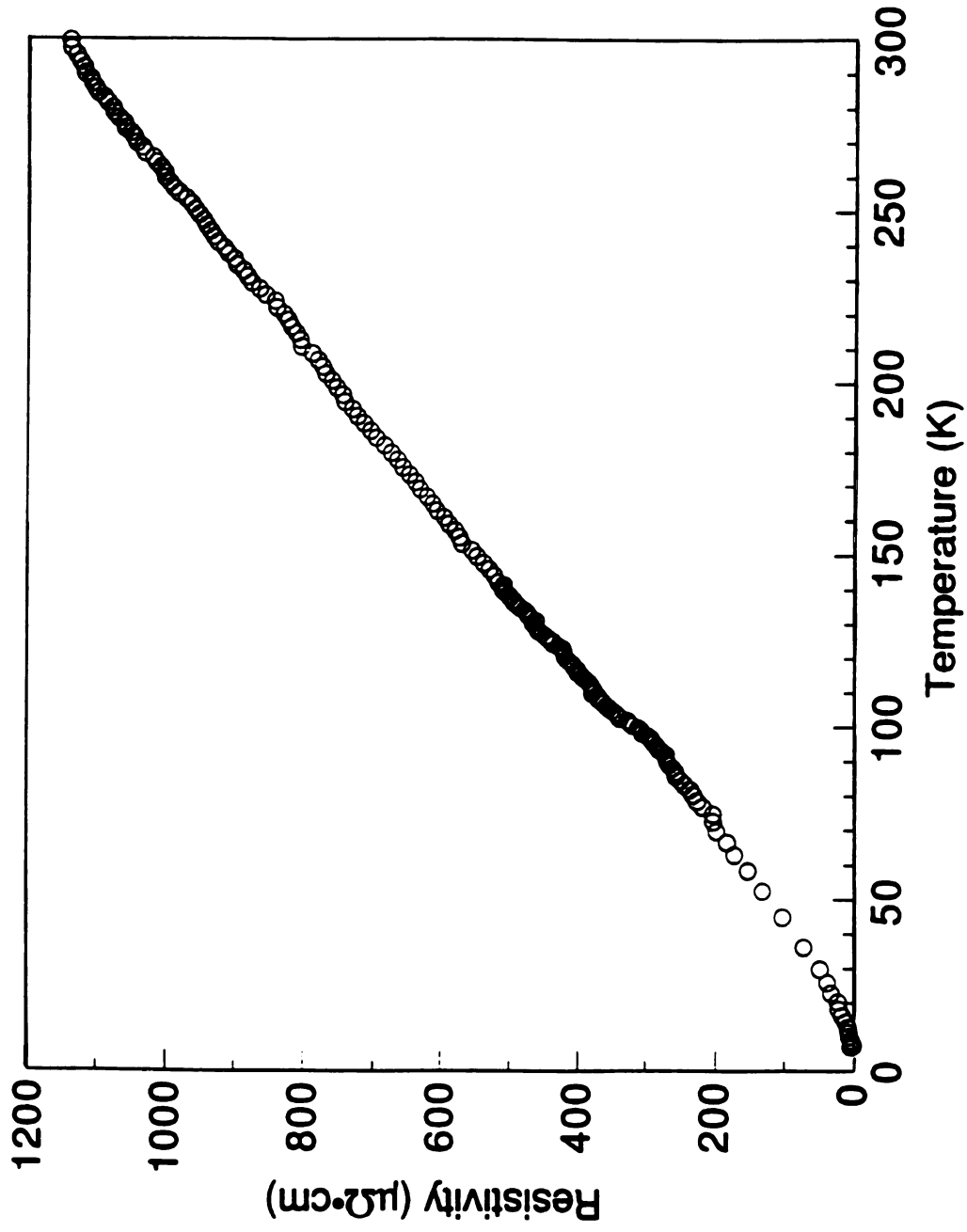


Figure 52. Four probe resistivity ($\mu\Omega\cdot\text{cm}$) data as a function of temperature for a single crystal of $\text{Cs}_3\text{Cu}_6\text{Te}_{10}$.

The temperature dependence of the thermoelectric power (Seebeck coefficient) shows a very small positive value of 1~6 $\mu\text{V/K}$ in the temperature range of 90~300 K as shown in Figure 53. The small and linearly increasing Seebeck coefficient with rising temperature indicates that $\text{Cs}_3\text{Cu}_8\text{Te}_{10}$ is a p-type metal as expected from the band filling argument advanced in the previous section.

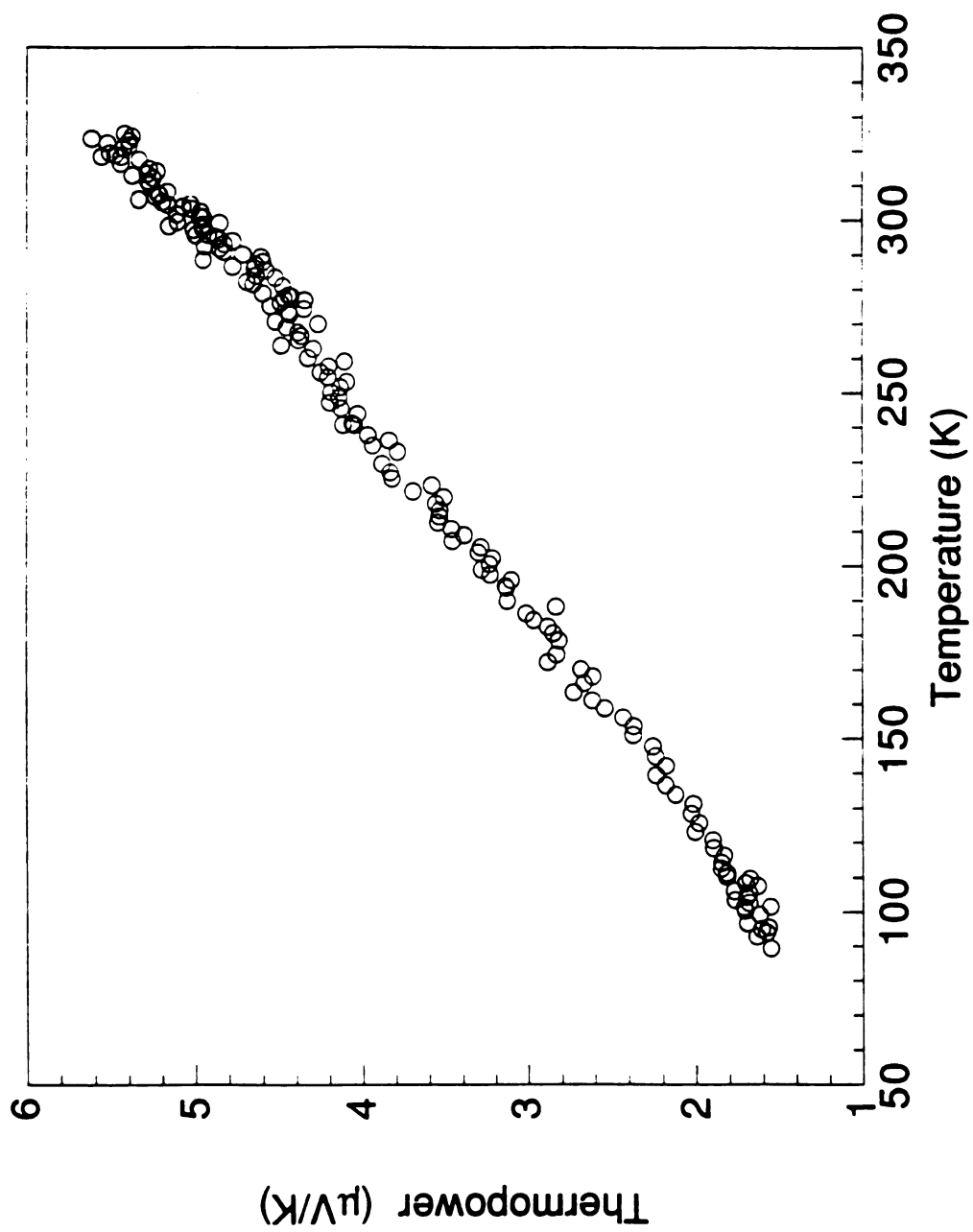


Figure 53. Variable-temperature thermoelectric power ($\mu\text{V}/\text{K}$) data for a single crystal of $\text{Cs}_3\text{Cu}_8\text{Te}_{10}$.

3.5. Magnetic Susceptibility of $\text{Cs}_3\text{Cu}_8\text{Te}_{10}$ (II)

Variable temperature magnetic susceptibility data for $\text{Cs}_3\text{Cu}_8\text{Te}_{10}$ over the temperature range 5-300 K are shown in Figure 54. When plotted as χ^{-1} vs temperature, the data above 30 K show temperature independent paramagnetism, while below 30 K the data follow a Curie-Weiss Law. This behavior is characteristic of metals (Pauli paramagnetism) containing a low concentration of paramagnetic impurities. The temperature independent Pauli paramagnetism ($\chi_p=23.4 \times 10^{-5}$ emu/mol) has been obtained by subtracting the Curie-Weiss portion of the paramagnetism from the measured magnetic susceptibility.

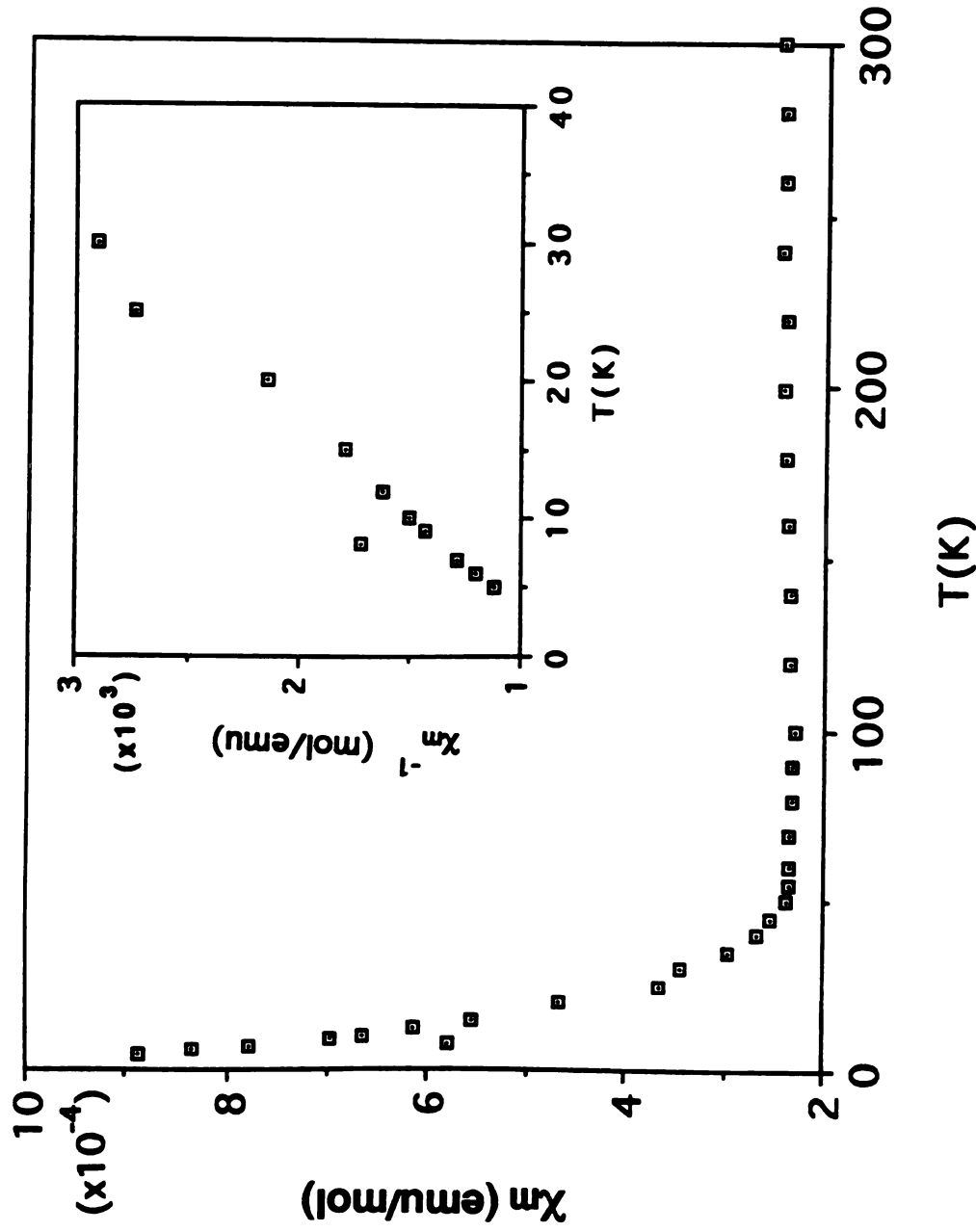


Figure 54. Variable-temperature magnetic susceptibility (emu/mol) data for polycrystalline $\text{Cs}_3\text{Cu}_6\text{Te}_{10}$. Inset: χ_m^{-1} (mol/emu) vs T .

CHAPTER 7

Synthesis and Characterization of Mixed Chalcogenide Compounds of $\text{KCu}_4\text{S}_2\text{Te}$, $\text{K}_3\text{Cu}_8\text{S}_4\text{Te}_2$, and $\text{Cu}_{17.6}\text{Te}_8\text{S}_{26}$

1. Introduction

The synthesis and characterization of new materials is the essential step to understanding materials properties, discovering new properties, and often leads to the technological advances. We have been exploring new ternary metal chalcogenide compounds using alkali metal polychalcogenide fluxes as solvents and reagents at an intermediate temperature regime ($150 < T < 500$ °C). We have been quite successful in synthesizing novel structural compounds of (poly)sulfides, (poly)selenides, and (poly)tellurides of various transition metals in which a variety of new structural motifs have been discovered.^{50,53,54} (see chapters 2-6) We believe that this molten salt synthesis method can be extended to other systems (e.g. a mixed-chalcogenide system) by combining, for example, K_2S and Te or K_2Te and S together. This approach could yield new materials with unusual structural features because of incorporation of two chalcogen atoms with different sizes atoms as well as coordination preference. In this chapter, we demonstrate our preliminary work in mixed chalcogenide systems. Two mixed-valence compounds, $\text{KCu}_4\text{S}_2\text{Te}$ and $\text{K}_3\text{Cu}_8\text{S}_4\text{Te}_2$ with interesting metallic properties, and one

three-dimensional compound, $\text{Cu}_{17.6}\text{Te}_8\text{S}_{25}$, were prepared in the mixed chalcogenide ($\text{K}_2\text{S}/\text{Te}$ and $\text{K}_2\text{Te}/\text{S}$) fluxes at 350-450 °C.

2. Experimental Section

2.1 Reagents

Chemicals were used as obtained: copper powder, electrolytic dust, purified, Fisher Scientific Co., Fair Lawn, NJ; tellurium powder, -100 mesh, 99.95% purity, Aldrich Chemical Co., Milwaukee, WI; sulfur powder, sublimed, J. T. Baker Chemical Co., Phillipsburg, NJ; potassium metal, analytical reagent, Mallinckrodt Inc., Paris, KY

2.2. Physical Measurements

Magnetic susceptibility measurements were performed on a MPMS Quantum Design SQUID magnetometer over the temperature range 5 K to 300 K for $\text{KCu}_4\text{S}_2\text{Te}$ (at 5 kG) and $\text{K}_3\text{Cu}_8\text{S}_4\text{Te}_2$ (at 7.5 kG) and over the temperature range 2 K to 300 K for $\text{Cu}_{17.6}\text{Te}_8\text{S}_{26}$ (at 100 G). Single crystals of each compound were manually selected for measurements and were used without grinding as random oriented single crystals. The data for $\text{KCu}_4\text{S}_2\text{Te}$ and $\text{K}_3\text{Cu}_8\text{S}_4\text{Te}_2$ were corrected for diamagnetic contributions of the sample holder. To obtain molar susceptibility the corrections for ion-core diamagnetic contributions from atomic constituents of $\text{KCu}_4\text{S}_2\text{Te}$ and $\text{K}_3\text{Cu}_8\text{S}_4\text{Te}_2$ were made using the values tabulated by Mulay¹⁰³. The magnetization of each compound was examined as a function of applied field from 250 G to 8 kG for $\text{KCu}_4\text{S}_2\text{Te}$ and $\text{K}_3\text{Cu}_8\text{S}_4\text{Te}_2$ (at 5 K) and from 200 G to 9.5 kG for

$\text{Cu}_{17.6}\text{Te}_8\text{S}_{26}$ (at 2 K). The magnetization of $\text{KCu}_4\text{S}_2\text{Te}$ and $\text{K}_3\text{Cu}_8\text{S}_4\text{Te}_2$ was found to vary linearly with the applied field, while the magnetization data for $\text{Cu}_{17.6}\text{Te}_8\text{S}_{26}$ showed saturation behavior above 3 kG. It started to converge at 600 G and remain constant above 3 kG as shown in Figure 55.

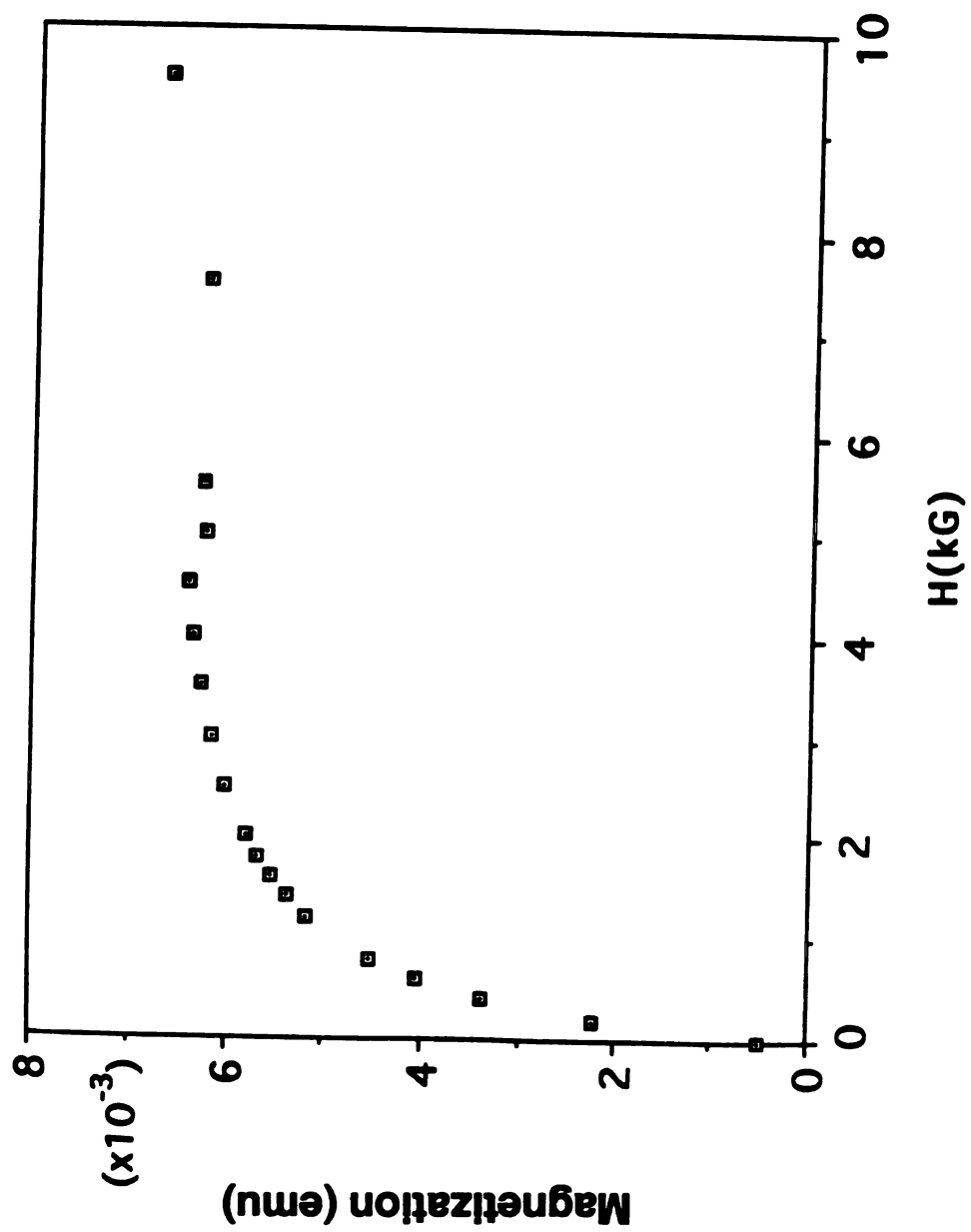


Figure 55. Magnetization (emu) data for polycrystalline $\text{Cu}_{17.6}\text{Te}_{8}\text{S}_{26}$ as a function of applied magnetic field (H).

Four-probe dc resistivity and thermoelectric power data for $\text{KCu}_4\text{S}_2\text{Te}$ were provided by Prof. Carl R. Kannewurf (Northwestern University) over the temperature range 5 K to 300 K. A computer automated measurement system was employed to obtain thermopower and resistivity data with both the current and thermal gradient applied along the (010) plane for $\text{KCu}_4\text{S}_2\text{Te}$. For all measurements, electrode connections to the small single crystals were made with the use of 25 and 60 μm gold wires and gold bonding paste.

Quantitative microprobe analyses of the compounds were performed on a Jeol 35CF scanning electron microscopy equipped with Tracor Northern TN 5500 X-ray microanalysis attachment. Single crystals of each sample were carefully picked and mounted on an aluminum stub using conducting silver paint to help dissipate charges that developed on the sample surface during measurements. Energy Dispersive Spectra (EDS) were obtained using the following experimental set-up:

X-ray detector position : 55 mm

Working distance : 39 mm

Accelerating voltage : 20 KV

Take-off angle : 27 deg

Beam current : 200 picoamps

Accumulation time : 100 seconds

Window : Be

A standardless quantitative analysis (SQ) program was used to analyze the X-ray spectra obtained. Since the Cu ratio is always overestimated due to the contribution from system Cu peaks, a correction factor ($\times 0.73$), determined by calibrating known K/Cu/Te compounds, was used to evaluate Cu percentage.

2.3. Synthesis

Chemicals were measured and loaded in Pyrex tubes under a dry nitrogen atmosphere in a Vacuum Atmospheres Dri-Lab glovebox. Potassium monosulfide (K_2S) and potassium monotelluride (K_2Te) were prepared in liquid ammonia from potassium and elemental sulfur (or tellurium) in a 2:1 ratio.

Potassium bis(μ_4 -sulfido)(μ_8 -telluro)tetracuprate(I,II), KCu_4S_2Te (I) 0.165 g (1.5 mmol) of K_2S , 0.048 g (0.75 mmol) of Cu and 0.510 g (4.0 mmol) of Te were mixed together and loaded in a Pyrex tube which was flame-sealed under vacuum ($\sim 10^{-3}$ torr). The tube was placed in a computer-controlled furnace and heated at 450 °C for 4 days and cooled slowly to 100 °C at a rate of 2 °C/hr then to 50 °C at a rate of 10 °C/hr. Black rectangular-shaped crystals were obtained by removing excess potassium polychalcogenides (K_2Te_x , K_2S_y , $K_2Te_nS_m$) with DMF under a N_2 atmosphere (yield: 83.6 % based on Cu used). A quantitative microprobe analysis performed on a large number of crystals with the EDS/SEM system gave an average composition of $KCu_{3.7}S_{2.0}Te_{1.1}$.

Tripotassium tetra(μ_4 -sulfido)bis(μ_6 -telluro)octacuprate(I,II), $K_3Cu_8S_4Te_2$ (II) 0.165 g (1.5 mmol) of K_2S , 0.032 g (0.5 mmol) of Cu and 0.319 g (2.5 mmol) of Te were mixed together and loaded in a Pyrex tube which was flame-sealed under vacuum ($\sim 10^{-3}$ torr). The tube was placed in a computer-controlled furnace and heated at 450 °C for 4 days and slowly cooled to 100 °C at a rate of 2 °C/hr, then to 50 °C at a rate of 10 °C/hr. Black needle-like crystals were obtained by removing excess potassium polychalcogenides (K_2Te_x , K_2S_y) with DMF under a N_2 atmosphere (yield: 71.4 % based on Cu used). A quantitative microprobe analysis performed on a large number of

single crystals with the EDS/SEM system gave an average composition of $K_3Cu_{8.3}S_{4.2}Te_{1.9}$.

Copper tellurium sulfide, $Cu_{17.6}Te_8S_{26}$ (III) 0.103 g (0.5 mmol) of K_2Te and 0.032 g (0.5 mmol) of Cu and 0.128 g (4.0 mmol) of S were mixed together and loaded in a Pyrex tube which was flame-sealed under vacuum ($\sim 10^{-3}$ torr). The tube was placed in a computer-controlled furnace and heated at 350 °C for 4 days and cooled slowly to 100 °C at a rate of 2 °C/hr, then to 50 °C at a rate of 10 °C/hr. Black cubic-shaped crystals were obtained by removing excess potassium polychalcogenides with DMF under a N_2 atmosphere. The products were contaminated with some amounts of yellow needle crystals of K_2TeS_3 ¹⁰⁷; these were easily removed by washing with water (yield: 45 % based on Cu used). A quantitative microprobe analysis performed on a large number of single crystals with the EDS/SEM system gave an average composition of $Cu_{17}Te_{7.6}S_{26}$.

2.4. X-ray Crystallographic Studies

All compounds were examined by X-ray powder diffraction for phase characterization and identification. The d-spacings for each compound were obtained from powder pattern recorded on a Phillips XRG-3000 computer-controlled powder diffractometer, operating at 40KV, 35 mA. Graphite monochromated Cu radiation was used. To verify product homogeneity, the d-spacings observed for the bulk materials were compared, and found to be in accord, with those calculated from the single crystal X-ray structure analysis data. The calculation of d-spacings was performed using the POWD10 program⁵⁶. The results are summarized in Tables 77-79.

Table 77. Calculated and Observed X-ray Powder Diffraction Pattern of $\text{KCu}_4\text{S}_2\text{Te}$

H K L	d_{calc} (Å)	d_{obs} (Å)	I/I _{max} (obs.)
0 0 1	10.22	10.16	94.9
0 0 2	5.11	5.09	23.0
1 0 0	3.87	3.87	9.3
1 0 1	3.62	3.63	18.3
0 0 3	3.40	3.40	21.5
1 0 2	3.08	3.08	69.7
1 0 3 (0 0 4)	2.55	2.55	40.2
1 1 2	2.415	2.408	51.3
1 1 3	2.135	2.131	100
0 0 5	2.044	2.042	49.1
2 0 0	1.9381	1.9372	37.0
1 1 4	1.8689	1.8638	16.6
1 0 5	1.8080	1.8056	20.1
0 0 6	1.7033	1.7023	65.4
2 1 2	1.6416	1.6392	26.0

Table 78. Calculated and Observed X-ray Powder Diffraction Pattern of $K_3Cu_8S_4Te_2$

H K L	d_{calc} (Å)	d_{obs} (Å)	I/I _{max} (obs.)
0 0 1	9.68	9.63	15.2
-2 0 1	7.33	7.25	100
0 0 3	3.22	3.23	22.8
-4 0 3 (6 0 0)	2.91	2.91	48.8
5 1 0	2.60	2.60	29.6
1 1 3	2.409	2.403	33.7
-5 1 3	2.212	2.211	15.2
-7 1 1	2.142	2.140	34.6
-1 1 4	2.090	2.086	31.2
6 0 3 (0 2 0)	1.962	1.962	34.6
-7 1 4 (-9 1 2)	1.7572	1.7500	22.1
-8 0 5	1.6383	1.6390	31.2

Table 79. Calculated and Observed X-ray Powder Diffraction Pattern of $\text{Cu}_{17.6}\text{Te}_8\text{S}_{26}$

H K L	$d_{\text{calc}} (\text{\AA})$	$d_{\text{obs}} (\text{\AA})$	I/I _{max} (obs.)
2 0 0	5.11	5.11	11.1
2 2 0	3.61	3.62	31.4
2 2 2	2.95	2.96	100
3 2 1	2.73	2.74	16.8
4 0 0	2.55	2.56	20.8
3 3 0 (4 1 1)	2.413	2.411	12.5
4 2 0	2.289	2.229	14.7
4 2 2	2.089	2.092	18.1
5 1 0 (4 3 1)	2.007	2.009	7.9
5 2 1	1.8692	1.8710	10.9
4 4 0	1.8099	1.8129	71.5
4 3 3	1.7558	1.7587	6.8
4 4 2	1.7064	1.7079	9.5
6 1 1	1.6609	1.6635	12.5
6 2 0	1.6188	1.6209	12.0
6 2 2	1.5435	1.5458	44.3

The single crystal data of $\text{KCu}_4\text{S}_2\text{Te}$ were collected on a Nicolet P3 four circle diffractometer with graphite monochromated Mo-K_α radiation using the θ - 2θ scan mode. The single crystal data of $\text{K}_3\text{Cu}_8\text{S}_4\text{Te}_2$ and $\text{Cu}_{17.6}\text{Te}_8\text{S}_{26}$ were collected on a Rigaku AFC6S diffractometer with graphite monochromated Mo-K_α radiation using the ω - 2θ scan mode. Accurate unit cell parameters for all compounds were obtained from least-squares refinement of the 2θ , ω , χ , and ϕ values of 20-25 machine-centered reflections. The stability of the experimental setup and crystal integrity were monitored by measuring three standard reflections periodically (every 100 reflections) during data collection. The intensities did not show any appreciable decay. Two absorption corrections were applied to the data of all compounds: an empirical absorption correction based on ψ scans for three reflections followed by a DIFABS⁵⁷ correction. The structure of (I) was solved with direct methods using SHELXS-86⁵⁸ and was refined with the SDP⁵⁹ package of crystallographic programs. The structures of (II) and (III) were solved with direct methods using SHELXS-86 and were refined with the TEXSAN⁶⁰ package of crystallographic programs. All calculations were performed on a VAXstation 3100 computer.

During the isotropic structural refinement of (III), high temperature factors of 9.678 and 3.881 \AA^2 are observed for Cu(2) and S(2) atoms respectively implying a partial site occupancy of these atoms. Thus, the site occupancies of Cu(2) and S(2) were refined individually by fixing every other atom position. The refined Cu(2) site occupancy was 46.64 % of that allowed, whereas the refined S(2) site occupancy was 105.53 %. Since this S(2) atom site occupancy is physically unrealistic, it was fixed at 100 %. Upon fixing the site occupancy of Cu(2) atom at 46.64 %, further isotropic refinement followed by DIFABS absorption correction gave an R/Rw value of 4.1/4.6 with Beq of Cu(2) and S(2) being 2.25 \AA^2 and 4.61 \AA^2 , respectively. Even though the temperature

factor of S(2) atom is large, anisotropic refinement of all atoms was carried out, resulting in final R/Rw value of 2.9/3.8. If the S(2) site occupancy is adjusted downwards by creating a small vacancy, we obtain a higher minimum R/Rw value of 3.0/4.1. Therefore, full site occupancy of S(2) seem reasonable even though its temperature factor is high at 4.587 \AA^2 . Based on this refinement, nonstoichiometric structural formula of $\text{Cu}_{17.6}\text{Te}_8\text{S}_{26}$ was obtained. The complete data collection parameters and details of the structure solution and refinement for (I), (II), and (III) are given in Table 80. The final atomic coordinates, temperature factors and their estimated standard deviations are shown in Tables 81-83.

Table 80. Summary of Crystallographic Data for $\text{KCu}_4\text{S}_2\text{Te}$, $\text{K}_3\text{Cu}_8\text{S}_4\text{Te}_2$, and $\text{Cu}_{17.6}\text{Te}_8\text{S}_{26}$

	compound		
	I	II	III
Formula	$\text{KCu}_4\text{S}_2\text{Te}$	$\text{K}_3\text{Cu}_8\text{S}_4\text{Te}_2$	$\text{Cu}_{17.6}\text{Te}_8\text{S}_{26}$
Formula weight	484.99	1009.10	2966.13
space group	P4/mmm	C2/m	I-43m
a (Å)	3.8762(7)	17.936(3)	10.2385(6)
b (Å)	3.8762(7)	3.912(3)	10.2385(6)
c (Å)	10.220(3)	9.924(2)	10.2385(6)
α (deg)	90.0	90.0	90.0
β (deg)	90.0	102.58(2)	90.0
γ (deg)	90.0	90.0	90.0
Vol (Å ³), Z	153.6(1), 1	679.6(8), 2	1073.27(7), 1
Temperature (°C)	23	23	23
Crystal size (mm)	0.13x0.13x0.05	0.57x0.05x0.05	0.13x0.10x0.08
Radiation	Mo-K α	Mo-K α	Mo-K α
μ (Mo-K α , cm ⁻¹)	195.9	180.2	152.8
D_{calc} (g/cm ³)	5.24	4.93	4.59
$2\theta_{\text{max}}$ (deg)	50	50	55
Scan method	$\theta/2\theta$	$\omega/2\theta$	$\omega/2\theta$
No. of data collected	627	1241	510
No. of unique data	117	697	258
No. of data used ($F_o^2 > 3\sigma(F_o^2)$)	107	589	222
No. of atoms	4	9	5
No. of variables	13	53	18
Phasing technique	Direct methods	Direct methods	Direct methods
Final R/R _w (%)	2.96/3.15	3.7/5.6	2.9/3.8
Max. shift/esd (last cycle)	0.0	0.0	0.0
Extinction coefficient	1.93×10^{-6}	N/A	6.09×10^{-5}

Table 81. Fractional Atomic Coordinates and B_{eq} Values for $\text{KCu}_4\text{S}_2\text{Te}$ with Their Estimated Standard Deviations in Parentheses

Atom	x	y	z	$B_{\text{eq}}^{\text{a}}, \text{\AA}^2$
Te	0	0	0	0.93(2)
Cu	1/2	0	0.8101(2)	1.67(3)
K	0	0	1/2	1.74(8)
S	1/2	1/2	0.6882(5)	1.10(6)

^a B values for anisotropically refined atoms are given in the form of the isotropic equivalent displacement parameter defined as $B_{\text{eq}} = (4/3)[a^2B_{11} + b^2B_{22} + c^2B_{33} + ab(\cos \gamma)B_{12} + ac(\cos \beta)B_{13} + bc(\cos \alpha)B_{23}]$.

Table 82. Fractional Atomic Coordinates and B_{eq} Values for $\text{K}_3\text{Cu}_8\text{S}_4\text{Te}_2$ with Their Estimated Standard Deviations in Parentheses

Atom	x	y	z	$B_{\text{eq}}^{\text{a}}, \text{\AA}^2$
Te	0.33526(5)	0	0.8650(1)	1.44(4)
Cu(1)	0.4811(1)	0	0.8508(2)	1.42(7)
Cu(2)	0.3882(1)	-1/2	0.7150(2)	2.10(8)
Cu(3)	0.2960(1)	0	0.5642(2)	2.24(9)
Cu(4)	0.4217(1)	-1/2	0.9838(2)	1.69(8)
S(1)	0.1569(2)	0	0.5158(3)	0.8(1)
S(2)	0.5293(2)	-1/2	0.7860(3)	0.8(1)
K(1)	1/2	0	1/2	1.7(2)
K(2)	0.3274(2)	0	1.2222(3)	1.7(1)

^a B values for anisotropically refined atoms are given in the form of the isotropic equivalent displacement parameter defined as $B_{\text{eq}} = (4/3)[a^2B_{11} + b^2B_{22} + c^2B_{33} + ab(\cos \gamma)B_{12} + ac(\cos \beta)B_{13} + bc(\cos \alpha)B_{23}]$

Table 83. Fractional Atomic Coordinates and B_{eq} Values for $\text{Cu}_{17.6}\text{Te}_8\text{S}_{26}$ with Their Estimated Standard Deviations in Parentheses

Atom	x	y	z	B_{eq}^{a} , Å ²
Te	0.25978(8)	0.2598	0.2598	1.1812(4)
Cu(1)	1/4	1/2	0	2.4(1)
Cu(2)	0.2149(7)	0	0	2.7(2)
S(1)	0.1108(3)	0.1108	0.3578(3)	1.60(9)
S(2)	0	0	0	4.587(5)

^a B values for anisotropically refined atoms are given in the form of the isotropic equivalent displacement parameter defined as $B_{\text{eq}} = (4/3)[a^2B_{11} + b^2B_{22} + c^2B_{33} + ab(\cos \gamma)B_{12} + ac(\cos \beta)B_{13} + bc(\cos \alpha)B_{23}]$.

3. Results and Discussion

3.1. Synthesis

Synthesis of the mixed chalcogenide compounds of $\text{KCu}_4\text{S}_2\text{Te}$ and $\text{K}_3\text{Cu}_8\text{S}_4\text{Te}_2$ has been readily achieved using mixed-chalcogenide fluxes ($\text{K}_2\text{S}/\text{Te}$) as solvents and reagents at 450°C as shown in eq 1.



where the ratios of $n/m/q$ are $3/1.5/8$ and $3/1/5$ for (I) and (II) respectively. Surprisingly, when we used another possible combination of mixed-chalcogenide flux ($\text{K}_2\text{Te}/\text{S}$) at 350°C as shown in eq 2,



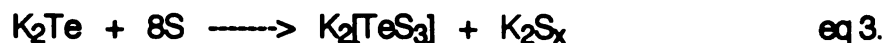
the new structural compound of $\text{Cu}_{17.6}\text{Te}_8\text{S}_{26}$ was obtained. The equations given above are not balanced and only show the reactants used (in left-hand side) and products isolated (in right-hand side). After reaction, excess mixed-chalcogenide fluxes were easily removed from the products by washing with DMF. All compounds are stable in the air and moisture for several days.

During the study of new ternary chalcogenide materials in the A_2Q_x flux, it came to our attention that it is possible to have mixed-chalcogenide fluxes by simply combining, for example, K_2S and Te or K_2Te and S . We expected new structural compounds in this mixed chalcogenide system due to the incorporation of two chalcogenides with different size into the lattice. We chose

S and Te because the combination of S and Se or Se and Te, which are similar in size, might result in positional disorder between them.

In the beginning small crystals of $\text{KCu}_4\text{S}_2\text{Te}$ were obtained in the reactant ratios $\text{K}_2\text{S}/\text{Cu}/\text{Te}$ of 1~4/1/8 at 350 °C with contaminations of elemental tellurium and a few yellow needle-like crystals of known K_2TeS_3 ¹¹². Since the K_2TeS_3 phase was soluble in water, it was easily removed from the product by washing with water. We varied reaction conditions in order to increase product homogeneity and single crystal size for charge transport property measurements. Upon changing Cu metal ratios and the reaction temperature, large single crystals (up to 2mm) of $\text{KCu}_4\text{S}_2\text{Te}$ were obtained as a pure phase from the 3/1.5/8 ratio at 450 °C. A parallel approach used in an effort to obtain a homogeneous $\text{KCu}_4\text{S}_2\text{Te}$ phase, was to lower the Te ratio at 450 °C. We thought this might suppress the elemental Te in the final product. However, it resulted in unexpected isolation of new mixed chalcogenide compound $\text{K}_3\text{Cu}_8\text{S}_4\text{Te}_2$ in high yield from the $\text{K}_2\text{S}/\text{Cu}/\text{Te}$ ratios of 3/1/5~6. In addition to the two new mixed chalcogenide compounds (I) and (II) there is at least one more promising phase in this system. Golden brown needle-like crystals were obtained as a minor phase from the 3/1/8 ratio at 350 °C along with $\text{KCu}_4\text{S}_2\text{Te}$. These crystals have the approximate compositions of KCu_2TeS from the EDS/SEM analysis. Unfortunately, attempts, to grow large single crystals of this new phase suitable for X-ray single crystal study, were unsuccessful. This new phase seems to compete with $\text{KCu}_4\text{S}_2\text{Te}$ at 350 °C, but is completely suppressed by increasing the reaction temperature to 450 °C.

Another choice for the mixed-polychalcogenide flux ($\text{K}_2\text{Te}/\text{S}$) showed redox chemistry associated with $\text{Te}^{2-}/4+$. In the sulfur-rich $\text{K}_2\text{Te}/\text{S}$ flux, sulfur atoms oxidize most of Te^{2-} to Te^{4+} while they are reduced to S^{2-} . As a result, $[\text{TeS}_3]^{2-}$ species are formed in the flux as shown in eq 3.



The $[\text{TeS}_3]^{2-}$ species in the flux can act as ligands to Cu^+ atoms to form $\text{Cu}_{17.6}\text{Te}_8\text{S}_{26}$. $[\text{TeS}_3]^{2-}$ ions are also crystallize with K^+ ions as K_2TeS_3 . Fortunately, they are quite soluble in water and can be easily removed by washing with water. $[\text{TeS}_3]^{2-}$ species are not formed in the $\text{K}_2\text{S}/\text{Te}$ flux because S^{2-} is already completely reduced species and can not oxidize Te atoms.

3.2. Description of Structures

3.2.1. Structure of $\text{KCu}_4\text{S}_2\text{Te}$ (I)

$\text{KCu}_4\text{S}_2\text{Te}$ is isostructural to the known mixed-valence compound KCu_4S_3 ⁶¹. The structure of $\text{KCu}_4\text{S}_2\text{Te}$ is shown in Figure 56. A tellurium atom replaces the eight-coordinate sulfur atom in KCu_4S_3 ^{61(a)}. The structure is composed of double layers and charge compensating K^+ ions. The $[\text{Cu}_4\text{S}_2\text{Te}]_n^{n-}$ double layer is made of fused anti PbO-type Cu_2STe layers. The plane composed of tellurium atoms along the (010) plane coincides with a mirror plane which bisects the $[\text{Cu}_4\text{S}_2\text{Te}]_n^{n-}$ double layer. This double layer is shown in Figure 57. Based on the formula $\text{KCu}_4\text{S}_2\text{Te}$ and on the assumption that the oxidation state on each S and Te atom is -2, the formal oxidation state on copper is +1 (three atoms) and +2 (one atom). However, the coexistence of Cu^{2+} and Q^{2-} is thermodynamically unstable with respect to electron transfer from the reducing Q^{2-} to the oxidizing Cu^{2+} . Thus, all copper atoms are +1 and the one electron vacancy (hole) resides on chalcogen atoms. The known mixed-valence compound KCu_4S_3 was also formulated as

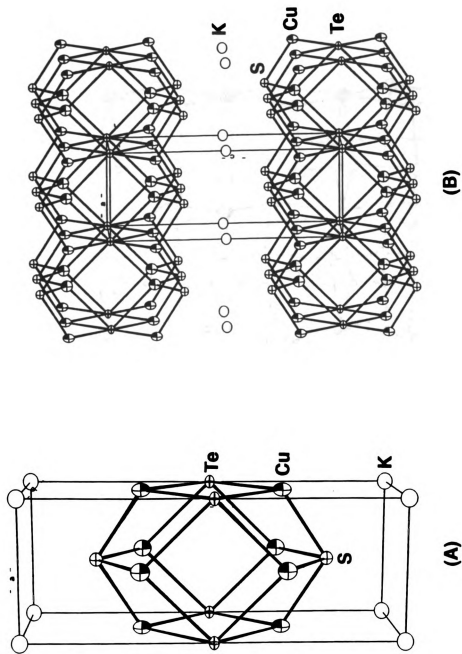


Figure 56. ORTEP representation of (A) the unit cell and (B) the layered framework of $\text{KCu}_4\text{S}_2\text{Te}$. The origin of the unit cell has been moved to $(0,0,1/2)$ in (A) for clear view of a building unit.

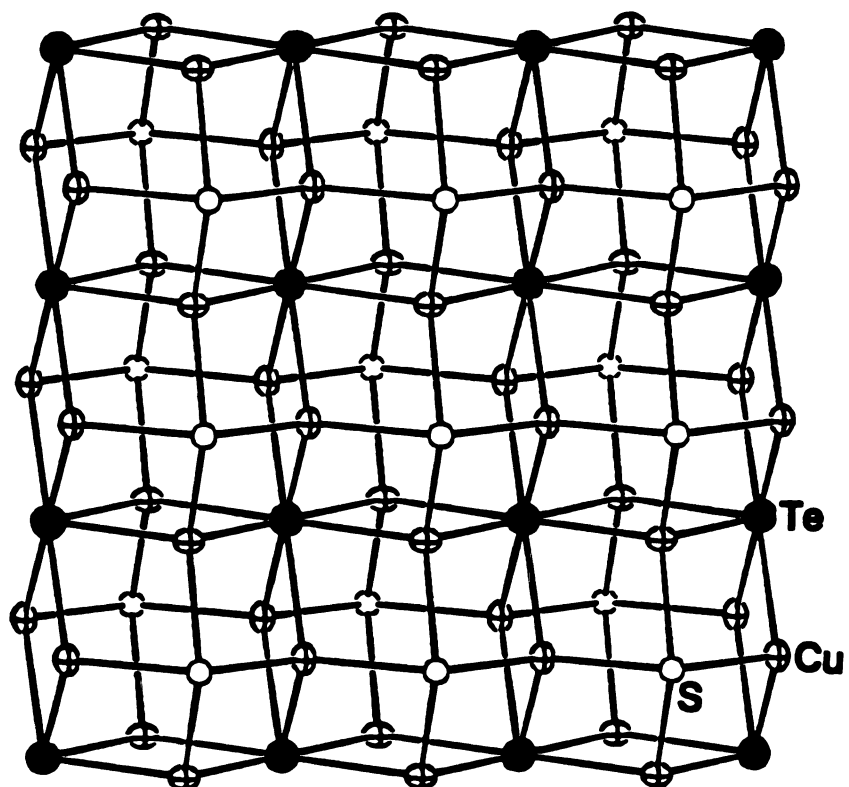


Figure 57. ORTEP representation of the $[\text{Cu}_4\text{S}_2\text{Te}]_n^{n-}$ layer. Black circles are Te, open circles are S, and crossed circles are Cu atoms.

$K^+(Cu^+)_4(S^{2-})_2S^{.61(a)}$ Since there is only one crystallographically distinct Te atom in the asymmetric unit and this is more likely to be oxidized compared to S atom, the hole probably resides on this Te atom. This results in -1 formal oxidation state of Te, creating a partially empty valence band. Thus the chemical formula can be represented as $K^+(Cu^+)_4(S^{2-})_2Te^-$. Of course, these are only the formal oxidation state. The actual description is more complicated due to small electronegativity difference among Cu, S, and Te atoms.

The Cu atoms are situated on a mm crystallographic site and have distorted tetrahedral geometry. They are bonded to two sulfur atoms and two tellurium atoms. The sulfur atoms, which are situated on a $4mm$ crystallographic site, are bonded to four Cu atoms and have a square pyramidal geometry. The Cu-S-Cu bond angles of $73.1(1)^\circ$ and $114.5(2)^\circ$ are comparable to those found in $KCu_4S_3^{61(a)}$. The tellurium atom on the $4/mmm$ site is bonded to eight Cu atoms with a square prismatic geometry. The Cu-S bond distance of $2.304(3) \text{ \AA}$ is very close to that ($2.312(2) \text{ \AA}$) of KCu_4S_3 . If one considers the effective ionic radius of Te^{1-} to be smaller than that of Te^{2-} , the Cu-Te bond distance should be shorter than the normal Cu-Te bond distance. However, the Cu-Te bond distance is in the normal range of $2.743(1) \text{ \AA}$. This is probably due to the higher coordination number (8) of Te atoms. The average S-Cu-S bond angle is $114.5(2)^\circ$, comparable to that found in KCu_4S_3 ($115.0(1)^\circ$). However, the Te-Cu-Te bond angle of $89.92(5)^\circ$ strongly deviates from the ideal tetrahedral angle. This is because substitution of a Te atom for a S atom in the parent compound KCu_4S_3 did not cause significant changes in the cell parameters along the a - and b -axis. One would have expected tellurium substitution to increase in cell parameters of (l) due to its larger size. However, similar chemical environments and spatial requirements of K^+ ions in both compounds prevent the cell parameters from changing along the a - and b -

axis. Thus, to accommodate a longer Cu-Te bond, the cell increases only along the crystallographic *c*-axis, resulting in a smaller Te-Cu-Te bond angle. There are short Cu---Cu contacts at 2.741(1) Å, very similar to that (2.757 Å) of KCu₄S₃. The Te-Te contacts of 3.8762(7) Å along the *a*- and *b*-axis are too large to be considered as a significant Te-Te interactions. Selected bond distances and angles are given in Table 84. There is only one crystallographically distinct K⁺ ion situated on a 4/*mmm* site. It is surrounded by eight sulfur atoms in a square prismatic geometry. It participates in ionic interactions only with S atoms. The average K--S distance is 3.349(3) Å which is close to that (3.351(2) Å) of KCu₄S₃^{61(a)}.

Table 84. Selected Bond Distances (Å) and Angles (deg) in $\text{KCu}_4\text{S}_2\text{Te}$ with Standard Deviations in Parentheses

Te-Cu	2.743(1) (x8)	Cu-Te-Cu	89.92(4) (x4)
		Cu-Te-Cu	90.09(4) (x4)
		Cu-Te-Cu	180.(0) (x4)
		Cu-Te-Cu	59.95(2) (x8)
		Cu-Te-Cu	120.05(2) (x8)
Cu-S	2.304(3) (x2)	Cu-S-Cu	114.5(2) (x2)
		Cu-S-Cu	73.1(1) (x4)
Cu-Cu	2.741(1)	Te-Cu-Te	89.92(5)
		Te-Cu-S	112.49(6) (x4)
K-S	3.349(3) (x8)	S-Cu-S	114.5(2)

3.2.2. Structure of $K_3Cu_8S_4Te_2$ (II)

$K_3Cu_8S_4Te_2$ is isostructural to the known mixed valence compound $K_3Cu_8S_6$ ⁷¹. The structure of $K_3Cu_8S_4Te_2$ is shown in Figure 58. It is composed of two-dimensional layers and charge balancing K^+ ions. The layer of $[Cu_8S_4Te_2]_n^{3n-}$ is made of two easily recognizable fragments: (a) $[Cu_4Q_4]_n^{3n-}$ type column found in $Na_3Cu_4Se_4$ (see Figure 11) and (b) the anti PbO-type CuQ layer found in $NaCuTe$ (see Figure 41). These two fragments are fused together to form the $[Cu_8S_4Te_2]_n^{3n-}$ layer. The $[Cu_8S_4Te_2]_n^{3n-}$ layer is shown in Figure 59. Based on the formula $K_3Cu_8S_4Te_2$ and on the assumption that the oxidation state on each S and Te atom is -2, the formal oxidation state on copper would be +1 (seven atoms) and +2 (one atom). However, Cu^{2+} ions are easily reduced to Cu^{+1} in the presence of reducing Q^{2-} ions. Thus, all copper atoms are +1 and the one electron vacancy (hole) resides on the chalcogen atoms. The known mixed-valence compound $K_3Cu_8S_6$ was formulated as $K^+_3(Cu^+)_8(S^{2-})_5S^{1-}$.⁷¹ Since there are two crystallographically equivalent Te atoms in the asymmetric unit and the Te atom is more likely to be oxidized compared to the S atom, the hole is expected to delocalize on the Te atoms. This gives -1.5 formal oxidation state for each Te atom, creating a partially empty valence band. Thus, the structural formula can be represented as $K^+_3(Cu^+)_8(S^{2-})_4(Te^{1.5-})_2$.

There are four crystallographically distinct Cu atoms in $K_3Cu_8S_4Te_2$. Two Cu atoms, Cu(1) and Cu(4), in the $[Cu_4Q_4]_n^{3n-}$ column have distorted trigonal planar geometry. Cu(1) atoms are bonded to two S(2) atoms at 2.287(2) Å and one Te atom at 2.650(2) Å. Cu(4) atoms are bonded to one S(2) atom at 2.262(4) Å and two Te atoms at 2.612 (2) Å. These Cu-Te bond distances are comparable to that of the three coordinate Cu atoms in

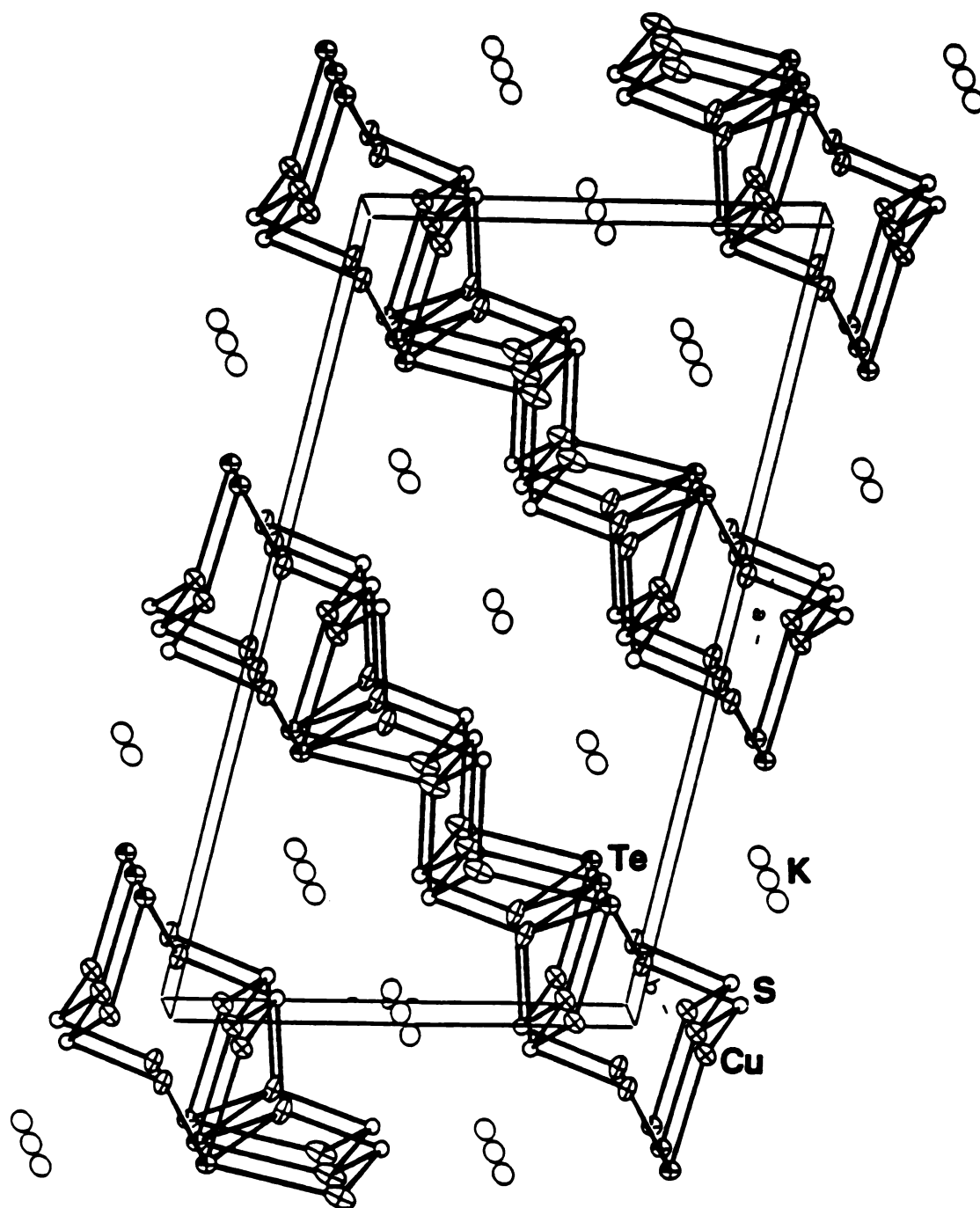


Figure 58. ORTEP representation of the unit cell of $K_3Cu_8S_4Te_2$.

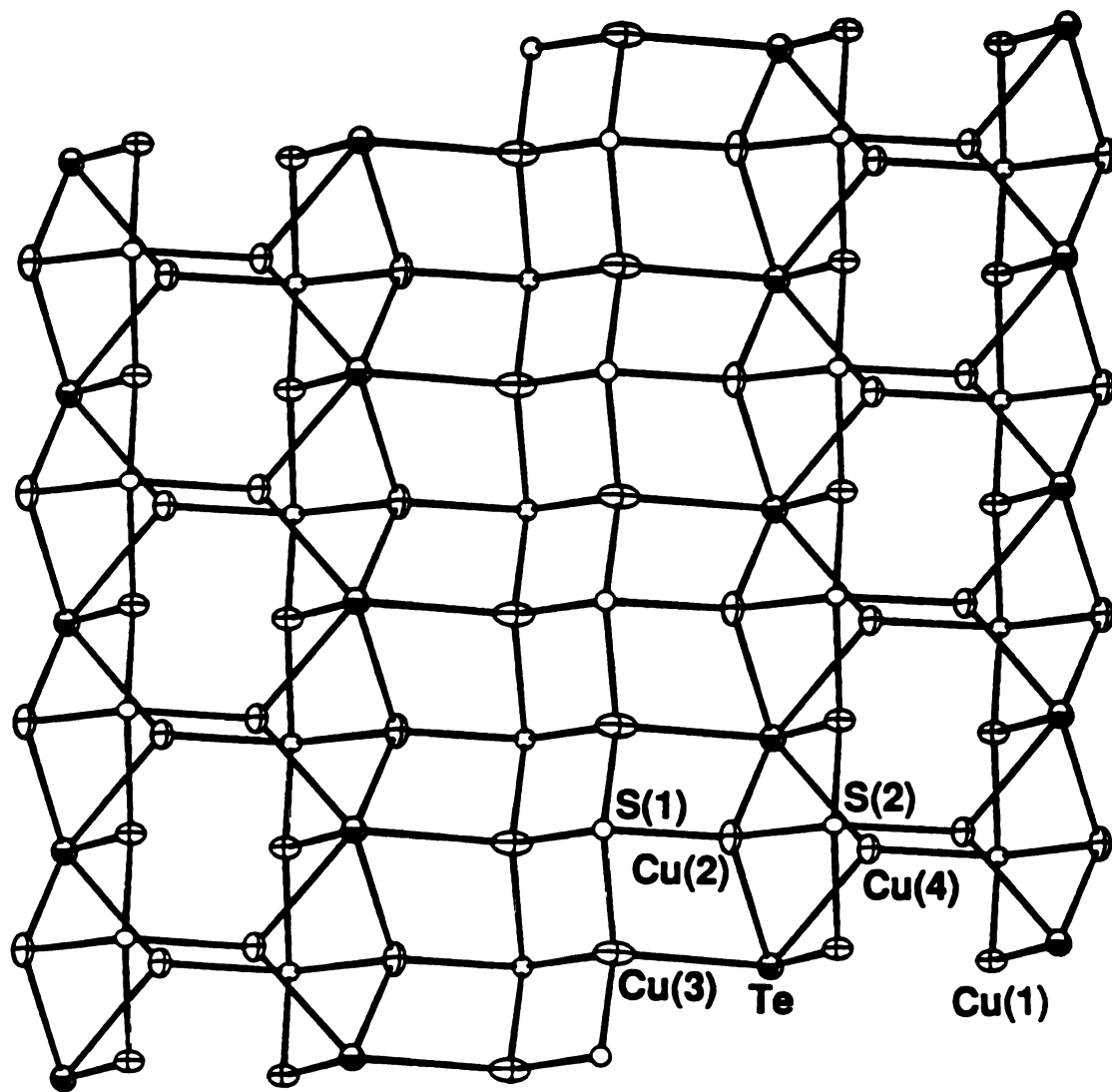
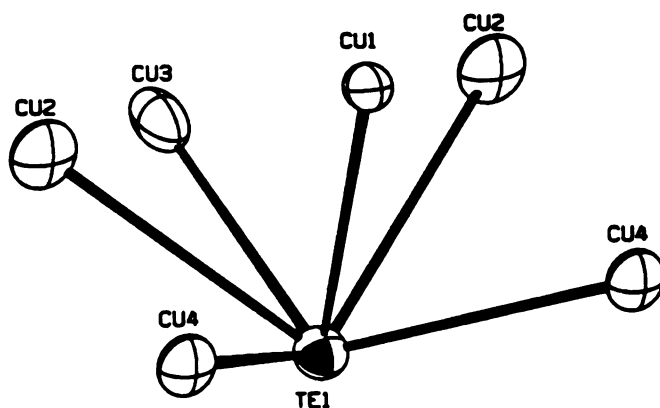


Figure 59. ORTEP representation and labeling scheme of the $[\text{Cu}_8\text{S}_4\text{Te}_2]_n^{3n-}$ layer.

NaCu_3Te_2 ⁹⁷ (2.575(8) Å). Two other Cu atoms (Cu(2) and Cu(3)) in the CuQ layer fragment have distorted tetrahedral geometry. Cu(2) atoms are bonded to two S atoms and two Te atom while Cu(3) atoms are bonded to three S(1) atoms and one Te atom. The average Cu-S bond distances are 2.37(15) Å for Cu(2) and 2.37(6) Å for Cu(3) which are very close to those of $\text{K}_3\text{Cu}_8\text{S}_6$ ⁷¹ (2.34(15) Å and 2.32(4) Å, respectively). The Cu-Te distances are 2.749(3) Å for Cu(2) and 2.914(3) Å for Cu(3). This Cu(3)-Te bond distance of 2.914(3) Å is slightly longer than the normal Cu-Te bond distances of known compounds with four coordinate Cu atoms. In $\text{K}_3\text{Cu}_8\text{S}_6$, the Cu-S bond distance corresponding to this Cu(3)-Te bond is much longer at 2.84 Å compared to the normal Cu-S bond distance of 2.30 Å. There are short Cu-Cu contacts in the range of 2.604(3)~2.779(2) Å.

There are two crystallographically distinct sulfur atoms and one tellurium atom in the asymmetric unit. Both sulfur atoms have square pyramidal geometry while the tellurium atom has 6 Cu atoms around it as shown in the following scheme.



This μ_6 -coordination of the chalcogen atom is unusual even though it is found in similar structural compound of KCu_3S_2 ⁷⁰. The average Cu-Te distance is 2.71(12) Å. Selected bond distances and angles are given in Table 85. There are two crystallographically distinct K atoms in the asymmetric unit located between the $[\text{Cu}_8\text{S}_4\text{Te}_2]_n^{3n-}$ layers. The K(1) atom has 4 sulfur atoms around it. The shortest K-S bond distance is 3.392(3) Å. This K(1) atom does not have any interaction with Te atoms. The K(2) atom has 3 Te atoms and 4 S atoms around it. The shortest K-Te and K-S distances are 3.412(3) Å and 3.127(4) Å respectively.

Table 85. Selected Bond Distances (Å) and Angles (deg) in $K_3Cu_8S_4Te_2$ with Standard Deviations in Parentheses

Cu(1)-S(2)	2.287(2) (x2)	Cu(2)-S(1)-Cu(3)	109.0(2)
Cu(2)-S(1)	2.257(4)	Cu(2)-S(1)-Cu(3)	74.4(1) (x2)
Cu(2)-S(2)	2.476(4)	Cu(3)-S(1)-Cu(3)	113.6(2)
Cu(3)-S(1)	2.435(4)	Cu(3)-S(1)-Cu(3)	68.7(1) (x2)
Cu(3)-S(1)	2.337(3) (x2)	Cu(1)-S(2)-Cu(1)	117.6(2)
Cu(4)-S(2)	2.262(4)	Cu(1)-S(2)-Cu(2)	69.77(9) (x2)
		Cu(1)-S(2)-Cu(4)	78.6(1) (x2)
		Cu(2)-S(2)-Cu(4)	115.8(2)
Cu(1)-Te	2.650(2)	Cu(1)-Te-Cu(2)	60.66(5) (x2)
Cu(2)-Te	2.749(2) (x2)	Cu(1)-Te-Cu(3)	88.11(7)
Cu(3)-Te	2.914(3)	Cu(1)-Te-Cu(4)	61.86(5) (x2)
Cu(4)-Te	2.612(2) (x2)	Cu(4)-Te-Cu(4)	96.96(8)
		Cu(2)-Te-Cu(2)	90.71(8)
		Cu(2)-Te-Cu(3)	58.69(5) (x2)
		Cu(2)-Te-Cu(4)	58.06(6) (x2)
		Cu(2)-Te-Cu(4)	122.43(7) (x2)
		Cu(3)-Te-Cu(4)	116.75(5) (x2)
Cu(1)-Cu(2)	2.728(2)	Te-Cu(1)-S(2)	116.93(9) (x2)
Cu(1)-Cu(4)	2.705(2)	S(2)-Cu(1)-S(2)	117.6(2)
Cu(2)-Cu(3)	2.779(2)	Te-Cu(2)-S(1)	117.38(8) (x2)
Cu(2)-Cu(4)	2.604(3)	Te-Cu(2)-S(2)	107.35(7) (x2)
Cu(3)-Cu(3)	2.693(3)	Te-Cu(2)-Te	90.71(8)
Cu(4)-Cu(4)	2.757(4)	S(1)-Cu(2)-S(2)	114.0(2)

Table 85. (cont'd)

K(1)-S(1)	3.402(3) (x2)	Te-Cu(3)-S(1)	102.2(1)
K(1)-S(2)	3.392(3) (x2)	Te-Cu(3)-S(1)	108.9(1) (x2)
		S(1)-Cu(3)-S(1)	111.3(1) (x2)
K(2)-S(1)	3.217(4) (x2)	S(1)-Cu(3)-S(1)	113.6(2)
K(2)-S(2)	3.245(4) (x2)	Te-Cu(4)-Te	96.96(8)
K(2)-Te	3.579(4)	Te-Cu(4)-S(2)	121.19(7) (x2)
K(2)-Te	3.462(3)		
K(2)-Te	3.462(3)		

3.2.3. Structure of $\text{Cu}_{17.6}\text{Te}_8\text{S}_{26}$ (III)

Structurally, the compound $\text{Cu}_{17.6}\text{Te}_8\text{S}_{26}$ is related to the tetrahedrite mineral class and can be represented by the general formula $\text{M}_{12}\text{X}_4\text{S}_{13}$ ($\text{M}=\text{Cu}, \text{Ag}, \text{Zn}, \text{Cd}, \text{Fe}, \text{Hg}$; $\text{X}=\text{Sb}, \text{As}, \text{Bi}$)¹¹³. $\text{Cu}_{17.6}\text{Te}_8\text{S}_{26}$ has a group IVB metal (Te atom) occupying the X site in $\text{M}_{12}\text{X}_4\text{S}_{13}$. The structure of $\text{Cu}_{17.6}\text{Te}_8\text{S}_{26}$ can be viewed as the derivative of the sphalerite structure (ZnS). One complete unit cell ($\text{Cu}_{12}\text{Te}_8\text{S}_{24}$)(Cu_6S) is shown in Figure 60. The Te is formally in the +4 oxidation state. In this structure there are easily recognizable TeS_3^{2-} units. These TeS_3^{2-} units, which are isoelectronic to SO_3^{2-} , bridge Cu atoms via sulfur atoms to form a three dimensional framework similar to that in sphalerite, but with large voids inside it. In fact, Te atoms occupy the tetrahedral Zn site in sphalerite but are bonded to only three sulfur atoms. The fourth coordination site is occupied by the Te lone electron pair. This results in relatively large empty cages (cavities) in the structure. These cavities are then filled with Cu_6S units as in the tetrahedrite structure. In tetrahedrite there are two Cu_6S units on the (0, 0, 0) and (1/2, 1/2, 1/2) positions per unit cell. However, the substitution of Te^{4+} for Sb^{3+} creates an electron deficiency in the framework resulting in the 53.3 % vacancy of Cu(2) atoms in Cu_6S . Therefore, the voids are actually filled with $\text{Cu}_{2.8}\text{S}$ units instead of Cu_6S units, with the 2.8 Cu atoms occupying equally the 6 possible sites. Thus, the structural formula unit of $\text{Cu}_{17.6}\text{Te}_8\text{S}_{26}$ can be reformulated as $[\text{Cu}_{12}(\text{TeS}_3)_8](\text{Cu}_{2.8}\text{S})_2$. Based on this nonstoichiometric structural formula and on the assumption that the formal charge of Te and S are +4 and -2 respectively, a nonintegral oxidation state is expected for Cu. There are two crystallographically distinct Cu atoms in the asymmetric unit. The Cu(1) atom in the $[\text{Cu}_{12}(\text{TeS}_3)_8]$ cage has slightly distorted tetrahedral geometry with four S(1) atoms around it. The average

3.2.3. Structure of $\text{Cu}_{17}\text{Te}_{28}$ (III)

Structurally, the compound $\text{Cu}_{17}\text{Te}_{28}$ is related to the tetrahedral mineral class and can be represented by the general formula $\text{M}_2\text{X}_4\text{S}_{12}$ ($\text{M}=\text{Cu, Ag, Zn, Cd, Fe, Hg, X}=\text{Sb, As, Bi, I, Te}$). $\text{Cu}_{17}\text{Te}_{28}$ has a group IVB metal (Te atom) occupying the X site in $\text{M}_2\text{X}_4\text{S}_{12}$. The structure of $\text{Cu}_{17}\text{Te}_{28}$ can be viewed as the derivative of the sphalerite structure (2Cu). One complete unit cell ($\text{Cu}_{12}\text{Te}_{24}$) is shown in Figure 80. The Te is formally in the +4 oxidation state. In this structure there are easily recognizable TeS_2 units. These TeS_2 units which are isolated in Sb_2S_3 have Cu atoms via sulfur atoms to form a three dimensional framework similar to that of sphalerite, but with large voids inside it. In fact, Te atoms occupy the tetrahedral Zn site in sphalerite but are bonded to only three sulfur atoms. The fourth coordination site is occupied by the Te lone electron pair. This results in relatively large empty cages (voids) in the framework. The voids are then filled with Cu_6 units as in the lattice structure. In describing these two Cu_6 units on the (0, 0, 0) and (1/2, 1/2, 1/2) positions per unit cell. However, the substitution of Te⁴⁺ for Sb^{3+} creates an electron deficiency in the framework resulting in the 23.3% vacancy of Cu(S) atoms in Cu_6 . Therefore, the voids are actually filled with Cu_5S units instead of Cu_6S units, with the 2.8 Cu atoms occupying equally the 6 possible sites. Thus the structural formula unit of $\text{Cu}_{17}\text{Te}_{28}$ can be reformulated as $[\text{Cu}_{12}\text{Te}_{24}]_2(\text{Cu}_5\text{S})_2$. Based on this nonstoichiometric structural formula and on the assumption that the formal charge of Te and S are +4 and -2 respectively, a nonintegral oxidation state is expected for Cu. There are two crystallographically distinct Cu atoms in the asymmetric unit. The Cu(1) atom in the $[\text{Cu}_{12}\text{Te}_{24}]$ cage has slightly distorted tetrahedral geometry with four S(1) atoms around it. The average

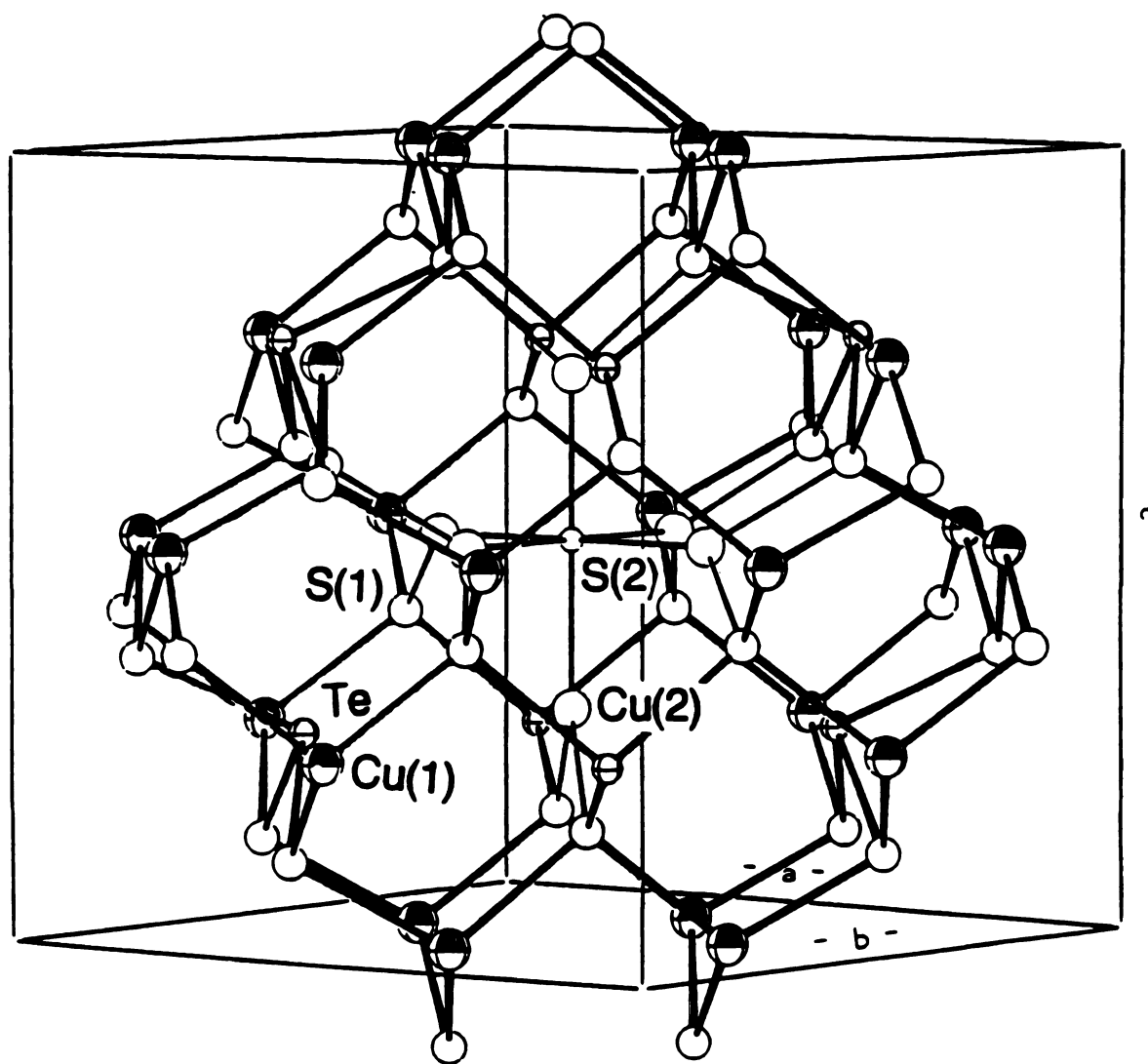


Figure 60. ORTEP representation and labeling scheme of the unit cell of $\text{Cu}_{17.6}\text{Te}_8\text{S}_{26}$.

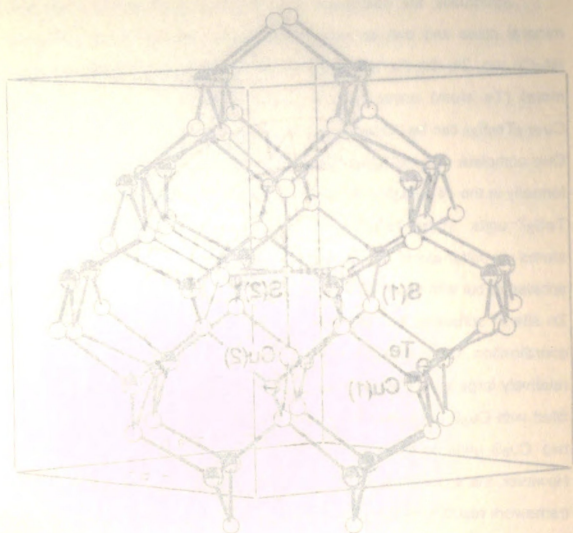


Figure 80. ORTEP representation and labeling scheme of the unit cell of $\text{Cu}_{7.8}\text{Te}_{8.25}$.

Cu(1)-S(1) bond distance is 2.333(3) Å which is comparable to that in the known $\text{Cu}_{12}\text{Sb}_4\text{S}_{13}$ ¹¹³. The Cu(2) atom of the $\text{Cu}_{2.8}\text{S}$ unit has trigonal planar geometry with one S(2) atom and two S(1) atoms around it. The average Cu(2)-S bond distance at 2.182(6) Å is slightly smaller than that (2.26(2) Å) in the known $\text{Cu}_{12}\text{Sb}_4\text{S}_{13}$, but is very similar to that (2.192(4) Å) of three coordinated Cu atoms in CuS ⁶². The coordination environments of the metal and S atoms are shown in Figure 61. The Te atoms are situated on a 3m crystallographic site, possessing trigonal pyramidal geometry with three sulfur atoms and one lone pair of electrons. The lone pairs of the Te atoms in the $\{\text{Cu}_{12}(\text{TeS}_3)_8\}$ cage are related with each other by a four fold screw axis. Four of them are pointing outside the cage and the rest are pointing inside the cage. The Te-S bond distance at 2.377(4) Å compares favorably to that (2.358(5) Å) of known BaTeS_3 ¹¹⁴. Without considering the Cu(2) site vacancy, the S(1) atom of the $\{\text{Cu}_{12}(\text{TeS}_3)_8\}$ cage has tetrahedral geometry with two Cu(1) atoms, one Cu(2) atom, and one Te atom around it, while the S(2) atom (on the -43m site) inside the cage has octahedral geometry with 6Cu(2) atoms around it. The Cu(2)-S(2) distance is 2.189(9) Å. Selected bond distances and angles are given in Table 86.

$\text{Cu}(1)-\text{S}(1)$ bond distance is $2.333(3)$ Å which is comparable to that in the known $\text{Cu}_{12}\text{S}_{24}\text{I}_{12}$. The $\text{Cu}(2)$ atom of the Cu_2S_2 unit has trigonal planar geometry with one $\text{S}(2)$ atom and two $\text{S}(1)$ atoms around it. The average $\text{Cu}(2)-\text{S}$ bond distance at $2.182(6)$ Å is slightly smaller than that ($2.26(2)$ Å) in the known $\text{Cu}_2\text{S}_2\text{I}_2$, but is very similar to that ($2.192(4)$ Å) of three coordinated Cu atoms in Cu_2S_2 . The coordination environments of the metal and S atoms are shown in Figure 81. The Te atoms are situated on a 3m crystallographic site, possessing trigonal pyramidal geometry with three sulfur atoms and one lone pair of electrons. The lone pairs of the Te atoms in the $\text{Cu}_{12}\text{Te}_2\text{S}_2\text{I}_2$ cage are related with each other by a four fold screw axis. Four of them are pointing outside the cage and the rest are pointing inside the cage. The Te-S bond distance at $2.377(4)$ Å compares favorably with $2.36(2)$ Å of known BaTe_2I_4 . Without coordination, the $\text{Cu}(1)$ and $\text{Cu}(2)$ atoms, one of the $\text{Cu}_{12}\text{Te}_2\text{S}_2\text{I}_2$ cage has tetrahedral geometry with two $\text{Cu}(1)$ atoms, one $\text{Cu}(2)$ atom, and one Te atom around it, which is $\text{Cu}(1)-\text{Cu}(1)-\text{Cu}(2)$ and $\text{Cu}(1)-\text{Cu}(2)-\text{Te}$ inside the cage has octahedral geometry, while $\text{Cu}(2)-\text{Cu}(2)-\text{Te}$ and $\text{Cu}(1)-\text{Cu}(1)-\text{Te}$ distance is $2.186(6)$ Å. Bonded bond distances and angles are given in Table 86.

given in Table 86

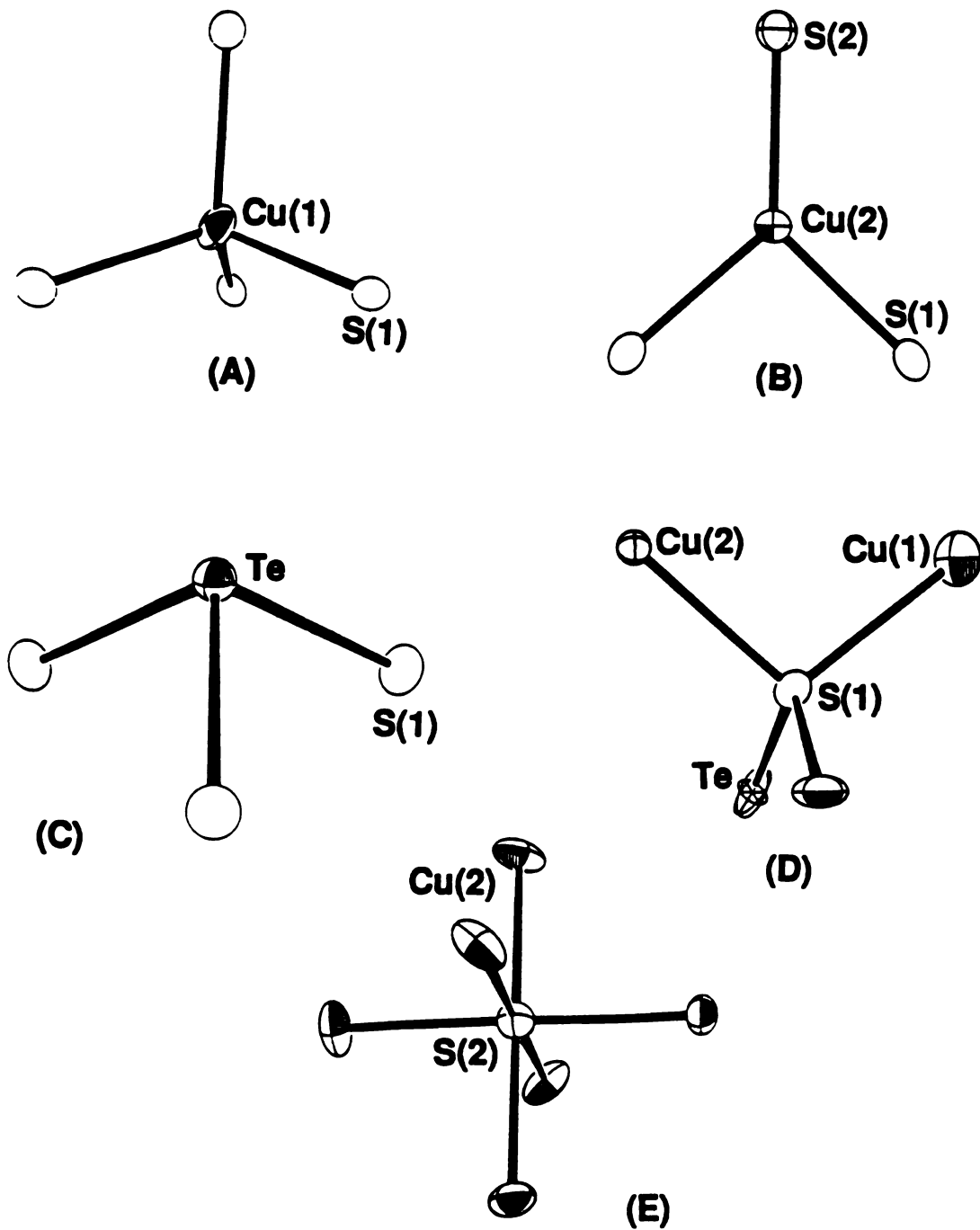


Figure 61. Coordination environments of (A) Cu(1) atom, (B) Cu(2) atom, (C) Te atom, (D) S(1) atom, and (E) S(2) atom in $\text{Cu}_{17.6}\text{Te}_8\text{S}_{26}$.

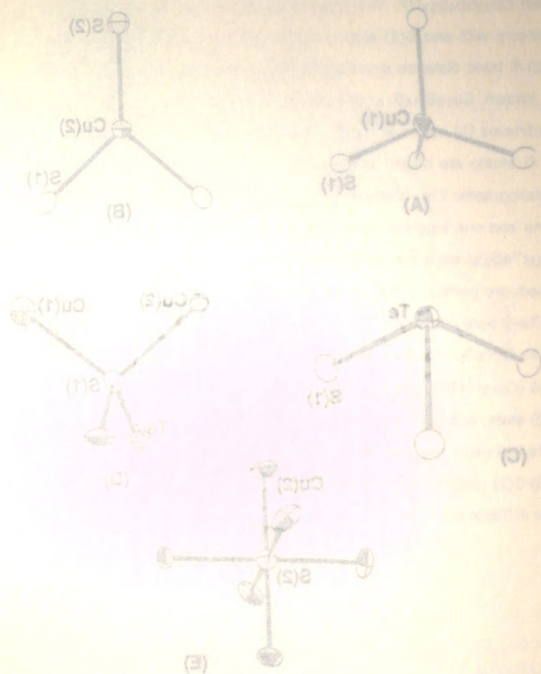


Figure 81. Coordination environments of (A) Cu(1) atom, (B) Cu(2) atom, (C) Te atom, (D) S(1) atom, and (E) S(2) atom in $\text{Cu}_{1.78}\text{Te}_{0.22}$.

Table 86. Selected Bond Distances (Å) and Angles (deg) in $\text{Cu}_{17.6}\text{Te}_8\text{S}_{26}$ with Standard Deviations in Parentheses

Te-S(1)	2.379(4) (x3)	S(1)-Te-S(1)	97.5(1) (x3)
Cu(1)-S(1)	2.332(2) (x4)	S(1)-Cu(1)-S(1)	111.93(9) (x2)
		(1)-Cu(1)-S(1)	104.7(2) (x2)
		S(1)-Cu(1)-S(1)	111.93(9) (x2)
Cu(2)-S(1)	2.171(5) (x2) S	S(1)-Cu(2)-S(1)	95.3(4)
Cu(2)-S(2)	2.201(7)	S(1)-Cu(2)-S(2)	132.4(2) (x2)
		Te-S(1)-Cu(1)	100.6(1) (x2)
		Te-S(1)-Cu(2)	112.7(2)
		Cu(1)-S(1)-Cu(1)	101.8(1)
		Cu(1)-S(1)-Cu(2)	119.1(1) (x2)
		Cu(2)-S(2)-Cu(2)	90.00 (x12)
		Cu(2)-S(2)-Cu(2)	180.00 (x4)

Table 88. Selected Bond Distances (Å) and Angles (deg) in $\text{Cu}_2\text{Te}_2\text{S}_8$ with Standard Deviations in Parentheses

$\text{Cu}(1)-\text{S}(1)$	2.332(2) (x4)	$\text{S}(1)-\text{Cu}(1)-\text{S}(1)$	97.2(1) (x3)
$\text{Cu}(1)-\text{S}(1)$	2.378(4) (x3)	$\text{S}(1)-\text{Te}-\text{S}(1)$	111.93(9) (x5)
$\text{Cu}(2)-\text{S}(2)$	2.501(7)	$\text{S}(1)-\text{Cu}(1)-\text{S}(1)$	104.7(2) (x2)
$\text{Cu}(2)-\text{S}(1)$	2.171(8) (x2) 8	$\text{S}(1)-\text{Cu}(1)-\text{S}(1)$	111.22(9) (x2)
$\text{Cu}(2)-\text{S}(2)$	2.501(7)	$\text{S}(1)-\text{Cu}(2)-\text{S}(1)$	92.3(4)
$\text{Cu}(1)-\text{S}(1)-\text{Cu}(1)$	97.2(1) (x3)	$\text{S}(1)-\text{Cu}(2)-\text{S}(2)$	135.4(2) (x2)
$\text{Cu}(1)-\text{S}(1)-\text{Cu}(2)$	100.8(1) (x2)	$\text{Te}-\text{S}(1)-\text{Cu}(1)$	115.7(2)
$\text{Cu}(1)-\text{S}(1)-\text{Cu}(2)$	115.7(2)	$\text{Te}-\text{S}(1)-\text{Cu}(2)$	101.8(1)
$\text{Cu}(1)-\text{S}(1)-\text{Cu}(1)$	101.8(1)	$\text{Cu}(1)-\text{S}(1)-\text{Cu}(2)$	119.1(1) (x2)
$\text{Cu}(1)-\text{S}(1)-\text{Cu}(2)$	119.1(1) (x2)	$\text{Cu}(2)-\text{S}(2)-\text{Cu}(2)$	90.00 (x12)
$\text{Cu}(2)-\text{S}(2)-\text{Cu}(2)$	90.00 (x12)	$\text{Cu}(2)-\text{S}(2)-\text{Cu}(2)$	180.00 (x4)
$\text{Cu}(2)-\text{S}(2)-\text{Cu}(2)$	180.00 (x4)		

3.3. Charge Transport Properties of $\text{KCu}_4\text{S}_2\text{Te}$ (I)

Based on the band filling arguments advanced above, $\text{KCu}_4\text{S}_2\text{Te}$ and $\text{K}_3\text{Cu}_8\text{S}_4\text{Te}_2$ are expected to be p-type metallic conductors. Charge transport measurements over the temperature range 5-300 K on single crystals of $\text{KCu}_4\text{S}_2\text{Te}$ along the (010) plane show that the resistivity at first decreases linearly with decreasing temperature, but at low temperatures levels off to a constant value (so called residual resistivity) as shown in Figure 62. The resistivity increases from $1.5 \times 10^{-5} \Omega\text{cm}$ at 5 K to $1.2 \times 10^{-4} \Omega\text{cm}$ at room temperature. These values compared favorably with those of KCu_4S_3 which are $1.67 \times 10^{-5} \Omega\text{cm}$ at 20 K and $2.5 \times 10^{-4} \Omega\text{cm}$ at room temperature. Even though KCu_4S_3 and $\text{KCu}_4\text{S}_2\text{Te}$ have the same number of charge carriers $\text{KCu}_4\text{S}_2\text{Te}$ might be expected to have increased conductivity due to the increased overlap between valence orbitals of the larger Te atoms. However, the similar conductivity values clearly suggest that substitution of Te for S has very little effect on the band structure. The temperature dependence of the thermoelectric power (Seebeck coefficient) shows a very small positive value of $1\sim 3 \mu\text{V/K}$ in the temperature range of 50~300 K as shown in Figure 63. The small and linearly increasing Seebeck coefficient with rising temperature indicates that $\text{KCu}_4\text{S}_2\text{Te}$ is a p-type metal.

Unfortunately, charge transport measurements on $\text{K}_3\text{Cu}_8\text{S}_4\text{Te}_2$ are not available yet. They are currently under investigation.

3.3. Charge Transport Properties of KCu_4S_2Te (I)

Unfortunately, charge transport measurements on KCu_4S_2Te are not available yet. They are currently under investigation.

Based on the band filling arguments advanced above, KCu_4S_2Te and $K_2Cu_8S_4Te_2$ are expected to be p-type metallic conductors. Charge transport measurements over the temperature range 5-300 K on single crystals of KCu_4S_2Te along the (010) plane show that the resistivity at first decreases linearly with decreasing temperature, but at low temperatures levels off to a constant value (so called residual resistivity), as shown in Figure 85. The resistivity increases from 1.5×10^{-2} Ohm at 5 K to 1.2×10^{-2} Ohm at room temperature. These values compared favorably with those of KCu_4S_2 which are 1.87×10^{-2} Ohm at 50 K and 2.6×10^{-2} Ohm at room temperature. Even though KCu_4S_2 and KCu_4S_2Te have the same number of charge carriers, KCu_4S_2Te might be expected to have increased conductivity due to the increased overlap between valence orbitals of the Te atoms. However, the similar conductivity values show that the substitution of Te for S has very little effect on the band structure. The structure dependence of the thermoelectric power (Seebeck coefficient) shows a very small positive value of 1-3 μ V/K in the temperature range of 50-300 K as shown in Figure 86. The small and linearly increasing Seebeck coefficient with rising temperature indicates that KCu_4S_2Te is a p-type metal.

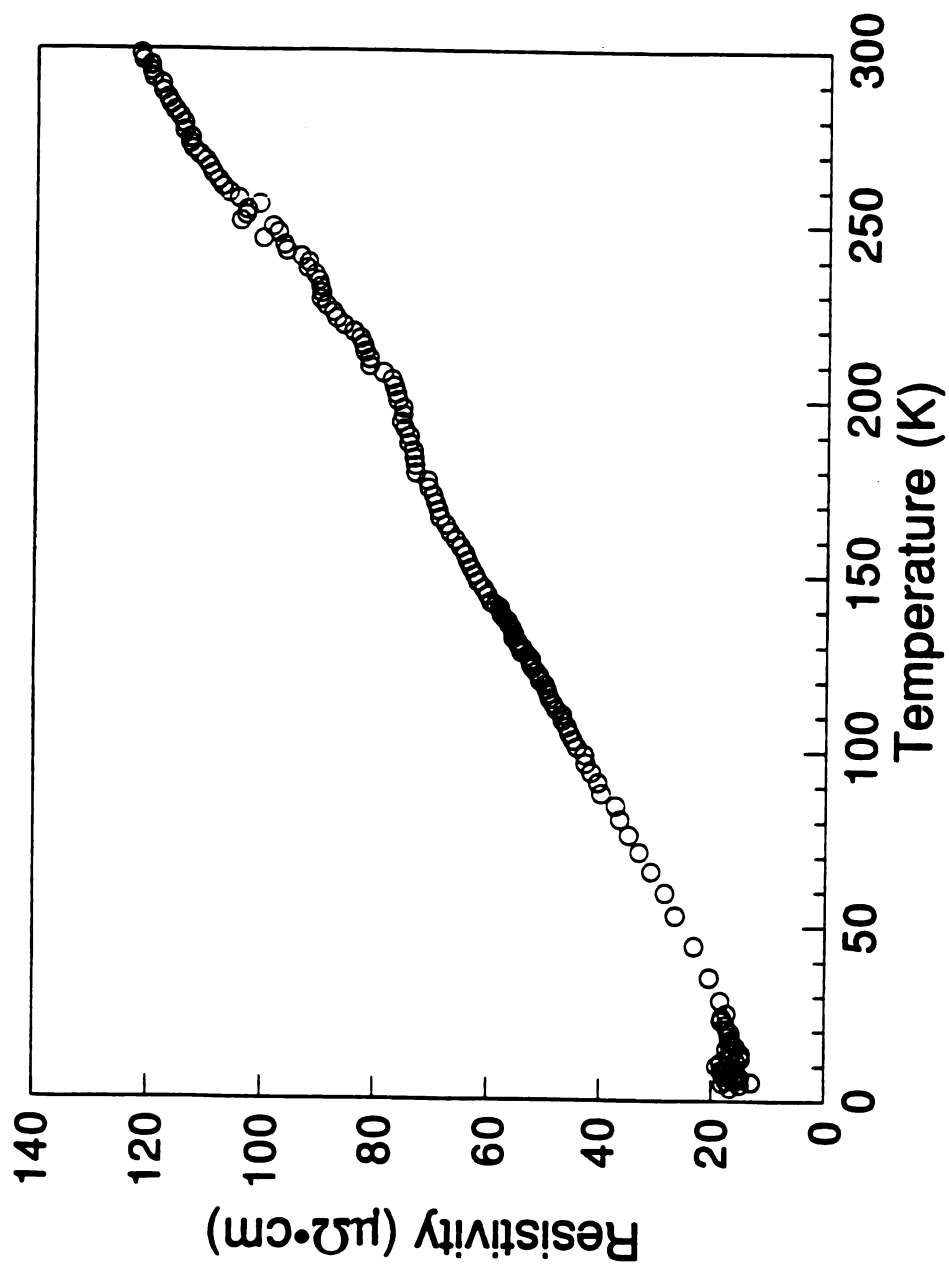
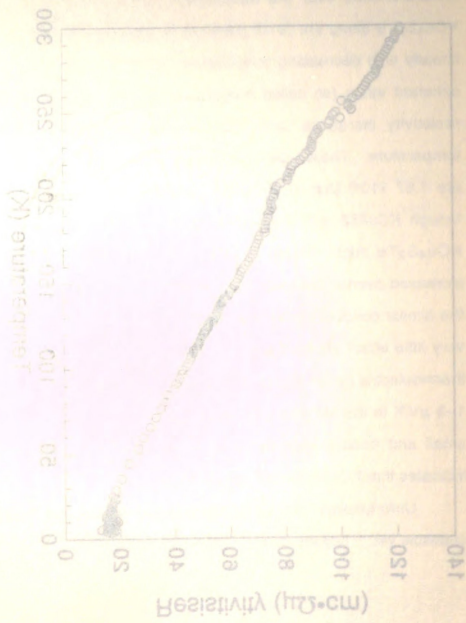


Figure 62. Four probe resistivity ($\mu\Omega\cdot\text{cm}$) data as a function of temperature for a single crystal of $\text{KCu}_4\text{S}_2\text{Te}$.

Figure 10. Plot of resistivity (ρ) versus length (L) for a cylindrical conductor. The data points show a linear relationship, indicating that resistivity is constant for a given material and geometry.



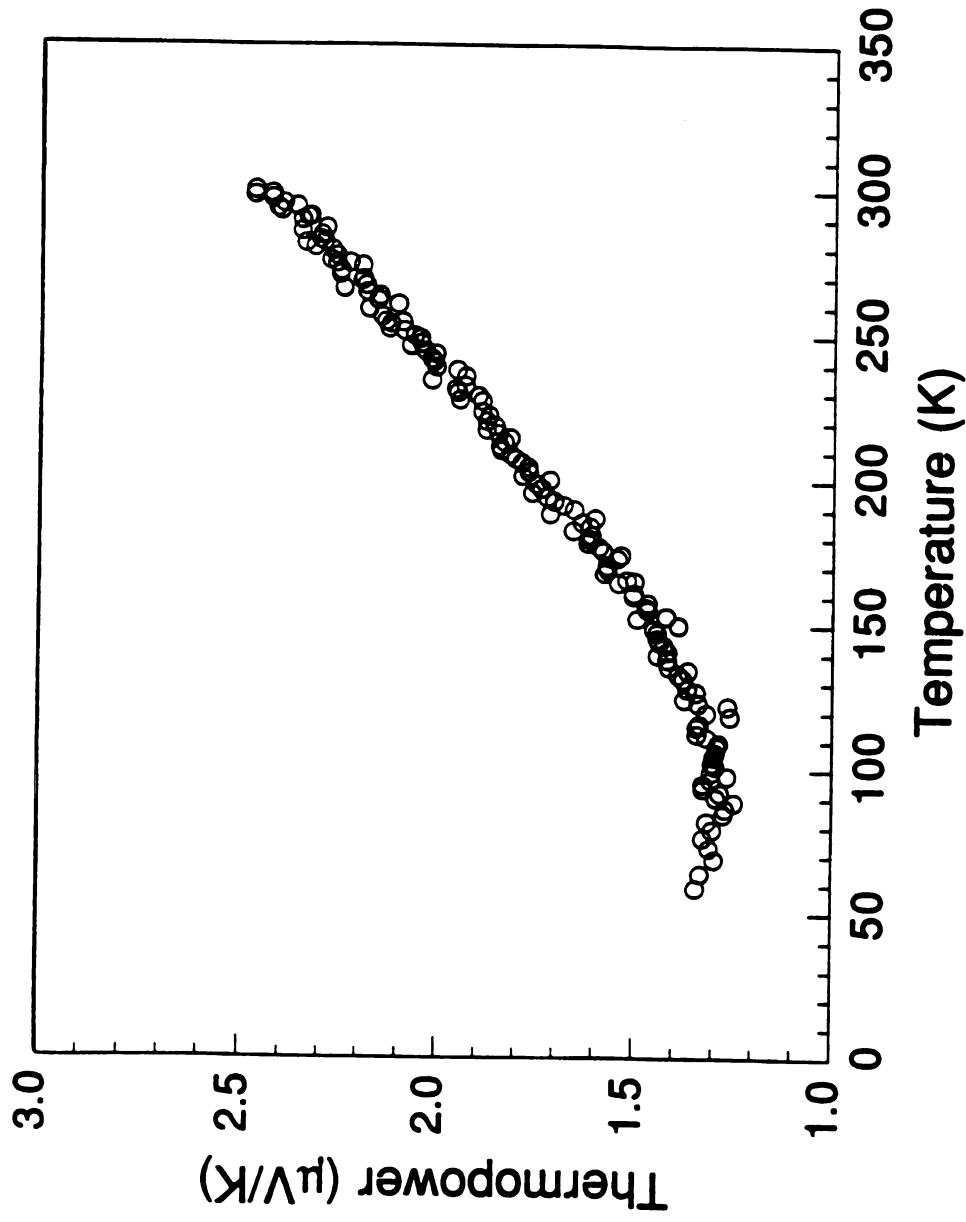
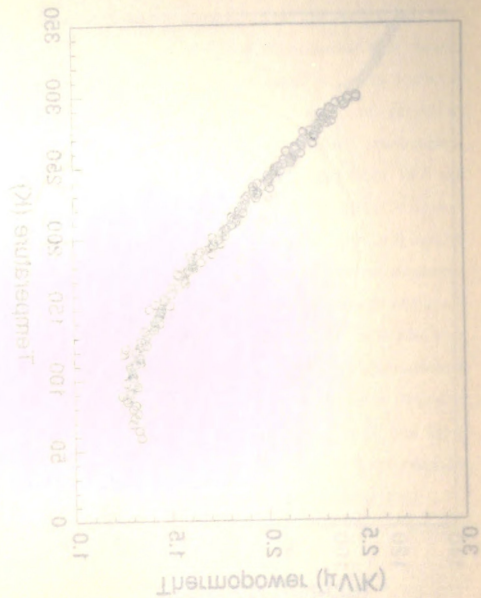


Figure 63. Variable-temperature thermoelectric power ($\mu\text{V/K}$) data for a single crystal of $\text{KCu}_4\text{S}_2\text{Te}$.

Figure 88: Variation of thermopower (mV/K) versus temperature (K) for a single crystal of $KCuF_3$.



3.4. Magnetic Susceptibility of $\text{KCu}_4\text{S}_2\text{Te}$ (I), $\text{K}_3\text{Cu}_8\text{S}_4\text{Te}_2$ (II) and $\text{Cu}_{17.6}\text{Te}_8\text{S}_{26}$ (III)

Variable temperature magnetic susceptibility data for $\text{KCu}_4\text{S}_2\text{Te}$ and $\text{K}_3\text{Cu}_8\text{S}_4\text{Te}_2$ are shown in Figures 64 and 65. They both show similar behavior; (a) temperature-independent paramagnetism above 50 K and (b) rapid increase in susceptibility below 50 K. When plotted as χ^{-1} vs temperature, for (I) the data below 10 K follow a Curie-Weiss Law and for (II) the data below 30 K follow a Curie-Weiss Law. This behavior is characteristic of metals (Pauli paramagnetism) containing a low concentration of paramagnetic impurities. The temperature independent Pauli paramagnetism ($\chi_p=9.7\times 10^{-5}$ emu/mol for (I); $\chi_p=30.5\times 10^{-5}$ emu/mol for (II)) have been obtained by subtracting the Curie-Weiss portion of the paramagnetism from the measured magnetic susceptibility. This Pauli-like behavior of (II) is quite different from the isostructural compound $\text{K}_3\text{Cu}_8\text{S}_6$ which is known to have resistivity and magnetic susceptibility anomalies associated with charge density wave (CDW) states^{71(b),(c)}. The CDW or spin density wave (SDW) state is one of the interesting physical properties observed in low-dimensional metals and is associated with the electronic instabilities (electron-electron repulsion).⁷⁷ A recent theoretical study¹¹⁵ on $\text{K}_3\text{Cu}_8\text{S}_6$ suggests that its observed anomalies do not originate from CDW instability, but are caused mostly by an order-disorder transition involving the Cu^+ ions of the energetically unfavorable long Cu-S bond (2.84 Å). Cu atoms move back and forth along this long Cu-S bond to shorten or lengthen Cu-Cu and Cu-S distances. These superlattice modulations and resistivity anomalies are not expected to occur in the higher chalcogenide analogues of $\text{A}_3\text{Cu}_8\text{S}_6$ because they have more reasonable Cu-Q (Q=Se, Te) bond distances. In fact, the substitution of Te for S, which

3.4. Magnetic Susceptibility of KCu_2S_2Te (I), $K_2Cu_8S_4Te_2$ (II) and $Cu_{17}S_8Te_{25}$ (III)

Variable temperature magnetic susceptibility data for KCu_2S_2Te and $K_2Cu_8S_4Te_2$ are shown in Figures 64 and 65. They both show similar behavior, (a) temperature-independent paramagnetism above 50 K and (b) rapid increase in susceptibility below 50 K. When plotted as χ^{-1} vs temperature, for (I) the data below 10 K follow a Curie-Weiss law and for (II) the data below 30 K follow a Curie-Weiss law. This behavior is characteristic of metals (Pauli paramagnetism) containing a low concentration of paramagnetic impurities. The temperature independent Pauli paramagnetism ($\chi_p = 2\mu_B^2 N_0$) emu/mol for (I); $\chi_p = 30.5 \times 10^{-5}$ emu/mol for (II) have been obtained by subtracting the Curie-Weiss portion of the paramagnetism from the measured magnetic susceptibility. The Pauli-like behavior of (I) is different from the isostructural compound KCu_4S_4 which is known to have resistivity and magnetic susceptibility anomalies associated with charge density wave (CDW) states.^{11(a), (c)} The CDW or spin density wave (SDW) state is one of the interesting physical properties observed in low-dimensional metals and is associated with the electronic instabilities (electron-electron repulsion).¹² A recent theoretical study¹³ on $K_2Cu_8S_4Te_2$ suggests that its observed anomalies do not originate from CDW instability, but are caused mostly by an order-disorder transition involving the Cu ions of the energetically unfavorable long Cu-S bond (2.84 Å). Cu atoms move back and forth along this long Cu-S bond to shorten or lengthen Cu-Cu and Cu-S distances. These superlattice modulations and resistivity anomalies are not expected to occur in the lighter chalcogenide analogues of $A_2Cu_8S_4$ because they have more reasonable Cu-O (Cu-Se) bond distances. In fact, the substitution of Te for S, which

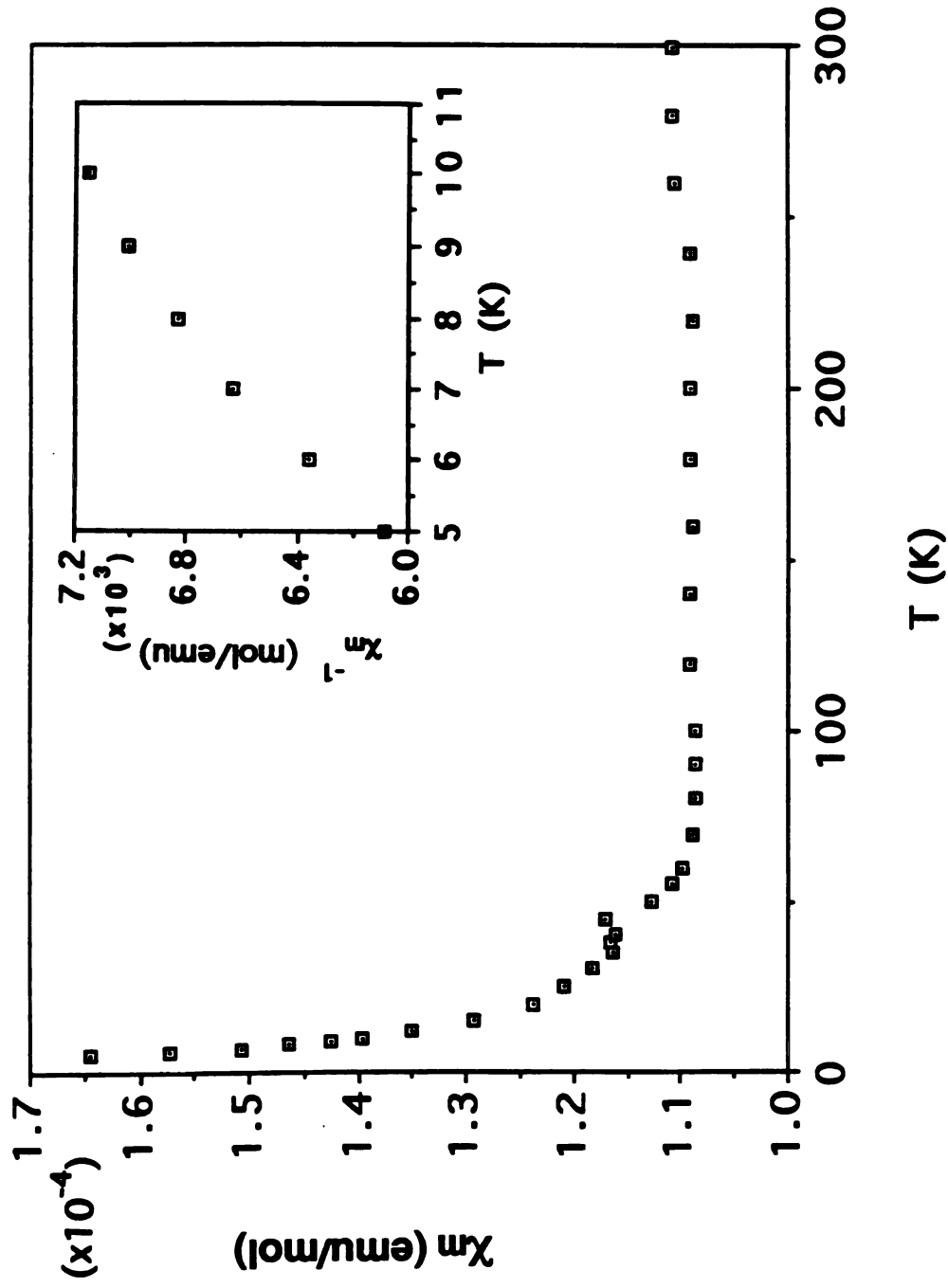


Figure 64. Variable-temperature magnetic susceptibility (emu/mol) data for polycrystalline $\text{KCu}_4\text{S}_2\text{Te}$. Inset: χ_m^{-1} (mol/emu) vs T .

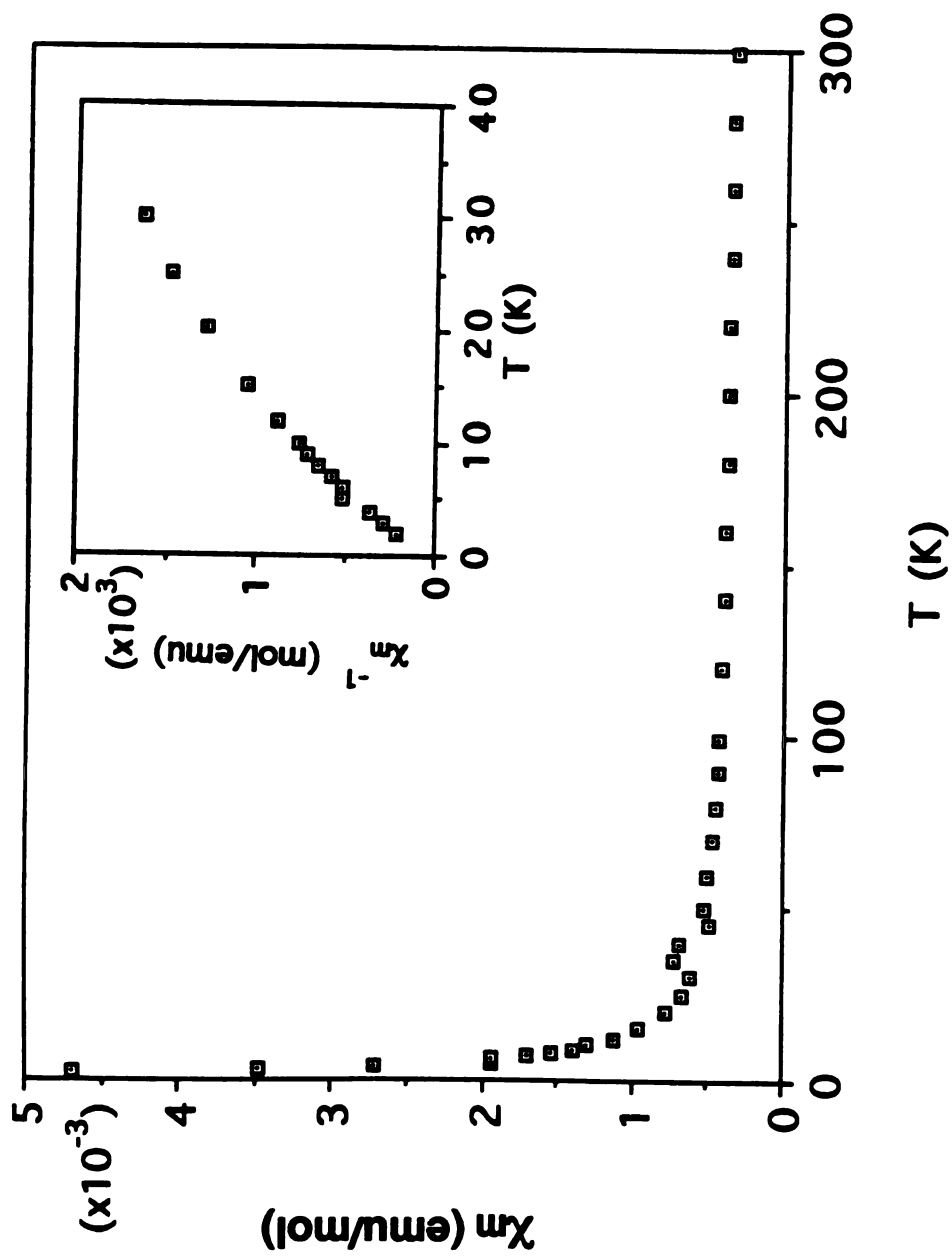
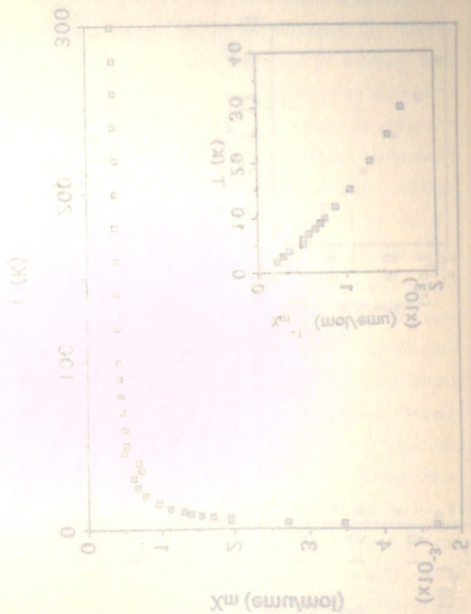


Figure 65. Variable-temperature magnetic susceptibility (emu/mol) data for polycrystalline $K_3Cu_8S_4Te_2$. Inset: χ_m^{-1} (mol/emu) vs T .

βοηθάει στην κατανόηση της μόνιμης ΔT (πυροκλάση) ως T
 Εξίσωση 62: Ανάπτυξη της θερμότητας με τη βοήθεια της εξίσωσης (επιπλέον) είναι ίσως



replaces the quite long Cu-S bond with reasonable Cu-Te bond (2.97 Å), does not allow any superlattice modulations or anomalies to occur in (II). Thus, (II) does not show any magnetic susceptibility anomalies, but shows Pauli-like behavior of a typical metallic conductor.

The magnetic susceptibility data for $\text{Cu}_{17.6}\text{Te}_8\text{S}_{26}$ are shown in Figure 66. They show antiferromagnetic behavior and quite strong magnetization of the materials. Because the magnetization shows field dependence we chose a magnetic field of 100 G; this field gives a valid linear field dependence. Based on the stoichiometry of $\text{Cu}_{17.6}\text{Te}_8\text{S}_{26}$, we could expect a maximum of 3 Cu^{2+} ions per formula unit. We were expecting weak paramagnetic behavior of this material since the known tetrahedrite compound $\text{Cu}_{12}\text{Sb}_4\text{S}_{12.7}$ exhibits paramagnetic properties due to the localized Cu^{2+} sites.¹¹⁶ However, the magnetic moment calculated at 300 K is 33 BM which is almost equivalent to 32 unpaired electrons per formula unit. Figure 67 shows the temperature dependence of the magnetic moments over the temperature range from 2 K to 300 K. Magnetic moments increase from 2.4 B.M. at 2K to 33 B.M. at 300 K. We are not quite sure of the origin of this stage. First, we suspected possible impurities in the sample but the X-ray powder diffraction pattern measured on the same sample showed only the pure $\text{Cu}_{17.6}\text{Te}_8\text{S}_{26}$. Further work is necessary to understand the magnetic properties of this material.

replaces the quite long Cu-S bond with reasonable Cu-Te bond (2.97 Å), does not allow any superlattice modulations or anomalies to occur in (ii). Thus, (ii) does not show any magnetic susceptibility anomalies, but shows Pauli-like behavior of a typical metallic conductor.

The magnetic susceptibility data for $\text{Cu}_{1.7}\text{Te}_{0.825}$ are shown in Figure 66. They show antiferromagnetic behavior and quite strong magnetization of the material. Because the magnetization shows field dependence we chose a magnetic field of 100 G; this field gives a valid linear field dependence. Based on the stoichiometry of $\text{Cu}_{1.7}\text{Te}_{0.825}$, we could expect a maximum of 3 Cu²⁺ ions per formula unit. We were expecting very low magnetic behavior of this material since the known tetrahedral compound $\text{Cu}_2\text{S}_{0.875}$ exhibits paramagnetic properties due to the localized Cu²⁺ spins.¹⁰ However, the magnetic moment calculated at 500 K is 0.8 BM which is almost equivalent to 33 unpaired electrons per formula unit. Figure 67 shows the temperature dependence of the magnetic moment over the temperature range from 2 K to 300 K. Magnetic moment increases from 2.4 BM at 2K to 0.8 BM at 500 K. We are not quite sure of the origin of this wide peak. First, we expected positive inputities in the sample but the X-ray powder diffraction pattern measured on the same sample showed only the pure $\text{Cu}_{1.7}\text{Te}_{0.825}$. Further work is necessary to understand the magnetic properties of this material.

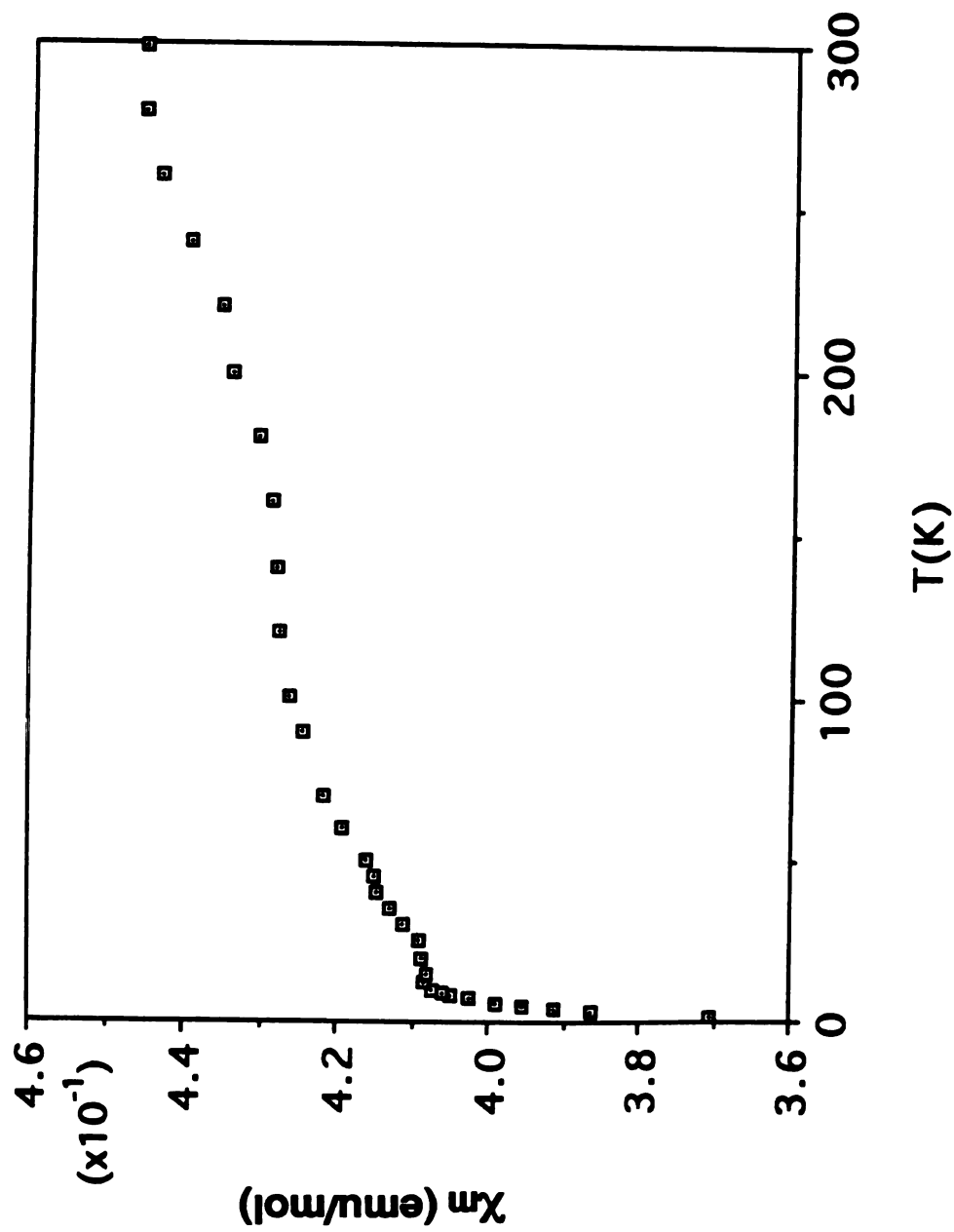
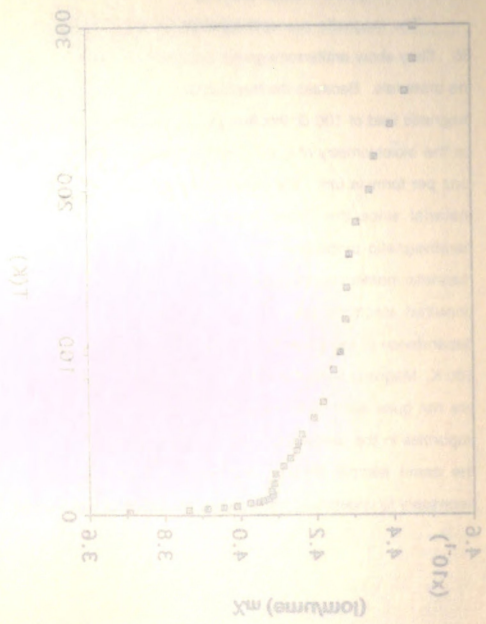


Figure 66. Variable-temperature magnetic susceptibility (emu/mol) data for polycrystalline $\text{Cu}_{17.6}\text{Te}_6\text{S}_{26}$.

βοηθητικός αριθμός
 Figure 68 Απεικόνιση της μεταβολής της αγωγιμότητας (αγωγιμότητα) σε σχέση με τη θερμοκρασία (K).



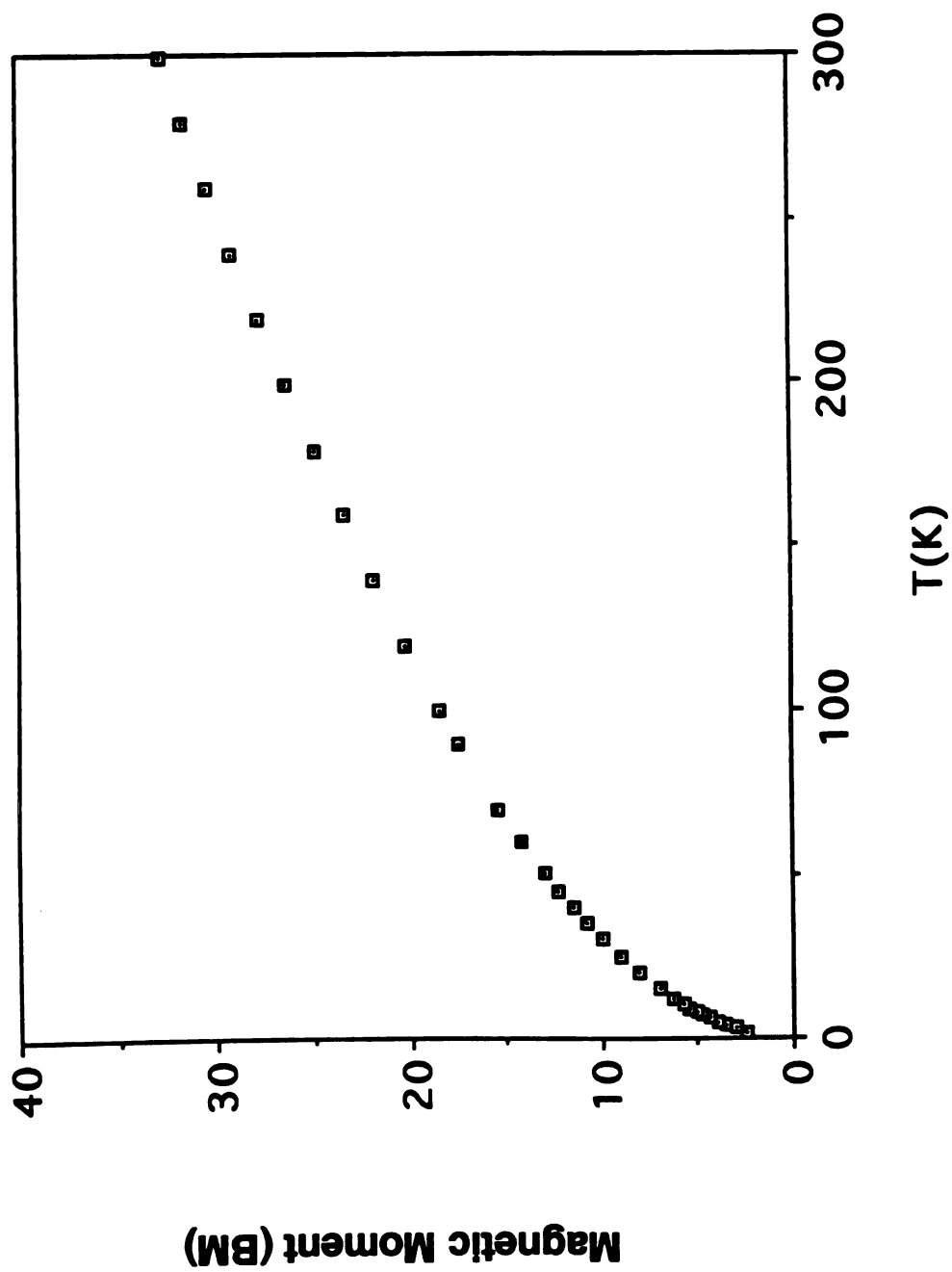
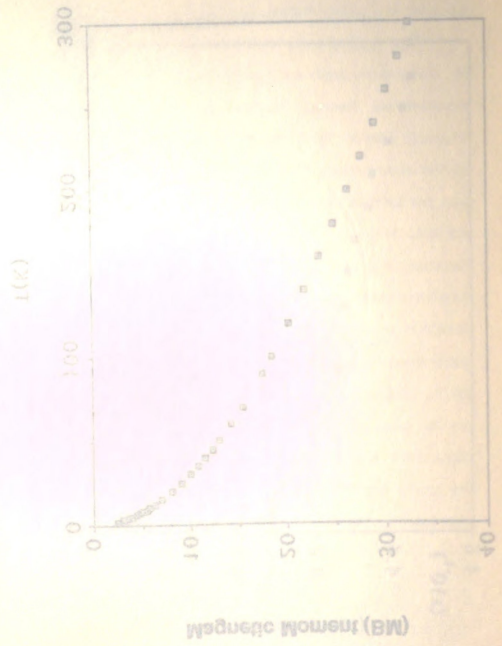


Figure 67. Temperature dependence of calculated magnetic moment (BM) of $\text{Cu}_{17.6}\text{Te}_8\text{S}_{26}$.

(MB) moment significant relationship to age, gender, and education level



The investigation of mixed chalcogenide compounds in K_2S/Te and K_2Te/S fluxes yielded quite promising results depending on the flux compositions and reaction temperatures. The compounds of KCu_4S_2Te and $K_3Cu_8S_4Te_2$ showed one important feature; Te atoms can have a preferential coordination environment over smaller sulfur atoms in a solid state lattice. This feature may make it possible to stabilize new structure-types which may not be possible otherwise. The compound of $Cu_{17.6}Te_8S_{26}$ highlights the potential use of the $[TeS_3]^{2-}$ unit as bridging ligands to stabilize extended solid compounds in the mixed-chalcogenide flux (A_2Te/S). The $[TeS_3]^{2-}$ unit, formed in the sulfur-rich flux, may be a potential ligand to use for the synthesis of new structural compounds. Since we have investigated only K_2S/Te and K_2Te/S mixed chalcogenide fluxes, there is certainly a great deal of exploration remaining for new mixed-chalcogenide compounds with other alkali metal (i.e. Na, Cs, Rb) Te/S fluxes.

The investigation of mixed chalcogenide compounds in K_2Te and K_2TeS fluxes yielded quite promising results depending on the flux composition and reaction temperatures. The compounds of KCu_4S_2Te and $K_3Cu_8S_4Te_5$ showed one important feature; Te atoms can have a preferential coordination environment over smaller sulfur atoms in a solid state lattice. This feature may make it possible to stabilize new structure-types which may not be possible otherwise. The compound of $Cu_4Te_8S_8$ highlights the potential use of the $[Te_3]^{2-}$ unit as bridging ligands to stabilize extended solid compounds in the mixed-chalcogenide flux ($AsTe_2$). The $[Te_3]^{2-}$ unit formed in the sulfur-rich flux, may be a potential ligand to use for the synthesis of new structural compounds. Since we have investigated only K_2Te and K_2TeS mixed chalcogenide fluxes, there is certainly a great deal of exploration remaining for new mixed-chalcogenide compounds with other alkali metal fluxes, Ca_2BdTeS fluxes.

CHAPTER 8

AuCuSe₄, a Novel Mixed Metal Chalcogenide Compound Incorporating Se₃²⁻ ligands

1. Introduction

We have demonstrated in the previous chapters (see chapters 2 and 3) that by using alkali metal polychalcogenide fluxes as solvents and reagents at intermediate temperatures, novel, low-dimensional polychalcogenide compounds in ternary *A/Cu/Q* and *A/Au/Q* systems can be isolated in crystalline form. Based on the success in these ternary systems, we have extend our work into the quaternary *A/Au/Cu/Q* system with the expectation of new polychalcogenide structural compounds. There is only one known chalcogenide compound containing Au and Cu metal, AuCuTe₄.¹¹⁷ This is known as kostovite mineral and contains Te₂²⁻ ligands. There are no known mixed metal polychalcogenide compounds containing higher polychalcogenide ligands (Q_x²⁻, *x* > 2). Prior to our work there were no general synthesis methods for polychalcogenide compounds.

In this chapter, we illustrate that our initial approach, using alkali metal polychalcogenide fluxes with mixed Cu and Au metal at 310 °C, leads to the synthesis and crystal growth of the new ternary mixed metal compound of

synthesis and crystal growth of the new ternary mixed metal compound of polychalogenide fluxes with mixed Cu and Au metal at 310 °C, leads to the fact that our initial approach, using alkali metal polychalogenide compounds.

Prior to our work there were no general synthesis methods for polychalogenide compounds containing higher polychalogenide mixed metal polychalogenide compounds containing higher polychalogenide known as kostovite mineral and contains Te_2^{2-} ligands. There are no known polychalogenide structural compounds containing Au and Cu metal, $AuCuTe_4$. This into the quaternary $AuAuCuTe_4$ system and our expectation of new compounds in ternary systems we have extended our work.

Based on the success in these ternary systems we have extended our work into the quaternary $AuAuCuTe_4$ system and our expectation of new intermediate temperatures, novel, low-dimensional polychalogenide compounds in ternary $AuCuTe_4$ and $AuAuTe_4$ systems can be realized in quaternary ternary systems.

We have demonstrated in the previous chapters (see chapters 2 and 3) that by using alkali metal polychalogenide fluxes as solvents and reagents, in

4. Introduction

$AuCuSe_4$, a Novel Mixed Metal Chalcogenide Compound Incorporating Se_2^{2-} ligands

CHAPTER 8

AuCuSe₄, containing bridging triselenide ligands with a novel three-dimensional structure.

2. Experimental Section

2.1 Reagents

Chemicals were used as obtained: gold powder, -325 mesh, 99.95 % purity, Cerac, Milwaukee, WI; copper powder, electrolytic dust, purified, Fisher Scientific Co., Fair Lawn, NJ; selenium powder, -100 mesh, 99.95 % purity, Aldrich Chemical Co., Milwaukee, WI; potassium metal, analytical reagent, Mallinckrodt Inc., Paris, KY.

2.2. Physical Measurements

FT-IR spectrum of AuCuSe₄ was measured as a pellet in a Csl matrix. The sample was ground with dry Csl into a fine powder and a pressure of about 6 tons was applied to the mixture to make a translucent pellet. The spectra was recorded in the far IR region (600 to 100 cm⁻¹) with the use of a Nicolet 740 FT-IR spectrometer.

Quantitative microprobe analysis was performed on a Jeol 35CF scanning electron microscopy equipped with Tracor Northern TN5500 X-ray microanalysis attachment. Single crystals of AuCuSe₄ were carefully picked and mounted on an aluminum stub with conducting silver paint to help dissipate charges that developed on the sample surface during measurements. Energy Dispersive Spectra (EDS) were obtained using the following experimental set-up:

AuCuSe_4 , containing bridging triselenide ligands with a novel three-dimensional structure.

2. Experimental Section

2.1. Reagents

Chemicals were used as obtained: gold powder, -325 mesh, 99.99% pure, Alfa Aesar, Milwaukee, WI; copper powder, electrolytic dust, purified, Alfa Aesar, Milwaukee, WI; selenium powder, -100 mesh, 99.99% pure, Scientific Co., Fair Lawn, NJ; potassium metal, analytical reagent, Aldrich Chemical Co., Milwaukee, WI; potassium metal, analytical reagent, Mallinckrodt Inc., Park, KY.

2.2. Physical Measurements

FT-IR spectrum of AuCuSe_4 was measured as a pellet in a CaF₂ matrix. The sample was ground with dry CaF₂ in a mortar and a pressure of about 6 tons was applied to the mixture to make a transparent pellet. The spectra was recorded in the far IR region (600 to 100 cm⁻¹) with the use of a Nicolet 740 FT-IR spectrometer.

Quantitative microprobe analysis was performed on a Jeol 350F scanning electron microscopy equipped with Tracor Northern TN5500 X-ray microanalysis attachment. Single crystals of AuCuSe_4 were carefully picked and mounted on an aluminum stub with conducting silver paint to help dissipate charges that developed on the sample surface during measurements. Energy Dispersive Spectra (EDS) were obtained using the following experimental set-

X-ray detector position : 55 mm

Working distance : 39 mm

Accelerating voltage : 20 KV

Take-off angle : 27 deg

Beam current : 200 picoamps

Accumulation time : 100 seconds

Window : Be

A standardless quantitative analysis (SQ) program was used to analyze the X-ray spectra obtained. Since the selenium ratio is always underestimated due to artifact of the program, a correction factor ($\times 1.86$), which was determined by calibrating with known K/Au/Se and K/Cu/Se ternary compounds, was used to evaluate the selenium percentage better. The analysis reported is the average of four individual measurements on different crystals.

2.3. Synthesis

Chemicals were measured and loaded in Pyrex tubes under a dry nitrogen atmosphere in a Vacuum Atmospheres Dri-Lab glovebox. Potassium monoselenide (K_2Se) was prepared in liquid ammonia from potassium metal and elemental selenium in a 2:1 ratio.

Copper gold tetraselenide, $AuCuSe_4$ (I) 0.094 g (0.6 mmol) of K_2Se , 0.098 g (0.5 mmol) of Au powder, 0.032 g (0.5 mmol) of Cu, and 0.624 g (8.0 mmol) of Se powder were mixed together and loaded in a Pyrex tube which was flame-sealed under vacuum ($\sim 10^{-3}$ torr). The tube was placed in a computer-controlled furnace and heated at 310 °C for 96 hrs and cooled slowly to 120 °C at a rate of 2 °C/hr, then to 50 °C at 35 °C/hr. Dark brown rod-shaped crystals were obtained with contamination (about 20 %) of $KAuSe_5$ by removing

Window: Be
 Accumulation time: 100 seconds
 Beam current: 500 picoamps
 Take-off angle: 37 deg
 Accelerating voltage: 20 KV
 Working distance: 39 mm
 X-ray detector position: 85 mm

A standardless quantitative analysis (SQ) program was used to analyze the X-ray spectra obtained. Since the selenium ratio is always underestimated due to the lack of the program, a correction factor ($\times 1.66$), which was determined by calibrating with known $KAuSe_2$ and K_2Se primary compounds, was used to evaluate the selenium percentage data. The analysis routine is the average of four individual measurements on different crystals.

3.3. Synthesis

Chemicals were measured and loaded in Pyrex tubes under a dry nitrogen atmosphere in a Vacuum Atmospheres D-145 glovebox. Potassium monoselenide (K_2Se) was prepared in liquid ammonia from potassium metal and elemental selenium in a 2:1 ratio.

Copper gold tetraselenide, $AuCuSe_4$ (t) (0.084 ± 0.008 mmol) of K_2Se , 0.098 ± 0.009 g (0.5 mmol) of Au powder, 0.032 ± 0.003 g (0.2 mmol) of Cu, and 0.054 ± 0.005 g (0.2 mmol) of Se powder were mixed together and loaded in a Pyrex tube which was flame-sealed under vacuum ($\sim 10^{-2}$ torr). The tube was placed in a computer-controlled furnace and heated at $210^\circ C$ for 96 hrs and cooled slowly to $120^\circ C$ at a rate of $2^\circ C/hr$, then to $80^\circ C$ at $55^\circ C/hr$. Dark brown rod-shaped crystals were obtained with contamination (about 20%) of $KAuSe_2$ by removing

excess potassium polyselenides with DMF under a N₂ atmosphere. A quantitative analysis performed on a number of crystals with the EDS/SEM gave an average composition of Au_{1.0}Cu_{1.0}Se_{4.1}. This compound is insoluble in all common organic solvents and stable with respect to hydrolysis and air oxidation for several days.

2.3. X-ray Crystallographic Studies

AuCuSe₄ was examined by X-ray powder diffraction for phase characterization and identification. The d-spacings were obtained from powder patterns recorded on a Phillips XRG-3000 computer-controlled powder diffractometer, operating at 40KV, 35 mA. Graphite monochromated Cu radiation was used. The d-spacings observed for the manually selected single crystals of AuCuSe₄ were compared, and found to be in accord, with those calculated from the single crystal X-ray structure analysis data. The calculation of d-spacings was performed using the POWD10 programs⁵⁶. The result is summarized in Table 87.

excess potassium polyselenide with DMF under a N_2 atmosphere. A quantitative analysis performed on a number of crystals with the EDX/SEM gave an average composition of $Au_{1.0}Cu_{1.9}Se_{4.7}$. This compound is insoluble in all common organic solvents and stable with respect to hydrolysis and air oxidation for several days.

2.3. X-ray Crystallographic Studies

$AuCuSe_4$ was examined by X-ray powder diffraction for phase characterization and identification. The d-spacings were obtained from powder patterns recorded on a Philips XRG 5000 computer-controlled goniometer, operating at 40 kV, 85 mA. Graphite diffracted Cu radiation was used. The d-spacings covered for the manually selected angle crystals of $AuCuSe_4$ were compared, and found to be in accord, with those calculated from the single crystal X-ray structure analysis data. The calculation of d-spacings was performed using the PCMD9 program. The results are summarized in Table 37.

Table 87. Calculated and Observed X-ray Powder Diffraction Patterns of AuCuSe₄

H K L	d_{calc} (Å)	d_{obs} (Å)	I/I _{max} (obs.)
0 0 1	8.08	8.09	14.1
-1 0 1	3.89	3.90	29.5
1 1 0	3.73	3.73	15.1
0 2 1	3.38	3.38	14.5
1 0 2	2.86	2.87	15.8
1 2 0	2.81	2.81	100
0 0 3	2.69	2.69	63.9
-1 2 2	2.354	2.356	8.9
1 0 3	2.227	2.229	8.9
2 0 0	2.155	2.155	25.9
-1 2 3	1.985	1.987	46.8
1 2 3	1.9117	1.9128	37.8
-1 0 4 (0 4 0)	1.8724	1.8639	32.8
-2 2 1	1.8379	1.8388	29.0
1 0 4	1.7905	1.7906	12.0
0 2 4	1.7764	1.7785	26.7
-2 0 3	1.7330	1.7343	16.4
1 4 0	1.7091	1.7100	6.1
-1 4 1	1.6800	1.6767	11.1
2 2 2	1.6622	1.6629	30.8
2 0 3	1.6375	1.6380	23.3

Table 87. Calculated and Observed X-ray Powder Diffraction Patterns of

AuCuSe₂

H K L	d_{calc} (Å)	d_{obs} (Å)	I_{max} (obs)
0 0 1	8.08	8.09	14 1
-1 0 1	3.89	3.90	28 2
1 1 0	3.73	3.73	18 1
0 2 1	3.38	3.38	14 2
1 0 2	2.82	2.82	12 2
1 2 0	2.81	2.81	12 0
0 0 3	2.69	2.70	22 0
-1 2 1	2.384	2.384	8 0
1 0 3	2.327	2.328	8 0
2 0 0	2.188	2.18	22 0
1 2 2	1.982	1.987	18 0
1 2 1	1.917	1.918	27 2
-1 0 4 (0 4 0)	1.8754	1.8698	32 2
-2 2 1	1.8372	1.8368	28 0
1 0 4	1.7908	1.7908	12 0
0 2 4	1.7364	1.7365	28 2
-2 0 2	1.7330	1.7343	18 4
1 4 0	1.7081	1.7100	8 1
-1 4 1	1.6800	1.6787	11 1
2 2 2	1.6252	1.6259	30 8
2 0 2	1.6225	1.6280	23 2

The X-ray single crystal data of AuCuSe₄ were collected on a Rigaku AFC6S diffractometer with graphite monochromated Mo-K_α radiation using the ω -2 θ scan mode. Accurate unit cell parameters were obtained from the least-squares refinement of the 2 θ , ω , χ , and ϕ values of 25 machine-centered reflections. The stability of the experimental setup and crystal integrity were monitored by measuring three standard reflections periodically (every 100 reflections) during data collection. The intensities did not show any appreciable decay. Two absorption corrections were applied to the data. The first was an empirical absorption correction based on ψ scans for three reflections; this was followed by DIFABS⁵⁷ correction. The structure of AuCuSe₄ was solved with direct methods using SHELXS-86⁵⁸ and was refined with the TEXSAN⁶⁰ package of crystallographic programs on a VAXstation 3100 computer. All atoms were refined anisotropically. The complete data collection parameters and details of the structure solution and refinement are given in Table 88. The final atomic coordinates, temperature factors and their estimated standard deviations are shown in Table 89.

The X-ray single crystal data of AuOSe_4 were collected on a Rigaku AFC6S diffractometer with graphite monochromated $\text{Mo-K}\alpha$ radiation using the ω - 2θ scan mode. Accurate unit cell parameters were obtained from the least-squares refinement of the 2θ , ω , χ , and ϕ values of 25 machine-centered reflections. The stability of the experimental setup and crystal integrity were monitored by measuring three standard reflections periodically (every 100 reflections) during data collection. The intensities did not show any appreciable decay. Two absorption corrections were applied to the data. The first was an empirical absorption correction based on ψ scans for three reflections; this was followed by DIFABS²⁷ correction. The structure of AuOSe_4 was solved with direct methods using SHELX-85²⁸ and was refined with the TEXSAN²⁹ package of crystallographic programs on a VAXstation 3700 computer. All atoms were refined anisotropically. The complete data collection parameters and details of the structure solution and refinement are given in Table 3. The final atomic coordinates, temperature factors and their estimated standard deviations are

shown in Table 6.

Table 88. Summary of Crystallographic Data for AuCuSe₄

	compound
	I
Formula	AuCuSe ₄
Formula weight	576.35
space group	P2 ₁ /m
<i>a</i> (Å)	4.318(2)
<i>b</i> (Å)	7.447(1)
<i>c</i> (Å)	8.099(1)
α(deg)	90.0
β(deg)	93.33(2)
γ(deg)	90.0
Vol (Å ³), Z	260.0(1), 2
Temperature (°C)	23
Crystal size (mm)	0.60x0.05x0.05
Radiation	Mo-Kα
μ (Mo-Kα, cm ⁻¹)	597.8
<i>D</i> _{calc} (g/cm ³)	7.36
2θ _{max} (deg)	60
Scan method	ω/2θ
No. of data collected	1698
No. of unique data	815
No. of data used (<i>F</i> _o ² > 3σ(<i>F</i> _o ²))	623
No. of atoms	5
No. of variables	35
Phasing technique	Direct methods
Final R/R _w (%)	5.1/5.5
Max. shift/esd (last cycle)	0.00
Extinction coefficient	1.01x10 ⁻⁵

Table 88. Summary of Crystallographic Data for AuCu₂

Extinction coefficient	1.01x10 ⁻⁸
(last cycle)	
Max. shift/lead	0.00
Final R/R _w (%)	5.15.5
Phasing technique	Direct methods
No. of variables	35
No. of atoms	5
(F _o ² -G _c (F _o ²))	
No. of data used	633
No. of unique data	412
No. of data collected	1159
Scan method	4.45°
2θ _{max} (deg)	73
D _{calc} (g/cm ³)	7.95
μ (Mo-Kα, cm ⁻¹)	72.5
Radiation	Mo Kα
Crystal size (mm)	0.80x0.50x0.15
Temperature (°C)	23
Vol (Å ³)	200.0(1)
Y(deg)	50.0
X(deg)	37.23(2)
φ(deg)	90.0
c (Å)	8.029(1)
b (Å)	7.447(1)
a (Å)	4.316(2)
Space group	P2 ₁ m
Formula weight	278.95
Compound	AuCu ₂

Table 89. Fractional Atomic Coordinates and B_{eq} Values for AuCuSe₄ with Their Estimated Standard Deviations in Parentheses

Atom	x	y	z	B_{eq}^{a} , Å ²
Au	1/2	0	0	0.60(3)
Se(1)	0.4162(3)	0.0013(2)	0.6951(2)	0.80(5)
Se(2)	0.0742(4)	1/4	0.6384(2)	0.86(6)
Se(3)	0.1445(4)	1/4	1.0623(2)	0.66(6)
Cu	-0.0248(6)	1/4	1.3423(3)	1.5(1)

^a B values for anisotropically refined atoms are given in the form of the isotropic equivalent displacement parameter defined as $B_{\text{eq}} = (4/3)[a^2B_{11} + b^2B_{22} + c^2B_{33} + ab(\cos \gamma)B_{12} + ac(\cos \beta)B_{13} + bc(\cos \alpha)B_{23}]$.

Table 89. Fractional Atomic Coordinates and B_{00} Values for AuCu₂S₂ with Their Estimated Standard Deviations in Parentheses

Atom	x	y	z	B_{00} , Å ²
Au	1/2	0	0	0.80(3)
Se(1)	0.4182(3)	0.0013(2)	0.8821(2)	0.80(2)
Se(2)	0.0742(4)	1/4	0.6884(2)	0.85(2)
Se(3)	0.1442(4)	1/4	1.0823(2)	0.60(6)
Cu	-0.0248(6)	1/4	1.2823(2)	1.6(1)

^a B values for anisotropically refined atoms are given in the form of the isotropic equivalent displacement parameter defined as $B_{00} = \frac{1}{3}(B_{11} + B_{22} + B_{33})$.

3. Results and Discussion

3.1. Synthesis and Spectroscopy

Synthesis of the novel mixed metal polychalcogenide compound AuCuSe₄ has been readily achieved using potassium polyselenide (K₂Se_x) fluxes as solvents and reagents at 310 °C as shown in eq 1.



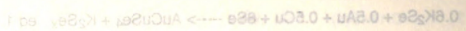
Our initial approach was to use reactant ratios of K₂Se/Cu/Au/Se (from 1/0.5/0.5/8 to 4/0.5/0.5/8) at 290 °C. Upon keeping the sum of the metal ratios as 1, the overall reactant ratios were same as those used in ternary A/Cu(or Au)/Q systems. During this study we identified at least two new phases, including AuCuSe₄, that were competing with ternary polychalcogenide compounds (e.g. KAuSe₂⁵⁰, KAuSe₅^{53(c)}, α-KCuSe₄⁵⁰). The presence of the competing ternary phases was not surprising because each metal has its own favorable coordination environment associated with the various polychalcogenide species in equilibrium in the K₂Se_x flux.

Microcrystals of AuCuSe₄ were obtained at 290 °C with contamination of KAuSe₅ as a minor phase from every reactant ratio except that of 2/0.5/0.5/8. The product looked like a coarse powder to the naked eye. Since the ratio of 1/0.5/0.5/8 gave slightly better crystalline material, we narrowed the search to reactant ratios around 1/0.5/0.5/8 and increased the reaction temperature to 310 °C to improve crystallinity. The 0.6/0.5/0.5/8 ratio gave single crystals of AuCuSe₄ suitable for X-ray single crystal study. However, the product was still contaminated with KAuSe₅. Another promising phase was isolated from the

3. Results and Discussion

3.1. Synthesis and Spectroscopy

Synthesis of the novel mixed metal polythioether compound AuCuSe_4 has been readily achieved using potassium polyselenide (K_2Se_x) fluxes as solvents and reagents at 310 °C as shown in eq 1.



Our initial approach was to use reactant ratios of $\text{K}_2\text{Se}_x/\text{AuCuSe}_4$ from 1.0 to 5.0. Upon keeping the rest of the reactant ratios as 1, the overall reactant ratios were same as those used in ternary AuCuSe_4 systems. During this study we identified at least two new phases including AuCuSe_4 that were competing with binary polythioethers compounds (e.g. KAuSe_2 , KCuSe_2 , K_2CuSe_3). The growth of the competing ternary phase was not surprising because each metal has its own favorable coordination environment associated with the various polythioether species in equilibrium in the K_2Se_x flux.

Microparticles of AuCuSe_4 were obtained at 250 °C with composition of AuCuSe_4 as a minor phase from every reactant ratio except that of 2.0 to 5.0. The product looked like a coarse powder to the naked eye. Since the ratio of 1.0 to 5.0 gave slightly better crystalline material, we narrowed the search to reactant ratios around 1.0 to 5.0 and increased the reaction temperature to 310 °C to improve crystallinity. The 0.6 to 5.0 ratio gave single crystals of AuCuSe_4 suitable for X-ray single crystal study. However, the product was still contaminated with KAuSe_2 . Another promising phase was isolated from the

reactant ratio 2/0.5/0.5/8 at 290 °C along with α -KCuSe₄ and KAuSe₂ both of which were identified by X-ray powder diffraction. This phase has the approximate composition of K₃Au₂Cu₃Se₂₀ by EDS/SEM quantitative analysis. However, its very poor crystallinity and very small, thin needle-like morphology made further characterization difficult. Further investigations to obtain better single crystals of this quaternary phase are under way.

In the far-IR region AuCuSe₄ exhibits spectral absorptions in the range of 170~235 cm⁻¹ due to Se-Se and/or Cu-Se and Au-Se stretching vibrations . Tentatively, we can assign a strong peak at 235 cm⁻¹ as a Se-Se stretching vibration and another strong peak at 217 cm⁻¹ to a M-Se stretching vibration. The spectrum is shown in Figure 68. It is usually difficult to interpret the IR spectra of metal polychalcogenide compounds without ambiguity because the Cu-Se, Au-Se, and Se-Se stretching frequencies fall in the same low-frequency IR region (200-340 cm⁻¹) and that systematic IR spectroscopic data for the various free ligands (Q_x²⁻, x=2-6) and metal chalcogenide complexes are still lacking.

reactant ratio 2.0:5.0:5.8 at 290 °C along with α -K₂Cu₂S₄ and KAu₂S₅ both of which were identified by X-ray powder diffraction. This phase has the approximate composition of KAu₂Cu₂S₅ by EDXSEM quantitative analysis. However, its very poor crystallinity and very small, thin needle-like morphology made further characterization difficult. Further investigations to obtain better single crystals of this duster phase are under way.

In the far-IR region AuCu₂S₄ exhibits spectral absorptions in the range of 170–265 cm⁻¹ due to Se–Se and Au–Se stretching vibrations. Tentatively, we can assign a strong peak at 233 cm⁻¹ as a Se–Se stretching vibration and another strong peak at 217 cm⁻¹ to a Au–Se stretching vibration. The spectrum is shown in Figure 9. It is usually difficult to interpret the spectra of metal polychalcogenide compounds without ambiguity because the Au–Se, Au–Se, and Se–Se stretching frequencies fall in the same low-frequency IR region (200–340 cm⁻¹) and that systematic IR spectral data for the various free ligands (O₂²⁻, S²⁻) and metal chalcogenide compounds are still

lacking.

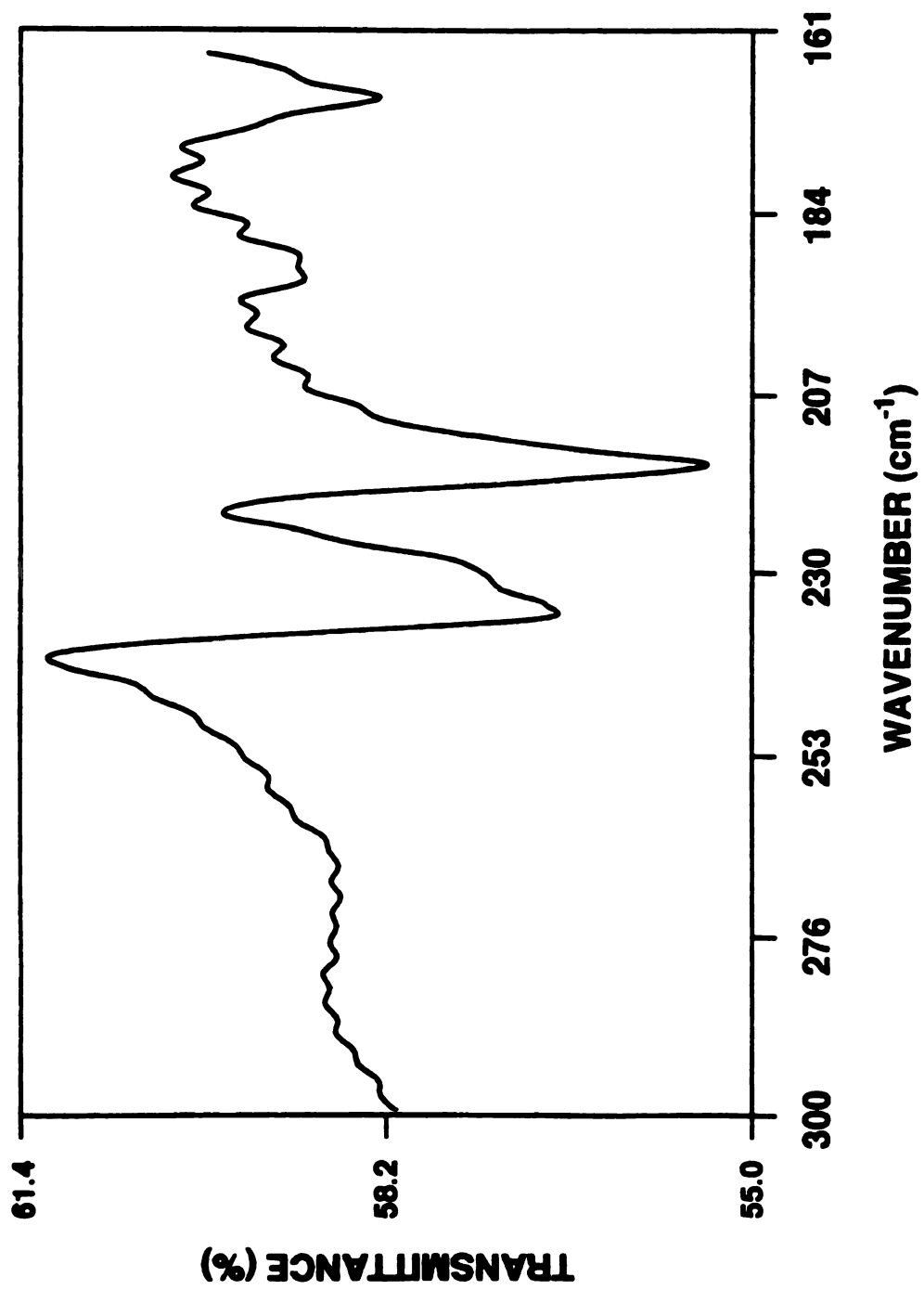
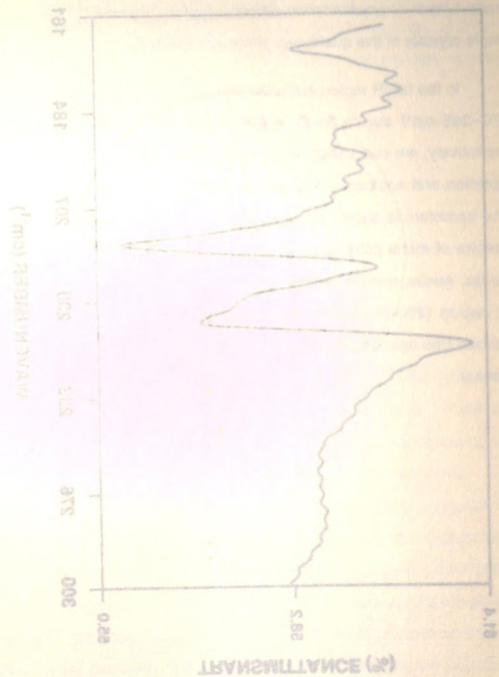
Figure 68. Far-IR spectrum of AuCuSe₄

Figure 18. Infrared spectrum of vinyl acetate.



3.2. Description of Structure

The structure of AuCuSe₄ is a unique three-dimensional framework with two types of small empty tunnels, as shown in Figure 69. As revealed by the structure this is a formally Au³⁺ and Cu⁺ compound with Se₃²⁻ and Se²⁻ fragments. Despite its somewhat complicated three-dimensional character, its structure is clearly anisotropic. Conceptually, we can decompose it into one-dimensional [Au(Se₃)Se]_nⁿ⁻ chains linked by Cu⁺ atoms. Two views of the [Au(Se₃)Se]_nⁿ⁻ chain are shown in Figure 70. In this chain, Se₃²⁻ ligands bridge Au atoms via their terminal selenium atoms and the square planar coordination of Au atoms are completed by the bridging monoselenides. The chains are centrosymmetric and run parallel to the crystallographic *b*-axis. The Au atoms are located on an inversion center. The average Au-Se bond distance is 2.479(5) Å which is similar to those of the Au³⁺ compounds K₃AuSe₁₃^{53(c)} (2.48(1) Å), Na₃AuSe₈⁵⁰ (2.499(1) Å), KAuSe₂⁵⁰ (2.475(1) Å), and NaAuSe₂⁵⁰ (2.48(2) Å) (see chapter 3). This [Au(Se₃)Se]_nⁿ⁻ chain is quite similar to the known [Au(Se₃)(Se₅)₂]_n³ⁿ⁻ chain (see page 115). Like the [Au(Se₃)(Se₅)₂]_n³ⁿ⁻ chain, the [Au(Se₃)Se]_nⁿ⁻ chain can, conceptually, be viewed as an oxidative addition product of Se₂²⁻ ligand to the Au⁺ atoms of the known [Au(Se₃)]_nⁿ⁻ chain (see page 112) as shown in eq 1.



However, the reduced chalcogenide ligands (Se²⁻ in the [Au(Se₃)Se]_nⁿ⁻ chain) act as bridging ligands to Au³⁺ ions.

These anionic [Au(Se₃)Se]_nⁿ⁻ chains are connected to each other by Cu atoms to form a stepped layer as shown in Figure 71. The Cu atoms are

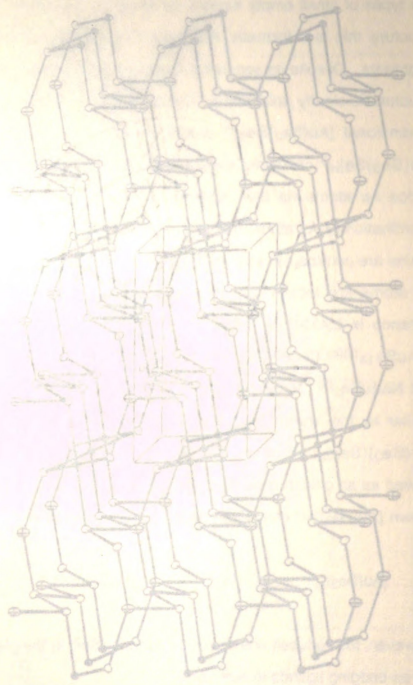
3.2. Description of Structure

The structure of AuCuSe_4 is a unique three-dimensional framework with two types of small empty tunnels, as shown in Figure 69. As revealed by the structure this is a formally Au^{2+} and Cu^{+} compound with 2Se_2^{2-} and 2Se^{2-} fragments. Despite its somewhat complicated three-dimensional character, its structure is clearly anisotropic. Conceptually, we can decompose it into one-dimensional $[\text{Au}(\text{Se}_2)_2\text{Se}]_n$ chains linked by Cu atoms. Two views of the $[\text{Au}(\text{Se}_2)_2\text{Se}]_n$ chain are shown in Figure 70. In this chain, Se_2^{2-} ligands bridge Au atoms via their terminal selenium atoms and the square planar coordination of Au atoms are completed by the bridging monochalcogens. The chains are centrosymmetric and run parallel to the crystallographic b axis. The Au atoms are located on an inversion center. The average Au-Se bond distance is $2.479(2) \text{ \AA}$ which is similar to those of the AuSe_2 compounds $(\text{K}_2\text{AuSe}_2\text{Se}_2^{2-})$ ($2.48(1) \text{ \AA}$), $(\text{NH}_4)_2\text{AuSe}_2\text{Se}_2$ ($2.439(1) \text{ \AA}$), $(\text{NH}_4)_2\text{AuSe}_2\text{Se}_2$ ($2.479(1) \text{ \AA}$), and $(\text{NH}_4)_2\text{Se}_2\text{Se}_2$ ($2.46(2) \text{ \AA}$) (see chapter 2). The $[\text{Au}(\text{Se}_2)_2\text{Se}]_n$ chain is quite similar to the known $[\text{Au}(\text{Se}_2)_2\text{Se}]_n$ chain (see page 112). We view the $[\text{Au}(\text{Se}_2)_2\text{Se}]_n$ chain as an oxidative addition product of Se_2^{2-} ligand to the Au^{+} atoms of the known $[\text{Au}(\text{Se}_2)]_n$ chain (see page 112) as shown in eq. 1.



However, the reduced dichalcogenide ligands (Se_2^{2-}) in the $[\text{Au}(\text{Se}_2)_2\text{Se}]_n$ chain act as bridging ligands to Au^{2+} ions. These anionic $[\text{Au}(\text{Se}_2)_2\text{Se}]_n$ chains are connected to each other by Cu atoms to form a stepped layer as shown in Figure 71. The Cu atoms are

Fig. 1. Crystal structure of the compound $\text{C}_{10}\text{H}_{10}\text{O}_2$. The structure is shown in the form of a ball-and-stick model. The atoms are represented by spheres, and the bonds are represented by sticks. The structure is a complex, three-dimensional lattice.



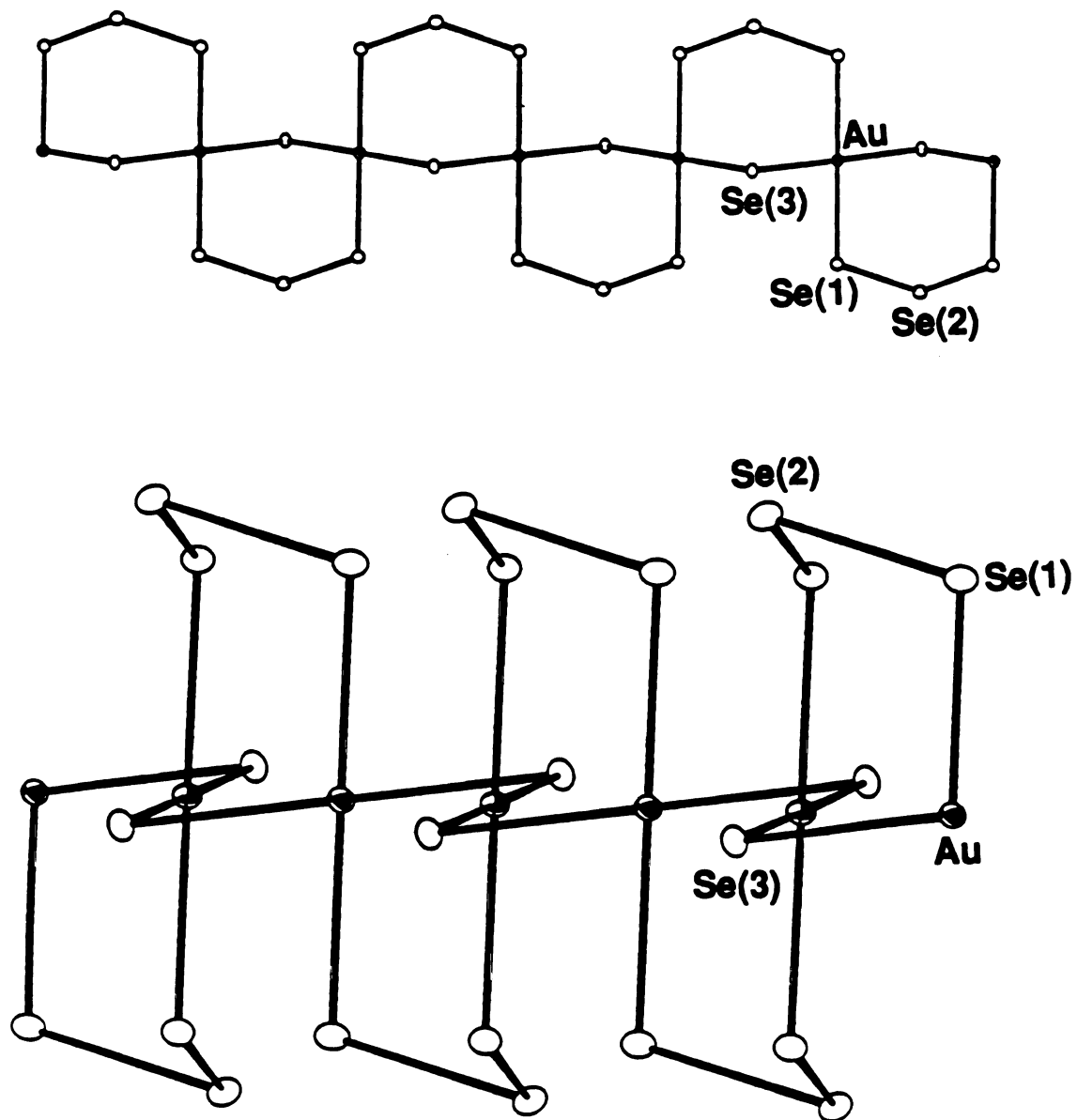


Figure 70. Two views of the $[\text{Au}(\text{Se}_3)(\text{Se})]_n^-$ chains with labeling scheme.

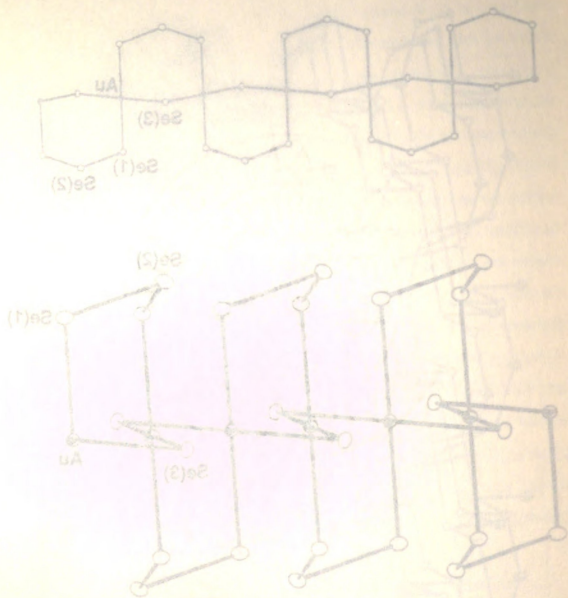


Figure 70. Two views of the $[Au(Se_3)_2]_n^-$ chains with labeling scheme.

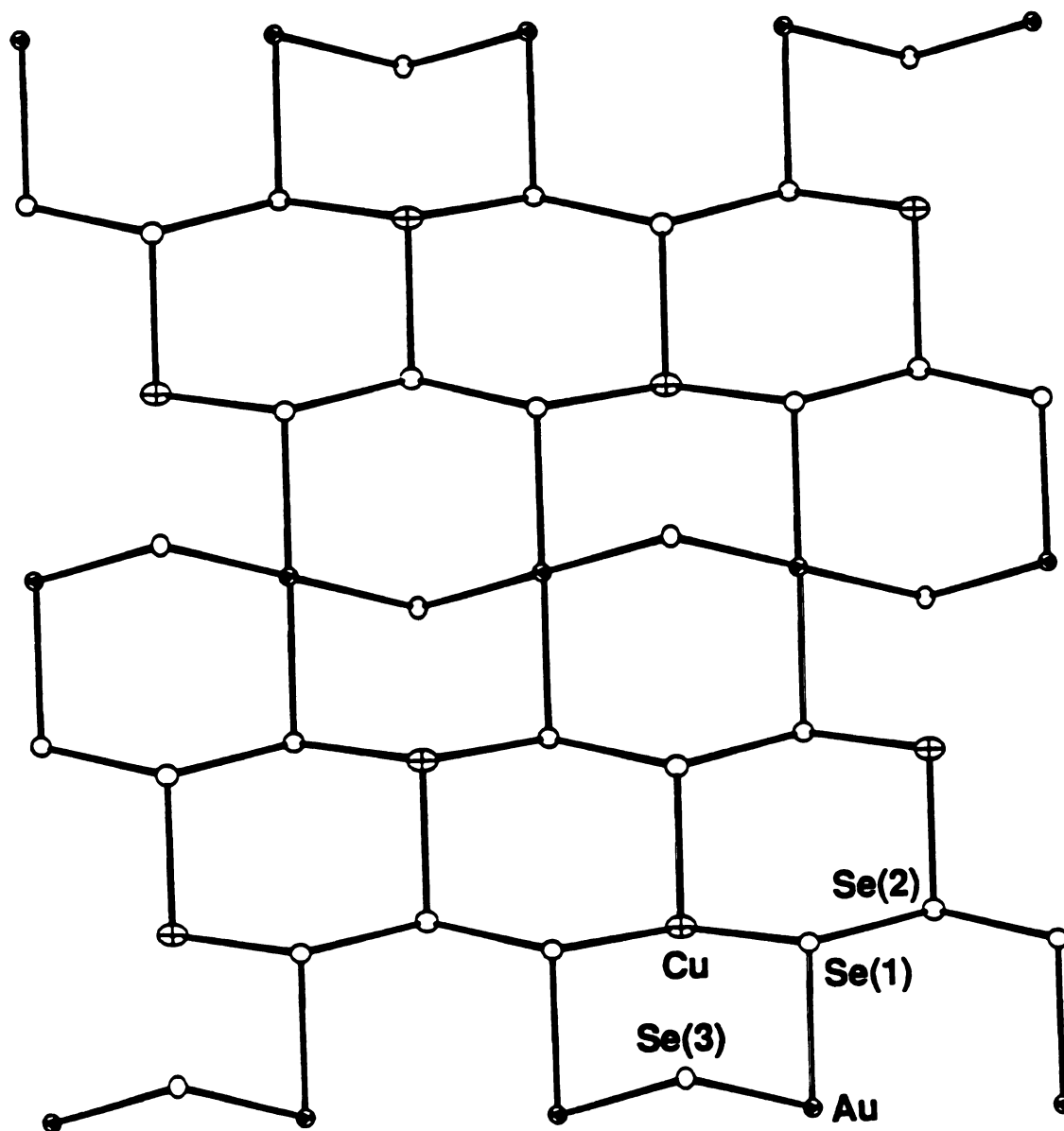


Figure 71. ORTEP representation and labeling scheme of one layer fragment of AuCuSe₄.

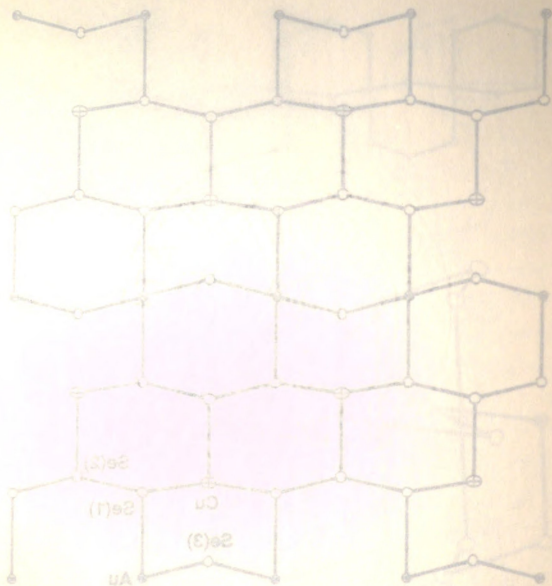
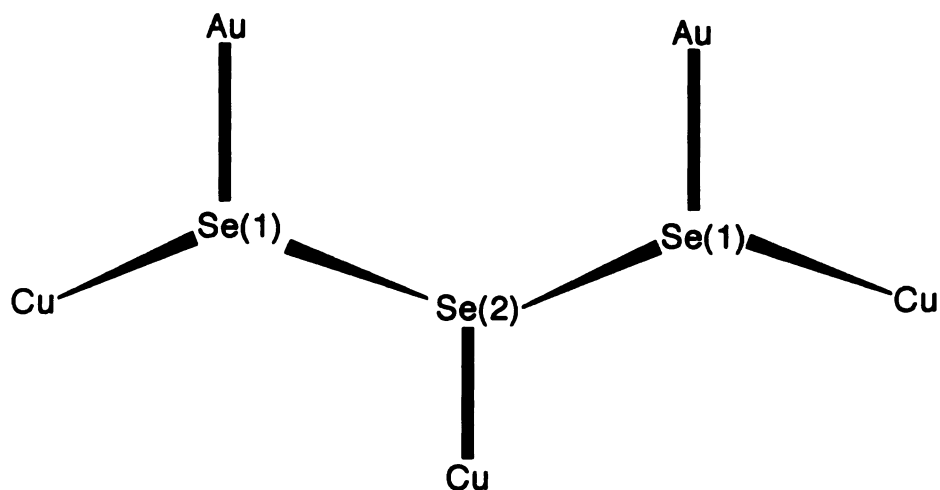


Figure 71. ORTEP representation and labeling scheme of one layer of AuCuSe_4 .

bonded to two terminal selenium atoms (Se(1)) of the Se_3^{2-} ligands of one $[\text{Au}(\text{Se}_3)\text{Se}]_n^{n-}$ chain and to one internal selenium atom (Se(2)) of the Se_3^{2-} ligands of a neighboring $[\text{Au}(\text{Se}_3)\text{Se}]_n^{n-}$ chain, resulting in a neutral two-dimensional AuCuSe_4 layer. As a result, Se_3^{2-} ligands are bonded to five metal atoms simultaneously as shown in scheme 1. To the best of our knowledge, this is the first example of such ligation of Se_3^{2-} in the known polychalcogenide chemistry.



Scheme 1

In the AuCuSe_4 layer, three-coordinate Cu atoms, situated on a crystallographic mirror plane, expand their coordination geometry to become tetrahedral by Cu-Se(3) bond formation between the layers, producing a three-dimensional structure. This creates two types of empty tunnels which are composed of 10-membered rings and 8-membered rings. These tunnels are quite small; the short dimensions are 3.254(3) Å for Cu--Se(1) and 3.283(3) Å for Se(1)--Se(1) in the 10-membered ring, and 4.036(1) Å for Se(3)--Se(3) in the 8-membered

bonded to two terminal selenium atoms (Se(1)) of the Se_2^{2-} ligands of one $[\text{Au}(\text{Se}_2)\text{Se}]_n$ chain and one internal selenium atom (Se(2)) of the Se_2^{2-} ligands of a neighboring $[\text{Au}(\text{Se}_2)\text{Se}]_n$ chain, resulting in a neutral two-dimensional AuCuSe_4 layer. As a result, Se_2^{2-} ligands are bonded to five metal atoms simultaneously as shown in scheme 1. To the best of our knowledge, this is the first example of such ligation of Se_2^{2-} in the known

polychalcogenide chemistry.



Scheme 1

in the AuCuSe_4 layer, three-coordinate Cu atoms situated on a crystallographic mirror plane, expand their coordination geometry to become tetrahedral by Cu-Se(3) bond formation between the layers, producing a three-dimensional structure. This creates two types of empty tunnels which are composed of 10-membered rings and 8-membered rings. These tunnels are quite small; the short dimensions are 3.254(3) Å for Cu-Se(1) and 3.283(3) Å for Se(1)-Se(1) in the 10-membered ring, and 4.036(1) Å for Se(2)-Se(2) in the 8-membered

ring. It should be noted that one of the tetrahedral Cu bond angles (Se(2)-Cu-Se(3)) is quite large at 152.3(1) deg. This is probably because the Cu atoms are derived from a linear rather than tetrahedral coordination. The Cu-Se(2) and Cu-Se(3) bond distances are relatively short at 2.423(3) Å, while Cu-Se(1) bond distances are long at 2.528(2) Å. Selected bond distances and angles are given in Table 90.

ring. It should be noted that one of the tetrahedral Cu bond angles ($\text{Se}(2)\text{-Cu-}\text{Se}(3)$) is quite large at $152.3(1)$ deg. This is probably because the Cu atoms are derived from a linear rather than tetrahedral coordination. The $\text{Cu-}\text{Se}(2)$ and $\text{Cu-}\text{Se}(3)$ bond distances are relatively short at $2.423(3)$ Å, while $\text{Cu-}\text{Se}(1)$ bond distances are long at $2.528(5)$ Å. Selected bond distances and angles are given in Table 90.

TABLE 90. Selected bond distances and angles

(Distances in Å, angles in degrees)



TABLE 90. Selected bond distances and angles (continued)

(Distances in Å, angles in degrees)

Se(1)-Cu-Se(2) 152.3(1)

Se(1)-Cu-Se(3) 108.5(2)

Se(2)-Cu-Se(3) 108.5(2)

Se(1)-Cu-Se(2)-Se(3) 108.5(2)

Se(1)-Cu-Se(3)-Se(2) 108.5(2)

Se(2)-Cu-Se(1)-Se(3) 108.5(2)

Se(3)-Cu-Se(1)-Se(2) 108.5(2)

Se(1)-Cu-Se(2)-Se(3)-Se(1) 108.5(2)

Se(1)-Cu-Se(3)-Se(2)-Se(1) 108.5(2)

Se(2)-Cu-Se(1)-Se(3)-Se(2) 108.5(2)

Se(3)-Cu-Se(1)-Se(2)-Se(3) 108.5(2)

Table 90. Selected Bond Distances (Å) and Angles (deg) in AuCuSe₄ with Standard Deviations in Parentheses

Au -Se(1)	2.475(1) (x2)	Se(1)-Au-Se(1)	180.00 (x2)
Au-Se(3)	2.483(1) (x2)	Se(1)-Au-Se(3)	98.26(5) (x2)
Se(1)-Cu	2.528(2) (x2)	Se(1)-Au-Se(3)	81.74(5) (x2)
Se(2)-Cu	2.411(3)	Se(1)-Cu-Se(1)	95.5(1)
Se(3)-Cu	2.423(3)	Se(1)-Cu-Se(2)	101.40(8) (x2)
		Se(1)-Cu-Se(3)	97.12(8) (x2)
		Se(2)-Cu-Se(3)	152.3(1)
Se(1)-Se(2)	2.396(2)	Au-Se(1)-Se(2)	104.28(6)
		Au-Se(1)-Cu	100.05(7)
		Se(2)-Se(1)-Cu	98.57(7)
		Se(1)-Se(2)-Se(1)	101.23(9)
		Se(1)-Se(2)-Cu	105.19(7)
		Se(1)-Se(2)-Cu	105.19(7)
		Au-Se(3)-Au	97.13(6)
		Au-Se(3)-Cu	114.44(6) (x2)

Table 90. Selected Bond Distances (Å) and Angles (deg) in AuCuSe₄ with Standard Deviations in Parentheses

Au-Se(1)	2.475(1) (x2)	Se(1)-Au-Se(1)	180.00 (x2)
Au-Se(3)	2.483(1) (x2)	Se(1)-Au-Se(3)	88.26(2) (x2)
Se(1)-Cu	2.258(2) (x2)	Se(1)-Au-Se(3)	81.74(2) (x2)
Se(2)-Cu	2.411(3)	Se(1)-Cu-Se(1)	92.2(1)
Se(3)-Cu	2.423(3)	Se(1)-Cu-Se(2)	101.40(8) (x2)
		Se(1)-Cu-Se(3)	97.12(8) (x2)
		Se(2)-Cu-Se(3)	122.9(1)
Se(1)-Se(2)	2.388(2)	Au-Se(1)-Se(2)	104.20(8)
		Au-Se(1)-Cu	100.05(1)
		Se(2)-Se(1)-Cu	98.17(1)
		Se(1)-Se(2)-Se(1)	181.20(2)
		Se(1)-Se(2)-Cu	102.13(1)
		Se(1)-Se(2)-Cu	107.10(1)
		Au-Se(2)-Au	97.13(8)
		Au-Se(2)-Cu	114.44(8) (x2)

Based on the oxidation states of the metal atoms (Cu^{1+} and Au^{3+}) which give rise to a completely filled valence band, AuCuSe_4 is expected to have semiconducting behavior. However, no effort to investigate the charge transport property of this material has been made due to small size of single crystals. Preliminary attempts to measure its band gap in the mid- and far-IR range did not show any spectral absorption. Work to grow larger single crystals for charge transport property measurements is in progress .

One interesting feature of this material is the charge neutrality of the framework; it does not require charge balancing counter cations. The fragment of this structure, the one-dimensional $[\text{Au}(\text{Se}_3)\text{Se}]_n^{n-}$ chain, would require charge balancing counter cations to be crystallized as a one-dimensional chain. However, the incorporated Cu atoms balance the charge, form covalent bonds with the chalcogenide ligands of the $[\text{Au}(\text{Se}_3)\text{Se}]_n^{n-}$ chain, and yield new structural framework. Even though the structural stoichiometry of AuCuSe_4 is same as that of the known AuCuTe_4 , AuCuSe_4 has unique structure. The structure of AuCuTe_4 ¹¹⁷, which has not been characterized well yet, is known as the derivative of AuTe_2 ¹¹⁸. This unique Se_3^{2-} containing compound of AuCuSe_4 underscores the great potential of the mixed metal system to explore new chalcogenide materials with unusual structures and perhaps interesting properties.

Based on the oxidation states of the metal atoms (Cu^{2+} and Au^{3+}) which give rise to a completely filled valence band, AuCu_2S_4 is expected to have semiconducting behavior. However, no effort to investigate the charge transport property of this material has been made due to small size of single crystals. Preliminary attempts to measure its band gap in the mid- and far-IR range did not show any spectral absorption. Work to grow larger single crystals for charge transport property measurements is in progress.

One interesting feature of this material is the charge neutrality of the framework; it does not require charge balancing counter cations. The fragment of this structure, the one-dimensional $[\text{Au}(\text{S}_2)_2\text{Se}]_n$ chain, would require charge balancing counter cations to be crystallized as a one-dimensional chain. However, the incorporated Cu atoms balance the charge from covalent bonds with the chalcogenide ligands of the $[\text{Au}(\text{S}_2)_2\text{Se}]_n$ chain and yield new structural framework. Even though the structural simplicity of AuCu_2S_4 is same as that of the known AuCu_2S_4 , AuCu_2S_4 has unique structure. The structure of AuCu_2S_4 which has not been characterized well yet, is known as the derivative of AuTe_2S_4 .¹⁸ This unique S_2^{2-} containing compound of AuCu_2S_4 underscores the great potential of the mixed metal system to explore new chalcogenide materials with unusual structures and perhaps interesting properties.

CHAPTER 9

Conclusion

In this work we have demonstrated that a new class of chalcogenide materials is accessible at intermediate temperatures using low-melting alkali-metal polychalcogenide fluxes as solvents and reagents. The alkali-metal polychalcogenide fluxes are now proven to be a significant synthesis tool in the field of chalcogenide chemistry. The low-dimensional polychalcogenide compounds presented here are beautiful examples of the structural diversity and bonding flexibility expressed by the polychalcogenide ligands in the polymeric solid lattices and rival that found in soluble molecular species. Especially, the redox chemistry associated with $\text{Au}^{1+/3+}$ ions in the polyselenide (A_2Se_x) fluxes represents the complex equilibria existing between various polychalcogenide species in the fluxes. The incorporation of structural units normally encountered in molecular chalcogenide complexes into polymeric structures should stimulate the interests of both molecular and solid state chemists. This, essentially solution, synthesis technique may eventually allow reaction control, currently available (only to some extent) in molecular chalcogenide chemistry. It could serve as an interface area between high- and low-temperature synthesis and should help bridge the ever narrowing chasm between molecular and solid state chemistry.

Low-dimensional monoselenide compounds and intriguing telluride compounds with two-dimensional framework to complicated three-dimensional

CHAPTER 9

Conclusion

In this work we have demonstrated that a new class of chalcogenide materials is accessible at intermediate temperatures using low-melting alkali-metal polychalcogenide fluxes as solvents and reagents. The alkali-metal polychalcogenide fluxes are now proven to be a significant synthesis tool in the field of chalcogenide chemistry. The low-dimensional polychalcogenide compounds presented here are peculiar examples of the structural diversity and bonding flexibility expressed by the polychalcogenide ligands in the polymeric solid lattices and their that found in simple molecular species. Especially, the redox chemistry associated with $\text{As}^{3+}/\text{As}^{5+}$ ions in the polychalcogenide $(\text{As}_2\text{S}_x)_n$ fluxes represents the complex equilibria existing between various polychalcogenide species in the fluxes. The incorporation of structural units normally encountered in molecular chalcogenide complexes into polymeric structures should stimulate the interests of both molecular and solid state chemists. This essentially solution synthesis technique may eventually allow reaction control, currently available (only to some extent) in molecular chalcogenide chemistry. It could serve as an interface area between high- and low-temperature syntheses and should help bridge the ever narrowing chasm between molecular and solid state chemistry.

Low-dimensional monochalcogenide compounds and intriguing telluride compounds with two-dimensional framework to complicated three-dimensional

cluster framework presented here show the remarkable structural complexity associated with multiple-bonding characteristics of chalcogens. The interesting electronic properties from semiconductors to metallic conductors highlighted the validity of this work in exploration of new chalcogenide materials. This intermediate temperature regime could serve as a new synthetic frontier where one can stabilize totally new structural chalcogenide compounds with perhaps unusual properties. These materials are considered as metastable or kinetically stable compared to the thermodynamically more stable high temperature counterparts.

The successful expansion of this method into mixed chalcogenide systems and mixed metal systems has shown another potential approach for the synthesis of new structural chalcogenide materials by incorporating two different sized chalcogen or metal atoms with their own preferential coordination environments into the polymeric lattice.

The remarkable ability of (poly)chalcogenide ligands, to form multidentate bonds to metal atoms and to catenate, bridges different substructures in two and three dimensions and makes the very large number of compounds accessible by this synthetic route.

It is evident that this is an exciting new synthetic area and thus far only the surface has been scratched. The bulk of this work and even more interesting chalcogenides are yet to come.

cluster framework presented here show the remarkable structural complexity associated with multiple-bonding characteristics of chalcogens. The interesting electronic properties from semiconductors to metallic conductors highlighted the validity of this work in exploration of new chalcogenide materials. This intermediate temperature regime could serve as a new synthetic frontier where one can stabilize totally new structural chalcogenide compounds with perhaps unusual properties. These materials are considered as metastable or kinetically stable compared to the thermodynamically more stable high temperature counterparts.

The successful expansion of this method into mixed chalcogenide systems and mixed metal systems has shown another potential approach for the synthesis of new structural chalcogenide materials by incorporating two different sized chalcogen or metal atoms in their own preferential coordination environments into the polymerized

The remarkable ability of polychalcogenide systems to form multibonded bonds to metal atoms and to stabilize bridges between different substructures in two and three dimensions and makes the very large number of compounds accessible by this synthetic route.

It is evident that this is an exciting new synthetic area and thus far only the surface has been scratched. The bulk of this work and even more interesting chalcogenides are yet to come.

LIST OF REFERENCES

1. (a) Rao, C. N. R.; Gopallakrishnan, J. *New Directions in Solid State Chemistry*; Cambridge University Press: New York, **1986**. (b) Hagemuller, P. *Preparative Methods in Solid State Chemistry*, Academic Press: New York, **1972**.
2. (a) Corbett, J. D. In *Solid State Chemistry: Techniques*; Cheetham, A. K., Day, P., Eds.; Oxford University Press: Oxford, **1987**. (b) West, A.R. *Solid State Chemistry and Its Applications*; John Wiley and Sons: New York, **1984**.
3. (a) Massoth, F. E.; Muralidhar, G. In *Proceedings of the Climax Fourth International Conference on the Chemistry and Uses of Molybdenum*; Barry, H. P., Mitchell, P. C. Eds.; Climax Molybdenum Company: Ann Arbor, Michigan, **1982**, p 343.
4. (a) Coucouvanis, D.; Toupadakis, A.; Koo, S. -M.; Hadjikyriacou, A. *Polyhedron* **1989**, 8, 1705-1716. (b) Clegg, W.; Christou, G.; Garner, D.; Sheldrick, G. M. *Inorg. Chem.* **1981**, 20, 1562-1566. (c) Pan, H. W.; Leonowicz, M. E.; Stiefel, E. I. *Inorg. Chem.* **1983**, 22, 672-678.
5. (a) Draganjac, M.; Simhon, E.; Kanatzidis, M. G.; Baenziger, N. C.; Coucouvanis, D. *Inorg. Chem.* **1982**, 21, 3321-3332. (b) Coucouvanis, D.; Swenson, D.; Stremple, D.; Baenziger, N. C. *J. Am. Chem. Soc.* **1979**, 101, 3392-3394. (c) Müller, A.; Krickemeyer, E.; Reinsch, U. Z. *Anorg. Allg. Chem.* **1980**, 470, 35-38.
6. Kanatzidis, M. G. *Comments Inorg. Chem.* **1990**, 10, 161-195.
7. (a) Ansari, M. A.; Ibers, J. A. *Coord. Chem. Rev.* **1990**, 100, 223-266. (b) Kolis, J. W. *Coord. Chem. Rev.* **1990**, 105, 195-219.
8. (a) Steigerwald, M. L.; Rice, C. E. *J. Am. Chem. Soc.* **1988**, 110, 4228-4231. (b) Steigerwald, M. L.; Sprinkle, C. R. *Organometallics* **1988**, 7, 245-246. (c) Steigerwald, M. L.; Sprinkle, C. R. *J. Am. Chem. Soc.* **1987**, 109, 7200-7201. (d) *Chemical Perspective in Microelectronic Materials*; Gross, M. E., Jasinski, J. M., Yates, J. T., Eds.; Materials Research Society Symposia Proceedings, **1989**, 131.(references therein)
9. Eichhorn, B. W.; Haushalter, R. C. *Inorg. Chem.* **1990**, 29, 728-731.

LIST OF REFERENCES

1. (a) Rao, C. N. R.; Gopalakrishnan, J. *New Directions in Solid State Chemistry*; Cambridge University Press: New York, 1988. (b) Hagenmuller, P. *Preparative Methods in Solid State Chemistry*; Academic Press: New York, 1973.

2. (a) Corbett, J. D. In *Solid State Chemistry*; Technique, Chestnut, A. K., Ed.; Oxford University Press: Oxford, 1987. (b) West, A. R. *Solid State Chemistry and its Applications*; John Wiley and Sons: New York, 1984.

3. (a) Masoff, F. E.; Murrill, G. In *Proceedings of the Glass Fourth International Conference on the Chemistry and Uses of Inorganic Borates*; H. P. Mitchell, R. C. Eads, Glass Division, Corning Glass Company, Ann Arbor, Michigan, 1982, p. 343.

4. (a) Coucouvanis, D.; Toubabidze, A. *J. Polym. Sci. Polym. Chem. Ed.* **1988**, *26*, 1705-1712. (b) Coucouvanis, D.; Shehrik, G. M. *Inorg. Chem.* **1981**, *20*, 1552-1553. (c) Pan, H. W.; Leonowicz, M. E.; Stibel, E. I. *Inorg. Chem.* **1982**, *21*, 572-573.

5. (a) Dragajac, M.; Simion, E.; Karcizka, M. G.; Benziger, N. C.; Coucouvanis, D. *Inorg. Chem.* **1983**, *22*, 2521-2525. (b) Coucouvanis, D.; Swanson, D.; Stempel, J. *J. Am. Chem. Soc.* **1979**, *101*, 3932-3934. (c) Miller, A.; Kalkmeyer, E.; Reinisch, U. *Z. Anorg. Allg. Chem.* **1980**, *470*, 35-38.

6. Karcizka, M. G. *Comments Inorg. Chem.* **1980**, *10*, 181-192.

7. (a) Ansel, M. A.; Ibers, J. A. *Coord. Chem. Rev.* **1980**, *100*, 223-288. (b) Koll, J. W. *Coord. Chem. Rev.* **1980**, *102*, 193-219.

8. (a) Steigerwald, M. L.; Rice, C. E. *J. Am. Chem. Soc.* **1988**, *110*, 4228-4231. (b) Steigerwald, M. L.; Spink, C. R. *Organometallics* **1988**, *7*, 245-248. (c) Steigerwald, M. L.; Spink, C. R. *J. Am. Chem. Soc.* **1987**, *109*, 7200-7201. (d) *Chemical Perspective in Microelectronic Materials*; Gross, M. E.; Jasinski, J. M.; Yates, J. T., Eds.; Materials Research Society: Symposium Proceedings, **1989**, *131*, (In French then).

9. Eichhorn, B. W.; Hauszalter, R. C. *Inorg. Chem.* **1980**, *29*, 728-731.

10. You, J. -F.; Snider, B. S.; Holm, R. H. *J. Am. Chem. Soc.* **1988**, 110, 6589-6591.
11. Marbach, G.; Strahle, J. *Angew. Chem., Int. Ed. Engl.* **1984**, 23, 246-247.
12. Wardle, R. W. M.; Bhaduri, S.; Chau, C. N.; Ibers, J. A. *Inorg. Chem.* **1988**, 27, 1747-1755.
13. Herrmann, W. A.; Rohrmann, J.; Herdtweck, E.; Hecht, C.; Ziegler, M. L.; Serhadli, O. *J. Organomet. Chem.* **1986**, 314, 295-305.
14. Coh, L. Y.; Wei, C.; Sinn, E. *J. Chem. Soc., Chem. Commun.* **1985**, 462-464.
15. Rueingold, A. L.; Bolinger, C.M.; Rauchfuss, T. B. *Acta Crystallogr.* **1986**, 42C, 1878-1880.
16. Giolando, D. M.; Papavassiliou, M.; Pickardt, J.; Rauchfuss, T. B. *Inorg. Chem.* **1988**, 27, 2596-2600.
17. Eichhorn, B. W.; Haushalter, R. C.; Cotton, F. A.; Wilson, B. *Inorg. Chem.* **1988**, 27, 4084-4085.
18. Haushalter, R. C. *Angew. Chem. Int. Ed. Engl.* **1985**, 24, 433-435.
19. Fritz, P. M.; Beck, W.; Nagel, U.; Polborn, K.; Herrmann, W. A.; Hecht, C.; Rohmann, J. *Z. Naturforsch.* **1988**, 43B, 665-670.
20. Scheidsteger, O.; Huttner, G.; Dehnicke, K.; Pebler, J. *Angew. Chem. Int. Ed. Engl.* **1985**, 24, 428.
21. Kanatzidis, M. G.; Huang, S. -P. *Inorg. Chem.* **1991**, 30, 3572-3575.
22. Kanatzidis, M. G.; Dhingra, S. *Inorg. Chem.* **1989**, 28, 2024-2026.
23. Kanatzidis, M. G.; Huang, S. -P. *Inorg. Chem.* **1989**, 28, 4667-4669.
24. Strasdeit, H.; Krebs, B.; Henkel, G. *Inorg. Chim. Acta* **1984**, 89, L11-L13.
25. Dhingra, S.; Kanatzidis, M. G. Unpublished result.
26. (a) Kanatzidis, M. G.; Huang, S. -P. *Angew. Chem. Int. Ed. Engl.* **1989**, 28, 1513-1514. (b) Huang, S. -P.; Kanatzidis, M. G. *Inorg. Chem.* **1991**, 30, 1455-1466.

10. You, J.-F.; Snider, B. S.; Holm, R. H. *J. Am. Chem. Soc.* **1988**, *110*, 6589-6591.
11. Madsch, G.; Strahle, J. *Angew. Chem., Int. Ed. Engl.* **1984**, *23*, 248-247.
12. Wardle, R. W. M.; Braduh, S.; Chau, C. N.; Ibers, J. A. *Inorg. Chem.* **1988**, *27*, 1747-1755.
13. Hermann, W. A.; Rohmann, J.; Herdtweck, E.; Hecht, C.; Ziegler, M. L.; Seifried, O. *J. Organomet. Chem.* **1988**, *319*, 295-302.
14. Corl, L. Y.; Wei, C.; Sinn, E. *J. Chem. Soc., Chem. Commun.* **1985**, 483-484.
15. Fuenfald, A. J.; Bölinger, C.M.; Rauchfus, T. B. *Acta Crystallogr.* **1988**, *45C*, 1878-1880.
16. Giolando, D. M.; Papavasiliou, M.; Pickardt, U.; Rauchfus, T. B. *Inorg. Chem.* **1988**, *27*, 2588-2590.
17. Eichhorn, B. W.; Hausler, R. G.; Gentry, T. A.; Wilson, B. *Inorg. Chem.* **1988**, *27*, 4084-4085.
18. Hausler, R. G. *Angew. Chem., Int. Ed. Engl.* **1988**, *27*, 433-435.
19. Filtz, P. M.; Beck, W.; Nagel, U.; Polster, K.; Hermann, W. A.; Hecht, C.; Rohmann, J. *Z. Naturforsch.* **1988**, *43b*, 655-670.
20. Scheidegger, O.; Hutner, G.; Delbecq, K.; Engel, J. *Angew. Chem., Int. Ed. Engl.* **1985**, *24*, 458.
21. Kanatzidis, M. G.; Huang, S.-P. *Inorg. Chem.* **1991**, *30*, 3875-3876.
22. Kanatzidis, M. G.; Diring, S. *Inorg. Chem.* **1989**, *28*, 5034-5036.
23. Kanatzidis, M. G.; Huang, S.-P. *Inorg. Chem.* **1988**, *27*, 4657-4660.
24. Straebel, H.; Krebs, B.; Henkel, G. *Inorg. Chim. Acta* **1984**, *89*, 111-113.
25. Diring, S.; Kanatzidis, M. G. Unpublished result.
26. (a) Kanatzidis, M. G.; Huang, S.-P. *Angew. Chem., Int. Ed. Engl.* **1989**, *28*, 1513-1514. (b) Huang, S.-P.; Kanatzidis, M. G. *Inorg. Chem.* **1987**, *26*, 1455-1466.

27. (a) Alonso Vante, N.; Jaegermann, W.; Tributsch, H.; Hönle, W.; Yvon, K. *J. Am. Chem. Soc.* **1987**, 111, 3251-3257. (b) Weisser, O.; Landa, S. *Sulfide Catalysis: Their Properties and Applications*; Pergamon: London, **1973**. (c) Chianelli, R. R.; Pecoraro, T. A.; Halbert, T. R.; Pan, W.-H.; Stiefel, E. I. *J. Catal.* **1984**, 86, 226-230. (d) Pecoraro, T. A.; Chianelli, R. R. *J. Catal.* **1981**, 67, 430-445.
28. (a) Smith, R. A. In *Semiconductors*; Cambridge University Press: **1978**, pp 438. (b) Barrett, B. E. et al. *Infrared Phys.* **1969**, 9, 35.
29. (a) Mickelsen, R. A.; Chen, W. S. In *Tenary and Multinary Compounds: Proceedings of the 7th Conference*; Deb, S.K., Zunger, A., Eds.; Materials Research Society, **1987**, pp 39-47. (b) Steward, J. M.; Chen, W. S.; Devancy, W. E.; Mickelsen, R. A. In *Tenary and Multinary Compounds: Proceedings of the 7th Conference*; Deb, S. K., Zunger, A., Eds.; Materials Research Society, **1987**, pp 59-64.
30. (a) Whittingham, M.S. *Science* **1976**, 192, 1126-1127. (b) Whittingham, M.S. *J. Solid State Chem.* **1979**, 29, 303-310.
31. Ballman, A. A.; Byer, R. L.; Eimerl, D.; Feigelson, R. S.; Feldman, B. J.; Goldberg, L. S.; Menyuk, N.; Tang, C.L. *Applied Optics* **1987**, 26, 224-227.
32. Rosenberger, F. In *Preparation and Characterization of Materials*; Honig, J. M., Rao, C. N. R., Eds.; Academic Press: New York, **1972**.
33. (a) Elwell, D.; Scheel, H. J. *Crystal Growth from High-Temperature Solutions*; Academic Press: London, **1975**. (b) *Molten Salts Handbook*; Janz, G. J., Ed.; Academic Press: New York, **1967**. (c) Mamantov, G. *Molten Salts*; Marcel Dekker: New York, **1969**.
34. (a) Wilke, K. -T.; Schultze, D.; Töpfer, K. *J. Cryst. Growth* **1967**, 1, 41-44. (b) Larson, G. H.; Sleight, A. W. *Phys. Lett.* **1968**, 28A, 203-204. (c) Sleight, A. W.; Jarret, H. S. *J. Phys. Chem. Solids* **1969**, 29, 868-870. (d) Harsy, M. *Mat. Res. Bull.* **1968**, 3, 483-487. (e) Shick, L. K.; von Neida, A. R. *J. Cryst. Growth* **1969**, 5, 313-314.
35. Heraldson, H.; Kjekshus, A.; Rost, E.; Steffensen, A. *Acta Chem. Scand.* **1963**, 17, 1283-1292.
36. (a) Burschka, C. *Z. Naturforsch* **1980**, 35B, 1511-1513. (b) Gattow, G.; Rosenberg, O. *Z. Anorg. Allg. Chem.* **1964**, 332, 269-280.
37. Haushalter, R.C. *Angew. Chem. Int. Ed. Engl.* **1985**, 24, 432-433.
38. Banda, R. M. H.; Craig, D. C.; Dance, I. G.; Scudder, M. L. *Polyhedron* **1989**, 19, 2379-2383.

35. (a) Alonso Valls, N.; Jaegermann, W.; Tüchtgen, H.; Hönle, W.; Yvon, K. *J. Am. Chem. Soc.* **1987**, *111*, 3251-3257. (b) Weisert, O.; Landa, S. *Surface Catalysis: Their Properties and Applications*; Pergamon: London, 1973. (c) Chinnell, R. R.; Pecora, T. A.; Halder, T. R., Eds. *Handbook of Catalysis*, 1984, **88**, 229-230. (d) Pecora, T. A.; Chinnell, R. R. *J. Catal.* **1981**, *67*, 430-445.
36. (a) Smith, R. A. In *Semiconductors*; Cambridge University Press: 1978, pp 438. (b) Barlett, B. E. et al. *Infrared Phys.* **1969**, *9*, 25.
39. (a) Mickelsen, R. A.; Chen, W. S. In *Ternary and Multinary Compounds: Proceedings of the 7th Conference*; Dir. S. K. Zunger, A. Eds.; Materials Research Society, 1987, pp 39-47. (b) Steward, J. M.; Chen, W. S.; Devany, W. E.; Mickelsen, R. A. In *Ternary and Multinary Compounds: Proceedings of the 7th Conference*; Dir. S. K. Zunger, A. Eds.; Materials Research Society, 1987, pp 59-64.
30. (a) Wittingham, M. S. *Science* **1979**, *192*, 1129-1137. (b) Wittingham, M. S. *J. Solid State Chem.* **1979**, *29*, 602-610.
31. Ballman, A. A.; Byer, R. L.; Eimer, D.; Pedigo, B. B.; Falman, B. J.; Goldberg, J. S.; Manlyk, N. *J. Appl. Phys.* **1987**, *59*, 238-237.
32. Rosenberger, F. In *Preparation and Characterization of Materials*; Hong, J. M., Ed.; Academic Press: New York, 1973.
33. (a) Ewell, D.; Schreier, H. J. *Appl. Phys. Lett.* **1977**, *31*, 1049-1050. *Solutions*; Academic Press: London, 1977. (b) Nelson, C. F. *Thin Solid Films*; Ed. J. Ed. Academic Press: New York, 1987. (c) Malmgren, M.; Mott, S.; Mott, S.; Mott, S. *Thin Solid Films* **1987**, *151*, 1-11.
34. (a) Wike, K. T.; Schurme, D.; Töpfer, K. *J. Appl. Phys.* **1987**, *61*, 41-44. (b) Larson, G. H.; Siegel, A. W. *Phys. Lett.* **1988**, *124*, 202-204. (c) Siegel, A. W.; Jaret, H. *J. Phys. Chem. Solids* **1969**, *30*, 625-670. (d) Harty, M. *Mater. Res. Bull.* **1988**, *3*, 483-487. (e) Strick, J. R.; Nolas, A. R. *J. Cryst. Growth* **1989**, *91*, 313-314.
35. Herlisen, H.; Klehrus, A.; Rogl, E.; Steffensen, A. *Acta Chem. Scand.* **1969**, *11*, 1289-1292.
36. (a) Butziska, C. Z. *Naturforsch.* **1989**, *34b*, 1511-1513. (b) Gallow, G.; Fosenberg, O. Z. *Angew. Allg. Chem.* **1984**, *32*, 289-290.
37. Hausler, R. C. *Angew. Chem. Int. Ed. Engl.* **1988**, *27*, 432-433.
38. Benda, R. M. H.; Craig, D. C.; Danos, J. G.; Soudier, M. L. *Polyhedron* **1989**, *10*, 2379-2383.

39. Kanatzidis, M. G.; Huang, S. -P. *J. Am. Chem. Soc.* **1989**, 111, 760-761.
40. Haradem, P. S.; Cronin, J. L.; Krause, R. A.; Katz, L. *Inorg. Chim. Acta* **1977**, 25, 173-179.
41. (a) Brec, R.; Evain, M.; Grenouilleau, P.; Rouxel, J. *Rev. Chim. Miner.* **1983**, 20, 283-294. (b) Brec, R.; Ouvard, G.; Evain, M.; Grenouilleau, P.; Rouxel, J. *J. Solid State Chem.* **1983**, 47, 174-184.
42. *Proceedings of the Fourth International Symposium on Molten Salts*; Blander, M., Newman, D. S., Mamantov, G., Saboungi, M. -L., Johnson, K., Eds.; Electrochemical Society: Pennington, NJ, **1990**; Vol. 84-2.
43. Diehl, R.; Nitsche, R. *J. Cryst. Growth* **1973**, 20, 38-46.
44. Scheel, H. J. *J. Cryst. Growth* **1974**, 24/25, 669-673.
45. (a) Sanjines, R.; Berger, H.; Levy, F. *Mat. Res. Bull.* **1988**, 23, 549-553. (b) Garner, R. W.; White, W. B. *J. Cryst. Growth* **1970**, 7, 343-347.
46. (a) *The Sodium-Sulfur Battery*; Sudworth, J. L., Tilley, A. R., Eds.; Chapman & Hall: London; New York, **1985**. (b) Fischer, W. *Mat. Res. Soc. Symp. Proc.* **1989**, 135, 541-551. (c) Powers, R. W.; Karas, B. R. *J. Electrochem. Soc.* **1989**, 136, 2787-2793.
47. *Gmelin's Handbuch der Anorganischen Chemie*; Verlag Chemie: Weinheim/Bergstr., FRG, **1966**; Sodium, Suppl. Part 3, pp 1202-1205 and reference therein.
48. Pearson, T. G.; Robinson, P. L. *J. Chem. Soc.* **1931**, 53, 1304-1314.
49. (a) Mathewson, G. H. *J. Am. Chem. Soc.* **1907**, 29, 867-880. (b) Klemm, W.; Sodomann, H.; Langmesser, P. *Z. Anorg. Allg. Chem.* **1939**, 241, 281-304.
50. Kanatzidis, M. G. *Chem. Mater.* **1990**, 2, 353-363.
51. (a) Sunshine, S. A.; Kang, D.; Ibers, J. A. *J. Am. Chem. Soc.* **1987**, 109, 6202-6204. (b) Sunshine, S. A.; Kang, D.; Ibers, J. A. *Mater. Res. Soc. Symp. Proc.* **1987**, 97, 391-396.
52. Kang, D.; Ibers, J. A. *Inorg. Chem.* **1988**, 27, 549-551.
53. (a) Kanatzidis, M. G.; Park, Y. *J. Am. Chem. Soc.* **1989**, 111, 3767-3769. (b) Kanatzidis, M. G.; Park, Y. *Chem. Mater.* **1990**, 2, 99-101. (c) Park, Y.; Kanatzidis, M. G. *Angew. Chem. Int. Ed. Engl.* **1990**, 29, 914-915.

39. Kanatzidis, M. G.; Huang, S. P. *J. Am. Chem. Soc.* 1989, **111**, 760-761.
40. Harwood, P. S.; Cronin, J. J.; Kraus, R. A.; Katz, L. *Inorg. Chim. Acta* 1977, **25**, 173-179.
41. (a) Brec, R.; Evain, M.; Grenouillere, P.; Rouxel, J. *Rev. Chim. Miner.* 1983, **20**, 283-294. (b) Brec, R.; Ouyed, G.; Evain, M.; Grenouillere, P.; Rouxel, J. *J. Solid State Chem.* 1983, **43**, 174-184.
42. Proceedings of the Fourth International Symposium on Molten Salts; Blander, M.; Newman, D. S.; Mamonov, G.; Sabounji, M.-L.; Johnson, K., Eds.; Electrochemical Society: Pennington, NJ, 1990. Vol. 84-2.
43. Dietl, R.; Nitsche, R. *J. Cryst. Growth* 1973, **20**, 38-48.
44. Scheel, H. J. *J. Cryst. Growth* 1974, **24**, 565-573.
45. (a) Sarjines, R.; Berger, H.; Lew, R. *Mater. Res. Bull.* 1988, **23**, 619-623. (b) Garter, R. W.; Winer, W. B. *J. Cryst. Growth* 1970, **1**, 243-247.
46. (a) The Sodium-Sulfur Battery; Sudworth, J. L.; Terry, A. R., Eds.; Chapman & Hall: London, New York, 1989. (b) Friesen, W. *Mater. Res. Soc. Symp. Proc.* 1988, **135**, 541-551. (c) Fawcett, R. G.; Kwasil, B. R. *J. Electrochem. Soc.* 1989, **136**, 2787-2790.
47. Gmelin's Handbuch der Anorganischen Chemie, 76th Ed. Chemie-Weinheim Verlag, FRG, 1985. Section: Inorg. Part 2, 25-1208 and telechem therein.
48. Pearson, T. G.; Robinson, R. L. *J. Chem. Soc.* 1941, 35, 1104-1114.
49. (a) Mathewson, G. H. *J. Am. Chem. Soc.* 1947, **69**, 887-890. (b) Klotz, W.; Sodomann, H.; Langmesser, R. *Z. Anorg. Allg. Chem.* 1939, **241**, 281-304.
50. Kanatzidis, M. G. *Chem. Mater.* 1990, **2**, 553-585.
51. (a) Sunahine, S. A.; Kang, D.; Ibers, J. A. *J. Am. Chem. Soc.* 1987, **109**, 6202-6204. (b) Sunahine, S. A.; Kang, D.; Ibers, J. A. *Mater. Res. Soc. Symp. Proc.* 1987, **82**, 391-395.
52. Kang, D.; Ibers, J. A. *Inorg. Chem.* 1988, **27**, 548-551.
53. (a) Kanatzidis, M. G.; Park, Y. *J. Am. Chem. Soc.* 1989, **111**, 3787-3789. (b) Kanatzidis, M. G.; Park, Y. *Chem. Mater.* 1990, **2**, 99-101. (c) Park, Y.; Kanatzidis, M. G. *Angew. Chem. Int. Ed. Engl.* 1990, **29**, 914-915.

54. (a) Park, Y.; Kanatzidis, M. G. *Chem. Mater.* **1991**, 3, 781-783. (b) Park, Y.; Degroot, D. C.; Schindler, J.; Kannewurf, C. R.; Kanatzidis, M. G. *Angew. Chem. Int. Ed. Engl.* **1991**, 30, 1325-1328.
55. (a) Meerschaut, A.; Rouxel, J. In *Crystal Chemistry and Properties of Materials with Quasi One-Dimensional Structures*; Rouxel, J., Ed.; D. Reidel Publishing Co.: **1986**, pp 205-279. (b) *Superconductivity in Ternary Compounds*; Fischer, O., Maple, M. B., Eds., Springer: Berlin, **1982**; Vols. I and II. (c) Chevrel, R. In *Superconductor Materials Science: Metallurgy, Fabrication and Applications*; Foner, S., Schwart, B.B., Eds.; Plenum Press: New York, **1981**; Chapter 10. (d) Whittingham, M.S. *Prog. Solid State Chem.* **1978**, 12, 41-99.
56. Smith, D. K.; Nichols, M. C.; Zolensky, M. E. POWD10: A Fortran IV Program for Calculating X-Ray Powder Diffraction Pattern, version 10, Pennsylvania State University, **1983**.
57. Walker, N.; Stuart, D. *Acta Crystallogr.* **1983**, 39A, 158-166.
58. Sheldrick, G. M. In *Crystallographic Computing 3*; Sheldrick G.M., Kruger, C., Doddard, R., Eds.; Oxford University Press: **1985**, pp175-189.
59. Frenz, B. A. The Enraf-Nonius CAD4 SDP System. In *Computing in Crystallography*; Delft University Press: Delft, Holland, **1978**, pp 64-71.
60. *TEXRAY Structure Analysis Package*, Molecular Structure Cooperation, **1985**.
61. (a) Rüdorff, W.; Schwarz, H. G.; Walter, M. *Z. Anorg. Allg. Chem.* **1952**, 269, 141-152. (b) Brown, D. B.; Zubieta, J. A.; Vella, P. A.; Wroblewski, J. T.; Watt, T.; Hatfield, W. E.; Day, P. *Inorg. Chem.* **1980**, 19, 1945-1950. (c) Klepp, K. O.; Boller, H.; Völlenkle, H. *Monatsh. Chem.* **1980**, 111, 727-733. (d) Burschka, C. *Z. Anorg. Allg. Chem.* **1980**, 463, 65-71.
62. (a) Takéuchi, Y.; Kudoh, Y.; Sato, G. *Z. Kristallogr.* **1985**, 173, 119-128. (b) Fjellrag, H.; Grønvold, F.; Stølen, S. *Z. Kristallogr.* **1988**, 184, 111-121. (c) Berry, L. G. *Am. Mineral.* **1954**, 39, 504-509. (d) Evans, H.T.; Konnert, J. A. *Am. Mineral.* **1976**, 61, 996-1000.
63. (a) Burschka, C. *Z. Naturforsch.* **1979**, 34b, 396-397. (b) Peplinski, Z.; Brown, D. B.; Watt, T.; Hatfield, W. E.; Day, P. *Inorg. Chem.* **1982**, 21, 1752-1755. (c) Whangbo, M. H.; Canadell, E. *Inorg. Chem.* **1990** 29, 1395-1387.
64. Müller, A.; Diemann, E. *Adv. Inorg. Chem.* **1987**, 31, 89-122.
65. Weller, F.; Adel, J.; Dehnicke, K. *Z. Anorg. Allg. Chem.* **1987**, 548, 125-132.

84. (a) Park, Y.; Kanatzidis, M. G. *Chem. Mater.* 1991, 3, 787-789. (b) Park, Y.; Degroot, D. C.; Schriber, J.; Kannewurf, C. R.; Kanatzidis, M. G. *Angew. Chem. Int. Ed. Engl.* 1991, 30, 1325-1328.
85. (a) Meerschaut, A.; Rouxel, J. In *Crystal Chemistry and Properties of Materials with Quasi-One-Dimensional Structures*; Fouzel, J., Ed.; D. Reidel Publishing Co.: 1988; pp. 505-523. (b) Superconductivity in Ternary Compounds; Fiechter, O.; Marez, M. B., Eds.; Springer: Berlin, 1982; Vols. I and II. (c) Oberst, R. In *Superconductor Materials Science: Metallurgy, Fabrication and Applications*; Foner, S.; Schwarz, B. B., Eds.; Plenum Press: New York, 1981; Chapter 10. (d) Whittingham, M. S. *Prog. Solid State Chem.* 1978, 12, 41-99.
86. Smith, D. K.; Nishio, M. O.; Zbarsky, M. E. POWD10: A Fortran IV Program for Calculating X-Ray Powder Diffraction Pattern; version 10; Pennsylvania State University: 1982.
87. Walker, N.; Suhl, D. *Acta Crystallogr.* 1992, 49A, 158-160.
88. Sheldrick, G. M. In *Crystallographic Computing 3*; Branders, G. M.; Kruger, C.; Dobbard, R., Eds.; Oxford University Press: 1988; pp. 151-159.
89. Frenz, B. A. *The Enraf-Nonius CAD4 SDC System in Computing in Crystallography*; Delft University Press: Delft, Holland, 1979; pp. 84-71.
90. TEXRAY; Structure Analysis Package; Molecular Structure Corporation: 1988.
91. (a) Rüdolph, W.; Schwarz, H. G.; Weller, M. Z. *Angew. Allg. Chem.* 1983, 568, 141-152. (b) Brown, D. R.; Zoungas, J. A.; Vlieg, R. A.; Wijkamp, J. T.; Watt, T.; Hatfield, W. E.; Day, P. *Inorg. Chem.* 1980, 19, 3042-3050. (c) Kiepp, K. O.; Boller, H.; Volz, H.; Munnich, G. *Inorg. Chem.* 1980, 19, 727-733. (d) Brutschka, C. Z. *Angew. Allg. Chem.* 1989, 62, 65-71.
92. (a) Takéuchi, Y.; Kubo, Y.; Sato, G. Z. *Kristallogr.* 1988, 113, 119-129. (b) Felling, H.; Gronov, F.; Steien, B. Z. *Kristallogr.* 1988, 113, 111-121. (c) Beryl, L. G. *Am. Mineral.* 1954, 39, 504-509. (d) Evans, H. T.; Könnert, J. A. *Am. Mineral.* 1978, 63, 998-1000.
93. (a) Brutschka, C. Z. *Naturforsch.* 1978, 34b, 398-397. (b) Papike, J.; Brown, D. B.; Watt, T.; Hatfield, W. E.; Day, P. *Inorg. Chem.* 1982, 21, 1752-1755. (c) Wragford, M. H.; Canadell, E. *Inorg. Chem.* 1980, 19, 1392-1397.
94. Müller, A.; Diemann, E. *Adv. Inorg. Chem.* 1987, 31, 89-122.
95. Weller, F.; Abel, J.; Drenke, K. Z. *Angew. Allg. Chem.* 1987, 60, 125-132.

66. Nagata, K.; Tshibashi, K.; Miyamoto, Y. *Jpn. J. Appl. Phys.* **1980**, 19, 1569-1573.
67. Kräuter, G.; Dehnicke, K.; Fenske, D. *Chem. -Ztg* ,**1990**, 114, 7-9.
68. (a) Jansen, M. *Angew Chem. , Int. Ed. Engl.* **1987**, 26, 1098-1111. (b) Scherbaum, F.; Huber, B.; Müller, G.; Schmitbaur, H. *Angew. Chem. Int. Ed. Engl.* **1988**, 27, 1542-1544. (c) Kahn, M. N. I.; King, C.; Heinrich, D. D.; Fackler, J. P., Jr.; Porter, L.C. *Inorg. Chem.* **1988**, 28, 2150-2154. (d) Fackler, J. P., Jr.; Porter, L. C. *J. Am. Chem. Soc.* **1986**, 108, 2750-2751.
69. (a) Dance, I. G. *Polyhedron* **1983**, 2, 1031-1043. (b) Hollander, F. J.; Coucouvanis, D. *J. Am. Chem. Soc.* **1977**, 99, 6288-6279. (c) Chadha, R.; Kumar, R.; Tuck, D. G. *J. Chem. Soc., Chem. Commun.* **1986**, 188-189. (d) Coucouvanis, D. ; Murphy, C. N.; Kanodia, S. K. *Inorg. Chem.* **1980**, 19, 2993-2988.
70. Burschka, C.; Bronger, W. *Z. Naturforsch* **1977**, 32B, 11-14.
71. (a) Burschka, C. *Z. Naturforsch.* **1979**, 34b, 675-677. (b) Haar, L. W.; Di Salvo, F. J.; Bair, H. E.; Fleming, R. M.; Waszczak, J. V.; Hatfield, W. E. *Phy. Rev.* **1987**, 35B(4), 1932-1938. (c) Fleming, R. M.; Haar, L. W.; Di Salvo, F. J. *Phy. Rev.* **1987**, 35B(10), 5388-5391.
72. Savelsberg, G.; Schäfer, H. *Z. Naturforsch* **1978**, 33B, 711-713.
73. Berger, R.; Eriksson, L. *J. Less-Common Met.* **1990**, 161, 101-108.
74. Savelsberg, G.; Schäfer, H. *Z. Naturforsch* **1978**, 33B, 370-373.
75. (a) Müller-Buschbaum, H. *Angew. Chem. Int. Ed. Engl.* **1989**, 28, 1472-1493. (b) Müller-Buschbaum, H. *Angew. Chem. Int. Ed. Engl.* **1991**, 30, 723-744. (c) Cava, R. J. *Science* **1990**, 247, 656-662. (d) Rao, C. N.; Raveau, B. *Acc. Chem. Res.* **1989**, 22, 106-113.
76. *Structural Inorganic Chemistry*, Wells, A. F., Ed.; Oxford University Press: New York, **1987**, p 538.
77. (a) Whangbo, M. -H. In *Crystal Chemistry and Properties of Materials with Quasi-One-Dimensional Structures*; Rouxel, J. Ed.; D. Reidel: **1986**, pp 27-85. (b) Whangbo, M. -H. *Acc. Chem. Res.* **1983**, 16, 95-101. (c) Canadell, E.; Whangbo, M. -H. *Inorg. Chem.* **1990**, 29, 1398-1401. (d) Whangbo, M. -H. *Electron Transfer in Biology and the Solid State: Inorganic compounds with Unusual Properties*; Johnson, M. K., Ed.; American Chemical Society: Washington, DC, **1990**, pp 269-286.
78. Park, Y.; Zhang, X.; Kanatzidis, M. G. work in progress.

76. Park, Y.; Zhang, X.; Kanatzidis, M. G. work in progress.
77. (a) Whangdo, M.-H. In *Crystal Chemistry and Properties of Materials with Guest-One-Dimensional Structures*; Rouxel, J. Ed.; D. Reidel: 1986; pp 27-85. (b) Whangdo, M.-H. *Acc. Chem. Res.* 1983, 16, 95-101. (c) Gansdell, E.; Whangdo, M.-H. *Inorg. Chem.* 1980, 19, 1388-1401. (d) Whangdo, M.-H. *Electron Transfer in Biology and the Solid State: Inorganic compounds with Unusual Properties*; Johnson, M. K., Ed.; American Chemical Society: Washington, DC, 1980; pp 289-298.
78. Structural Inorganic Chemistry; Wells, A. F., Ed.; Oxford University Press: New York, 1987; p 238.
79. Rao, C. N.; Ravasu, B. *Acc. Chem. Res.* 1989, 22, 105-112.
80. (a) Müller-Buschbaum, H. *Angew. Chem. Int. Ed. Engl.* 1989, 28, 1472-1493. (b) Müller-Buschbaum, H. *Angew. Chem. Int. Ed. Engl.* 1987, 26, 732-744. (c) Cava, R. J. *Science* 1980, 207, 686-692. (d) Rao, C. N.; Ravasu, B. *Acc. Chem. Res.* 1989, 22, 105-112.
81. Savio, F. J. *Phys. Rev.* 1977, 155(10), 2984-2987.
82. Savio, F. J.; Baur, H. E.; Flaming, R. M.; Wenzel, V.; Haffner, W. E. *Phys. Rev.* 1987, 355(4), 1982-1988. (c) Flaming, R. M.; Haffner, W. E. *Phys. Rev.* 1987, 355(4), 1982-1988.
83. (a) Buschka, C. Z. *Naturforsch.* 1973, 28b, 672-677. (b) Haffner, W. E.; Buschka, C. Z. *Naturforsch.* 1973, 28b, 672-677.
84. Buschka, C.; Bronger, W. Z. *Naturforsch.* 1973, 28b, 11-14.
85. 1980, 19, 2993-2995.
86. (a) Conover, D.; Muroy, C. M.; Kanoh, S. K. *Inorg. Chem.* 1989, 28, 189-199. (b) Conover, D.; Kumar, R.; Tuck, D. G. *J. Chem. Soc. Chem. Commun.* 1988, 1989.
87. (a) Jansen, M. *Angew. Chem. Int. Ed. Engl.* 1987, 26, 1098-1111. (b) Schürbaum, F.; Hüder, G.; Schmittau, H. *Angew. Chem. Int. Ed. Engl.* 1988, 27, 1242-1244. (c) Kahn, M. N.; King, C.; Heinrich, D. *J. Solid State Chem.* 1988, 82, 2120-2124. (d) Fackler, J. P., Jr.; Forder, L. C. *Inorg. Chem.* 1988, 27, 250-257. (e) Fackler, J. P., Jr.; Forder, L. C. *J. Am. Chem. Soc.* 1988, 110, 2520-2521.
88. Krüster, G.; Dehnick, K.; Fenske, D. *Chem.-Ztg.* 1980, 114, 7-9.
89. Nagata, K.; Teribashi, K.; Miyamoto, Y. *Jpn. J. Appl. Phys.* 1980, 19, 1569-1573.

79. (a) Roberts, L. E. J. *MTP International Review of Science, Solid State Chemistry*; Vol 10, p 241. (b) Bronger, W. *Angew. Chem. Int. Ed. Engl.* **1981**, 20, 52-62. (c) Meerschaut, A.; Gressier, P.; Guemas, L.; Rouxel, J. *J. Solid State Chem.* **1984**, 51, 307-314. (d) Böttcher, P. *Angew. Chem. Int. Ed. Engl.* **1988**, 27, 759-772. (e) Krebs, B. *Angew. Chem. Int. Ed. Engl.* **1983**, 22, 113-134.
80. Klepp, K. O.; Bronger, W. *J. Less-Common Met.* **1987**, 132, 1173-179.
81. Klepp, K. O.; Bronger, W. *J. Less-Common Met.* **1987**, 127, 65-71.
82. Klepp, K. O.; Bronger, W. *J. Less-Common Met.* **1988**, 137, 13-20.
83. Rabenau, A.; Schulz, H. *J. Less-Common Met.* **1976**, 48, 89-101.
84. *Structural Inorganic Chemistry*, Wells, A. F., Ed.; Oxford University Press: New York, **1987**, p 414.
85. Bronger, W.; Gönter, O. *J. Less-Common Met.* **1972**, 27, 73-79.
86. (a) Merz, K. M., Jr.; Hoffman, R. *Inorg. Chem.* **1988**, 27, 2120-2127. (b) Jansen, M. *Angew. Chem., Int. Ed. Engl.* **1984**, 23, 1098-1109. (c) Mehrotra, R.; Hoffman, R. *Inorg. Chem.* **1978**, 17, 2187-2189.
87. Scheldrich, W. S.; Braunbeck, H. G. *Z. Naturforsch.* **1989**, 44B, 1397-1401.
88. Sommer, H.; Hoppe, R. *Z. Anorg. Allg. Chem.* **1978**, 443, 201-211.
89. Toshikazu, O. *J. Appl. Crystallogr.* **1974**, 7, 396-397.
90. *Comprehensive Inorganic Chemistry*, Bailar, J. C., Emeléus, H. J., Nyholur, R., Trotman-Dickenson, A. F., Eds.; Pergamon Press: **1973**; Vol. 3, p 311.
91. (a) von Schnering, H. -G.; Nönle, W. *Chem. Rev.* **1988**, 88, 243-273. (b) von Schnering, H. -G. *Angew. Chem. Int. Ed. Engl.* **1981**, 20, 33-51. (c) Schafer, H. *Ann. Rev. Mat. Sci.* **1985**, 15, 1-41. (d) Bronger, W.; Müller, P. *J. Less-Common Met.* **1984**, 100, 241-247. (e) Bronger, W. *Angew. Chem. Int. Ed. Engl.* **1981**, 20, 52-62.
92. Axtell, E.; Park, Y.; Kanatzidis, M. G. manuscript in preparation.
93. (a) Donika, F. G.; Kiosse, G.; Radautsan, S. I.; Semiletov, S. A.; Zhitar, V. *F. Sov. Phys. Crystallogr.* **1968**, 12, 745-749. (b) Boorman, R. S.; Sutherland, J. K. *J. Mat. Sci.* **1969**, 4(8), 658-671. (c) Barnett, D. E.; Boorman, R. S.; Sutherland, J. K. *Phys. Status Solidi* **1971**, 4(1)A, K49-K52.

79. (a) Roberts, L. E. J. MTP International Review of Science, Solid State Chemistry; Vol 10, p 241. (b) Bronger, W. *Angew. Chem. Int. Ed. Engl.* **1981**, 20, 22-23. (c) Meerschaut, A.; Gressler, P.; Guemas, L.; Rouxel, J. *J. Solid State Chem.* **1984**, 51, 307-314. (d) Böttcher, P. *Angew. Chem. Int. Ed. Engl.* **1988**, 27, 759-772. (e) Krebs, B. *Angew. Chem. Int. Ed. Engl.* **1983**, 22, 113-124.
80. Klöpp, K. O.; Bronger, W. *J. Less-Common Met.* **1987**, 132, 1173-1179.
81. Klöpp, K. O.; Bronger, W. *J. Less-Common Met.* **1987**, 132, 65-71.
82. Klöpp, K. O.; Bronger, W. *J. Less-Common Met.* **1988**, 137, 13-20.
83. Rabenau, A.; Schulz, H. *J. Less-Common Met.* **1978**, 48, 88-101.
84. *Structural Inorganic Chemistry*, Wells, A. F., Ed., Oxford University Press, New York, **1987**, p 414.
85. Bronger, W.; Gönter, O. *J. Less-Common Met.* **1973**, 37, 73-79.
86. (a) Metz, K. M. Jr.; Hoffman, R. *Inorg. Chem.* **1978**, 17, 2150-2157. (b) Jansen, M. *Angew. Chem. Int. Ed. Engl.* **1984**, 23, 1038-1109. (c) Meitner, R.; Hoffman, R. *Inorg. Chem.* **1978**, 17, 2167-2189.
87. Scheilich, W. S.; Brundock, G. E. *Washington* **1989**, 449, 1297-1401.
88. Sommer, H.; Hoppe, R. E. *Angew. Chem.* **1979**, 449, 201-211.
89. Toshiyazu, O. *J. Appl. Crystallogr.* **1974**, 7, 194-197.
90. *Comprehensive Inorganic Chemistry*, Bala, J. G.; Emelius, H. J.; Nyholm, R.; Tolman-Dickenson, F., Eds., Pergamon Press, **1973**, Vol. 8, p 311.
91. (a) von Schnering, H.-G.; Nölde, W. *Chem. Rev.* **1988**, 68, 243-273. (b) von Schnering, H.-G. *Angew. Chem. Int. Ed. Engl.* **1981**, 20, 33-37. (c) Schärer, H. *Ann. Rev. Mat. Sci.* **1988**, 18, 1-41. (d) Bronger, W.; Müller, P. *J. Less-Common Met.* **1984**, 100, 241-247. (e) Bronger, W. *Angew. Chem. Int. Ed. Engl.* **1981**, 20, 25-29.
92. Adell, E.; Park, Y.; Kanabida, M. G. *manuscript in preparation.*
93. (a) Donika, F. G.; Klose, G.; Rabauts, S. I.; Semilov, S. A.; Zhitik, V. *F. Sov. Phys. Crystallogr.* **1988**, 12, 745-748. (b) Boorman, R. S.; Sutherland, J. K. *J. Mat. Sci.* **1982**, 41B, 858-871. (c) Bamert, D. E.; Boorman, R. S.; Sutherland, J. K. *Phys. Status Solidi* **1971**, 41(A), K49-K52.

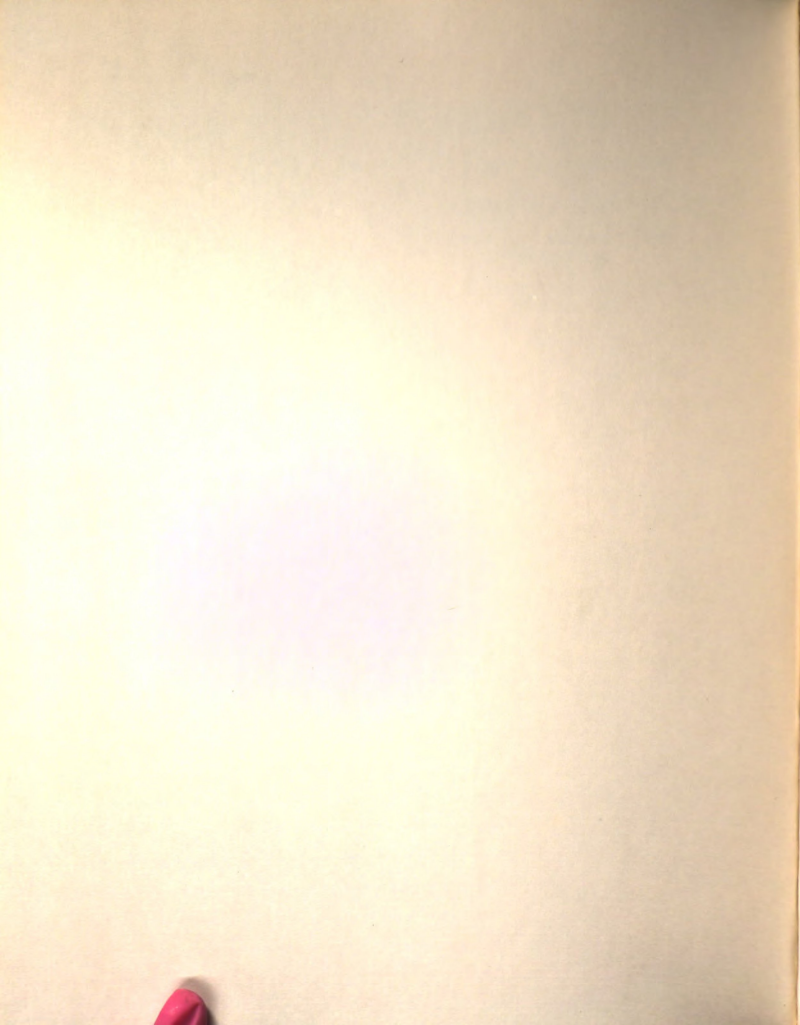
94. (a) Grey, I. E. *J. Solid State Chem.* **1974**, 11, 128-134. (b) Cohen, S.; Rendon-DiazMiron, L. E.; Steinfink, H. *J. Solid State Chem.* **1978**, 25, 179-187. (c) Hoggins, J. T.; Steinfink, H. *Acta Crystallogr.* **1977**, 33B, 673-678.
95. Schils, H.; Bronger, W. *Z. Anorg. Allg. Chem.* **1979**, 456, 187-193.
96. Bronger, W.; Schils, H. *J. Less-common Met.* **1982**, 83, 279-285.
97. (a) Berger, R.; Van Bruggen, C. F. *J. Less-Common Met.* **1984**, 99, 113-123. (b) Berger, R. *J. Less-Common Met.* **1989**, 147, 141-148.
98. Berger, R.; Eriksson, L. *J. Less-Common Met.* **1990**, 161, 165-173.
99. Berger, R. *Eur. J. Solid State Inorg. Chem.* **1988**, 25, 279-288.
100. (a) Bernstein, J.; Hoffmann, R. *Inorg. Chem.* **1985**, 24, 4100-4108. (b) Hulliger, F. *Structural Chemistry of Layer-Type Phases*; Levy, F., Ed.; Reidel: Dordrecht, Netherlands, **1976**.
101. Klepp, K. O. *Z. Naturforsch.* **1987**, 426, 130-134.
102. Savelsberg, G.; Schäfer, H. *Mat. Res. Bull.* **1981**, 16, 1291-1297.
103. Mulay, L. N. *Theory and Applications of Molecular Paramagnetism*; Boudreaux, E. A., Mulay, L. N., Eds.; Wiley: New York, **1976**, pp 494-495.
104. (a) Anderko, K.; Schubert, K. *Z. Metallkde.* **1954**, 45, 371-378. (a) Patzak, I. *Z. Metallkde.* **1956**, 47, 418-420. (c) Hulliger, F. *Structural Chemistry of Layer-Type Phases*; Levy, F., Ed.; D. Reidel Publishing Co: **1976**; Vol 5, pp133-135.
105. a) Jellinek, F. *MTP international Review of Science Inorganic Chemistry Series one*; Sharp, D. W. A., Ed.; Butterworths: London, **1972**; Vol 5, pp 339-396. (b) Folmer, J. C. W.; Jellinek, F. *J. Less-Common Met.* **1980**, 76, 153-162.
106. (a) Hoffmann, R.; Zheng, C. *J. Phys. Chem.* **1985**, 89, 4175-4181. (b) Burdett, J. K. *Chem. Rev.* **1988**, 88, 3-30. (c) Tremel, W.; Hoffmann, R.; Silvestre, J. *J. Am. Chem. Soc.* **1986**, 108, 5174-5187.
107. (a) Roof, L. C.; Pennington, W. T.; Kolis, J. W. *J. Am. Chem. Soc.* **1990**, 112, 8172-8174. (b) Adams, R. D.; Wolfe, T. A.; Eichhorn, B. W.; Haushalter, R. C. *Polyhedron*, **1989**, 21, 701-703. (c) Haushalter, R. C. *Angew. Chem. Int. Ed. Engl.* **1985**, 24, 433-435.

- Angew. Chem. Int. Ed. Engl. 1985, 24, 433-435.
- Hausalter, R. C. *Polyhedron*, 1988, 21, 701-708. (c) Hausalter, R. C. 115, 8175-8174.
- (d) Adams, R. D.; Wolfe, T. A.; Ehrhorn, B. W.; Roof, L. C.; Pennington, W. T.; Koles, J. W. *J. Am. Chem. Soc.* 1990, 112, 8175-8174.
- Silverste, J. *J. Am. Chem. Soc.* 1988, 110, 5174-5187.
- Budelt, J. K. *Chem. Rev.* 1988, 88, 3-30. (c) Tienel, W.; Hoffmann, R.; Hoffmann, R.; Zeng, C. *J. Phys. Chem.* 1988, 89, 4175-4181. (d)
- 75, 158-162.
- 389-399. (b) Folmer, J. C. W.; Jellinek, F. *J. Less-Common Met.* 1980, Series one; Sharp, D. W. A., Ed.; Butterworths: London, 1973, Vol. 5, pp
- (f) Jellinek, F. *WTP International Review of Science Inorganic Chemistry* 1978, Vol. 5, pp133-152.
- Patzek, I. *Z. Metallkunde* 1988, 41, 419-420. (a) Hülliger, F. *Structural Chemistry of Layer-Type Phases*; Levy, F., Ed.; Reidel Publishing Co. 1978.
- (a) Andenko, K.; Schirmer, K. *Z. Metallkunde* 1984, 45, 317-318. (a)
- Boudreau, E. A.; Muly, L. N. Eds. *Wiley, New York*, 1975, pp 484-495.
- Muly, L. N. *Theory and Applications of Molecular Photoacoustics*; Savelberg, G.; Schuster, H. *Adv. Phys. Chem.* 1981, 16, 121-127.
101. Klapp, K. O. *Z. Metallkunde* 1987, 49, 150-154.
- Reidel: Dordrecht, Netherlands, 1978.
- Hülliger, F. *Structural Chemistry of Layer-Type Phases*; Levy, F., Ed.
- (a) Bernstein, J.; Hoffmann, H. *Prog. Chem.* 1988, 24, 4100-4108. (b)
89. Berger, R. *Eur. J. Solid State Inorg. Chem.* 1988, 25, 279-288.
98. Berger, R.; Eriksson, L. *J. Less-Common Met.* 1980, 81, 155-173.
123. (d) Berger, R. *J. Less-Common Met.* 1980, 81, 141-148.
- (a) Berger, R.; Van Brugger, O. F. *J. Less-Common Met.* 1984, 92, 113.
98. Bronger, W.; Schils, H. *J. Less-Common Met.* 1982, 89, 279-282.
95. Schils, H.; Bronger, W. *Z. Anorg. Allg. Chem.* 1979, 458, 187-193.
- 873-878.
- 179-187. (c) Hodgins, J. T.; Steinik, H. *Acta Crystallogr.* 1977, 33B.
- Rendon-DiazMiron, J. E.; Steinik, H. *J. Solid State Chem.* 1978, 23.
- (a) Gray, I. E. *J. Solid State Chem.* 1974, 11, 128-134. (b) Cohen, S.

108. Kittel, C. *Introduction to Solid State Physics*, 5th Ed.; John Wiley & Sons: New York, 1976, pp 413-416.
109. Klepp, K. O. *J. Less-Common Met.* 1987, 128, 79-89.
110. Zhang, X.; Kanatzidis, M. G. unpublished result.
111. Ternansky, R. J.; Balogh, D. W.; Paquette, L. A. *J. Am. Chem. Soc.* 1982, 104, 4503-4504.
112. Eisenmann, B.; Katzer, H.; Schäfer, H.; Weiss, A. *Z. Naturforsch.* 1969, 246, 456-457.
113. (a) Charnock, J. M.; Garner, C. D.; Patrick, R. A. D.; Vaughan, D. J. *J. Solid State Chem.* 1989, 82, 279-289. (b) Wuensch, B. J. *Z. Kristallogr.* 1964, 119, 437-453. (c) Pauling, L.; Newmann, E. W. *Z. Kristallogr.* 1934, 88, 54-62.
114. (a) Gerl, H.; Eisenmann, B.; Roth, P.; Schäfer, H. *Z. Anorg. Allg. Chem.* 1974, 407, 135-143. (b) Jumas, P. J. -C.; Ribes, M.; Maurin, M.; Philippot, E. *Acta Crystallogr.* 1976, 32B, 444-448.
115. Whangbo, M. -H.; Canadell, E. submitted for publication.
116. (a) Kawai, S.; Ito, Y.; Kiriya, R. *Kobutsugaku Zasshi* 1972, 10(6), 487-489. (b) Kiriya, R. *Mem. Inst. Sci. Ind. Res., Osaka Univ.*, 1977, 34, 23-38.
117. (a) Tendeloo, G. V.; Amelinckx, S. *Acta Crystallogr.* 1986, 42B, 121-130. (b) Hulliger, F. *Structural Chemistry of Layer-Type Phases*; Lévy, F., Ed.; D. Reidel Publishing Co: 1976; Vol 5, pp 228-229.
118. (a) Pertlik, F. *Z. Kristallogr.* 1984, 169, 227-236. (b) Janner, A.; Dam, B. *Acta Crystallogr.* 1989, 45A, 115-123. (c) Tunnel, G.; Pauling, L. *Acta Crystallogr.* 1952, 5, 375-381. (d) Tendeloo, G. V.; Gregoriades, P.; Amelinckx, S. *J. Solid State Chem.* 1983, 50, 321-334. (e) Tendeloo, G. V.; Gregoriades, P.; Amelinckx, S. *J. Solid State Chem.* 1983, 50, 335-361. (f) Schutte, W. J.; Boer, J. L. *Acta Crystallogr.* 1988, 44B, 486-494.

108. Kittel, C. Introduction to Solid State Physics, 5th Ed.; John Wiley & Sons: New York, 1978; pp 413-418.
109. Kiepp, K. O. J. Less-Common Met. 1987, 158, 78-88.
110. Zhang, X.; Kanatzidis, M. G. unpublished result.
111. Temensky, R. J.; Balogh, D. W.; Padgett, L. A. J. Am. Chem. Soc. 1982, 104, 4503-4504.
112. Eisenmann, B.; Kaiser, H.; Schröter, H.; Weiss, A. Z. Naturforsch. 1989, 34b, 458-457.
113. (a) Charnock, J. M.; Garner, C. D.; Pattick, R. A. D.; Veighan, D. J. J. Solid State Chem. 1999, 82, 279-288. (b) Wutschn, B. J. Z. Kristallogr. 1984, 119, 437-453. (c) Pauling, L.; Newman, E. W. Z. Kristallogr. 1934, 88, 54-62.
114. (a) Gerl, H.; Eisenmann, B.; Hoff, P.; Schröter, H. Z. Anorg. Allg. Chem. 1974, 401, 130-143. (b) Jumas, P. J.-C.; Hibon, M.; Mautin, M.; Philippot, E. Acta Crystallogr. 1978, 32B, 444-448.
115. Whangdo, M.-H.; Candolfi, E. submitted for publication.
116. (a) Kawai, S.; Ito, Y.; Kiyama, R. Monatsber. Dtsch. Akad. Wiss. 1973, 105B, 487-488. (b) Kiyama, R. Mem. Inst. Sci. Res. Osaka Univ. 1973, 24, 29-36.
117. (a) Tondello, G. V.; Amelinckx, S. Acta Crystallogr. 1988, 32B, 127-130. (b) Mulliger, F. Structural Chemistry of Layer-Type Phases, Lévy, F., Ed.; Deibel Publishing Co: 1976; Vol. 5, pp 528-529.
118. (a) Perlik, F. Z. Kristallogr. 1984, 159, 227-236. (b) Janner, A.; Darm, B. Acta Crystallogr. 1988, 42A, 118-123. (c) Tunnel, G.; Pauling, L. Acta Crystallogr. 1982, 37, 375-381. (d) Tondello, G. V.; Gregorades, P.; Amelinckx, S. J. Solid State Chem. 1983, 50, 321-334. (e) Tondello, G. V.; Gregorades, P.; Amelinckx, S. J. Solid State Chem. 1983, 50, 335-351. (f) Schulte, W. J.; Boer, J. L. Acta Crystallogr. 1988, 44B, 468-494.

108. Kittel, C. Introduction to Solid State Physics, 5th Ed.; John Wiley & Sons: New York, 1976; pp 413-418.
109. Kiepp, K. O. J. Less-Common Met. 1987, 158, 79-88.
110. Zhang, X.; Kanatzidis, M. G. unpublished result.
111. Temensky, R. J.; Balogh, D. W.; Padgett, L. A. J. Am. Chem. Soc. 1982, 104, 4503-4504.
112. Eisenmann, B.; Katzer, H.; Schröter, H.; Weiss, A. Z. Naturforsch. 1989, 54b, 458-457.
113. (a) Charneck, J. M.; Garner, C. D.; Pattick, R. A. D.; Vaughan, D. J. J. Solid State Chem. 1989, 82, 270-289. (b) Wunscher, B. J. Z. Kristallogr. 1984, 119, 457-459. (c) Pauling, L.; Newman, E. W. Z. Kristallogr. 1934, 88, 54-62.
114. (a) Gehl, H.; Eisenmann, B.; Hoff, P.; Schröter, H. Z. Anorg. Allg. Chem. 1974, 401, 130-143. (b) Jumas, F. J. C.; Hibard, M.; Maudry, M.; Philippiot, E. Acta Crystallogr. 1978, 34b, 444-448.
115. Whangdo, M.-H.; Canadell, E. submitted for publication.
116. (a) Kawai, S.; Ito, Y.; Kishigami, H. J. Phys. Chem. 1972, 76, 4877-4880. (b) Kishigami, R. Mem. Inst. Sci. Res. Osaka Univ. 1972, 28, 23-38.
117. (a) Tendeloo, G. V.; Amelinckx, S. Acta Crystallogr. 1988, 44b, 101-109. (b) Hülliger, F. Structural Chemistry of Layered Phases; ILL, F. 52, D. Reidel Publishing Co.: 1976; Vol. 2, pp 228-232.
118. (a) Perlik, F. Z. Kristallogr. 1984, 166, 227-236. (b) Jenner, A.; Durr, B. Acta Crystallogr. 1988, 44A, 115-123. (c) Tümpel, G.; Pauling, L. Acta Crystallogr. 1982, 37b, 381-387. (d) Tendeloo, G. V.; Gregorčič, P.; Amelinckx, S. J. Solid State Chem. 1983, 50, 321-334. (e) Tendeloo, G. V.; Gregorčič, P.; Amelinckx, S. J. Solid State Chem. 1983, 50, 335-381. (f) Schürle, W. J.; Boer, J. L. Acta Crystallogr. 1988, 44b, 488-494.



MICHIGAN STATE UNIV. LIBRARIES



31293010490963

MICHIGAN STATE UNIV. LIBRARIES



31293010490963